CoMS_ 2020/21

Construction Materials for a Sustainable Future

Proceedings of the 2nd International Conference CoMS 2020/21

Volume 2

20-21 April 2021
Online Conference

Conference Program Committee

- Andraž Legat (chair)
- Ivana Banjad Pečur
- Dubravka Bjegović
- Mirjana Malešev
- Vlastimir Radonjanin
- Wolfram Schmidt
- Andreas Rogge
- Aljoša Šajna

Organizing Committee

- Aljoša Šajna (chair)
- Sabina Jordan
- Ema Kemperle
- Darko Korbar
- Sabina Dolenec
- Matej Michelizza
- Petra Horvat

Scientific Committee

- Andrej Anžlin
- Boris Azinović
- Ivana Banjad Pečur
- Ana Baričević
- Dubravka Bjegović
- Uroš Bohinc
- Meri Cvetkovska
- Sabina Dolenec
- Vilma Ducman
- Roland Göttig
- Lucija Hanžič
- Miha Hren
- Ksenija Janković
- Sabina Jordan
- Friderik Knez
- Lidija Korat
- Tilmann Kuhn
- Andreja Kutnar
- Andraž Legat
- Marjana Lutman

- Mirjana Malešev
- Katja Malovrh Rebec
- Ksenija Marc
- Sebastjan Meža
- Kristina Mjornell
- Ana Mladenovič
- Laurens Oostwegel
- Alexander Passer
- Vlastimir Radonjanin
- Wolfram Schmidt
- Marjana Serdar
- Ruben Snellings
- Irina Stipanović
- Aljoša Šajna
- Andrijana Sever Škapin
- Goran Turk
- Rok Vezočnik
- Johan Vyncke
- Vesna Žegarac Leskovar
- Aleš Žnidarič

TABLE OF CONTENTS

1 | **Lina Ammar, Kinda Hannawi, Aveline Darquennes**

Effect of crystalline admixtures on deformation and self-healing

UP

CoMS_
2020/21

EFFECT OF CRYSTALLINE ADMIXTURES ON DEFORMATION AND SELF-HEALING

Lina Ammar, Kinda Hannawi and Aveline Darquennes

Laboratoire de Génie Civil et Génie Mécanique (LGCGM), Institut National des Sciences Appliquées de Rennes (INSA Rennes), France
e-mail: Lina.Ammar@insa-rennes.fr, Kinda.Hannawi@insa-rennes.fr, Aveline.Darquennes@insa-rennes.fr

SUMMARY: Today, several solutions were designed to limit the concrete deformation. One of them consists of using Crystalline Admixture "CA" reducing the shrinkage of the cementitious materials. In the present research study, deformations and healing capacity of mortars containing two types of CA are evaluated on a Portland cement mortar as well as their microstructure (porosity, hydration products). To monitor the healing process, specimens are pre-cracked at 28 day-old and stored under water. The evolution of the crack dimensions is measured by means of 2D optical microscope observations after 35 and 120 days of curing. The results show that the addition of CSA and MgO-based expansive agents reduces effectively the mortar shrinkage and leads to the formation of supplementary products such as brucite and ettringite. The addition of a high content of CSA-based expansive agent is an interesting solution to ensure a self-healing capacity.

KEY WORDS: Crystalline Admixtures, Repair, Self-healing, Shrinkage, Swelling,

1 INTRODUCTION

Today, many concrete structures are deteriorated due to exposure to severe climate and work conditions for a long period of time. Consequently, in recent years, the concrete repairing processes have significantly increased and the rehabilitation costs are exceeding the investments of building new structures [1]. The used solutions and techniques are closely related to the available technologies for repairing [1-2]. To obtain a good repair mortar for the damaged structure, the design and selection of products for repair works need to be adjusted. In this direction, the self-healing materials are proposed as a promising cost-effective solution to improve the durability of the concrete structure [3].

The objective of the present work is to evolve the effect of Crystalline Admixtures (CA) added into the repair mortars to limit their shrinkage and to improve their healing capacity. The construction market contains several types of CA that are normally used to reduce the mortar permeability and/or shrinkage [4]. As reported in "ACI Committee 212" [4], CA consist of proprietary active chemicals provided in a carrier of cement and sand. The active chemicals react with water to produce supplementary products into the concrete porosity. To reduce shrinkage [5-9], several types of admixtures can be used: iron powder, alumina powder, calcium oxide, calcium sulfoaluminate and magnesia. Their chemical reaction with water leads to macroscopic volume expansion due to the formation of a large content of expansive products at early age. The crystallization and swelling pressures of these products allow compensating/reducing the autogenous shrinkage of cementitious materials [8]. The magnesia and calcium sulfoaluminate are treated in several studies [5-11]. The addition of MgO-based expansive agents leads to the formation of brucite reducing the autogenous shrinkage [5-7]. On the other hand, it appears that the addition of a shrinkage reducer into a cement matrix also reduces the crack dimensions [9-11]. The cementitious materials with 10% of calcium sulfoaluminate based expansive agent (CSA-type) were able to seal cracks up to 300 μm by the formation of ettringite inside the cracks [9-11]. This process is known as the self-healing mechanism. A self-healing material can be described as a material having a capacity of repairing its damage (cracks, deformations, etc.) relying on its own generic materials [12-15]. This mechanism takes place under moisture conditions thanks to the hydration of unhydrated particles and the carbonation of hydration products (autogenous healing), as well as the formation of supplementary products (autonomous healing). This process contributes to close partially or totally the cracks [12-14].

In the present work, two types of shrinkage reducing admixtures are tested: magnesia and calcium sulfoaluminate (MgO and CSA – type). Their effect on the repair mortars deformations under several types of curing (autogenous and

wet/dry cycles) is investigated, as well as their self-healing capacities. Moreover, their microstructure is also characterized at 28 days.

2 EXPERIMENTAL INVESTIGATIONS

2.1 Materials and mixture proportions

Three mortars made with a Portland cement (CEM I 52.5 N), standard sand (0/2), and two types of Crystalline Admixtures (CA) are studied (Table 1). Their Water/Binder and Sand/Binder ratios are equal to 0.45 and 2 respectively. Two types of shrinkage reducing admixtures are tested: MgO and CSA-based expansive agents in the mixtures named respectively *Mg5* and *CSA10* hereafter. The CA proportions are given in Table 1. Their proportion is based on the values recommended by the manufacturer, as well as on the results from the literature [5-11]. To determine the effect of CA, a mortar without CA –named *Ref*– is also tested. To obtain acceptable and similar workability (Table 1), a superplasticizer (Sika ViscoFlow-800 Power) is added (0.3% of cement mass).

Table 1: Mortar proportions (%) – Fresh mortars properties

Composition	*Ref*	*Mg5*	*CSA10*
Cement 52.5 N	100	95	90
Crystalline additive	-	5	10
Average slump (cm)	11.5	11	12
Air content (%)	2.1	3.5	3.5

2.2 Experimental program

2.2.1 Deformations

To monitor deformations, 9 prismatic specimens (4x4x16 cm^3) are made for each studied mixture. At 1 day old, three specimens are sealed with a double layer of aluminium foil to prevent moisture loss and obtain autogenous condition at 20°C (Fig. 1a). The other samples are kept at 20 ± 2 °C and 95 ± 5% of Relative Humidity (RH) until 28 days old. The total deformation measured is related to the hydration process and to the hydric exchanges between the specimens and their environment. At 28 days old, three specimens are stored under water (Water Curing - *WC*) and the others undergone Curing Cycles (*CC*) at 20°C. These last combine water and air curing at 20 ± 2 °C and 95 ± 5% of RH. Each cycle goes on for 3 days. The water exchanges between samples and their environment are monitored by means of their mass loss.

The deformation measurements are made using a retractometer with 1 μm of precision (Fig. 1b) for about 50 days. The total and autogenous deformations *(ε)* are then calculated using Equation (1), and the mass variation *(Δm)* is calculated using Equation (2):

$$\varepsilon(t) = \frac{L_i(t) - L_0}{L_0} \tag{1}$$

$$\Delta m(t) = \frac{m_i(t) - m_0}{m_0} \tag{2}$$

Where L_0 and m_0 are the initial length *(mm)* and mass *(g)* respectively measured on 1-day old specimens (just after demoulding). $L_i(t)$ and $m_i(t)$ are the length *(mm)* and mass *(g)* respectively measured at time *t*.

In order to understand the measurements of the autogenous deformation, the Internal Relative Humidity (IRH) is monitored on two cylindrical specimens characterized by a diameter (ϕ) equal to 5 cm and a height (H) equal to 6 cm. The measurements are made using a sensor of a thermo-hygrometer placed in a drill of 3.5 cm length in each specimen (Fig. 1c).
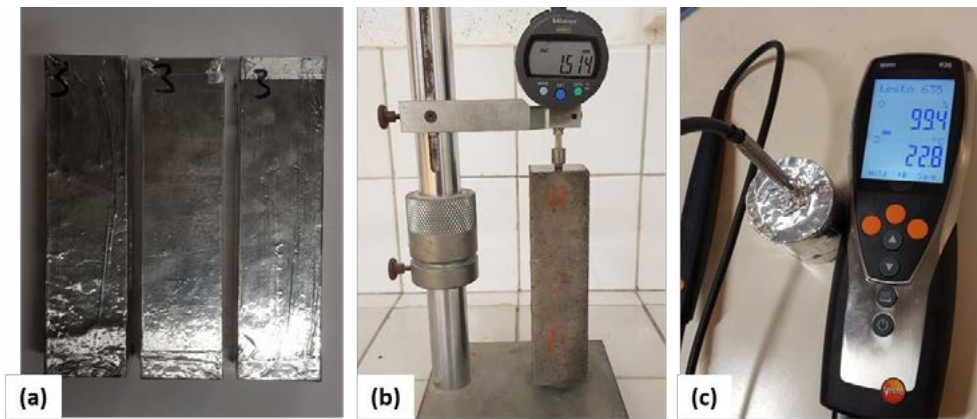
Figure 1: Specimens with a double layer of aluminum foils (a) – Retractometer for length measurement (b) – Internal Relative Humidity (IRH) measurement (c).

2.2.2 Microstructure

Microstructure (hydration products, porosity) of the studied mixtures is characterized on 28 days old specimens kept at 20 ± 2 °C and 95 ± 5 of % RH. The content of hydration products (portlandite, brucite, and calcite) is determined using ThermoGravimetric Analysis (TGA) by means of Equations 3, 4, and 5. Before the test, dried samples are crushed and ground. After, about 70-90 mg of powder is placed in a nitrogen environment and its temperature varies from 20 to 1000°C with a rate of 10°C/min. The decomposition of brucite, portlandite and calcite occurs as follows:

- Brucite ~ 250 _ 400°C [16];

$$Mg(OH)_2 \rightarrow MgO + H_2O \qquad (3)$$

- Portlandite ~ 400 _ 600°C [17];

$$Ca(OH)_2 \rightarrow CaO + H_2O \qquad (4)$$

- Calcite ~ 600 _ 1000°C [18];

$$CaCO_3 \rightarrow CaO + CO_2 \qquad (5)$$

For porosity, sorption analysis in a nitrogen environment is performed on powder samples (900-1000 mg) dried at 105°C for 24 hours. According to the International Union of Pure and Applied Chemistry "IUPAC" [19], the pore size of cementitious materials can be classified as micropores (< 2 nm), mesopores (2 _ 50 nm) and macropores (> 50 nm). So, nitrogen sorption analysis is adapted to identify mesopores.

2.2.3 Self-healing

To analyse the effect of CA on the crack healing, the following methodology is used: (1) specimens cracking, (2) monitoring the geometrical parameters of cracks (width and total area) on specimens' surfaces.

Cracking of specimens: 7x7x28 cm^3 specimens are demoulded at 1 day old and stored at 20 ± 2 °C and 95 ± 5 of % RH. The mortar specimens are cracked at 28 days old by means of three points bending test with a loading speed of 0.03 mm/min. The test is stopped when a crack opening (on the bottom face) reaches a value equal to 200 μm. During the test, the crack width is monitored using a specific ruler. After, it is measured using an optical microscope, and it varies from 120 to 200 μm. Then, all specimens are stored under water on the no-cracked face. The specimens from the same mixture are stored in the same container.

Evaluation of crack: To monitor the geometrical crack parameters and thus the self-healing process, two zones

(height = 3 cm) along the crack are analysed: one located on the lateral face and the other on the bottom face of the tested specimens. The crack width is measured on zones representative of the global crack, i.e. without defects, such as missing pieces of the cementitious matrix, parallel cracks, inclined crack path, etc. For each zone, ten points are chosen to measure the crack width during the healing process. The crack evolution is monitored using a reflective microscope. Then, the pictures are analyzed by means of "Image J" software. Each picture is binarized to separate the solid phase (white pixel) and the void (black pixel) related to the crack. The pixel size is equal to 14 µm. Crack width and total area are measured at the cracking day (28 days old) and 35 and 120 days after cracking. So, the Self-Healing Rate (*SHR*) is calculated using Equation 6.

$$SHR(t) = 1 - \frac{Crack\ area\ (t)}{Initial\ Crack\ area} \tag{6}$$

3 RESULTS AND DISCUSSION

3.1 Autogenous and total deformations

Figure 2 shows the evolution of the autogenous deformation and the IRH for all the studied mortars. It can be clearly seen that *Ref* shows the highest autogenous deformation with a value equal to -475 µm/m at 50 days. Mortars with CA shrink during the two first days and reach a value equal to -238 µm/m for *Mg5* and -74 µm/m for *CSA10* at 2 days. The autogenous shrinkage is followed by a swelling with an amplitude equal to 139 µm/m for *Mg5* and 146 µm/m for *CSA10*. This deformation reaches its maximal value at about 5 days. After this age, the mortars shrink and reach a deformation equal to -200 µm/m for *Mg5* and -300 µm/m for *CSA10* at 57 days.

The IRH decreases fast during the first week for all the studied mortars. The kinetics is slightly faster for *Ref* in agreement with its autogenous shrinkage evolution. After, the IRH evolution slows down and reaches a value equal to 89.1%, 86.4%, 84.3% at 55 days for *Mg5*, *CSA10,* and *Ref* respectively. Thus, mixtures characterized by a lower shrinkage also show a higher IRH – in agreement with the Kelvin law. During the swelling phase of *Mg5* and *CSA10*, IRH is decreasing. So, this deformation is probably related to the formation of swelling products into the porous network.
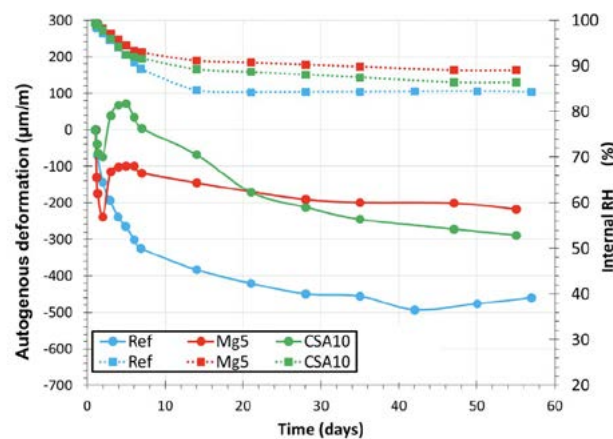
Figure 2: Evolution of the autogenous deformation (continuous line) and the Internal Relative Humidity (IRH - dotted line)
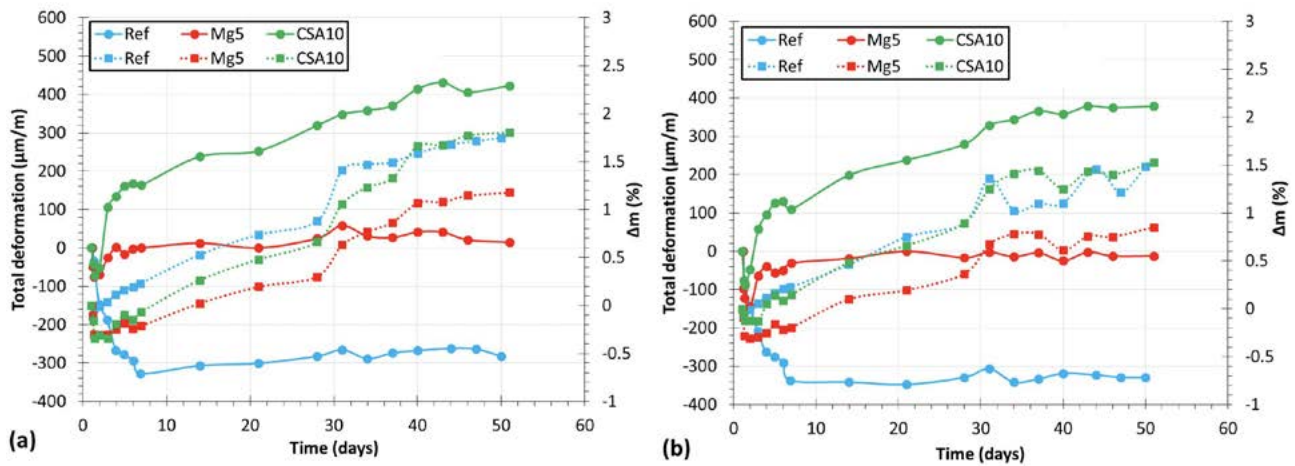
Figure 3: Total deformation (continuous line) and mass variation (dotted line) of the three studied mortars stored under *WC* (a) and *CC* (b)

Figure 3 shows the evolution of the total deformation and the mass variation for the three studied mortars. For both curing conditions, the main results are summarized hereafter:

- *Ref* shrinks fast during the first 7 days. After, its deformation tends to vary around a constant value equal to -300 µm/m. The specimen's mass directly increases, and this variation is slightly higher for specimens stored under *WC* (a difference of 0.3% at 50 days). The curing conditions after 28 days doesn't affect the total deformation.

- *Mg5* shrinks during the first 2 days until a value equal to about 100 µm/m and its mass decreases (-0,3%). After, its deformation is characterized by a swelling cancelling the shrinkage. During this period, its mass is kept constant. After a week, its deformation is stabilized and kept constant. But its mass is increasing. The curing conditions after 28 days affect the mass variation with a higher value for *WC* (a difference of 0.4% at 50 days), but not the deformation.

- *CSA10* shrinks slightly during the first day (about 80 µm/m) and its mass also decreases. Then, it swells very quickly and its shrinkage is cancelled before 3 days. From this age, its mass is increasing as well as its swelling. This last is increasing until 40 days and reaches a constant value equal to about 400 µm/m. The curing conditions after 28 days affect the mass variation with a higher value for *WC* (a difference of 0.5% at 50 days), but not the deformation.

For all the studied mortars, the total deformation presents a shrinkage during the first week mainly due to the hydration reactions. Indeed, the total deformation at 7 days is equal or inferior to the autogenous shrinkage. When water exchanges are possible between the specimens and their environment, the addition of CA allows reducing/cancelling the shrinkage. These results agree with other research works [20-22]. They also observed that the addition of an expansive agent allows reducing shrinkage at early age and leads to a swelling at long term. In this study, the expansion is more important for *CSA10*. This can be explained by the fact that 10% of CSA-based expansive agent is a significant percentage. It accelerates the formation of the swelling products like ettringite. Notice that an important expansion after 28 days can sometimes lead to cracking into concrete [22]. However, no cracks are observed on the tested specimens after 50 days. To better understand these results, the porosity and the main crystalline phases of the studied mortars are characterized.

3.2 Microstructure

Hydration products. From TGA, brucite, portlandite and calcite contents are measured. The results are shown in Table 2. Portlandite and calcite are found into the three mortars. Their content is slightly lower for *CSA10*. Brucite is only found in *Mg5*. This confirms that the growth of brucite is favored in solutions rich in magnesium ions Mg^{2+} [5].

Table 2: Brucite, portlandite, and calcite contents at 28 days (%).

Mass (%)	Mg(OH)$_2$	Ca(OH)$_2$	CaCO$_3$
Ref	-	9.1	2.3
Mg5	4.2	9.0	1.9
CSA10	-	7.4	1.1

Porosity. Figure 4 shows the pore distributions. The results show clearly that *Mg5* and *CSA10* have a lower volume of mesopores (2-50 nm), probably due to the formation of a more important content of hydration products leading to a smaller porous network at the mesoscale.
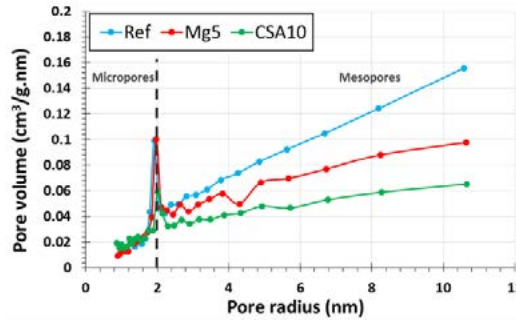
Figure 4: Pore distribution measured by sorption analysis.

3.3 Self-healing results

Figure 5 presents the Self-Healing Rate for both the bottom and lateral cracks. On the bottom face, the initial crack width is superior to 120 µm, while the initial crack width on the lateral face is smaller than 100 µm. After 35 days of water curing, bottom cracks of *Ref* and *CSA10* are healed over 90%; while 65% of *Mg5* crack is healed. The increase of water curing duration improves slightly the healing process: *SHR* is increased by 10% after 120 days of water curing for all the studied mortars. The lateral cracks of all the studied mixtures are completely healed after 35 days of water curing. It confirms that the crack size affects the healing kinetics.

For crack widths superior to 100 µm, a MgO-based expansive agent seems to reduce the healing capacity of *Mg5*. Its smaller mesoporosity could explain this behavior. Indeed, it limits the water flow through the crack, slows down the ionic exchanges and thus, delays self-healing. The CSA-based expansive agent does not seem to affect the self-healing process in comparison with the results obtained for *Ref*. The difference in behavior between *Mg5* and *CSA10* could be related to their shrinkage reducer content. In the case of *CSA10*, it could lead to a more important content of anhydrous particles on the crack surface – available for self-healing. This hypothesis will be checked later thanks to measurements of hydration advancement (TGA, calorimetry).
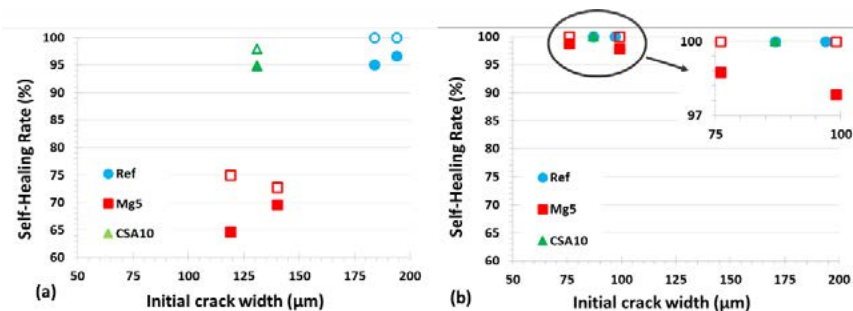
Figure 5: Self-Healing Rate for *Ref*, *Mg5* and *CSA10* after 35 days (●) and 120 days (○) of healing for the bottom (a) and lateral (b) cracks.

4 CONCLUSIONS

In this research study, the effect of two types of shrinkage reducer, MgO and CSA-based expansive agents, on the deformations and the healing process was investigated. The experimental results show that the addition of MgO and

CSA-based expansive agents reduces effectively the mortar shrinkage. When the porous network become too small to contain new hydrates such as brucite and ettringite, the crystalline pressures lead to a swelling of mortar matrix. On the other hand, the formation of brucite and ettringite in *Mg5* and *CSA10* respectively can explain their smaller mesopore volume. This could limit the water exchanges between the crack and the sound mortar matrix as well as the hydration of the anhydrous particles into the sound matrix. It can slow down the self-healing kinetics. However, this effect could be cancelled with an important content of anhydrous particles along the crack. This hypothesis has to be confirmed by supplementary tests.

REFERENCES

[1] Nunes, V-A. et al.: Mechanical compatibility and adhesion between alkali-activated repair mortars and Portland cement concrete substrate, *Construction and Building Materials*, Vol. 215 (2019), pp. 569-581

[2] Dufka, A., Bodnarova, L.: The analysis of the behavior of alkali-activated materials applied as repair mortar, *Advanced Materials Research*, Vol. 1100 (2015), pp. 50-55

[3] Breugel, K-V.: Is there a market for self-healing cement-based materials? Proceedings of the first International Conference on Self-Healing Materials, 18-20 April 2007, Noordwijk aan Zee, The Netherlands

[4] American Concrete Institute ACI Committee 212. Report on Chemical Admixtures for concrete (2010)

[5] Qureshi, T. et al.: Autogenous self-healing of cement with expansive minerals-I: Impact in early age crack healing, *Construction and Building Materials*, Vol. 192 (2018), pp. 768-784

[6] Sherir, M. A-A. et al.: Self-healing and expansion characteristics of cementitious composites with high volume of fly ash and MgO-type expansive agent, *Construction and Building Materials*, Vol. 127 (2016), pp. 80-92

[7] Sherir, M. A-A. et al.: The influence of MgO-type expansive agent incorporated in self-healing system of Engineered cementitious Composites, *Construction and Building Materials*, Vol. 149 (2017), pp. 164-185

[8] Yang, L. et al.: Mitigation techniques for autogenous shrinkage of ultra-high-performance concrete – A review, *Composites Part B*, Vol. 178 (2019), pp. 107456

[9] Zhang, Y. et al.: Effect of addition rate of expansive additive on autogenous shrinkage and delayed expansion of ultra-high strength mortar, Journal of Advanced Concrete Technology, Vol. 16 (2018), pp. 250-261

[10] Termkhajornkit, P. et al.: Self-healing ability of fly ash-cement systems, *Cement and Concrete Composites*, Vol. 31 (2009), pp. 195-203

[11] Sisomphon, K. et al.: Effect of exposure conditions on self-healing behavior of strain hardening cementitious composites incorporating various cementitious materials, *Construction and Building Materials*, Vol. 42 (2013), pp. 217-224

[12] Hearn, N.: Self-sealing, autogenous healing and continued hydration: What is the difference? *Materials and Structures*, Vol. 31 (1998), pp. 653-567

[13] Neville, A.: Autogenous healing, a concrete miracle? *Concrete International*, Vol. 24 (2002)

[14] Edvarsen, C.: Water permeability and autogenous healing of cracks in concrete, ACI Materials Journal, (1999), pp. 448-454

[15] Dry, C.: Matrix cracking repair and filling using active and passive modes for smart timed release of chemicals from fibers into cement matrices, Smart Material Structures, Vol. 3 (1994), pp. 118-123

[16] Wang, J-A. et al. : Characterizations of the thermal decomposition of brucite prepared by sol-gel technique for synthesis of nanocrystalline MgO, *Materials Letters*, Vol. 35 (1998), pp. 317-323

[17] Alonso, C., Fernandez, L.: Dehydration and rehydration processes of cement paste exposed to high temperature environments, *Journal of Materials Science*, (2004), pp. 3015-3024

[18] Pei., Y.: Effets du chauffage sur les matériaux cimentaires – impact du "self-healing" sur les propriétés de transfert, Thèse de doctorat : Génie Civil, Ecole Centrale de Lille, (2016)

[19] Moretti, P. et al. : Pore size distribution of mortars produced with agroindustrial waste, *Journal of Cleaner Production*, Vol. 187 (2018), pp. 473-484

[20] Gao, P-W. et al.: Hydration and expansion properties of novel concrete expansive agent, *Key Engineering Materials*, Vols. 405-406 (2009), pp. 267-271

[21] Huang, S. et al.: Effect of fly ash on expansion properties of concrete added with expansive agents, *Advanced Materials Research*, Vols. 393-395 (2012), pp. 684-687

[22] Zhang, Y. et al.: Effect of addition rate of expansive additive on autogenous shrinkage and delayed expansion of ultra-high strength mortar, *Journal of Advanced Concrete Technology*, Vol. 16 (2018), pp. 250-261

2

Anžlin Andrej, Bohinc Uroš, Hekič Doron, Kreslin Maja, Kalin Jan, Žnidarič Aleš

Comprehensive permanent remote monitoring system of a multi-span highway bridge

COMPREHENSIVE PERMANENT REMOTE MONITORING SYSTEM OF A MULTI-SPAN HIGHWAY BRIDGE

Anžlin Andrej[1], Bohinc Uroš[2], Hekič Doron[3], Kreslin Maja[4], Kalin Jan[5], Žnidarič Aleš[6]

[1,2,3,4,5,6] Slovenian Nationa Building and Civil Engineering Institute, Department of Structures
Dimičeva ul. 12, 1000 Ljubljana
e-mail: andrej.anzlin@zag.si

SUMMARY: As part of the reconstruction of a multi-span viaduct on a Slovenian highway, a permanent remote monitoring system with over 200 sensors was established. Several parameters are monitored on different parts of the viaduct by means of temperature sensors, accelerometers, strain gauges, long-gauge deformation and Fibre Bragg Grating (FBG) sensors. In this way strains, frequencies and temperatures on external prestressed beam cables, carbon fibre rebars used for the flexural strengthening of a deck overhang, pier caps and prestressed beams are measured and stored into the on-site central data acquisition system. This paper presents architecture of the permanent bridge monitoring system and preliminary results of the measurements.

KEY WORDS: permanent monitoring; structural health monitoring, bridge WIM; sensors; viaduct

1 INTRODUCTION

The statement that monitoring enhances our understanding of structures goes back to Leonardo da Vinci. In the 19th century the principles were established and the 20th century was devoted to developing basic methodologies. When computers, sensors and recorders became mature in the 1990s, the need for research and development was recognized by the European Comimsission and several projects related to monitoring were funded, e.g. the FP5 project IMAC [1], SAMCO Network [2], etc.

Conventional health monitoring systems have been developed to monitor bridge performance and, in some cases, the deterioration processes, with the aim to assess bridge safety. But these systems are only telling one half of the story, as they do enhance knowledge about bridge capacity but give no information about the causes of increased stresses [3]. In general, monitoring is focussed on applications in extraordinary cases and therefore does not reach daily practice. The value of monitoring must be better communicated with the bridge managers and owners, and must focus more on overall benefits of its implementation, with respect to extended lifetime of the bridges, improved mobility, environmental benefits etc. [4]. Therefore, as a part of comprehensive remediation measures undertaken on a multi-span highway bridge in Slovenia, the design and initial results of established monitoring process that measures both, response of the viaduct and the traffic loading, are presented in this paper.

2 HISTORY OF RAVBARKOMANDA VIADUCT

The first highway in Slovenia, the A1 motorway, started with the construction works of the Vrhnika - Postojna section in May 1970 and was divided into three subsections. In 1972, a Ravbarkomanda viaduct was constructed, crossing the two-lane railway line, state and local road (Figure 1). The viaduct consists of two separate structures. The right viaduct VA0174-D (traffic direction to Unec) and left viaduct VA0175-L (traffic direction to Postojna) consist of 17 and 15 spans, with total lengths of 591.4 m and 552.8 m, respectively. Both superstructures have four breaking units with five expansion joints.

Each superstructure consists of four prefabricated 2.2 m heigh I-shaped pre-stressed beams at 3.15 axial distances (Figure 1). These are connected with each other by pre-stressed transverse beams. The bridge deck is supported by elastomeric bearings. The supporting structure consists of polygonal hollow-box bridge piers and pier caps. This allows sufficient width to support the entire bridge deck. The columns were constructed with a sliding formwork, where, for ease of implementation, the unusual placement of stirrups, on the inner side of the longitudinal bars, was used [5]. Due to such implementation, stirrups cannot fulfill two very important tasks, they do not ensure the confinement of the concrete core and do not prevent the buckling of the longitudinal reinforcement.
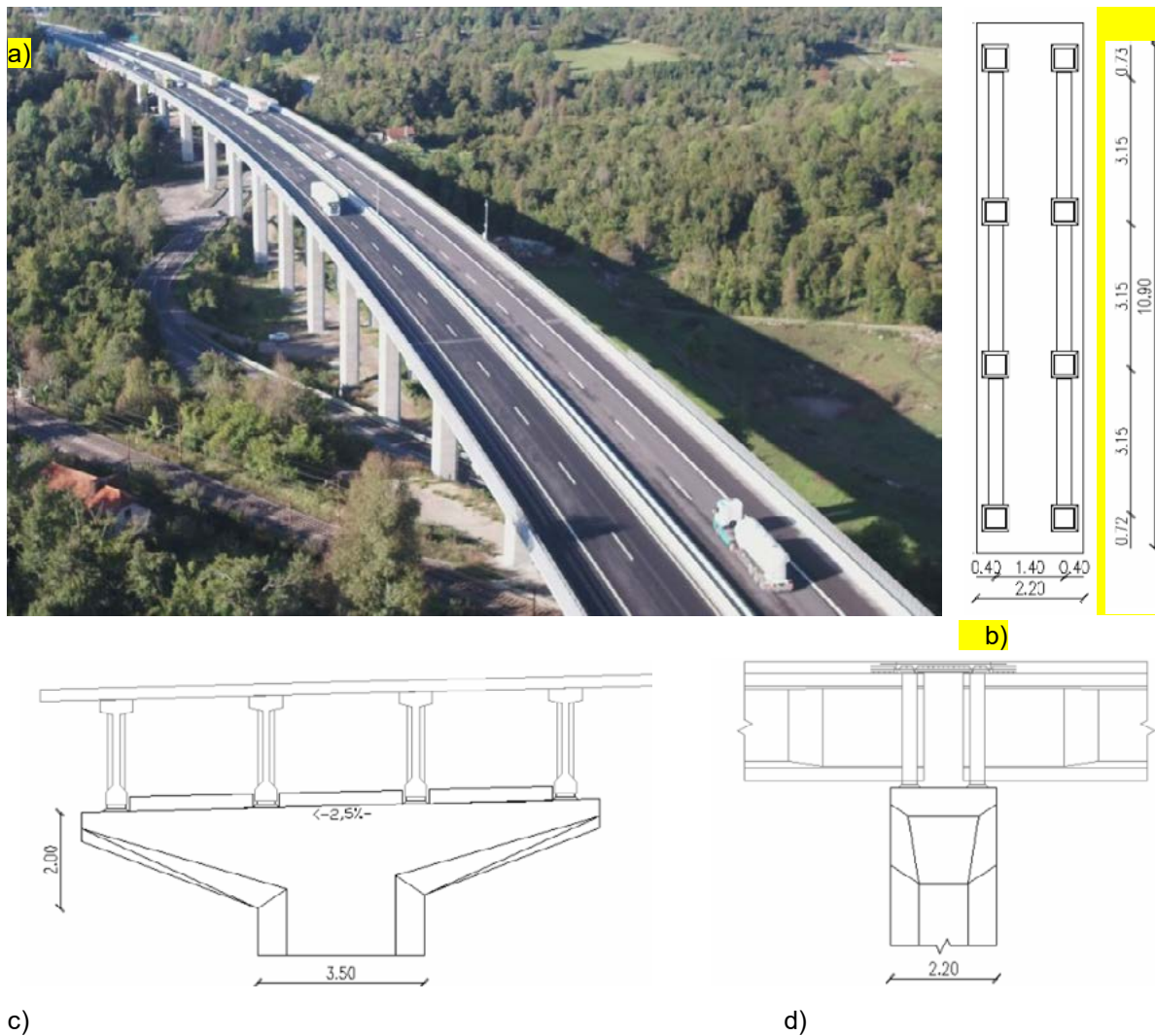
Figure 1: Ravbarkomanda viaduct: (a) aerial photo (Postojna direction), (b) plan view of pier cap, (c) pier cap and superstructure cross section, (d) side view of pier cap and superstructure
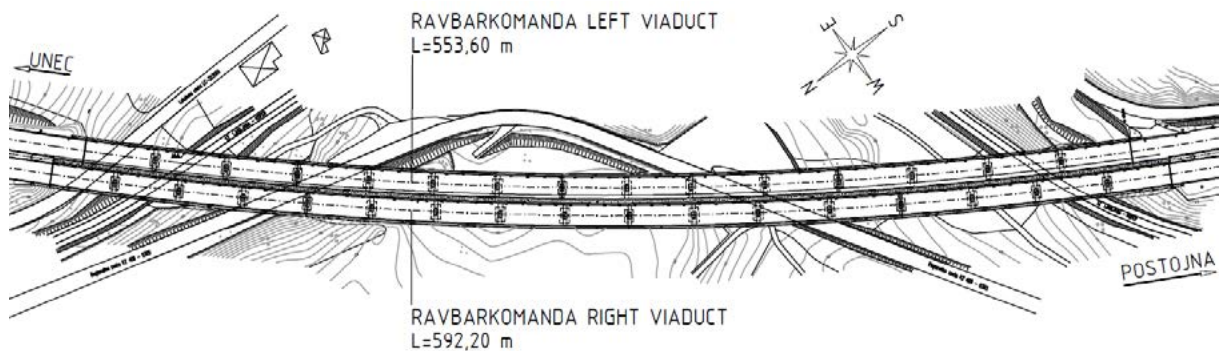
Figure 2: Plan view of Ravbarkomanda viaduct

The right viaduct is supported by sixteen 9 to 36 m high piers and the left viaduct by fourteen 14 to 36 m high piers. The polygonal cross-section of all piers is the same. The dimensions of the cross-section are 350/220 cm, with the corners cut at 60 cm with an angle of 45 °. The wall thickness is 30 cm.

During the nearly 50 years of viaducts history, several remediation works had been carried out. In 1988, the first rehabilitation works of the bridge piers were undertaken. In 1996, the major reconstruction of the superstructure was carried out, during which additional external cables were installed due to the corroded pre-stressed cables on the external I-shaped prefabricated beams (Figure 3, left).

Figure 3: Corrosion of prestressed I-shaped beam in 1996 (left) [6] and experimental studies of scaled bridge pier (right)

Analytical and experimental studies of the seismic response of the Ravbarkomanda viaduct and related box-shaped pillar structures have shown [7] that the combined bending-shear failure could occur in the case of shorter columns due to insufficient transverse reinforcement (Figure 3, right). On the basis of these studies, in 2008, the piers of the supporting structure were strengthened in order to increase the seismic capacity of the structure and to mitigate the damage in a case of severe seismic event. This was achieved by applying additional 10 cm thick concrete jacket around the bridge piers. The height of the concrete wrap corresponded to the design length the plastic hinge and the total height of the pier in the cases of higher and shorter piers, respectively, where the critical shear resistance of the columns was observed.

3   OVERVIEW ON MONITORING SYSTEM

Monitoring system, installed on the bridge, can be segmented in two groups. First part consists of the sensors, used for measuring the response of the structure (accelerometers, strain gauge sensors, long-gauge deformation sensors, FBG sensors). Second part is intended for measuring the loads, i.e. temperature sensors and strain sensors on the beams. The latter serve both for long-term monitoring of the bridge response and for measuring axle loads [8], which is important for advanced structural health monitoring system. In this way the impact of traffic can be deducted from the measured response of the bridge. Monitoring covers measurements on four key structural elements of the viaduct:

- strain and temperature measurements on the bottom side of the beams to monitor the performance of 50 years old prefabricated concrete beams,
- acceleration and temperature measurements on the external prestressed cables to monitor long-time losses or increases of pre-stressed forces,
- strain and temperature measurements on the carbon fibre rebars which are placed in the bridge slab, perpendicular to traffic direction, in order to strengthen the deck overhang in the high tensile stress regions, to monitor the effectivenss of strengthening and long time behaviour after being exposed to high temperature load during the pavement construction
- strain measurements in the high tensile stress regions of the pier caps to monitor flexural behaviour of neary 50 years old pier caps in case of increasing traffic loading.

There are two central data units located on the bridge for this monitoring project. Data from all sensors is stored at the on-site data acquisition system. The post-processing and evaluation of the measurements is performed on the off-site server, which is connected to the system by an optical connection.

The traffic loads are measured with a bridge weigh-in-motion (B-WIM) system. It applies outputs of the strain sensors, which are mounted on the lower side of the girders, temperature sensors and axle detection sensors. Detailed description of B-WIM system installation, calibration and data acquistion can be found for example in [9]. The weighing results are out of scope of this paper. Only the measurements with strain-gauges will be presented in this paper.

The scheme of the entire monitoring is shown in Figure 4. Blue colour indicates spans, where beam strains are measured, green lines indicates locations of the external prestressed cables where accelerations are measured, hatch indicates spans, where carbon fibre rebars strain measurements are performed and purple lines indicate location of pier cap's measurements.
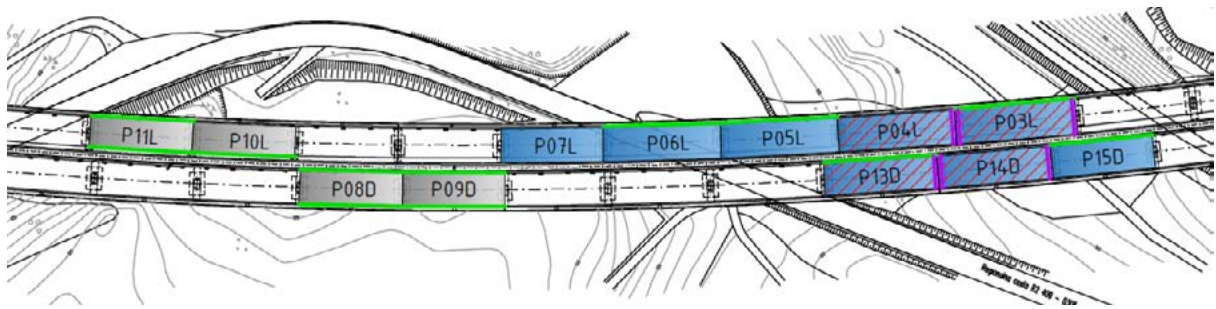
Figure 4: Scheme of monitoring

3.1 Strain measurements on beams

Flexural strains at the midspan of the beams are measured with 20 electrical resistance strain gauges in 3 spans on the right viaduct and with overall 26 electrical resistance strain gauges in 5 spans on the left viaduct. Figure 5 (left) shows strain gauge location at the midspan of the span number 15 on the right viaduct. On the Figure 5 (right), a closer look at the strain sensors is shown. Four strain sensors with a half Wheatston bridge were used at this location. Tempature near beam strain measurements location is captured by two temperature sensors in the span 14 of the right viaduct and by two temperature sensors in the span 4 of the left viaduct.

Figure 5: Two strain gauge locations on external and internal beams of the right viaduct – marked with red line (left) and 4 strain gauge sensors, all mounted at the same location on external beam of the left viaduct (right)

Data storage from all sensors to the on-site central data acquisition system runs continuously, while data post-processing is performed automatically every hour off-site on the central server, where hourly minimums, maximums and averages are calculated and compared with critical values. Figure 6 shows values of strains, induced by traffic in the period between January 2018 and June 2019. Traffic induced strains are calculated as the difference between maximum and minimum value within the measured event, wherby event is presence of one or more heavy vehicles on the bridge. Every point on the graph represents strains induced by one event.

3.2 Measurements of accelerations on external prestressed cables

One of the main reasons for rehabilitation of the Ravbarkomanda viaduct in 1996 was the severe corrosion, found on internal prestressed cables in the external prefabricated concrete beams. Load-bearing capacity of the superstructure was endangered and therefore the missing load-bearing capacity was ensured with additional external post-tensioned cables on the beams, which are located on the edges of superstructrure.
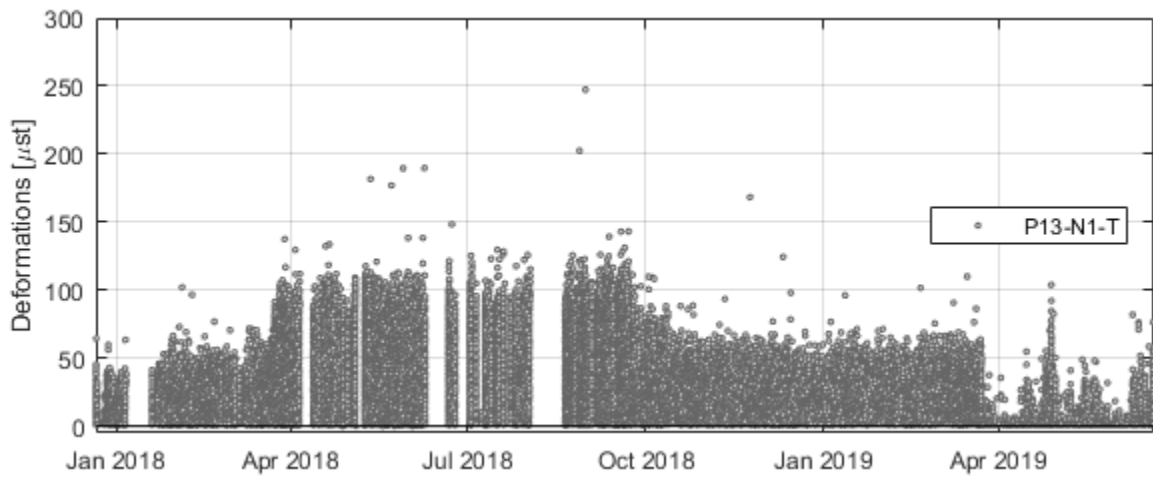
Figure 6: Traffic induced strains for beam in field number 13 of the right viaduct

External prestressing cables consist of High Density Polyethylene (HDPE) tubes in which prestressing steel strands, composed of 7 wires and the protective grout. Different configurations of prestressing cables, with different number of HDPE tubes or different number of strands are mounted on different beams. The 7-wire strand is shown in Figure 7 (left) and a prestressing cable consisting of 3 HDPE tubes with overall 6 strands is shown in Figure 7 (right).
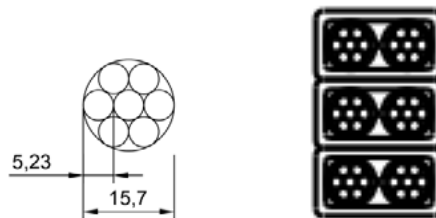
Figure 7: 7-wire prestressing steel strand (left) and prestressing cable with 3 HDPE tubes and overall 6 strands

Acceleration measurements of overall 12 cables on the right and 12 on the left viaduct are continuously undertaken. Additionally, the temperature measurements near accelerometers are performed using 4 sensors on each of the two viaducts. Accelerations of cables are measured with IEPE accelerometers mounted on the selected prestressing cables, as shown in Figure 8.

Figure 8: Prestressing cable consisting of 3 HDPE tubes and overall 6 strands with accelerometer (left) and accelerometer (right) on the left viaduct

Similarly as in the case of strains, data storage from sensors to the on-site central data acquisition system runs continuously, while data post-processing is performed automatically at 1-hour intervals. The aim of acceleration measurements is to monitor the fundamental frequency of the cable, which is related to the level of axial tension force in the prestressed cable. In this way the continuity of pre-stressing force is monitored indirectly. Every hour, the fundamental frequency is calculated within the 1-hour window, using the fast Fourier transform (FFT) [10] and is compared with the

treshold values. As an example, Figure 9 shows the variation of fundamental frequencies in the field number 15 of the right viaduct in the period between April 2018 and June 2019.
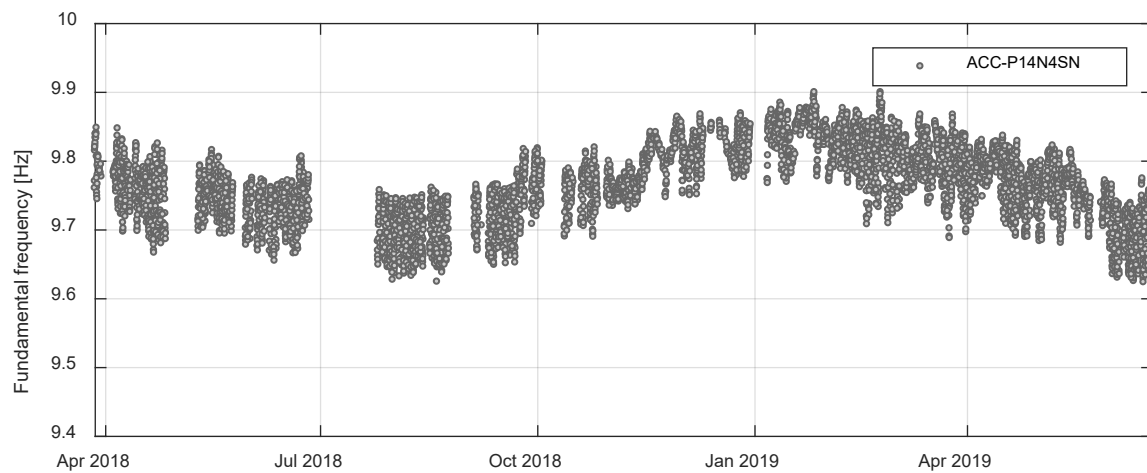
Figure 9: Hourly variation of fundamental frequencies of prestressing cable in field number 15 of the right viaduct

3.3 Carbon fibre rebar strain measurements

Deck overhangs were strengthened with near surface mounted carbon fibre rebars due the widening and installation of the concrete safety barriers. Overall, 40 FBG sensors were installed on the right and left viaduct, respectively, 20 pieces for each span (Figure 10).

Figure 10: FBG sensor glued on carbon rod (left) and installed carbon fibre rebars on the right viaduct (right)

Sensors were mounted on the carbon fibre rebars, as shown in Figure 10 (left). Rebars were afterwards installed in the precast grooves of the deck overhangs, glued with epoxy resin and covered with waterproofing and asphalt layer. Figure 10 (right) shows installed strain sensors in the span number 13 of the right viaduct. In addition, 16 temperature FBG sensors were installed in both viaducts, 4 sensors per each instrumented span. Time variation of the measured strains in carbon fibre rebars in the period between March 2018 and June 2019, induced by all loads except traffic, is shown in Figure 11. Each point on the graph represent hourly average of the minimum values measured within one minute block.
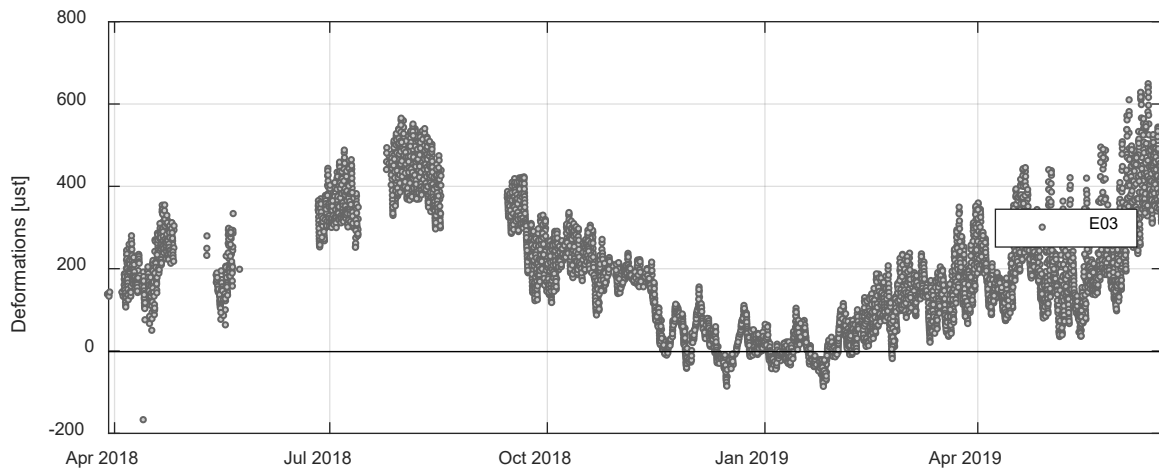
Figure 11: Hourly average strains in carbon fibre rebars, induced by all loads except traffic in the field number 13 of the right viaduct

3.4 Pier caps strain measurements

Overall 12 Smartec SOFO sensors were installed on a pier caps. Strain measurements are calcualted using the relative measured displacements divided by the sensor length, which is one or two meters. An installed sensor at the side of the pier cap in shown in Figure 12. In the Figure 13, hourly values of strains, induced by all loads (traffic, temperature, etc.) in the period between December 2018 and August 2019 are shown. Each point in the strain diagram represents hourly average of the measured strains.

Figure 12: Smartec SOFO sensor, installed at the side of the pier cap on the left viaduct: covered (a) and uncovered (b)
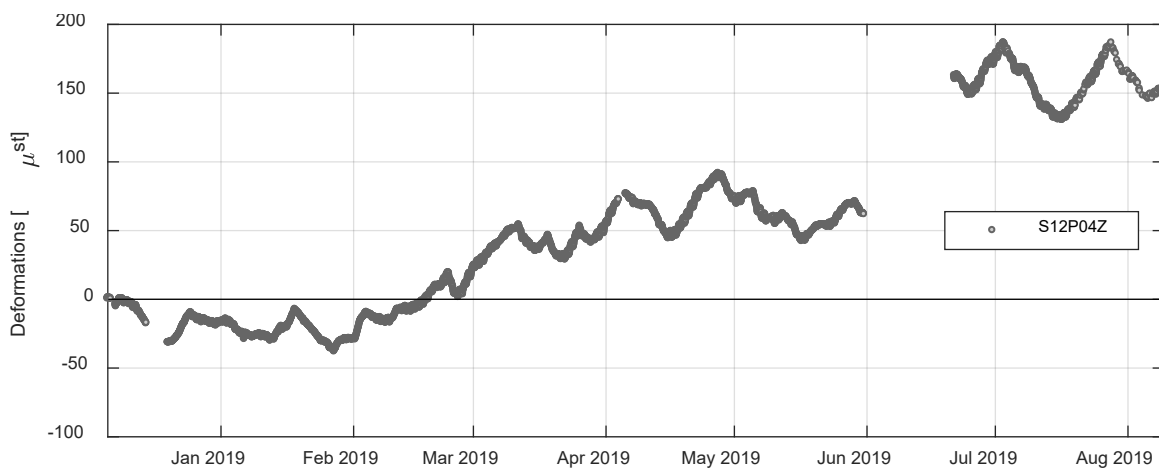
Figure 13: Hourly values of strains for sensor on the pier 12 of the left viaduct

4   CONSLUSIONS

The design and construction of the permanent monitoring systems on a multi-span highway bridge is presented in this paper. The bridge performance is monitored using over 200 sensors which are installed in order to measure the response of the bridge under traffic and ambiental loads. The system covers measurements on four key structural elements of the structure, i.e. pre-stressed cabels, carbon fibre rebars, pier caps and prefabricated beams. Acceleration and temperature measurements on the external pre-stressed cables are perfomed to monitor long-time losses or increases of pre-stressed forces. This is obtained by estimating the hourly variation of the fundamental frequency by analysing the spectral reposne of the cables. Strain and temperature measurements on the carbon fibre rebars which are placed in the bridge slab, perpendicular to traffic direction, are monitored to investigate the effectivenss of strengthening and long time behaviour ofcarbon rebars, after being exposed to high temperature load during the pavement construction. Strain measurements in the high tensile stress regions of the pier caps are performed to monitor flexural behaviour of neary 50 years old pier caps in case of increasing traffic loading. Finally, strain and temperature measurements are performed on the bottom side of the beams to monitor the long time behaviour of 50 years old prefabricated concrete beams.

The results confirm that the established monitoring system has effeicively detected the bridge response due to the environmental and traffic loads and has at the same time detected some significant events during the recondstruction of the structure, such as asphalt removal and change of traffic regime. In addition, invaluable data, in the cases of exceptional transport, was obtained, which can be used to verify performance of the viaduct in such extreme load cases. The results also imply that a less conservative and more optimal approach could be used in the assessments of realistic structural safety of bridges and, consequently, in the design of the necessary rehabilitation measures.

ACKNOWLEDGMENTS

REFERENCES

[1] IMAC: Integrated monitoring and assessment of cables, Europen Comission, Brussels, (2004)
[2] SAMCO F08b: Guideline for Structural Health Monitoring, European Comission, Brussels, (2006)
[3] Lydon, M., Taylor, S.E., Robinson D., Callender, P., Doherty,C., Grattan S. K. T. & OBrien E. J.: Development of a Bridge Weigh-in-Motion Sensor: Performance Comparison Using Fiber Optic and Electric Resistance Strain Sensor Systems, *IEEE Sensors Journal*, Vol. (14) No. 12, pp. 4284-4296, (2014)
[4] C. 1402: Quantifying the value of structural health monitoring, COST, Brussels (2019)
[5] Vidrih, Z.: *Potresni odziv betonskih mostov s pomanjkljivimi konstrukcijskimi detajli*, Doctoral dissertation, University of Ljubljana, Ljubljana, (2012).
[6] Archive DRSI: Viadukta Ravbarkomanda: sanacija levega in desnega objekta, junij 95-oktober 97
[7] ZAG P 0632/04-620-1, Poročilo o modelni preiskavi prototipa votlega stebra viadukta Ravbarkomanda, ZAG, Ljubljana, (1997)
[8] Moses, F.: Weigh-In-Motion system using instrumented bridges, *ASCE Transportation Engineering Journal*, Vol. (105), No. 3, pp. 233-249, (1979)
[9] Richardson J., Jones S. L., Brown A., Obrien E. J. & Hajializadeh, D. On the use of bridge weigh-in-motion for overweight truck enforcment, *International Journal of Heavy Vehicle Systems*, Vol. (21), No. 2, pp. 83-104, (2014)
[10] Press, W. H., Teukolsky, S. A., Vetterling, W. T. & Flannery, B. P. *Numerical Recipes: The Art of Scientific Computing*, 3rd. ed., Cambridge: Cambridge University Press, (2007)
[11] Žnidarič, A., Kalin, J. & Kreslin, M. Improved accuracy and robustness of bridge weigh-in-motion systems. *Structure and Infrastructure Engineering*, Vol. (14), No. 4, p. 13, (2017)

3

Suzana R. Draganić, Jasmina J. Dražić, Mirjana M. Malešev, Mirjana Đ. Laban, Olivera R. Bukvić

Energy efficiency improvement and fire safety of high-rise residential buildings' façades

CoMS_
2020/21

ENERGY EFFICIENCY IMPROVEMENT AND FIRE SAFETY OF HIGH-RISE RESIDENTIAL BUILDINGS' FAÇADES

Suzana R. Draganić[1], Jasmina J. Dražić[2], Mirjana M. Malešev[3], Mirjana Đ. Laban[4], Olivera R. Bukvić[5]

[1,2,3,4,5] University of Novi Sad, Faculty of Technical Sciences, Department of Civil Engineering and Geodesy
Trg Dositeja Obradovica 6, 21000 Novi Sad, Serbia
e-mail: suzanav@uns.ac.rs, dramina@uns.ac.rs, miram@uns.ac.rs, mlaban@uns.ac.rs, olivera.bukvic@uns.ac.rs

SUMMARY: In the second half of the XX century several dozens of high-rise residential buildings were built in Novi Sad, with different variants of external walls. After years of exploitation and lack of regular maintenance, there is a need for renewal of their facades in order to comply with the requirements of contemporary technical regulations and standards. The problems of buildings' thermal renewal are closely related to fire safety issues, thus applied solutions have to meet both the energy efficiency and fire safety requirements. Within the first part of the paper, evolution of Serbian regulations in the field of thermal protection and fire safety of façades is presented. In the second part an analysis of the possibilities for improving the energy performance of high-rise residential buildings in Novi Sad, through a case study, was carried out. The issue of optimal thermal insulation material selection in the façade renewal process was considered.

KEY WORDS: high-rise residential buildings; façade renewal; thermal insulation; energy efficiency; fire safety.

1 INTRODUCTION

Buildings are responsible for approximately 40% of EU energy consumption and 36% of the CO_2 emissions, making them the single largest energy consumer in Europe. Currently, about 35% of EU's buildings are over 50 years old and almost 75% of the building stock is energy inefficient, while only 0,4-1,2% of the building stock is renovated each year [1]. Therefore, improving the energy performance of buildings is crucial for reaching the EU's 2030 climate and energy targets and one of the most common measures is installation of an additional thermal insulation layer on facades. As the problems of buildings' thermal renewal are closely related to fire safety issues, applied renewal solutions have to meet both the energy efficiency, as well as fire safety requirements.

The total number of dwellings in the Republic of Serbia (RS) is 3,23 million [2] which clearly indicates the potential for energy savings in this sector. Housing stock built in the second half of the XX century is built according to the currently out-dated energy regulations which results with the average energy consumption that exceeds 150 KWh/m^2 per year, while in developed European countries is below 50 kWh/m^2 [3]. In addition, the fire safety regulations in analysed period were rather modest, without detailed guidelines, so today these buildings pose a particular problem when it comes to taking protective measures to reduce the risk of fire and its spread when a fire occurs.

In the second half of the XX century more than 41.223 apartments were built in Novi Sad. Half of the buildings are built with industrial building technology (50%), while others are built in a traditional manner (36%) or by applying advanced construction technology (14%) [4]. There are about 70 high-rise residential buildings (buildings with 11 or more storeys), mostly built with the prestressed industrial prefabricated IMS building technology. Previous research [5] has indicated low fire safety level of these buildings. The collected and processed statistics on the fire occurrence indicate a constant increase in the number of fires in multi-storey residential buildings, as well as the increase in the percentage of residential fires in the total number of fires [6]. Also, unsatisfactory technical condition was determined on most façade elements [4]. After years of exploitation and lack of regular maintenance, there is a need for renewal of these buildings, as well as for the improvement of façade performances in order to comply with the contemporary technical regulations requirements.

The RS is currently in the process of intensive harmonization of technical regulations with EU legislation, so significant changes have been made in the areas of design and construction of buildings [7], construction products [8] and fire protection [9]. *Safety in case of fire* and *energy economy and heat retention* represent two of seven basic requirements that construction products and buildings must satisfy for an economically reasonable working life, subject to normal maintenance, which applies also to the existing buildings in renewal process [8,10]. Facades are usually renewed by applying an additional thermal insulation layer. However, selection of materials with satisfactory thermal but poor reaction-

UP

to-fire performance can contribute to the spread of fire along the facade which can result in catastrophic consequences – as evidenced by the increased number of fires in residential buildings in the world.

In order to perceive limitations in the renewal solution selection, evolution of Serbian regulations in the field of thermal protection and fire safety of façades is presented within the first part of the paper. In the second part an analysis of the possibilities for improving the energy performance of high-rise residential buildings in Novi Sad, through a case study, was carried out. The issue of optimal thermal insulation material selection in the façade renewal process was considered.

2   LIMITATIONS IN THE SELECTION OF A FAÇADE RENEWAL SOLUTION WITH RESPECT TO SERBIAN LEGISLATION

2.1 ENERGY EFFICIENCY AND THERMAL PROTECTION OF BUILDINGS

After the World War II, the energy required to heat a building was determined by calculations [11] directed towards satisfying thermal comfort, while the thermal transmittance (U-value) was not a limiting parameter for the external walls.

The first requirements for thermal protection of the external building walls were defined in 1967 [12]. The regulation defined the maximum U-values for the perimeters walls, for the three climate zones (Figure 1). Due to the lack of calculation methods, the defined requirements represented a temporary solution, until the adoption of the first normative that exclusively concerned the thermal protection of buildings, in 1970 [13]. The required U-values were reduced and the relevant data for the calculation were given. It was stated that the structures and elements of buildings must be protected against moisture, which indicated the introduction of the *water vapour diffusion* parameter in the thermal calculation.
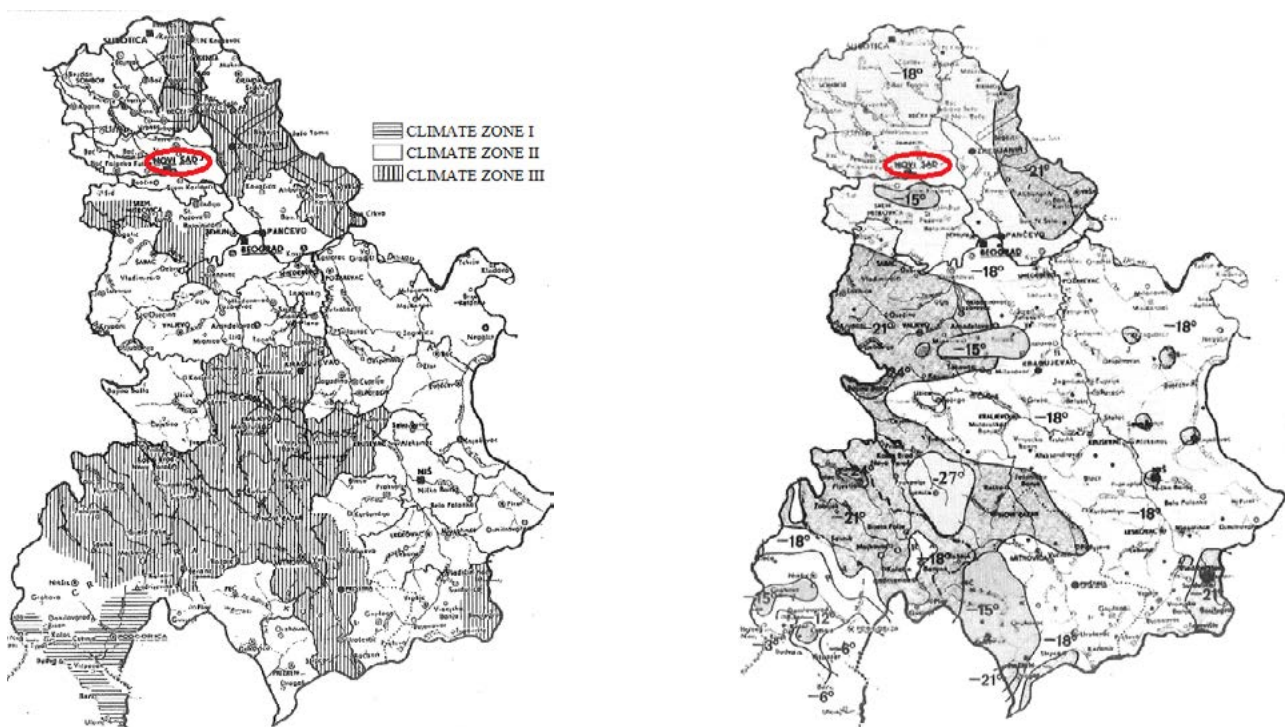
Figure 1: Map of Serbia and Montenegro: left - climate zones; right - external design temperatures [14]

A significant step forward in the field of thermal protection of buildings was made in 1980 with the adoption of the U.J5 series of mandatory standards for the heat in civil engineering. Standards defined thermal protection requirements in design and construction of buildings [14], U-value calculation methods [15], water vapour diffusion calculation methods [16] and thermal stability calculation methods for external building structures in summer period [17]. In addition to upgrading the thermal protection requirements, the importance of adopting the U.J5 standards is reflected in the introduction of the *water vapour diffusion* and *summer regime treatment* parameters in the thermal calculation. By introducing the category of *specific heat losses for the building as a whole* and reducing the boundary U-values, thermal protection regulations [14,15] were innovated in 1987. In the following period, minor revisions and modifications of

standards [14-16,17] were made, with the latest innovation made in 1998 [14] which introduced category of *specific heat losses for characteristic rooms*.

From 2012, designing of building thermal protection is governed by the regulations on energy efficiency and certification of buildings [18,19] which ensures the implementation of European legislation in the field of energy efficiency of buildings in Serbia. In case of renewal of the existing buildings, U-value for external walls is limited to 0,4 W/m²K and the building is energy efficient if the minimum requirements of thermal comfort are fulfilled and if annual energy consumption for heating does not exceed 70 kWh/m² per year. Meeting the energy efficiency requirements of the building is proved with *Elaborate on energy efficiency* that has to be enclosed with the technical documentation in order to obtain approval for execution of energy rehabilitation works [20].

Table 1 shows the evolution of U-value requirements for external building walls in the II climate zone.

Table 1: The required U-values for external building walls for the II climate zone dependent on the year of regulation

U-value (W/m²K)	Year of regulation				
	1967	**1970**	**1980**	**1987**	**2011**
External building wall (II climate zone)	1,55	1,45	0,93	0,90	0,40 (existing buildings) 0,30 (new buildings)

2.2 FIRE SAFETY OF HIGH-RISE RESIDENTIAL BUILDINGS' FACADES

Fire safety of facades in high-rise residential buildings in RS is regulated by the *Law on Fire Protection* [9] which was revised and changed several times during the second half of the XX century [21,22], as well as with *Regulation on technical norms for the protection of high-rise buildings from fire* [23]. Meeting the fire safety requirements of the building is proved with *Elaborate on fire safety* that has to be enclosed with the technical documentation in order to obtain approval for execution of energy rehabilitation works [20].

The first regulation relating exclusively to high-rise buildings [24] was adopted in 1984 which defined high-rise building as a building where a height of its last storey's floor, intended for human habitation, exceeds 22 m in relation to the surrounding ground that is accessible to the fire-fighting and rescue vehicles and from which it is possible to intervene with the use of motor ladders or other special vehicles for extinguishing and rescuing from heights. By modifications of this Regulation in 2011 the height of high-rise buildings increased to 30 m. Modification of requirements for external walls of high-rise residential buildings is presented in Table 2. As it can be seen, in case of design, construction and reconstruction of high-rise buildings, all exterior wall components are required to be non-combustible.

Table 2: Modification of requirements for external walls of high-rise (HR) residential buildings

REQUIREMENTS FOR EXTERNAL WALLS	2015	2017		2018 (current)
	all HR buildings	30 m - 40 m	40 m +	all HR buildings
Reaction-to-fire class of the system	A1	A2-s1,d0	A1	**A2-s1,d0**
Reaction-to-fire class of components				
External layer/layers	A1	A2-s1,d0	A1	**A2-s1,d0**
Substructure	not specified	not specified	not specified	**A2**
Insulation layer	A1	A1	A1	**A1**

In order to improve the fire safety of buildings' facades, *Regulation on technical requirements for fire safety of external building walls* [25] was adopted in 2016. Regulation prescribes the technical requirements for fire safety of building materials intended for external wall construction which must be fulfilled when designing, constructing, reconstructing, upgrading, adapting, using and maintaining buildings. Buildings are classified into five categories – A, B, V1, V2 and G. High-rise buildings were primarily (2016) classified into G category, where the buildings higher than 22 m belonged. However, with the last modification of the regulation [25], the G category is limited to 30m in terms of building height,

which led to exclusion of high-rise buildings from categorization. According to the regulation [25] if the external thermal insulation composite system (ETICS) or other system components partly composed of combustible materials are being used to improve the energy efficiency of the existing building, then a continuous non-combustible horizontal barriers, at least 1 m high, must be installed on facades at each floor structure level.

3 CASE STUDY: SELECTION OF THE THERMAL INSULATION MATERIAL FOR THE FAÇADE RENEWAL OF THE HIGH-RISE RESIDENTIAL BUILDING IN NOVI SAD

First phase of case study included collecting basic information about the building which was the starting point for identification of existing types of facade walls and for U-value calculation (Table 3).

Table 3: Basic data on the analysed building and types of facade walls

ANALYSED BUILDING – BASIC DATA	
	The freestanding high-rise residential building is located in Novi Sad, in Novo Naselje area. The 13-storey building is built in IMS precast system in the 80's. There are two types of external building walls: type A – facade prefabricated panels and type B – facade walls within the loggia. The façade prefabricated elements are multi-layer concrete panels, with and without openings, with different lengths, and constant height. They are mounted as exterior walls between two floor structures, anchored to them with their upper and lower parts. The façade walls in the loggia are made of gas concrete blocks.
TYPES OF FACADE WALLS	
	type A – facade panel: 1. concrete 8 cm; 2. expanded polystyrene 6 cm; 3. concrete 6 cm; **type B – facade wall within the loggia:** 1. plaster 1,5 cm; 2. gas concrete blocks 20 cm; 3. plaster 1,5 cm;

The façade walls do not meet the current thermal protection regulations ($U_{2012} < 0,4$ W/m^{2}K) [18], so it is proposed to install an additional thermal insulation layer on external side of walls. Apart from improving the energy efficiency of the building (by reducing the U-value), the installation of external thermal insulation on the building facade protects the existing façade elements and significantly slows down the process of deterioration [4]. Additionally, external thermal insulation prevents water vapour condensation and allows the accumulation of heat in the walls, contributing to the thermal comfort as well. The installation of external thermal insulation allows continuous thermal insulation of the facade, thus avoiding the occurrence of thermal bridges. However, external façade insulation of high-rise buildings requires the use of scaffolding which significantly increases costs in regard to internal insulation.

Second phase included selection of thermal insulation materials. Only non-combustible thermal insulation materials were considered in order to meet required fire safety criteria given in Table 2, however it is very important to emphasize that, beside reaction to fire of insulation layer, reaction to fire of the whole facade system has to be considered.

Physical properties of selected thermal insulation materials are presented in Table 4. In addition to its low thermal conductivity, *mineral wool* has high resistance to moisture damage, good acoustic properties, it is non-flammable and it will not melt until temperatures reach 1000 °C [26]. *Cellular concrete* is an ecological, mineral insulation material based on the raw materials sand, lime, cement, and water. It is non-flammable, dimensionally stable and prevents mold problems. Material is breathable so moisture is temporarily stored, then re-released into the ambient air. It is also non-combustible and free of toxic emissions [27].

Table 4: Physical properties of the thermal insulation materials used in the case study

THERMAL INSULATION MATERIAL	Stone wool	Glass wool	Cellular concrete
Density (kg/m^3)	100	21	115
Thermal conductivity (W/mK)	0,035	0,034	0,045
Specific heat (kJ/kgK)	1	1	1,3
Water vapour diffusion resistance factor	1	1	3
Fire classification	A1	A1	A1

In third phase, three renewal solutions were proposed for both types of facade walls (Figure 2):

Variant I: ETICS with stone wool (A-I and B-I walls)

Variant II: panel system with glass wool (A-II and B-II walls)

Variant III: ETICS with cellular concrete (A-III and B-III walls)
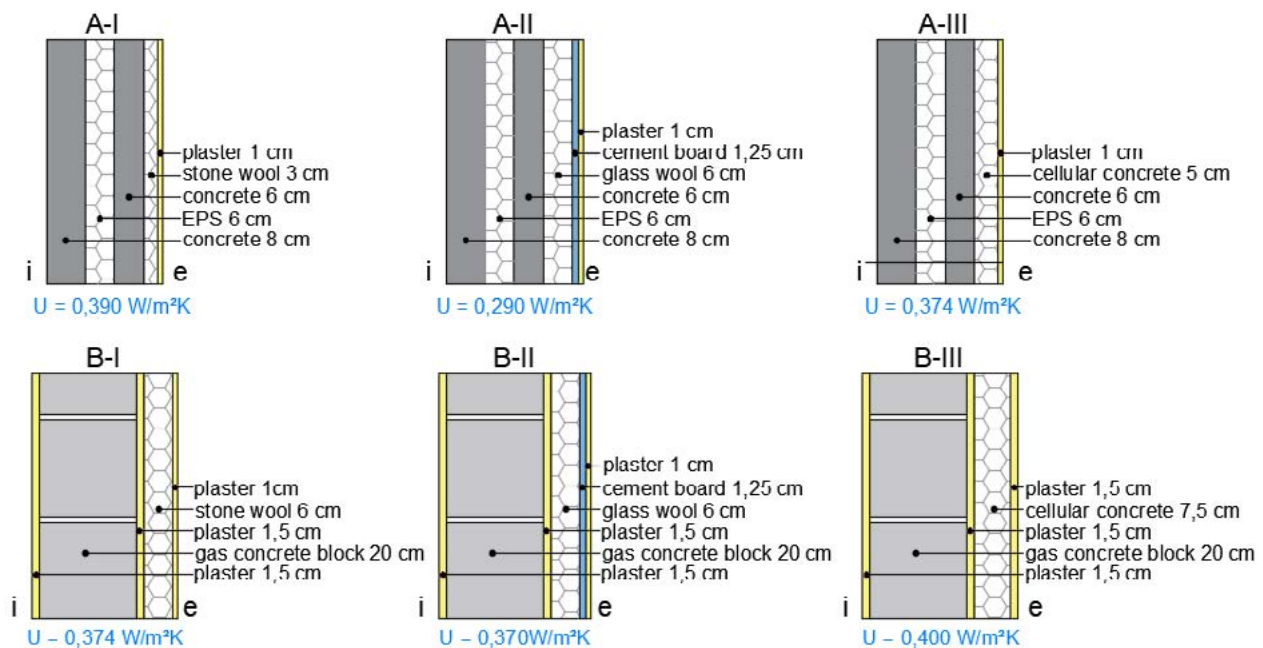
Figure 2: Proposed façade systems with improved U-values

In variant I, ETICS is composed of a hard stone wool panels, fixed to the substrate through bonding products and mechanical fasteners. A thin, reinforced layer is applied over the insulation, and an additional final protective layer.

In variant II, façade system is composed of a metal substructure, semi-rigid glass mineral wool insulation panels and a waterproof, non-combustible cement board reinforced with fiberglass mesh, made of pure mineral lightweight concrete. First, a metal sub-structure is placed on the existing wall through mechanical fasteners, after which the glass wool is placed between the substructure supports and fixed to the substrate in the same manner as stone wool in the variant I. In the last step the cement boards are fasten to substructure and a final decorative layer is applied.

In variant III, ETICS is composed of a cellular concrete panels and the installation is similar to variant I installation.

In order to meet the new thermal protection requirements, the minimum required thickness of thermal insulation layer was determined for all three variants and for both types of facade walls. Improved U-values are shown in Figure 2. In the case of the facade A-II system, the calculation showed that 5 cm of glass wool is sufficient to achieve a satisfactory U-value. However, as the thickness of this layer is conditioned by the substructure dimensions, consequently a larger thickness was chosen (6 cm).

Within the last phase the proposed solutions were analysed in the context of: (1) application on existing walls, (2)

vulnerability to mechanical damages, (3) resistance to wind action and (4) costs of selected façade system components.

(1) Since the analysed building is over 35 years old, damages, such as spalling, flacking and cracking, have appeared on the façade walls. Thus, there is a need to perform assessment of the substrate onto which the ETICS will be applied, as well as to prepare the substrate. There are several methods of testing the substrate for its suitability for the application of ETICS, as well as measures to be carried out on the existing walls before application of ETICS [28]. For application of variant II system, no special substrate preparation is required, which gives it an advantage over the other two systems.

(2) The integrity of proposed systems is essential to achieve the desired building efficiency and to obtain the expected level of performance [29]. Even minor mechanical damage (caused by acts of vandalism, hail or other) to the finishing ETICS coat makes it easier for the water to infiltrate the enclosure and lead to moisture accumulation within the façade. It speeds up the process of its degradation and any possible accumulation of moisture in the thermal insulation coat reduces the effectiveness of the thermal insulation [30]. In this context, façade system with glass wool has advantage over the other two systems, thanks to cement boards that protect it against external influences.

(3) Wind action represents the main load that the façade must withstand. ETICS shows some problems regarding the operational reliability, being vulnerable to wind action. Pulling off ETICS from the building façade is most of the time caused by the failure of the adhesive bond between the mortar and the wall [31]. In this context, variant 2 is re-imposed as the optimal solution with remark that dimensions and cross-sections of the substructure must be matched to the effects of wind pressure and wind suction [32]. For all three variants, an additional analysis of the wind effect on the system should be made to ensure their stability and reliability.

(4) Initial investment funds, exploitation phase costs, as well as return period of investment funds are considered to be among the indicators of financial parameters through which the proposed solutions can be observed. Initial energy rehabilitation costs include thermal insulation material costs, costs of other façade system components (bonding products, mesh, anchor, bolts, plaster, etc.), as well as the cost of installation (involving labour and the use of scaffolding), which depend on the building type and complexity, its location, accessibility, condition of substrate and other. Assuming that the scaffolding costs and costs of final protective layer for all three proposed solutions would be similar, following façade system components were subjected to cost analysis: thermal insulation material, cement board (including metal sub-structure and mechanical fasteners) which appears in the variant V-II, as well as components needed for fixing of insulation material to the substrate (bonding products and mechanical fasteners) in variants V-I and V-III (Table 5).

Table 5: The estimated costs for components used in analysed façade systems

Façade system	Components	Type A walls			Type B walls			Rank of proposed solution
		Layer thickness	Cost	Total cost	Layer thickness	Cost	Total cost	
V-I	Stone wool	3 cm	4 €/m^2	7 €/m^2	6 cm	6,5 €/m^2	9,5 €/m^2	1
	Fixing of insulation material	-	3 €/m^2		-	3 €/m^2		
V-II	Glass wool	6 cm	5,5 €/m^2	25,5 €/m^2	6 cm	5,5 €/m^2	25,5 €/m^2	3
	Cement board	1,25 cm	20 €/m^2		1,25 cm	20 €/m^2		
V-III	Cellular concrete	5 cm	8 €/m^2	11 €/m^2	7,5 cm	16,5 €/m^2	19,5 €/m^2	2
	Fixing of insulation material	-	3 €/m^2		-	3 €/m^2		

As glass wool is produced in rolls or in the form of semi-rigid panels, it cannot be applied within ETICS, so proposed solution requires the use of non-combustible panels, which affects the price increase of this system making it the most expensive of all proposed solutions. In case of type A walls, variant V-II is over three and a half times more expensive than V-I variant and more than twice as expensive as V-III variant, while variant V-III is almost 60% more expensive than V-I variant. In case of type B walls, variant V-II is over two and a half times more expensive than V-I variant and 30% more expensive than V-III variant, while variant V-III is twice as expensive as V-I variant. Price analysis imposes stone wool (V–I façade system) as the cheapest choice for building renewal. However, these systems differ significantly in terms of durability. Therefore, for all three variants, the whole life cycle cost analysis should be performed in order to determine the most cost-effective solution.

4 CONCLUSIONS

Potential energy savings in the building sector, through renewal of existing housing stock, are greater than in any other sector, while energy efficiency of buildings is one of the key factors for reducing greenhouse gas emissions. The installation of an additional layer of thermal insulation on the facades is one of the most common measures envisaged to improve the energy efficiency of existing buildings. The selection of materials for the energy rehabilitation must not impair the fire safety of the building. The design and materialization of façade elements belong to a group of key factors for the fire development and fire spread, significantly affecting the fire safety of the building.

In Serbia, after the World War II, rapid industrialization of the cities, followed by intense urbanization, caused the need to build a large number of apartments, mostly built with industrial building technology. In the period of design and construction of these buildings the criteria for thermal protection and low energy consumption were still not relevant or have just begun to be considered. Also, meeting the fire safety requirements was usually reduced to the legal minimum which was not sufficient. Additionally, no special attention was paid to the maintenance of these buildings during exploitation which resulted with unsatisfactory technical condition of most façade elements. Consequently, the quality level of such buildings, in terms of durability, energy efficiency and fire safety, is very low and it is therefore necessary to renew these buildings, in order to prolong their lifetime and to comply with the contemporary requirements.

The research subject is high-rise residential building built in Novi Sad in the second half of the XX century and the possibilities of improving its energy performance through facade restoration. The research focused on the optimal selection of insulation material that would simultaneously improve the thermal protection and provide the necessary fire safety level. The selection included non-combustible thermal insulation materials and resulted with three renewal solutions that meet both energy efficiency and fire safety requirements.

Insulating materials must guarantee acceptable performance throughout the whole life cycle of the building, but thermal performance is not the only parameter that should be addressed when selecting an insulator [33]. Therefore, the proposed solutions were analysed in the context of application on existing walls, vulnerability to mechanical damages, resistance to wind action and costs of selected façade system components. Results indicated that the façade system with glass wool is optimal solution in terms of application to the existing walls and resistance to damages and wind action. At the same time, the solution requires notably more investment than the other two solutions. In terms of costs, stone wool is the cheapest thermal insulation material for the façade renewal of a high-rise residential building in Novi Sad, and, on the other hand, the most vulnerable solution.

Application of new materials, more strict requirements for energy efficient buildings, renewal of existing building stock and especially the latest high-rise building fire events in the world [34], involving the combustible façade system, initiate the need for a more detailed fire safety analysis of facades. Significant efforts to improve fire safety of buildings in Europe have been identified, as a new method for assessment and classification of the fire performance of facades is under development [35, 36].

Energy efficiency and fire safety legislation defines the frameworks and sets restrictions, which must be respected when designing new or renovating existing buildings. If the problem is viewed comprehensively, choosing the best solution requires analysis from several different aspects and the implementation of an adequate optimization method. Moreover, considering the repetition of the structural solutions of the façade and the number of buildings constructed, this kind of analysis, directed to the possibilities for improving the overall performance of residential buildings, can be the starting point for rebuilding a group of buildings or entire urban blocks.

ACKNOWLEDGMENTS

REFERENCES

[1] European Commission 2020, <u>Energy performance of buildings directive article</u>, Accessed: 2020-02-06

[2] Census of Population, Households and Dwellings in the Republic of Serbia, <u>Comparative overview of the number of households in 1948-2011 and dwellings in 1971-2011</u>, Statistical Office of the Republic of Serbia, Belgrade, (2014)

[3] Ćirović, N. et al: <u>Energy efficiency on to examples of remote heating in Serbia</u>, Proceedings of 10th International Scientific Conference on Science and Higher Education in Function of Sustainable Development, pp. 56-65, ISBN 978-86-83573-90-5, Mećavnik-Drvengrad, Užice, October 2017

[4] Laban, M.: Improvement of envelope performances of multi-floor residential prefabricated and semi-prefabricated buildings in Novi Sad, PhD thesis, University of Novi Sad, Faculty of Technical Sciences, Novi Sad (2012)

[5] Milanko. V. et al: Fire safety problems of residential towers, Proceedings of 2nd International Scientific Conference on Fire Engineering, pp. 255-261, ISBN 80-89241-03-4, Lučenec, Slovakia, October 2006

[6] Fire and Rescue Unit Novi Sad, Directorate for Emergency Situations, Serbian Ministry of Internal Affairs, 2018

[7] Law on Planning and Construction (Official Gazette RS, no. 72/2009, 81/2009, 64/2010, 24/2011, 121/2012, 42/2013, 50/2013, 98/2013, 132/2014, 145/2014, 83/2018, 31/2019 and 37/2019)

[8] Law on Construction Products (Official Gazette RS, no. 83/2018)

[9] Law on Fire Protection (Official Gazette RS, no. 111/2009, 20/2015, and 87/2018)

[10] <u>The Construction Products Regulation No 305/2011</u>

[11] DIN 4701: 1947 Rules for calculating building heat demand

[12] Regulation on minimal technical requirements for residential buildings (Official Gazette SFRY, no. 45/1967)

[13] Regulation on technical measures and provisions for thermal protection of buildings (Official Gazette SFRY, no. 35/1970)

[14] SRPS (JUS) U.J5.600 (1980, 1987, 1989, 1998) Heat in civil engineering – Requirements for design and manufacturing of buildings

[15] SRPS (JUS) U.J5.510 (1980, 1987) Heat in civil engineering – Coefficient of heat transfer in buildings

[16] SRPS (JUS) U.J5.520 (1980, 1997) Heat in civil engineering – Calculation of water vapour diffusion in buildings

[17] SRPS (JUS) U.J5.530 (1980, 1990, 1997) Heat in civil engineering – Calculation of damping factor and lating of temperature oscillations in the summer period through the exterior building partitions

[18] Regulations on energy efficiency in buildings (Official Gazette RS, no. 61/2011)

[19] Regulation on conditions, content and the way of issuing certificate of energy performances of buildings (Official Gazette RS, no. 69/2012)

[20] Regulation on content, method and manner of development and performing control of technical documentation according to class and intended use of the structure (Official Gazette RS, no. 73/2019)

[21] Law on Fire Protection (Official Gazette FPRY, no.18/56 and Official Gazette SFRY, no. 25/70)

[22] Law on Fire Protection (Official Gazette of Serbia, no. 37/88 and Official Gazette RS, no. 53/93, 67/93 and 48/94)

[23] Regulation on technical norms for the protection of high-rise buildings from fire(Official Gazette RS, no. 80/2015, 67/2017 and 103/2018)

[24] Regulation on technical norms for the protection of high-rise buildings from fire (Official Gazette SFRY, no. 7/84 and Official Gazette RS, no. 86/2011)

[25] Regulation on technical requirements for fire safety of external building walls (Official Gazette RS, no. 59/2016, 36/2017 and 6/2019)

[26] Abu-Jdayil, B. et al: Traditional, state-of-the-art and renewable thermal building insulation materials: An overview, *Construction and Building Materials*, Vol. 214 (2019), pp. 709–735, ISSN: 0950-061

[27] <u>Multipor mineral insulation board</u>, Accessed: 2020-02-06

[28] European association for ETICS: <u>European guideline for the application of ETICS</u>, Accessed: 2020-02-09

[29] Tavares, J. et al: Computational models applied to the service life prediction of External Thermal Insulation Composite Systems (ETICS), *Journal of Building Engineering*, Vol. 27 (2020), pp. 1-12, E-ISSN: 2352-7102

[30] Sudol et al: <u>Impact resistance of external thermal insulation systems</u>, MATEC Web of Conferences, Volume 163, 8th Scientific-Technical Conference on Material Problems in Civil Engineering, pp. 1-8, ISBN: 978-2-7598-9052-1, Cracow, Poland, June 2018, DOI: <u>10.1051/matecconf/201816308004</u>

[31] Adrian-Cosmin, B. et al: Alternative Solution for Thermal Rehabilitation of Buildings with Polystyrene Panels, *Procedia Engineering,* Vol. 181 (2017), pp. 712-717, ISSN: 1877-7058

[32] <u>Technical solutions for drywall exteriors</u>, Knauf AQUAPANEL Exterior Wall, Accessed: 2020-02-10

[33] Schiavoni, S. et al: Insulation materials for the building sector: A review and comparative analysis, *Renewable and Sustainable Energy Reviews*, Vol. 62, (2016), pp. 988-1011, ISSN 1364-0321

[34] The Guardian, <u>Grenfell Tower fire</u>, Accessed: 2020-02-10

[35] Boström, L. et al: Development of a European approach to assess the fire performance of facades, Project Number: 2018/3848, EU DG, ISBN 978-92-79-88000-1, doi:10.2873/954759, European Commission (2018)

[36] RISE Research Institutes of Sweden, 2020: <u>Finalisation of the European approach to assess the fire performance of facades</u>, Accessed: 2020-12-18

4

Girts Bumanis, Jelizaveta Zorica, Rihards Gailitis, Andina Sprince, Diana Bajare

Microstructural investigation of phosphogypsum based ternary system binder

UP

MICROSTRUCTURAL INVESTIGATION OF PHOSPHOGYPSUM BASED TERNARY SYSTEM BINDER

G. Bumanis[1], J. Zorica[1], R. Gailitis[2], A. Sprince[2], D. Bajare[1]

[1] Materials Department of Building Materials and Products, Riga Technical University,
Kalku iela 1, LV-1658, Riga, Latvia
e-mail: girts.bumanis@rtu.lv

[2] Institute of Building and Reconstruction, Riga Technical University, Riga, Latvia
Kalku iela 1, LV-1658, Riga, Latvia
e-mail: andina.sprince@rtu.lv

SUMMARY: The construction industry is developing through the implementation of global trends, such as the problem of conservation of earth resources, which with each passing day becomes more relevant. Reduction of waste and its harmfulness from extractive industries and amending is set as goal of European Parliament and the Council by directive 2006/21/EC, which can be carried out by using waste in the production of building materials. A promising example and in the same time challenging material is phosphogypsum (PG) – gypsum waste coming from fertilizer production plants, which could be used as a potential replacement of natural gypsum. Since there are legislation limits and prejudice coming from society regarding to PG, direct use of PG as substitution of natural gypsum products is problematic. Solution offered in this paper in utilization of PG is associated with the development of an advanced and new type of binder which has much lower carbon footprint comparing to Portland-cement while the strength properties are similar to Portland cement. A ternary binder based on PG, waste metakaolin and Portland cement was researched in this study. Proposed material could contain up to 70% of PG while the optimal design of ternary binder (50 wt% of PG) composition in water-saturated conditions could give compressive strength up to 50 MPa at the age of 28d. Binder microstructure, chemical and mineralogical composition was investigated by SEM, EDX and XRD. Results of ternary binder was compared both for PG and commercially available gypsum plaster in composition. Presented material proved to be competitive binder to create composites such as mortars similar to materials based on traditional Portland cement.

KEY WORDS: phosphogypsum, gypsum cement pozzolan, microstructure, chemical composition

1 INTRODUCTION

The potential of PG as secondary raw material in construction industry is high if compared to other building materials from the point of view of total energy consumption and CO_2 emissions [1]. Traditionally, the PG is contaminated with technological impurities such as orthophosphoric acid, sulfuric acid, calcium orthophosphate, calcium fluoride, hexafluorosilicic acid, phosphates and other rare element earth metals [2]. There are technological solutions implemented in production plants where the impurities are eliminated by washing PG with water or by separation of coarse and fine particles, as the particle size fractions above 160 and below 25 μm have highest percentage of impurities in PG. The drawback of this approach is related to high water demand during the purification process - up to 4 m^3 of water is necessary to wash 1 ton of PG [3]. The PG contamination is also eliminated by using a combined method when PG is washed with a smaller amount of water, and the rest of the acid admixtures are neutralized by adding the alkaline nature additives such as slacked lime or zeolites [4], [5]. In this case the soluble impurities are converted to insoluble matters such as calcium orthophosphates of the hydroxyl apatite group and fluorides, having little influence on the properties of binder [6]. Considering the availability of various gypsum-rich waste streams, there is a strong interest in finding applications that could be both economically viable and sustainable.

New tendencies of using potential hazardous materials as secondary raw materials is associated with the dissolution of hazardous content concentration coming from waste material in other building materials [7]. In this case the final product total volume has less hazardous constituents and usually fits into the limitations brought by legislation. PG as secondary raw material could follow the mentioned approach and there are some working examples. The most simple way it is to use not more than 5% of PG as an additive to the Portland cement [8]. The application of PG as an additive in

cement mortar was also evaluated in other article and it was determined that a cement mortar with an addition of 30 % of calcined PG gave the optimum results [9]. The researches to produce traditional gypsum binders based on PG is widely published but they have rather limited practical application due to specific nature of PG [10].

A more complicated and effective way of the utilization of PG is to create an advanced and new type of binder which has a much lower carbon footprint comparing to the Portland-cement while remaining similar strength properties to Portland cement. Several such approaches are previously published, i.e. fly ash–lime–phosphogypsum ternary binder has been studied by the S.Kumar before. Two waste-stream materials were used and only lime is defined as a primary resource, the calcination temperature (900-1100°C) of latter is lower compared to Portland cement. In this case the amount of PG in the binder was in the range from 10-40%. However, the disadvantage comparing to Portland cement is low compressive strength – which could be in range from 2-4MPa [11]; nevertheless it is reasonable if it is compared to the lime binder and hydraulic lime binder. Higher strength results were obtained in ternary binder system phosphogypsum–steel slag–granulated blast-furnace slag (GGBS)–limestone cement, where the content of PG was from 25-65%, while the amount of slag was from 22-48%. The obtained strength at the age of 28 days was up to 45 MPa while the obtained binder is characterized with fast setting time (initial setting time 6-9 min, final 10-12 min) [12]. These results are more comparable to traditional binders while the problem could be a fast setting time. The fast setting may not benefit the engineering application, because there is not enough time for casting before the cement sets. In some case it was reported that the citric acid in amount from 0.03-0.15 wt% of cement could retard setting time significantly. The use of citric acid could increase the open time from 25 to 47 min while the set retard tended to slightly reduce compressive strength of the binder [13]. In ternary systems where Portland cement is present, superplasticizer can be used and low water-binder ratio can be achieved. The use of polycarboxylate acid-based superplasticizer could be used from 0.75-1.75 wt%; however, reports say that it could slightly reduce early compressive strength of the material while final strength tended to increase [13]. These aspects regarding to the utilization of PG in new types of binder should be considered by choosing mixture composition including use of chemical admixtures. A novel material presented in this study has potential of PG valorisation of 50 wt.% in ternary system binder based on PG, waste metakaolin (known as industrial wastes) and Portland cement. The superplasticizer and set time controller was used as chemical admixtures in mixture compositions.

2   MATERIALS AND METHODS

Dihydrate phosphogypsum ($CaSO_4 \cdot 2H_2O$) analysed in this work is the waste generated by fertilizer production plant AB Lifosa (Lithuania) in wet-process phosphoric acid production, where apatite from the Kovdor mine, Kola peninsula, Russia, is decomposed by sulphuric acid. To produce 1t of orthophosphoric acid about 3.0-4.5 t of PG is obtained [14]. At the enterprise, volcanic origin Cola apatite (Kirov and Kovdor) (containing F_2 1-2%, P_2O_5 - about 38% as phosphorus) is used as a raw material in the production of phosphoric acid. Besides, phosphorites of sedimentary origin from other countries (Morocco, Jordan, Kazakhstan (Karatau), Algeria, South Africa Republic) are used. Two types of PG could be obtained from the production plant regarding the technological process used – PG dihydrate and PG hemihydrate. The PG dihydrate was used as secondary raw material in the present research. Chemical composition of raw materials is given in Table 1. The initial pH of PG is in the range from 2.2-2.9 while during the storage it can increase gradually. The PG was dried at 60°C (moisture content 9-12 wt.%) and milled to powder-like particles with collision milling in semi-industrial disintegrator with the rotational speed of 50Hz. Then the calcium sulphate hemihydrate binder was obtained by treatment of milled gypsum powder at temperature 180°C for 4h. Commercial gypsum plaster (BG) was used to compare the characteristic technological properties of obtained binder.

The other components of the binder were metakaolin as supplementary cementitious material and Portland cement CEM I 42.5N (CEM). Chemical composition of CEM are given in table 1. The initial setting time was 182 min and the final setting – 224 min (according to LVS EN 196-3), the normal consistency was 28.2% (according to LVS EN 196-3). Blaine fineness of cement was 3787cm^2/g (according to LVS EN 196-6). Na equivalent was 1.68. Compressive strength after 1 day was 15.4 MPa, after 2 days – 32.9 MPa, after 7 days – 48.8 MPa and after 28 days – 60.5 MPa. Waste metakaolin (WMK) was obtained from the porous glass granule production factory "Stikloporas" UAB (Lithuania). Metakaolin is a by-product from the final stage of expanded glass granule production, where kaolinite clay powder is used as a substance for anti-agglomeration, and is heated at the 850°C temperature for 40-50 min. According to the XRD analysis a halo of amorphous metakaolin is in 2θ region from 15 to 30°, some minor crystalline phases were also detected in WMK: quartz (SiO_2) and Halloysite $Al_2Si_2O_5(OH)_4$. The specific surface area of the WMK is 15.86 m²/g. Loss of ignition for metakaolin was 11.5%. MKW is a mostly amorphous dehydration product of kaolinite, $Al_2(OH)_4Si_2O_5$, which exhibits strong

pozzolanic activity often used in the concrete industry as a supplementary cementitious material. The particle size distribution of materials used in the preparation of ternary binder is given in Figure 2.

Sika ViscoCrete G-2 is a high-performance superplasticizer/water reducer based on polycarboxylate (PCE) polymer technology. PCE is formulated for applications in systems with high calcium sulphate content or pure gypsum based-binders. Gips RETARD (TKK d.o.o., Slovenia) is a powdered citric acid-based admixture (R), which was used for regulating the setting time of gypsum. Gips RETARD was added to the dry binder mixture and mixed thoroughly before water were added.

Table 1. Chemical composition of raw materials used to prepare novel building material, [weight %]

Element	Commercial gypsum BG	Phosphogypsum PG	Metakaolinite MKW	Cement CEM I 42.5N
SiO_2	3,73	1,07	51,80	22,64
Al_2O_3	1,68	0,70	34,20	5,93
Fe_2O_3	0,46	0,22	0,50	3,26
CaO	35,64	37,16	0,10	57,04
MgO	3,92	0,21	0,10	4,26
SO_3	30,90	37,38	-	3,30
Na_2O	0,31	0,48	0,60	0,10
K_2O	-	-	-	2,40
TiO_2	0,05	0,11	0,60	0,38
Cl.	-	-	-	0,14
P_2O_5	-	0,57	-	0,46
LOI	22,43	19,24	11.5	-
Total	99,42	99,74	99,60	99,90
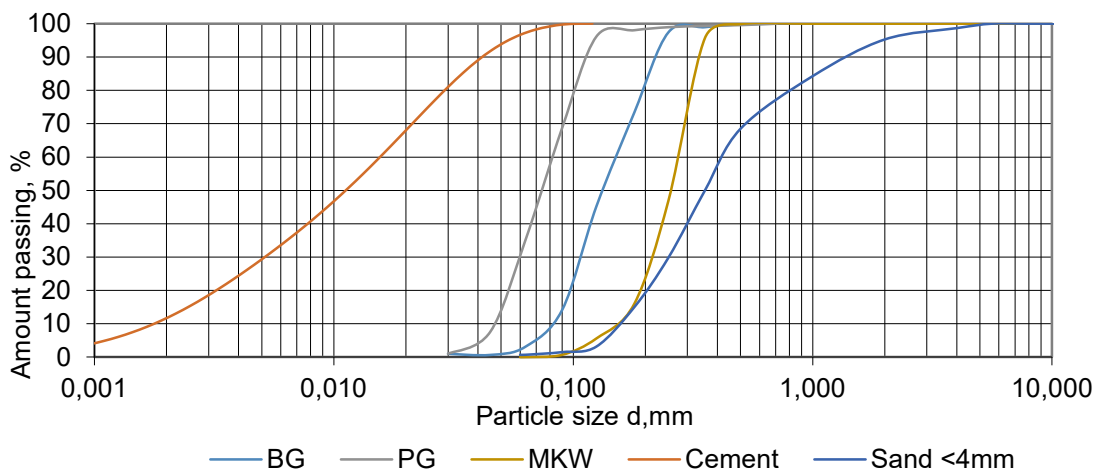
Figure 1. The article size distribution of the raw materials used to prepare novel building material.

Prepared mixture composition is given in Table 2. First two compositions were GCP binder pastes (GCP-PG and GCP-BG). The difference between two of them is that in one case, commercial gypsum binder is used (abbreviation with BG), in other phosphogypsum binder is used (abbreviation with PG). The amount of PCE was 1.5% from the total amount of binder while set retarder R was 0.2%. Set retarder was used for samples with PG as it has a shorter set time comparing to commercial gypsum [10]. The W/B ratio was 0.34 for both mixtures. Other two mixtures were based on two mentioned binder pastes, but additional washed quartz sand (0/2mm) was incorporated into the mixture composition with binder-sand ratio 1:1.75. The W/B ratio slightly increased with the incorporation of sand.

Mixing procedure of binder pastes was similar to traditional cement mortars. First, dry components including set retarder, were homogenized for 2 minutes. Then powder gradually was added into the water and superplasticizer mixture and homogenized for 2 minutes before casting. Mortar was mixed similar as the pastes, while the sand and extra water were added to the pre-mixed paste. Samples were cast in 20x20x20mm or 40x40x160mm moulds for further testing.

Table 2. Mixture composition of prepared GCP binder paste and GCP mortar used to prepare a prototype.

Mixture	PG	BG	CEM	MKW	G-2	R	Sand 0/2mm	W/B
GCP-PG	1		0.4	0.4	1.5%	0.2%	-	0.34
GCP-BG		1	0.4	0.4	1.5%	-	-	0.34
GCP-PG-S	1		0.4	0.4	1.5%	0.2%	1.75	0.36
GCP-BG-S		1	0.4	0.4	1.5%	-	1.75	0.36

The setting time of the obtained binder was tested using the Vicat apparatus. Consitency of fresh mortar was tested with the Suttard's viscometer. Early age (24h) and 28d compressive strength was determined. Samples were water cured. After 28 days samples were removed from water and tested, while at the age of 35d air dry samples were tested. Samples with dimension of 20x20x20 mm were tested using Zwick Z100 with testing speed 0.5mm/min. The specific gravity and total porosity were determined by using Le Chatelier flask. The mineralogical composition was determined by X-ray diffraction (XRD) (PAN analytical X'Pert PRO). The macrostructure of the material was observed by a digital microscope at a magnification of 40 and 120x. Scanning Electron Microscopy (SEM) with Energy Dispersive Spectroscopy (EDS) was used (JEOL JSM 820 + IXRF systems 500 digital processing, Japan) for microscopic analysis of binder paste with 20 kV voltage.

3 RESULTS

3.1 Physical and mechanical properties

The bulk density of hardened binder is given in the Table 3. The density of binder paste GCP-BG is slightly lower comparing to GCP-PG (1609 to 1766 kg/m^3) which can be explained by the finer particle distribution for PG and denser structure of the paste. Similar tendencies were observed for mortar. The bulk density of a mortar material increased to 1886 and 2027 kg/m^3 for GCP-BG-S and GCP-PG-S respectively. The total porosity for GCP-PG and GCP-BG was 23 and 29 vol.%, while for mortar it was even lower - 11 and 17 vol.% for GCP-PG-S and GCP-BG-S. The low porosity is associated with low W/B ratio which is also similar to traditional concrete nature [15]. This phenomenon had an influence also on the compressive strength of the materials presented.

The consistency of fresh material was strongly affected by the amount of superplastizicer and low water content. The initial mixing of binder powder with water and plasticizer gives stiff mixture while during the intensive mixing, the effect of superplasticizer takes place and very viscous mixture was obtained with flow diameter – 295 mm for GCP-BG and 370 mm for GCP-PG. The low W/B ratio of the paste (GCP-PG and GCP-BG) gives similar consistency as for ultra-high performance concrete [16]. The flow for GCP-PG was higher which is associated with the finer particle nature of PG. The prepared mortar was less viscous comparing to paste while the effect of superplasticizer was also present and high workability obtained. The flow of mortar was from 210-230 mm.

The setting time was longer for GCP-PG and GCP-PG-S as set retarder was purposely used in mixture composition. The initial setting time was from 130-165 min for binder paste and mortar. The final set time was longer for GCP-PG (280 min) than for mortar GCP-PG-S (170 min) as it was more viscous to initiate the set of the paste. GCP-BG and GCP-BG-S initial setting time was slightly influenced by the mineral additives (t_{in} 70 and 75 min respectively), while the final set time longer was for GCP-BG (130 min) and was reduced to mortar GCP-BG-S (85 min).

Table 3. Physical properties of the ternary binder and mortar

Mixture	Consistency by Suttard viscosimeter, mm	Setting time		Dry density, kg/m^3	Total porosity, vol.%
		Initial, min	Final, min		
GCP-PG	370	165	280	1766±9	23±2,2
GCP-PG-S	230	130	170	2027±14	11±1,2
GCP-BG	295	70	130	1609±24	29±2,4
GCP-BG-S	210	75	85	1886±38	17±1,9

The compressive strength results are given in Figure 2. The compressive strength increased during the water curing similar to for Portland cement binder. The strength after demolding at 24h was identical among all materials (13-15 MPa). The further curing resulted in slower strength gain for mortars (GCP-PG-S and GCP-BG-S). At the age of 28d after water-

curing the strength reached 50 MPa for GCP-PG and 30 MPa for GCP-BG. The strength increase was not observed between 7 and 28 d for GCP-BG. The mortar strength reached 26 MPa for GCP-BG-S and 43 MPa for GCP-PG-S. After sample drying material strength increased significantly at the age of 35 d. The GCP-PG reached 88 MPa while GCP-PG-S mortar reached 50MPa. Binder GCP-BG had 49 MPa mortar GCP-BG-S had 39 MPa respectively. Such result is highly competitive and promising compared to traditional Portland cement mortars. The higher strength results obtained for materials based on PG could be explained by the fine nature of PG giving more reactive nature for ternary binder. Also commercial gypsum BG could contain other additives which could lead to lower strength results.
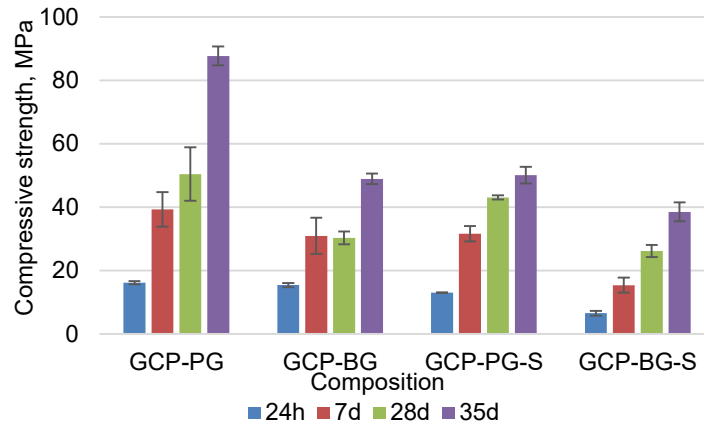
Figure 2. The compressive strength of ternary binder and mortar.

3.2 Structural and chemical investigation

The macrostructure of GCP-PG mortar is given in Figure 3. The difference between binder types (PG or BG) did not influence the appearance of the macrostructure of the material. Mortar has a homogenous structure where individual sand filler grains and the binder can be identified. As 50 wt.% of the binder is gypsum, the material has a white appearance which is characteristic for gypsum binders. The whitish appearance could be an advantage for the creation of exposed architectural or structural elements. Also, the strength of mortar reached up to 50 MPa. The failure of the mortar was mostly in the transition zone of aggregate and binder. Small black inclusions as remains of foam glass granules originated from waste metakaolin were indicated, which could to be a negative factor influencing the strength of the binder and mortar.
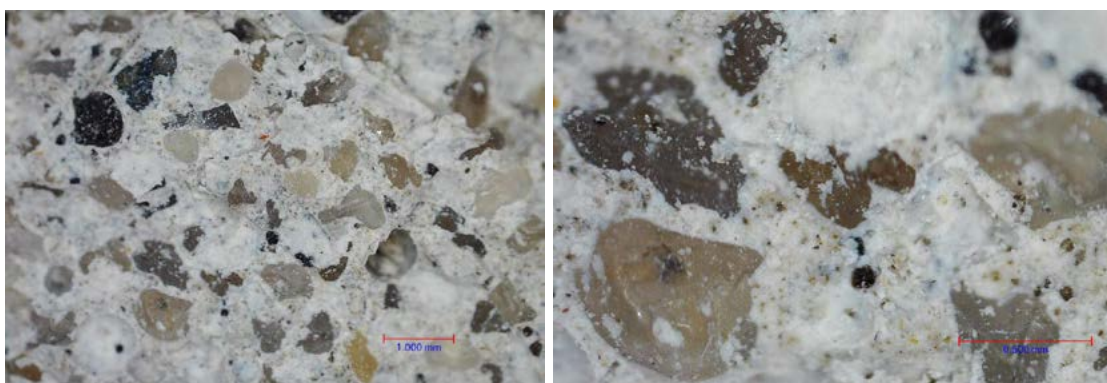
Figure 3. Typical macrostructure of the ternary system mortar.

The microstructure of the ternary binder (GCP-PG and GCP-BG) is given in Figure 4. It has a complex fine-grained structure with the large monolithic structure in smaller magnification (500x). The magnification at 2000x reveals the interaction between binder components and different regions can be identified.
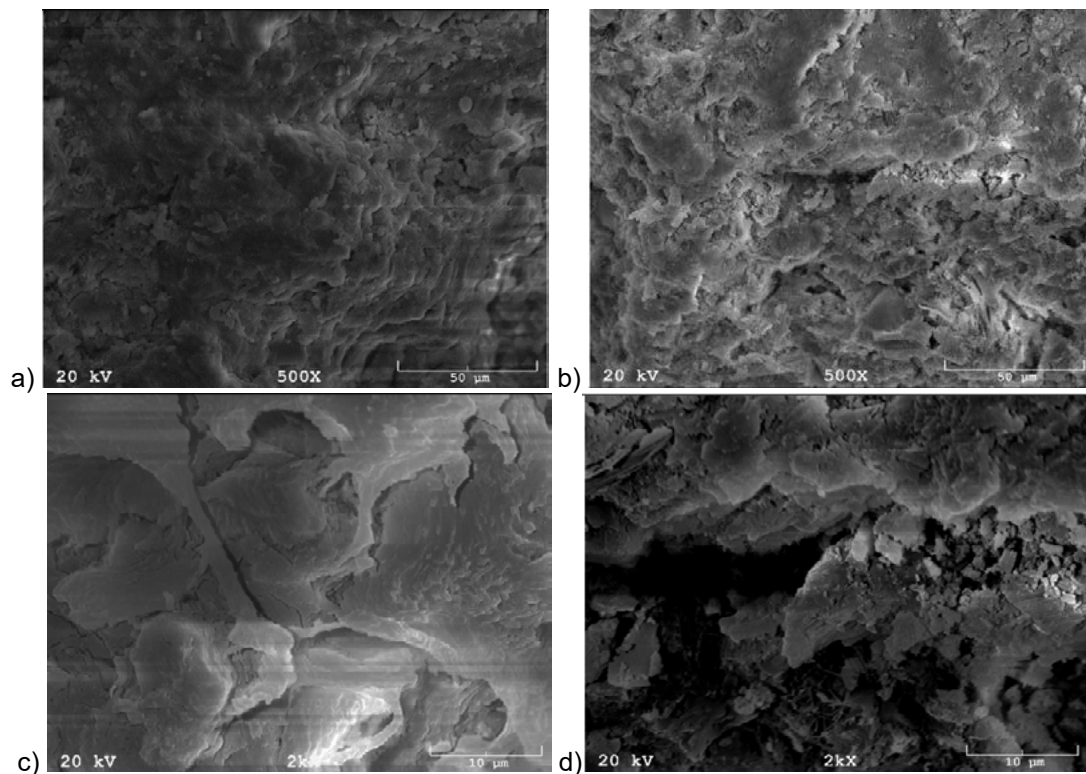
Figure 4: Microstructure of the ternary binder detected by SEM in magnification of 500x and 2000x. a), c) GCP-PG, b), d) GCP-BG.

XRD results is given in Figure 5. The mineralogical composition of a ternary binder powder were investigated before hydration (Figure 5 c,d). Bassanite ($CaSO_4 \cdot 0.5H_2O$, ref 33-0310), calcium silicate oxide ($Ca_3(SiO_4)O$, ref 73-0599) and quartz (SiO_2, ref 78-1252) were identified from the source dry materials of GCP-PG. GCP-BG had the same three minerals as for GCP-PG, while additionally a dolomite ($CaMg(CO_3)_2$, ref 36-0426) and an anhydrite $Ca(SO_4)$, ref 72-0916) were also detected, which is associated with the composition of commercial BG. The phase change after binder hydration were observed (Figure 5 a,b). Also ternary binder contained gypsum, cement and pozzolan, the only phases which were identified in a hydrated GCP-PG mixture where gypsum ($Ca(SO_4)(H_2O)_2$ (74-1433), quartz (SiO_2, ref 78-1252) and ettringite ($Ca_6(Al(OH)_6)_2(SO_4)_3(H_2O)_{26}$,ref 72-0646). The formation and presence of the ettringite in such a late hydration stage is associated with high gypsum content in the mixture. In such a way, expansions can occur from excessive calcium sulfoaluminate formation after hardening and continue until the gypsum becomes depleted, that is why pozzolan was added and according to previous studies addition of pozzolan could even eliminate delayed ettringite formation [17]. In mixture composition GCP-BG ettringite was not detected. Besides minerals coming from raw materials (dolomite, quartz), a gypsum ($Ca(SO_4)(H_2O)_2$ (74-1433) and also gypsum hemihydrate $Ca(SO_4)(H_2O)_{0.5}$ were detected, which could be formed slowly from the hydration of the anhydrite.

The EDX analysis of the GCP-PG binder is given in Figure 6. Large amount of Ca element was identified in most EDX points analysed, which is associated with the fact that Ca is present in all binder components (phosphogypsum, cement and metakaolin). The gypsum source in the structure can be identified through element S which comes from PG binder ($CaSO_4$ $0.5H_2O$). Small quantities of Al and Si were identified as elements coming from metakaolin and cement. This explains the fact that no cement minerals were identified by XRD. The XRD analysis of raw material mixture and hardened binder was investigated while no strong new mineralogical peaks were identified. Mostly transition between gypsum hemihydrate and gypsum dihydrate were observed.
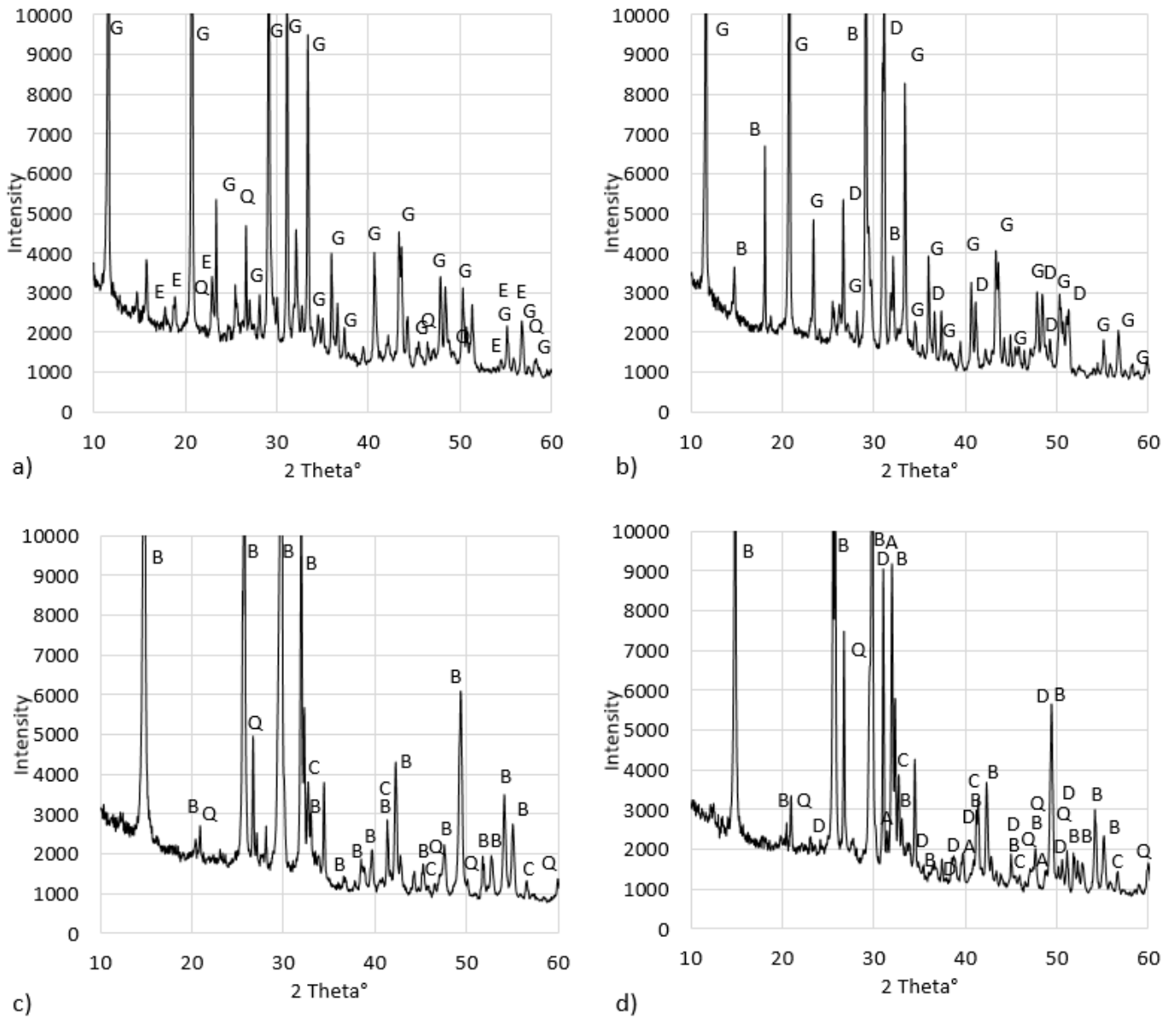
Figure 5. Mineralogical characterisation of raw material mixture and hydrated paste of ternary binder: a) Hydrated GCP-PG; b) hydrated GCP-BG, c) raw mixture of GCP-PG, d) raw mixture of GCP-BG. B- Bassanite ($CaSO_4*0.5H_2O$, ref 33-0310), C - calcium silicate oxide ($Ca_3(SiO_4)O$, ref 73-0599), Q - quartz (SiO_2, ref 78-1252), D - dolomite ($CaMg (CO_3)_2$, ref 36-0426), A - anhydrite $Ca(SO_4)$, ref 72-0916), G - gypsum ($Ca(SO_4)(H_2O)_2$ (74-1433), E - ettringite ($Ca_6(Al(OH)_6)_2(SO_4)_3(H_2O)_{26}$,ref 72-0646).
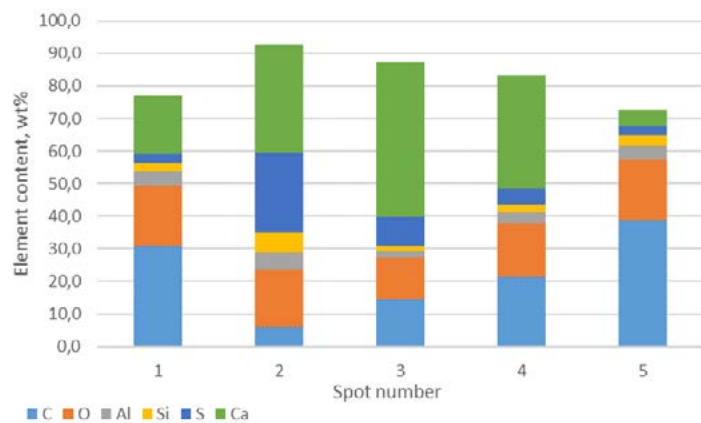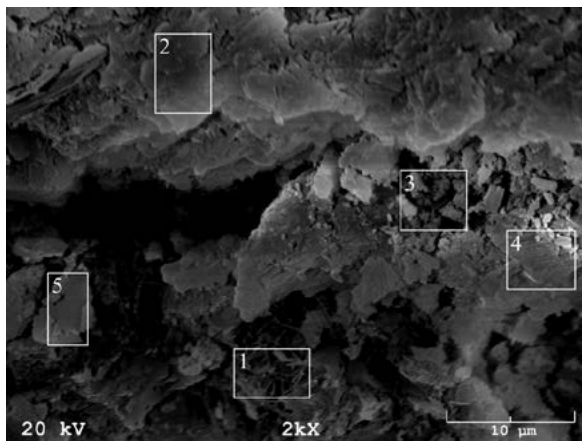
Figure 6. EDX analysis of GCP-PG binder

4 CONCLUSIONS

High strength binder material could be developed through a ternary system containing major part of gypsum, Portland cement and metakaolin. Waste phosphogypsum and metakaolin could be recycled through the development of advanced binder with technological properties similar to traditional cementitious binders. The mixture composition with low W/B ratio was developed with the efficient introduction of superplasticizer. Superplasticizer ensured high workability of the paste. The set time of a binder could be adjusted by the help of the set retarder effectively and the set time characteristics are similar to the one of Portland cement. Compressive strength up to 90 MPa of the hardened dry binder was reached. The binder proved to be suitable to produce mortar with a strength of up to 50 MPa. Also, traditional chemical and mineralogical composition investigation by XRD and EDX did not prove complex cementitious mineral formation; nevertheless, the evidence of phase transformation was detected and will be investigated in further research. Besides of technological properties durability, shrinkage/expansion and long term properties should be evaluated, as long as gypsum with cement can form hazardous compounds such as ettringite which could lead to loss of integrity of the material.

ACKNOWLEDGMENTS

REFERENCES

[1] Kaminskas A., Energiją tausojančių statybinių medž iagų technologijos. 2002.

[2] Nizevičienė, D. et al, Mechanical Activation on Phosphogypsum: Hydrosodalite System, *Waste and Biomass Valorization*, pp. 1–7, May 2018.

[3] Kaziliunas A., et al., The study of neutralization of the dihydrate phosphogypsum impurities," *Ceram. - Silikaty*, vol. 50, no. 3, pp. 178–184, 2006.

[4] Gazdič D., Dvořák K., and Hájková I., Laboratory Burning of Anhydrite from Phosphogypsum, *Adv. Mater. Res.*, vol. 1100, pp. 60–63, 2015.

[5] Nizevičienė D., et al. The treatment of phosphogypsum with zeolite to use it in binding material, *Constr. Build. Mater.*, vol. 180, pp. 134–142, Aug. 2018.

[6] Singh M., Effect of phosphatic and fluoride impurities of phosphogypsum on the properties of selenite plaster, *Cem. Concr. Res.*, vol. 33, no. 9, pp. 1363–1369, Sep. 2003.

[7] Labrincha J., et al., "From NORM by-products to building materials," in Naturally Occurring Radioactive Materials in Construction: Integrating Radiation Protection in Reuse (COST Action Tu1301 NORM4BUILDING), *Elsevier*, 2017, pp. 183–252.

[8] Taher M. A., Amine A. M., and Damarany B. K., Effect of partial substitution of raw gypsum with thermally treated phosphogypsum on the properties of Portland Pozzolanic Cement, *Adv. J. Chem. A*, 2019.

[9] Gong X., et al Effects of Phosphogypsum and Calcined Phosphogypsum Content on the Basic Physical and Mechanical Properties of Portland Cement Mortar, *J. Test. Eval.,* vol. 48, no. 5, p. 20180380, Sep. 2020.

[10] Bumanis G. et al. Technological properties of phosphogypsum binder obtained from fertilizer production waste, *Energy Procedia*, vol. 147, pp. 301–308, Aug. 2018.

[11] Kumar S., Fly ash-lime-phosphogympsum hollow blocks for walls and partitions, *Build. Environ.*, vol. 38, no. 2, pp. 291–295, Feb. 2003.

[12] Huang Y. and Lin Z. S., Investigation on phosphogypsum-steel slag-granulated blast-furnace slag-limestone cement, *Constr. Build. Mater.*, vol. 24, no. 7, pp. 1296–1301, Jul. 2010.

[13] Zhang G., Li G., and Li Y., Effects of superplasticizers and retarders on the fluidity and strength of sulphoaluminate cement, *Constr. Build. Mater.,* vol. 126, pp. 44–54, Nov. 2016.

[14] Nizevičienė D., et al. The treatment of phosphogypsum with zeolite to use it in binding material, *Constr. Build. Mater.*, vol. 180, pp. 134–142, Aug. 2018.

[15] Bajare D. et al. High performance and conventional concrete properties affected by ashes obtained from different type of grasses, *in American Concrete Institute, ACI Special Publication*, 2012, no. 289 SP.

[16] Žvironaite J., et al. Effect of limestone particles on rheological properties and hardening process of plasticized cement pastes, *Medziagotyra*, vol. 21, no. 1, pp. 143–148, 2015.

[17] Nguyen V. H., et al. The effect of natural pozzolan on delayed ettringite formation of the heat-cured mortars, *Constr. Build. Mater.*, vol. 48, pp. 479–484, 2013.

5

Nina Gartner, Miha Hren, Tadeja Kosec, Andraž Legat

Electrochemical corrosion tests on steel in alkali-activated materials

CoMS_
2020/21

ELECTROCHEMICAL CORROSION TESTS ON STEEL IN ALKALI-ACTIVATED MATERIALS

N. Gartner[1], M. Hren[1], T. Kosec[1] and A. Legat[1]

[1] Slovenian Nationa Building and Civil Engineering Institute, Department of Materials
Dimiceva ul. 12, 1000 Ljubljana
e-mail: nina.gartner@zag.si

SUMMARY: One of the potential alternatives to Ordinary Portland Cement (OPC) are Alkali-Activated Materials (AAMs). The service life of reinforced concrete structures greatly depends on the corrosion resistance of embedded steel reinforcement. Due to the wide range of AAMs and their diverse properties, corrosion processes of steel in these materials are relatively unknown. Corrosion monitoring methods or their interpretations in certain cases cannot be directly transferred from the ones for OPC materials. The chemical compositions of pore solution in different AAMs influence the results of electrochemical measurements and their interpretations. Within this research, three different alkali-activated mortar mixes were prepared, based on fly ash, slag or metakaolin. Pore solutions were extracted from each mortar and chemical analysis was acquired. Different electrochemical corrosion measurements were performed on steel submerged to synthetic pore solutions. In parallel, ordinary carbon steel reinforcing bar was installed in the same types of alkali-activated mortar mixes. Specimens were exposed to wet/dry cycles with saline solution and periodic measurements of electrochemical impedance spectroscopy (EIS) were performed. Measured parameters in both systems were analysed and compared. It was concluded that electrochemical measurements in pore solutions can provide basic overview on corrosion behaviour in different AAMs environments. Periodic EIS measurements enabled monitoring of corrosion initiation and propagation on steel reinforcement in AAMs, although the information on the corrosion type is missing. Interpretation of results depends on visual analysis of corrosion damages after the end of exposure, providing information on corrosion type and intensity. The continuation of research on corrosion monitoring techniques will be performed by using Electrical Resistance (ER) sensors and Coupled Multi-Electrode Array (CMEA) sensors.

KEY WORDS: corrosion, alkali-activated mortars, pore solution extraction, electrochemical corrosion techniques, visual analysis;

1   INTRODUCTION

Concrete is the most widely used man-made building material in the world. During the production of its main component, ordinary Portland cement (OPC), the estimated 5–8 % of global anthropogenic CO_2 emissions are released [1,2]. Alkali-Activated Materials (AAMs) use supplementary cementitious materials (SCMs) as a total replacement of OPC and are one of the potential alternatives to OPC containing binders for a wide range of possible applications [3,4]. AAMs are formed by the reaction between various aluminosilicate precursors, often in the form of industrial by-products, and alkaline activators. Wide range of combinations form materials with various properties and applicabilities [4]. The use of AAMs for reinforced concrete elements raises the issue of steel corrosion, which is the main cause of their premature failure. The loss of alkalinity and the ingress of chloride ions are the primary causes of steel corrosion in OPC concrete [2]. However, the pore solutions in AAMs can significantly differ from OPC-based cements in terms of their chemical, mineralogical and redox characteristics [5], which can strongly influence all phases of corrosion process and causing difficulties with interpretation of parameters obtained by electrochemical tests usually used for corrosion tests in cementitious materials. The difference between corrosion processes in concrete mixes (also alkali-activated materials) and solutions is that the anodic and cathodic sites are spatially localized due to the porous and inhomogeneous structure of the concrete [6]. Therefore, information on corrosion rate in concrete should contain information on corrosion type, i.e. if it is placed uniformly across the surface or it is more localized. Commonly used electrochemical monitoring techniques, such as electrochemical impedance spectroscopy [7], potentiodynamic polarization tests, or linear polarisation resistance measurements, generally do not differentiate between general and localized corrosion and the corrosion damage can only be evaluated when steel is destructively removed from the concrete. The aim of this paper is to evaluate electrochemical methods for testing steel corrosion in different AAM mixes and in their pore solutions, and to compare the results obtained in both environments.

2 MATERIALS AND METHODS

2.1 Experiments in Alkali-Activated Mortars

Mortar mix-designs used in this research were developed by RILEM TC 247-DTA, which was aiming at development of recommendations for durability testing of alkali-activated materials [8–11]. Three types of mortars designed for assessing the sulphate resistance were selected, based on three different precursors, i.e. fly-ash (FA8), steel slag (S3a-661) and metakaolin (MK2). The exact mortar mixture designs are presented in Table 1.

Compressive strength [12] measured after 56 days on tested mortars were: MK2 (70 MPa) > S3a-661 (60 MPa) > FA8 (39 MPa). The results of Hg porosimetry showed the following proportion of pores in tested mortars: FA8 (15 %) > MK2 (14 %) > S3a-661 (11 %).

Table 1: Mortar mix-designs used in this study [8–11].

Mortar / [g]	FA8	S3a-661	MK2
Flay ash (V-378/14)	455.9	-	-
Slag (V-138/15)	-	557.4	-
Metakaolin (V-63/15)	-	-	450.0
Water glass (V-25/15)	168.5	22.4	-
Water glass (V-502/14)	-	-	372.0
NaOH (V-44/15)	-	33.4	37.8
NaOH solution 41.7 % (wt.) NaOH + 58.3 % (wt.) H2O	64.4	-	-
Tap water	17.7	232.3	5.0
CEN Standard sand (EN 196-1)	1350.0	1350.0	1350.0

Three parallel specimens for each mortar mix were prepared for corrosion tests. Specimens were cast in prism shaped moulds in dimensions of $3{\times}3{\times}10$ cm^3. Cold ribbed steel reinforcing bar type B 500B (1.0439 [13]) with diameter Φ6 mm was embedded in each specimen. Both ends of steel bar were protected with epoxy based coating in a way that the length of 9 cm in the middle was unprotected and the surface area of 17 cm^2 was exposed to mortar. Steel bar was covered with 7 mm mortar cover. After casting specimens were cured in humidity chamber for 28 days. After curing specimens were exposed to wetting / drying cycles with 3.5 % of NaCl solution from the pool on the top of each specimen. One cycle was one week long – 3 days of wetting and 4 days of drying.

Electrochemical Impedance Spectroscopy (EIS) measurements were performed once in each cycle, i.e. on the last day of wetting period. Steel reinforcing bar embedded in mortar specimen was used as working electrode, a graphite electrode and a saturated calomel electrode (SCE) submerged in top pool of the specimen served as the counter and reference electrode, respectively. The EIS measurements were performed using a Gamry Ref600 potentiostat. All potentials refer to the SCE scale. EIS measurements were performed at open circuit potential (OCP) in the frequency range from 65 kHz to 5 mHz with 11 points per decade and an amplitude of ±10 mV. The total impedance ($|Z|_{total}$) values were estimated as impedances ($|Z|$) at the lowest measured frequencies with deducted solution resistance (R_s) values.

j_{corr} values were calculated using the Stern-Geary equation; an estimated constant B = 0.026 V was used [14]. $|Z|_{total}$ was used as a near estimation for polarisation resistance (R_p) in calculations from EIS parameters. v_{corr} values were calculated according to Equation 1 [7] using atomic mass value AM = 55.85, Faraday constant F = 9.65×10^4 As, valence n = 2, and steel density ρ = 7.89 g/cm^3.

$$v_{corr} = \frac{AM \cdot j_{corr}}{n \cdot F \cdot \rho}$$

Equation 1

At the end of exposure, mortar specimens were broken and visual inspection of corrosion damages on steel bars was performed by means of macroscopic images. Visual analysis was performed as a complementary method for verification of electrochemical measurements by determination of corrosion type and intensity.

2.2 Experiments in Alkali-Activated Mortar pore solutions

Three different AAMs mixes (Table 1) were cast in cylinder shaped moulds and cured in a sealed plastic foil. Due to insufficient humidity of mortar after 28 days of curing specimens were broken into smaller (approx. 3-4 cm) pieces and slowly re-wetted with drops of distilled water in a way that no extra water was left out of the mortar. After one day from drip-wetting, pore solutions were extracted from mortars with high-pressure device (up to 1000 MPa) [15,16]. Extracted pore solutions were further analysed for their pH and chemical composition using ion-exchange chromatography system 940 Professional IC Vario (Metrohm). Based on the results, simulated pore solutions were prepared. The pH was adjusted with the ratio of silicate in OH^- ions. Exact chemical compositions of simulated pore solutions are presented in Table 2.

Table 2: Chemical compositions of simulated pore solutions, prepared on the basis analysed pore solutions extracted from alkali-activated mortars (Table 1).

Mortar (Table 1)	pH	Salts [g/L]								
		NaCl	KCl	K_2SO_4	Na_2SO_4	$NaNO_3$	Na_2HPO_4	NaOH	KOH	$Na_2Si_2O_5$ (72 wt.%)
FA8	12.36	0.053	-	1.502	22.871	-	7.859	2.081	-	79.968
S3a-661	12.52	-	0.400	0.914	-	-	-	1.430	1.805	196.486
MK2	12.37	0.054	-	0.089	0.275	0.646	-	5.840	-	184.670

Simulated pore solutions (Table 2) were used as the electrolyte for different electrochemical corrosion measurements. Experiments were performed in standard corrosion cell. The working electrodes were made of disc steel with surface area of 0.785 cm^2 and similar composition and microstructure to that used for the concrete reinforcement (Table 3). The tablets were polished before the experiments by means of SiC paper grit 600 and placed in ethanol ultrasonic bath. A graphite electrode served as the counter electrode, and a saturated calomel electrode (SCE) was used as the reference electrode.

Table 3: Chemical composition of steel sheet used as a working electrode in electrochemical measurements.

C [wt.%]	P [wt.%]	S [wt.%]	Cu [wt.%]	N [wt.%]	C_{eq} [wt.%]
0.14	0.008	0.012	0.073	0.006	0.23

Three electrochemical techniques were performed: linear polarisation resistance (LPR) measurements, electrochemical impedance spectroscopy (EIS) and cyclic potentiodynamic polarization (CPD) scans, in that sequence order. The LPR measurement was performed after 90 min stabilization in exposure environment. Measuring potential interval was set from –20 mV up to +20 mV at open-circuit potential (E_{oc}) measured before the measurement. The scan rate was 0.1 mV/s and sampling period was 1 s. The EIS measurement was performed at E_{oc}. The frequency range was set from 65 kHz to 5 mHz, measured 11 points per decade. The total impedance ($|Z|_{total}$) values were estimated as impedances ($|Z|$) at the lowest measured frequencies with deducted solution resistance (R_s) values. By means of CPD measurements, the polarization potential was scanned from −0.25 V vs. E_{oc} to +0.75 V vs. reference potential (E_{ref}) and back to −0.25 V vs. E_{oc}, with a scan rate 1 mV/s and sampling period 1 s.

j_{corr} values were calculated using the Stern-Geary equation and v_{corr} values were calculated according to Equation 1, with the same parameters as for measurements in mortars (see chapter 2.1.2). $|Z|_{total}$ was used in calculations as a near estimation for polarisation resistance (R_p).

3 RESULTS

3.1 Results in Alkali-Activated Mortars pore solutions

First, measurements were performed in three simulated AAM pore solutions (Table 2).

Linear polarisation resistance (LPR) showed small differences between measurements in different pore solutions. Polarisation resistance values are relatively high and represent corrosion rates lower than 1 μm/year.

Figure 1: Scattering of R_p values measured with LPR in AAMs pore solutions.

Electrochemical impedance spectroscopy (EIS) curves measured in simulated pore solution are presented as Nyquist and Bode plots (Figure 2). Impedance responses have similar shapes, but the lowest impedance values were measured on steel in S3a-661 (slag) pore solution, higher in FA8 (fly ash) pore solution and the highest in MK4 (metakaolin) pore solution. Parameters of total impedance ($|Z|_{total}$) and calculated corrosion rates (v_{corr}) are presented in Table 4.
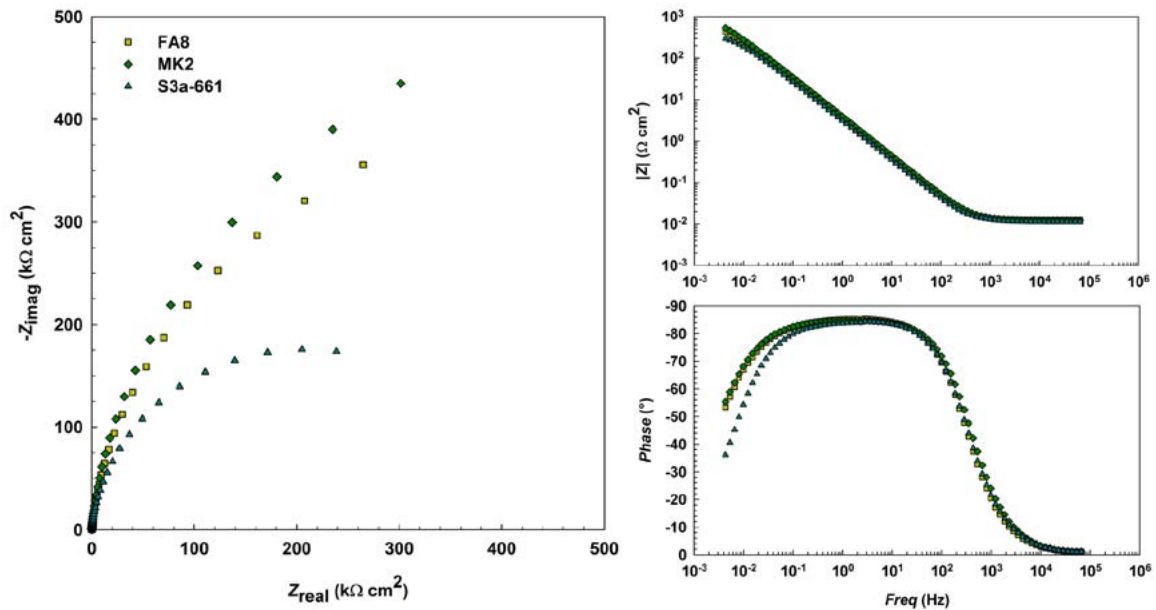
Figure 2: Representative EIS spectra recorded in three AAMs solutions.

Table 4: Total impedance ($|Z|$) values measured with EIS measurements and calculated corrosion rates (v_{corr}) in different AAMs pore solutions.

AAM solution type	$|Z|_{total}$ [kΩ·cm^2]	v_{corr} [μm/year]
FA8	412	0.7
S3a-661	326	0.9
MK2	545	0.6

Cyclic potentiodynamic polarization (CPD) scans measured on steel in different simulated pore solutions are presented in Figure 3. The shapes of CPD curves are similar in all pore solutions; steel exhibits pseudo positive region. After potential is reversed, negative hysteresis is observed, which indicates that pitting is not likely to occur. Measured current density (j_{corr}) is the lowest for steel in MK4 (metakaolin) pore solution, highest in FA8 (fly ash) pore solution and the highest in S3a-661 (slag) pore solution. Similar as in the case of EIS measurements, the MK4 pore solution represents the least corrosive environment.
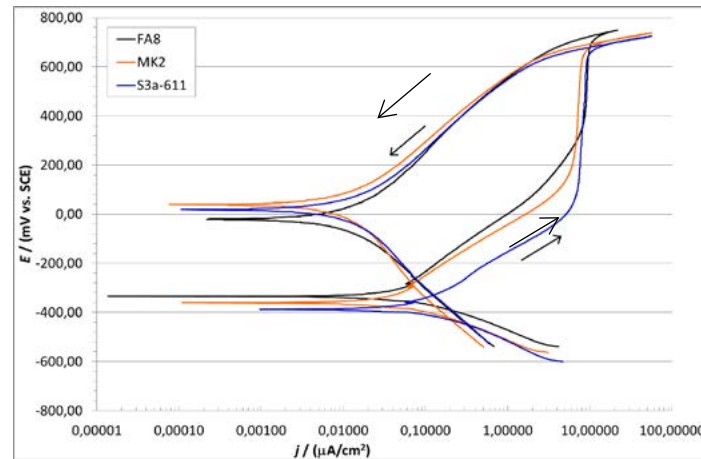
Figure 3: Representative CPD scans recorded in three AAMs solutions.

Table 5: Current density (j_{corr}) and corrosion potential (E_{corr}) values measured with EIS measurements and calculated corrosion rates (v_{corr}) in different AAMs pore solutions.

AAM solution type	E_{corr} [mV]	j_{corr} [$\mu A/cm^2$]	v_{corr} [$\mu m/year$]
FA8	−336	0.06	0.7
S3a-661	−365	0.09	1.0
MK2	−340	0.04	0.5

The corrosion rates were calculated from parameters measured with three different electrochemical methods: polarisation resistance (LPR) measurements, electrical impedance spectroscopy (EIS) and cyclic potentiodynamic polarization (CPD) scans. j_{corr} values were calculated using the Stern-Geary equation and v_{corr} values were calculated according to Equation 1, as described in Experimental. All three electrochemical methods show very similar results (Table 6), with very low corrosion rates below 1 $\mu m/year$. The highest corrosion rates were measured in S3a-661 (slag) and the lowest in MK2 (metakaolin) mortar pore solution.

Table 6: Calculated corrosion rates (v_{corr}) in three different AAMs pore solutions with three different electrochemical techniques: LPR, EIS and CPD.

AAM solution type	LPR v_{corr} [$\mu m/year$]	EIS v_{corr} [$\mu m/year$]	CPD v_{corr} [$\mu m/year$]
FA8	0.5	0.7	0.7
S3a-661	0.8	0.9	1.0
MK2	0.3	0.6	0.5

3.2 Results in Alkali-Activated Mortars

Electrochemical impedance spectroscopy (EIS) measurements were periodically performed during wetting/drying cycles on steel reinforcement bars embedded in three alkali-activated mortar (AAM) mixes (Table 1). Spectra show (Figure 4 and Figure 5) that shapes differ among different mortars and also change significantly during the exposure period. The resistance of exposure media (mortar) increases with each cycle.
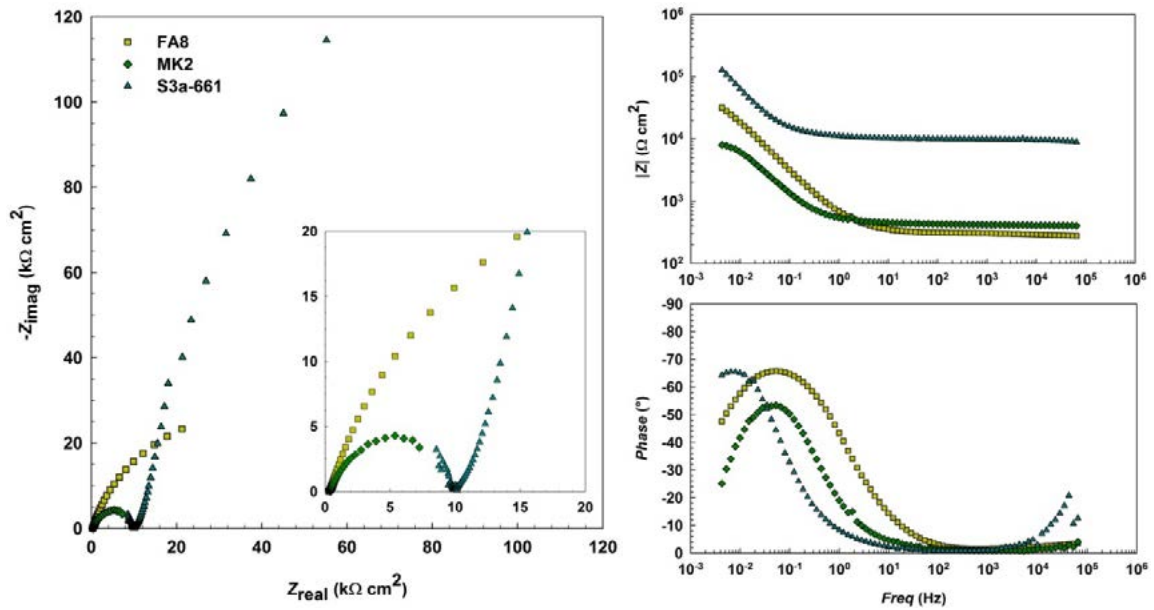
Figure 4: Representative EIS spectra recorded in 1st wetting / drying cycle in three alkali-activated mortars.
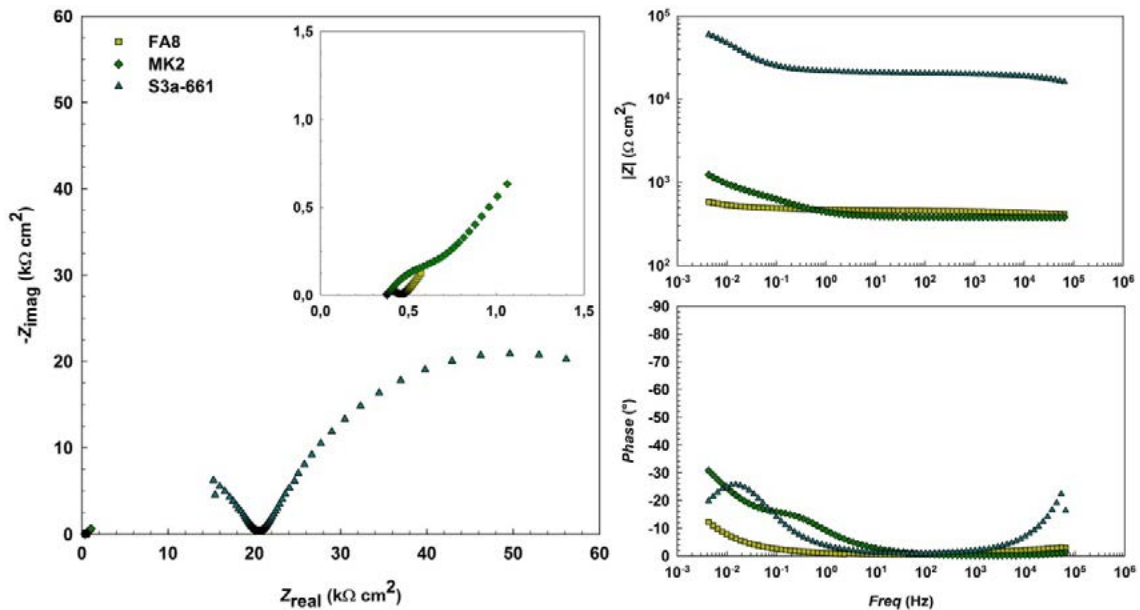
Figure 5: Representative EIS spectra recorded in 17th wetting / drying cycle in three alkali-activated mortars.

Values of total impedance ($|Z|_{total}$) measured in mortar are significantly lower from values measured in pore solutions; consequently, corrosion rates (v_{corr}) are higher already from initial measurements (Table 7). The corrosion processes intensify over time of exposure, since measured parameters of total impedance ($|Z|_{total}$) values and consequently corrosion rates (v_{corr}) are increasing with time (Table 7). This is expected due to the presence of Cl^- ions in mortar which are increasing by each cyclic wetting with 3.5 % NaCl solution. The measured rise of v_{corr} is especially high in FA8 mortar, where values gradually go from 10 μm/year in the 1st wetting/drying cycle to 2400 μm/year in 17th cycle. The increase of v_{corr} values measured in MK2 mortar is lower (from 40 μm/year to 350 μm/year in 17 cycles), but significant. However, steel embedded in S3a-661 mortar is still not experiencing significant corrosion rates after 17 cycles of exposure (v_{corr} is up to 8 μm/year).

Contrary to measurements in pore solution, electrochemical impedance spectroscopy (EIS) curves also show shapes which differ among different mortars and change significantly during the exposure period (Figure 4 and Figure 5). The resistance of exposure media (mortar) is also rising with each cycle.

45

Table 7: Total impedance ($|Z|_\text{total}$) values measured with EIS measurements and calculated corrosion rates (v_corr) in different alkali-activated mortars.

AAM solution type	$|Z|_\text{total}$ [kΩ·cm²]		v_corr [μm/year]	
	Week 1	Week 17	Week 1	Week 17
FA8	31	0.1	10	2400
S3a-661	117	39	3	8
MK2	8	857	40	350

After 17 weeks of exposure, mortar specimens were demolished and steel bars were analysed. Visual inspection of steel bars (Figure 6) confirmed the intensity of corrosion activities measured with electrochemical impedance spectroscopy (EIS) technique. Images of steel bar embedded in FA8 (fly ash) mortar (Figure 6a) show severe corrosion damages – surface is rough due to local pits merged together in large areas of corrosion damages with visible reduction of rebar diameter. Damages on steel bar embedded in MK2 mortar (Figure 6b) are clearly visible and locally fairly deep. However, damages on steel bar embedded in S3a-661 mortar (Figure 6c) are very few and shallow, limited to edge areas. As seen from Figure 6 the comparison of visual damages corresponds with EIS results, which indicate the highest corrosion rates on steel in FA8 mortar, significant corrosion rates on steel in MK2 mortar and very low corrosion rates on steel in S3a-661 mortar. However, considering real area of corrosion damages, calculated local corrosion rates would be even higher.

Figure 6: Corrosion damages on steel bar embedded in a) FA8, b) S3a-661 and c) MK2 mortar after 17 cycles of exposure.

4 CONCLUSIONS

In this study corrosion properties of steel exposed to different alkali-activated material environments, i.e. solid mortars and their pore solutions, is presented. The following conclusions can be made:

- Measurements in simulated pore solution using linear polarisation resistance (LPR) technique, electrical impedance spectroscopy (EIS) and cyclic potentiodynamic polarization (CPD) scans show similar results, namely steel in MK2 (metakaolin) pore solution is the most corrosion resistant and steel in S3a-661 (slag) pore solution is the least corrosion resistant. The distinction of corrosion properties between different pore solutions can also be observed from the results of the used electrochemical techniques. These differences could be more expressed if chlorides were present.

- Initial corrosion rates (v_corr) of steel measured in solid mortars differ significantly from corrosion rates measured in their pore solutions. It is assumed that the steel/mortar interface properties and locally separated anodic and cathodic areas play significant role in corrosion processes of steel in alkali-activated mortars, which cannot be completely explained by simplified pore solution conditions. In time of exposure, these differences are more significant due to the presence of Cl^- ions.

- Electrochemical measurements were complemented by visual inspection, which provides information on corrosion type and therefore real corrosion damage areas which should be considered with interpretation of measured results.

- Methods which distinguish type of corrosion damages should be used for a comprehensive understanding of corrosion mechanisms in alkali-activated mortars. The use of X-ray computed microtomography should also be considered as a method complementary to electrochemical methods.

ACKNOWLEDGMENTS

REFERENCES

[1] Scrivener, K.L.; Kirkpatrick, R.J.: Innovation in Use and Research on Cementitious Material, *Cement and Concrete Research*, 38 (2008) 128–136

[2] Van Deventer, J.S.J.: Chapter 10 - Progress in the Adoption of Geopolymer Cement. In: *Handbook of Low Carbon Concrete*, Butterworth-Heinemann, (2017), pp. 217–262

[3] Provis, J.L.; Bernal, S.A.: Geopolymers and Related Alkali-Activated Materials. *Annu. Rev. Mater. Res.*, 44 (2014) 299–327

[4] Provis, J.L.: Alkali-Activated Materials, *Cement and Concrete Research*, 114 (2018) 40–48

[5] Criado, M.; Provis, J.L. Alkali Activated Slag Mortars Provide High Resistance to Chloride-Induced Corrosion of Steel, *Frontiers in Materials*, (2018) 5

[6] Alonso, C. et al.: Relation between Resistivity and Corrosion Rate of Reinforcements in Carbonated Mortar Made with Several Cement Types, *Cement and Concrete Research*, 18 (1988) 687–698

[7] Kelly, R.G. et al.: *Electrochemical Techniques in Corrosion Science and Engineering*, Marcel Dekker, Inc. (2003)

[8] Provis, J.L. et al.: RILEM TC 247-DTA Round Robin Test: Mix Design and Reproducibility of Compressive Strength of Alkali-Activated Concretes, *Mater Struct*, 52 (2019) 99

[9] Gluth, G.J.G. et al.: RILEM TC 247-DTA Round Robin Test: Carbonation and Chloride Penetration Testing of Alkali-Activated Concretes, *Mater Struct*, 53 (2020) 21

[10] Winnefeld, F. et al.: RILEM TC 247-DTA Round Robin Test: Sulfate Resistance, Alkali-Silica Reaction and Freeze–Thaw Resistance of Alkali-Activated Concretes, *Mater Struct*, 53 (2020) 140

[11] Gluth, G.; Rickard, W.: Design and Characterization of Fly Ash-Based Geopolymer Concretes for a Round-Robin Durability Testing Program In: *Proceedings of the Geopolymers: the route to eliminate waste and emissions in ceramic and cement manufacturing,* Engineering Conferences International / Società Ceramica Italiana: Hernstein, Austria, (2015), pp. 67–70

[12] Technical Committee CEN/TC 51. European Standard EN 196-1, *Methods of Testing Cement - Part 1: Determination of Strength*, European Committee for Standardization: Brussels, Belgium, (2016)

[13] Technical Committee ECISS/TC 100. European Standard EN 10027-2, *Designation Systems for Steels - Part 2: Numerical System*, European Committee for Standardization: Brussels, Belgium, (2015)

[14] Schiegg, Y. Monitoring of Corrosion in Reinforced Concrete Structures. In: *Corrosion in Reinforced Concrete Structures*, Woodhead Publishing Limited: Cambridge, England, (2005), pp. 46–70

[15] Cyr, M.; Daidié, A. Optimization of a High-Pressure Pore Water Extraction Device, *Review of Scientific Instruments*, 78 (2007) 023906

[16] Cyr, M. et al.: A. High-Pressure Device for Fluid Extraction from Porous Materials: Application to Cement-Based Materials, *Journal of the American Ceramic Society*, 91 (2008) 2653–2658

6

Barbara Horvat, Vilma Ducman

Influence of curing/drying methods including microwave heating on alkali activation of waste casting cores

INFLUENCE OF CURING/DRYING METHODS INCLUDING MICROWAVE HEATING ON ALKALI ACTIVATION OF WASTE CASTING CORES

B. Horvat[1], V. Ducman[2]

[1,2] Slovenian Nationa Building and Civil Engineering Institute, Department of Materials
Dimičeva ul. 12, 1000 Ljubljana
e-mail: barbara.horvat@zag.si, vilma.ducman@zag.si

SUMMARY: Within previous investigation alkali activation of waste casting cores at room temperature did not give promising results, i.e. when the precursor was gently ground and sieved below 600 µm the alkali activated material fell apart at demolding, and when the precursor was ground below 90 µm, the alkali activated material did not solidify in more than 2 years. , Therefore different drying/curing methods were applied to enhance the reaction. Waste casting cores were prepared in two granulations (sieved below 600 µm and below 90 µm), activated with Na-water glass and 10 M NaOH, cured at different temperatures (70 °C and room temperature), and subsequently cured/dried at three different conditions: room temperature, 110 °C, and irradiated with microwaves. The highest compressive strength, 25 MPa, was gained with subsequent curing/drying at 110 °C. The lowest density, 0.5 kg/l, with compressive strength above 3 MPa, was achieved with subsequent curing/drying with microwaves.

KEYWORDS: Waste casting cores; Alkali activation; Curing; Drying; Microwaves; Mechanical strength.

1   INTRODUCTION

Alkali activated materials (AAM) can be produced from different waste materials containing enough Si and Al in the amorphous phase, which react with alkalis and form an aluminosilicate network (ASN) of SiO4 and AlO4 tetrahedrons that are joined by oxygen bridges. In the network, the negative charge localized on Al^{3+} is compensated with positive ions from alkali liquid [1]. Most researched precursors for alkali activation are metakaolin [2], fly-ash [3], slag [2] and their mixtures [2]. The technology was proved also in praxis:

  • airport runway in Brisbane, Australia [4], where for precursors blast furnace slag and fly-ash were used,
  • 4-floor public house (University of Queensland's Global Change Institute) in Queensland, Australia [5], where floors are made from 33 precast panels that are made from slag and fly ash-based geopolymer concrete.

Alkali activated foams (AAF) represent added value to the alkali activated materials, as being porous, lightweight with the potential to be used as fire-resistant thermal and/or acoustic insulators [6]. Porosity can be achieved with several methods:

  • mechanical process using preformed air bubbles [6],
  • chemical reaction of foaming agents (Na-perborate, Na-lauryl sulphate, Al powder, H_2O_2, metal silica impurities contained in silica fumes etc.) with alkali activated slurry of precursor and source of alkali, where gases are formed and trapped in the liquid network [7],
  • chemical reactions of ingredients present in the precursor(s) with alkali and/or alkali glass, i.e. self-foaming [8],
  • removal of hydrated water from alkali activated material with temperature [9],
  • replica method with removal (combustion, decomposition) of "sacrificed" material like organic compounds, plastic, carbon, sulphate [10],
  • bloating of the precursor at high temperatures [11],
  • etc.

Casting cores which are also the subject of the present paper, are commonly produced with three different methods: coldbox (binder hardens sand with chemical reaction without addition of thermal energy [12]), hotbox (binder hardens sand with heat [12]) and warmbox/shellbox (binder in the outer layer of sand core hardens with heat [13]). Binders can be inorganic like alkali glass, cement, clay, bentonite, which are gas emission-free, or organic like furan, phenolic urethane, phenol-formaldehyde resin, which lead to emission of health-hazardous gasses during exposure to casting metal [14].
Drying is an important part of the core preparation process. Common drying method with implementing heat in a

furnace is just surface drying [15], drying with the use of gasses in casting core production is semi-volumetric (depending on if the gas is only around the core or blown through tubes into the core, depending on the viscosity of the fluid [16]), while drying with microwaves is volumetric [15]. When drying with the surface method, samples are dried to a certain depth of the bulk sample, which depends on the temperature applied and time on the temperature, while volumetric drying is drying throughout the whole bulk's volume at the same time in short(er) time [15] where high(er) temperatures can take place [17] that can also change the mineralogical composition, size of grains, which makes procedure useful also for (pre)sintering of ceramics [18]. The volumetric drying is a consequence of dielectric polarization of molecules with electromagnetic irradiation [19] with wavelengths from 1 mm to 1 m, frequency 300 GHz to 300 MHz respectively [20].

A newer emission-free warm-box method is where microwaves are used for heating to harden the binder consisting of alkali glass and alkali on the surface of quartz sand (which is not alkali activated synthesis, just binding of quartz sand into a mould). Results of all research available so far are showing that using microwave technology gives better strength and uses less energy than alternatives [12], therefore the use of microwave irradiation in connection to the alkali activated synthesis using waste casting cores might contribute to increase of mechanical properties too.

In the present study shell-box casting cores were prepared in 2 different granulation, 3 different alkali activating mixtures and with 3 different drying procedures to assess the influence of drying/curing methods on properties of final AAM, and to thus determine optimal preparation method.

2 MATERIALS AND METHODS

2.1 Analysis of precursor

Waste casting cores (WCC) from company Termit d.d. (Drtija, Slovenia), labelled 10 09 06 (according to the Classification list of waste from Official Gazette of the Republic of Slovenia, no. 20/01 Annex 1), used in the study are shell-box cores that could not be further used due to the damage in the factory.

X-ray fluorescence on melted discs (XRF; Thermo Scientific ARL Perform'X Sequential XRF) and X-ray powder diffraction (XRD; Empyrean PANalytical X-ray Diffractometer, Cu X-Ray source) analysis were performed with material dried at 70 °C for 24 h (WTB Binder), ground with the vibrating disk mill (Siebtechnik) and sieved below 90 μm. XRF analysis was done with software UniQuant 5, XRD analysis with X'Pert Highscore plus 4.1. Rietveld refinement using external standard (a pure crystal of Al_2O_3) was implemented on XRD pattern to estimate the amount of amorphous phase and minerals present in waste casting cores.

Fourier-transform infrared spectroscopy (FTIR; PerkinElmer Spectrum Two) was performed on a sample that was ground with the vibrating disk mill and sieved below 90 μm.

Scanning electron microscopy (SEM; Jeol JSM-IT500) investigation was performed under high vacuum conditions on dried samples.

2.2 Preparation of alkali activated samples

Waste casting cores were dried at 70 °C for 24 h, ground with a pestle and mortar and sieved below 600 μm, or ground in a vibrating disk mill and sieved below 90 μm.

Alkali activation was performed by addition of 10 M NaOH (Donau Chemie Ätznatron Schuppen, EINECS 215-785-5) to Na-water glass (Geosil, 344/7, Woelner) in equal mass amounts. Liquids were stirred until the mixture became clear, and then poured into the sample in mass ratio "waste material : alkali : alkali glass" 2.5:1:1 (if not stated otherwise) under constant mixing for 1 min. The slurry was poured into plastic moulds of dimensions 25x12x12 mm3, cured at 70 °C for 24 h, demoulded, subsequently cured (because curing at 70 °C for 24 h was not enough) at room temperature, with kitchen microwave (Gorenje Microwave oven MO 17DV, 2.45 GHz, 700 W) for different times or until the sample was completely dry, or in drying chamber at 110 °C for 24 h (WTB Binder).

2.3 Analysis of AAM

Measurement of compressive strength of alkali activated casting cores was performed with compressive and bending strength testing machine (ToniTechnik ToniNORM) 1 month after solidification.

Density was determined by weighting the sample and dividing its mass with geometrically determined volume.

Fourier-transform infrared spectroscopy (FTIR; PerkinElmer Spectrum Two) was performed on alkali activated sample which was dried with different methods.

The surface and microstructure of selected samples were investigated with the scanning electron microscope (SEM; Jeol JSM-IT500) under high vacuum conditions.

3   RESULTS AND DISCUSSION

3.1   Analysis of precursor

SEM micrographs of WCC ground in a mortar with pestle and waste casting cores ground in vibrating disk mill are presented in Figure 1 (a) and (b) respectively. Precursor sieved below 600 µm (a) consists of particles with smooth edges, smooth surface and sizes generally above 100 µm, while precursor sieved below 90 µm (b) is powder-like consisting of particles with sharp edges and smooth surface. The damaged surface is seen already on particles of precursor gently ground and sieved below 600 µm (red circle in Figure 1 (a)), which is a consequence of destroying linking bridges connected with the sand base [21].
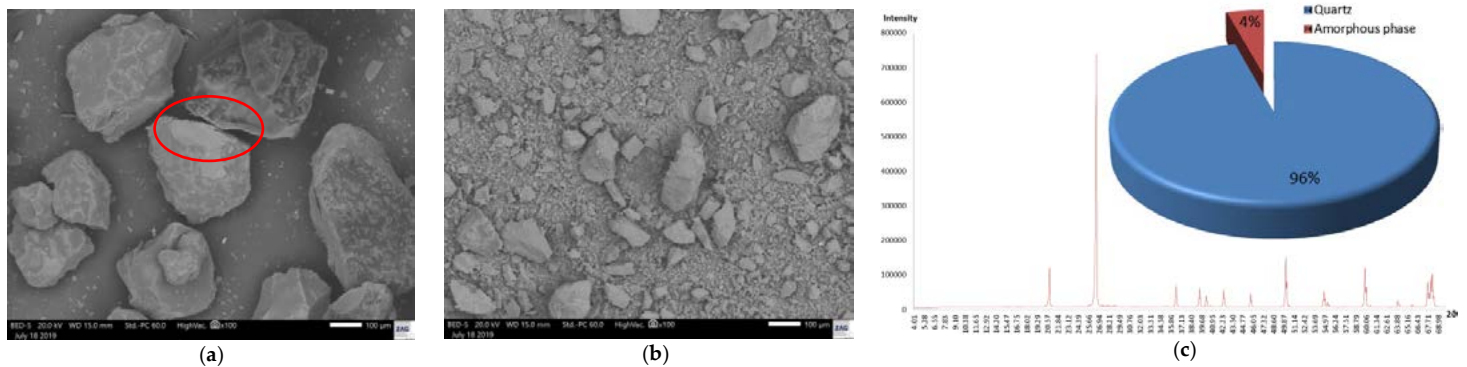
Figure 1: SEM micrographs of WCC. (a) Gently ground in a mortar with pestle and sieved below 600 µm (red circle: damaged surface); (b) ground in vibrating disk mill and sieved below 90 µm, (c) XRD pattern of WCC and on the inset its Rietveld refinement.

Chemical analysis was performed by means of XRF. It showed that there is a small mass percentage of K (0.09%), Ca (0.10%) and Al (1.33%), while Si is in aboundance (44.60%). With Rietveld refinement performed on XRD pattern (see Figure 1 (c)) the mass percentage of crystalline and amorphous phase was estimated. Only quartz (96%) was found to be in crystalline phase, meaning that there is only a small amount of Al, K and Mg in precursor useful for alkali activation.

Determination of the presence of an organic compound in WCC was performed utilizing FTIR, which is presented in Figure 2. Frequency 2980 cm^{-1} corresponds to C-H values of alkyl groups (orange vertical line in Figure 2) [22], frequencies around 1450 cm^{-1} correspond to C-H$_2$ and C-H$_3$ bendings from aromatic ring (phenol from the phenol-formaldehyde resin used in casting core production, purple vertical lines in Figure 2) [23], frequencies 3340 cm^{-1} and 1635 cm^{-1} correspond to O-H in water (blue vertical lines in Figure 2) [24], while Si-O bonds are from 950 to 1110 cm^{-1}, Si-O from quartz around 800 cm^{-1} [25].
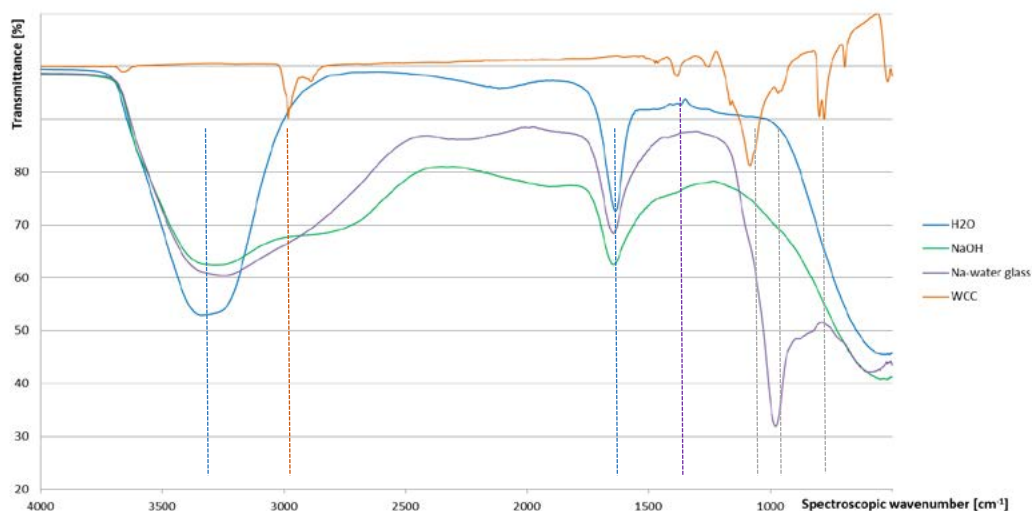
Figure 2: FTIR of all ingredients used in alkali activation. Dashed blue lines O-H bonds, dashed orange lines C-H bonds, dashed purple lines aromatic C-H$_2$ and C-H$_3$ bonds, dashed grey lines Si-O bonds.

3.2 Analysis of bulk AAM

Compressive strength and density are presented in Table 1 and vary according to the preparation of the precursor (degree of milling), ratio precursor : 10 M NaOH : Na-water glass, and drying method. From the results given in Table 1, it can be concluded that:

• to achieve higher mechanical properties, it is better that precursor is ground and sieved below 90 μm (smaller particles, more surface), otherwise, the experiment is not successful,

• in case of bigger particles of the precursor amount of liquid phase is crucial, i.e. if there is not enough liquid phase, successful demolding is not possible,

• in case of smaller particles of the precursor amount of liquid phase has to be low enough to gain higher final compressive strength, at least when using surface drying method,

• the highest influence on final properties has used the method of subsequent curing/drying:

• if samples were subsequently cured/dried on mild conditions (room conditions, RC), AAM did not even solidify in more than 2 years,

• if samples were subsequently cured/dried with surface drying at 110 °C, density was comparable or lower to samples dried at RC, but samples did solidify and had compressive strength up to 25 MPa when particles of the precursor were smaller,

• if samples were subsequently cured/dried with volumetric drying method (microwaves), AAM solidified in the shortest time, density lowered, as well as compressive strength if particles of precursor were smaller, i.e. there was no difference in compressive strength when volumetric or surface drying at 110 °C were performed on AMM synthesized from precursor consisting of bigger particles,

• density and compressive strength showed time dependence on irradiation with microwaves presented also in Figure 3.

Table 1: Compressive strength and density of prepared AAM. RC = room conditions, MW = microwave.

Preparation of precursor	Precursor : 10M NaOH : Na-water glass	Curing conditions	Subsequent drying method	Density [kg/l]	Compressive strength [MPa]
< 600 μm	3.75 : 1 : 1	70 °C 24 h	RC	*	
< 600 μm	3.3 : 1 : 1	70 °C 24 h	RC		
< 600 μm	2.5 : 1 : 1	70 °C 24 h	RC	1.60	Does not solidify
< 600 μm	2.5 : 1 : 1	70 °C 24 h	110 °C 24 h	1.55	17.61
< 600 μm	2.5 : 1 : 1	70 °C 24 h	MW 0.66 min	1.49	17.55
< 90 μm	3.3 : 1 : 1	70 °C 24 h	RC	1.62	Does not solidify
< 90 μm	3.3 : 1 : 1	70 °C 24 h	110 °C 24 h	1.60	24.98
< 90 μm	3.3 : 1 : 1	70 °C 24 h	MW 0.66 min	1.20	5.55
< 90 μm	2.5 : 1 : 1	70 °C 24 h	RC	1.64	Does not solidify
< 90 μm	2.5 : 1 : 1	70 °C 24 h	110 °C 24 h	1.03	11.42
< 90 μm	2.5 : 1 : 1	70 °C 24 h	MW 0.08 min	1.46	0.25
< 90 μm	2.5 : 1 : 1	70 °C 24 h	MV 0.17 min	1.46	0.34
< 90 μm	2.5 : 1 : 1	70 °C 24 h	MV 0.33 min	1.24	0.77
< 90 μm	2.5 : 1 : 1	70 °C 24 h	MV 0.5 min	0.94	0.78
< 90 μm	2.5 : 1 : 1	70 °C 24 h	MW 0.66 min	0.90	5.71
< 90 μm	2.5 : 1 : 1	70 °C 24 h	MW 0.83 min	0.71	2.90
< 90 μm	2.5 : 1 : 1	70 °C 24 h	MW 1 min	0.73	2.70
< 90 μm	2.5 : 1 : 1	70 °C 24 h	MW 1.17 min	0.78	2.86
< 90 μm	2.5 : 1 : 1	70 °C 24 h	MW 1.5 min	0.59	2.10
< 90 μm	2.5 : 1 : 1	70 °C 24 h	MW 2 min	0.70	2.26
< 90 μm	2.5 : 1 : 1	70 °C 24 h	MW 3 min	0.64	1.95
< 90 μm	2.5 : 1 : 1	70 °C 24 h	MW 4 min	0.72	1.90
< 90 μm	2.5 : 1 : 1	70 °C 24 h	MW 5 min	0.72	1.07

* = not solidified

Dependence of time irradiation with microwaves on density and compressive strength of sample prepared from precursor ground in vibrating disk mill and sieved below 90 μm, mixed with 10 M NaOH and Na-water glass in ratio 2.5:1:1 respectively, are presented in Figure 3. Density lowers with an early time of irradiation and reaches an approximately constant value. Compressive strength starts increasing with irradiation, reaches peak soon (sample is completely dried) and starts slower decline (melting).
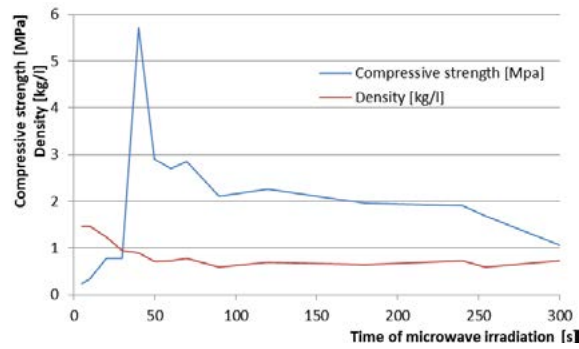
Figure 3: Compressive strength and density of samples prepared from precursor ground in vibrating disk mill and sieved below 90 μm, mixed with 10 M NaOH and Na-water glass in ratio 2.5:1:1 respectively, in the dependence of irradiation with microwaves for a different amount of time.

Beside weak solidification at milder curing conditions (70 °C) and difficulties at demolding (shape of the prism was easily damaged after primary curing, AAM reacted with glass surface when subsequently curried/dried at 110 °C), there was no shrinkage noticed. However, when the precursor used was from smaller particles (sieved below 90 μm), foaming was noticed as can be seen on SEM micrographs in Figure 4 to Figure 6, which were performed on last four AAM presented in Table 2, where the difference in the preparation of AAM is only the method of drying. AAM dried at room conditions had the spherical shape of pores (Figure 4 (a)) that measured in average 265.5 μm in diameter (standard deviation is 94.3 μm, maximal diameter found under SEM was 471.4 μm). Pores of AAM dried at 110 °C lost the spherical shape (Figure 5 (a)) and became bigger due to coalescence of pores, i.e. average SEM diameter was 281.8 μm (standard deviation is 172.7 μm, maximal diameter found under SEM was 858.2 μm). Pores of AAM dried with microwaves for 0.66 min also lost the spherical shape (Figure 6 (a)) and got even bigger, i.e. average SEM diameter was 485.2 μm (standard deviation is 261.3 μm, maximal diameter found under SEM was 1109 μm).

EDXS mappings in Figures 4 to Figure 6 (1st EDXS row) are performed on 1000-times magnified micrographs (Figure 5 to Figure 6 (b)). On all EDXS mappings, it is clear, that Al, Si and Na, important in alkali activation, are not uniformly distributed. The intensity of C compared to the intensity of other elements on EDXS is stronger on sample dried at room temperatures, compared to intensity when the sample was dried at 110 °C, and with microwaves. The intensity of O is comparable to Na when the sample was dried at room conditions. With drying at 110 °C the intensity of O increases also to the part where Si is detected but is still less intensive compared to sample dried with microwaves, where the intensity of O is the same where Na and Si are detected. The conclusion from these results is that organic compound blocks reaction of alkali and non-organic part of precursor, which is presented on EDXS in Figure 6 performed on the part marked with a red square, where Na and Si are separated (Na represent the envelope of Si), O is present in both areas (where Si and Al were detected).
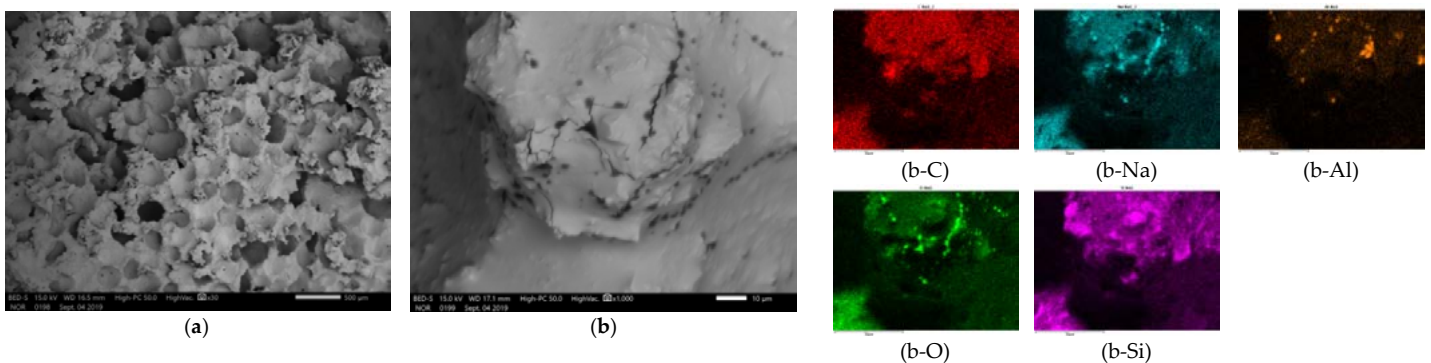
Figure 4: SEM micrographs of AAM, which was prepared from precursor sieved below 90 μm and alkali activated in ratio precursor : 10 M NaOH : Na-water glass = 2.5 :1 :1, dried at room conditions. Magnification (a) 30, (b) 1000. (b-chemical element) EDXS mapping on (b) of the detected chemical element.

In Figure 4 (b), Figure 5 (b) and Figure 6 (b) "matrix" of alkali activated material is presented, which is smooth when dried at room conditions (Figure 4 (b)), and becomes rough with harsher drying conditions (Figure 5 (b) and Figure 6 (b)), where unreacted non-organic part of precursor starts to appear.
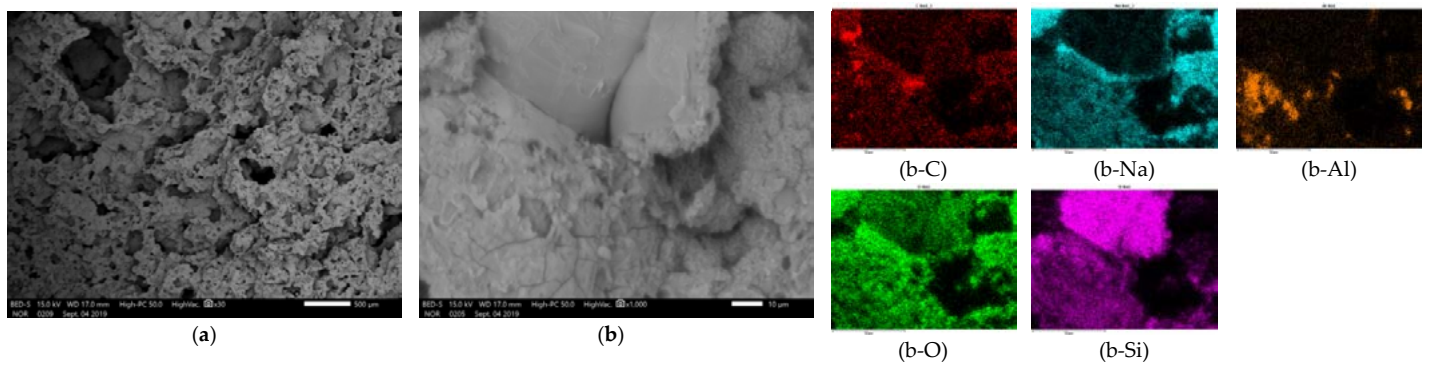
Figure 5: SEM micrographs of AAM, which was prepared from precursor sieved below 90 µm and alkali activated in ratio precursor : 10 M NaOH : Na-water glass = 2.5 :1 :1, dried at 110 °C. Magnification (a) 30, (b) 1000. (b-chemical element) EDXS mapping on (b) of the detected chemical element.
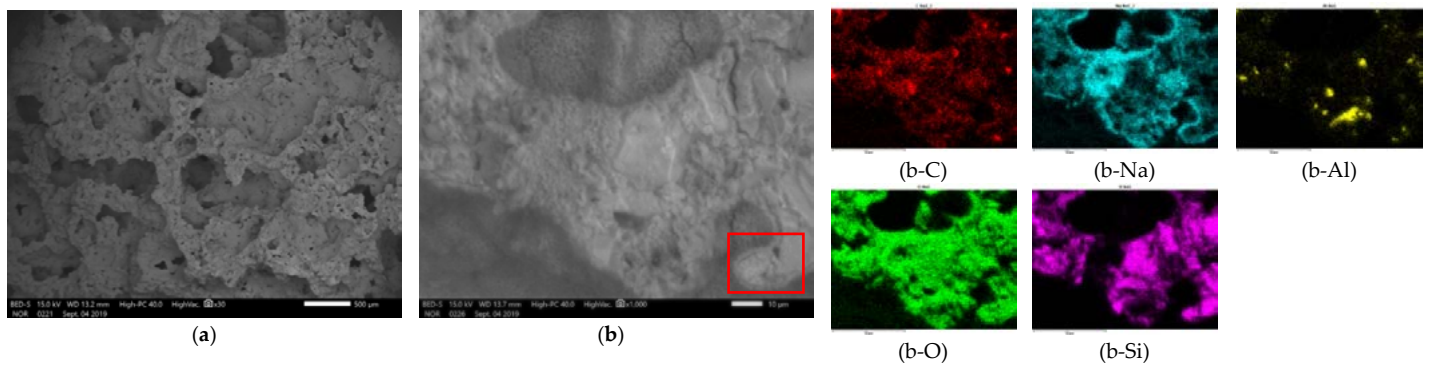
Figure 6: SEM micrographs of AAM, which was prepared from precursor sieved below 90 µm and alkali activated in ratio precursor : 10 M NaOH : Na-water glass = 2.5 :1 :1, dried with microwaves for 0.66 min. Magnification (a) 30, (b) 1000. (b-chemical element) EDXS mapping per chemical element of the area (b).

The foaming process starts with the addition of alkali to precursor and is a consequence of degradation of organic compound present in the precursor: C-H bonds are present only in the precursor as can be seen in Figure 7. FTIR on sample dried at room temperature could be "hiding" the C-H peak of alkyl groups in the wide O-H peak arising from water, which disappears in solidified samples dried at 110 °C and with microwaves.
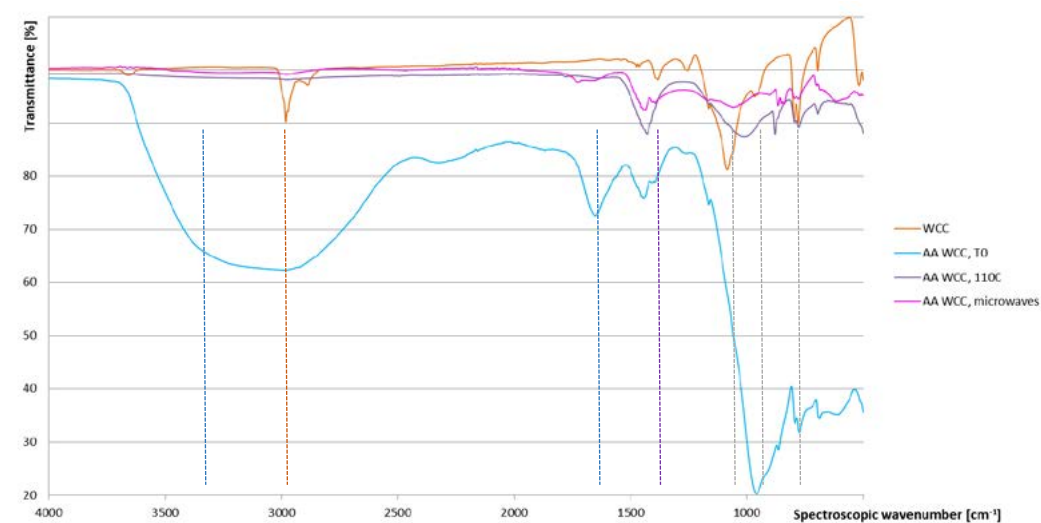
Figure 7: FTIR of precursor and AAM dried with different methods. Blue lines O-H bonds, orange lines C-H bonds, dashed purple lines aromatic C-H_2 and C-H_3 bond, grey lines Si-O bonds.
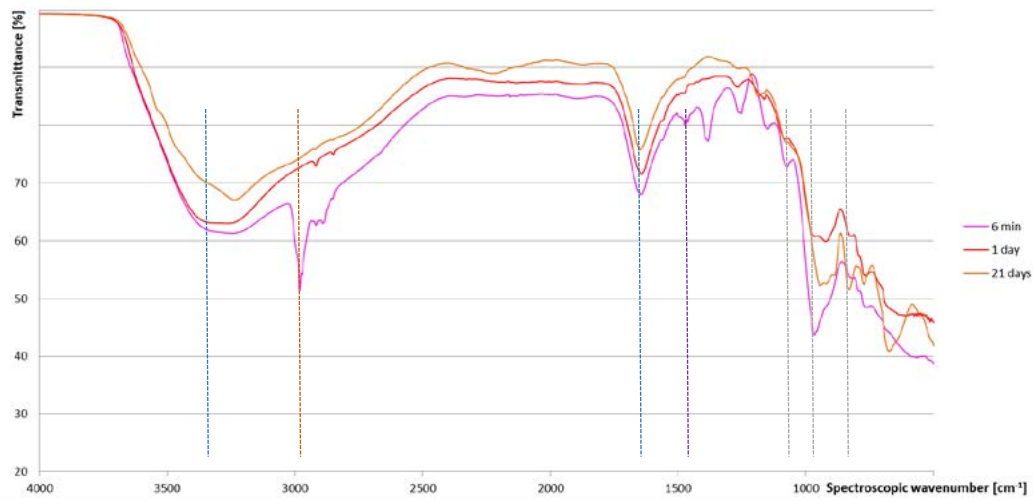
Figure 8: FTIR time dependence of AAM dried at room temperature. Blue lines O-H bonds, orange lines C-H bonds, dashed purple lines aromatic C-H_2 and C-H_3 bonds, grey lines Si-O bonds.

Time dependence of C-H peak from alkyl groups was followed with FTIR from the early time of alkali activation. Peak started to disappear in "O-H peak" with time after the addition of alkali, as is seen in Figure 8. Peak disappearing was accompanied by a foaming process that was not present in a sample without a clear C-H peak.

Time dependence of drying/curing of alkali activated WCC (pre-cured at 70 °C for 24 h) with microwave radiation is presented in Figure 9 and compared to the sample cured for 1 h at room temperature (early stages of curing of alkali activated material) and to the sample cured at 70 °C for 24 h. C-H peak (orange line) and O-H peak "merge" and decrease with time of microwave irradiation, i.e. samples radiated for at least 50 s lose the intense smell (merged peak) and water (the peak at 1635 cm^{-1} disappears). However, the highest compressive strength has the sample irradiated for 40 s (green line in Figure 9) according to Figure 3.
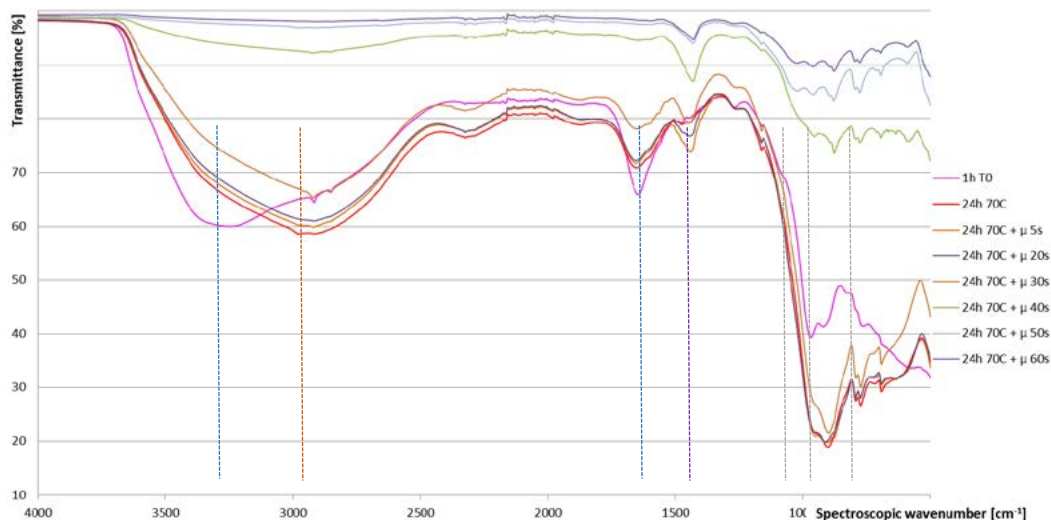
Figure 9: FTIR of AAM dried for 1 h at room temperature and at 70 °C for 24 h without and with additional irradiation with microwaves for different times. Dashed blue lines represent O-H bonds, dashed orange lines C-H bonds, dashed purple lines aromatic C-H_2 and C-H_3 bonds, dashed grey lines Si-O bonds.

4   CONCLUSIONS

Chemical and mineralogical analyses of waste casting cores were performed, AAM was synthesized, their density and compressive strength were determined, and chemical bonds were followed to determine the influence of different drying methods.

It was shown that waste casting cores can be used as a precursor in alkali activation if drying methods are performed under harsher conditions:

• AAM prepared from waste casting cores sieved below 600 μm did not bind good enough to withhold its own mass at demolding, if mass ratio "waste material : alkali : alkali glass" was higher from 2.5:1:1, and if not dried at 110 °C for 24 h or in the microwave. Drying did not have a high impact on density and both methods resulted in a similar value of compressive strength;

• AAM prepared from waste casting cores sieved below 90 μm foamed, was rubber-like and wet for already more than 2 years, unless dried at 110 °C for 24 h or with microwaves. Compressive strength and density showed dependence on the drying procedure, i.e. lower density and lower strength were reached with drying with microwaves. Dependence on mass ratio "waste material : alkali : alkali glass" was also observed, i.e. more liquid phase resulted in lower density and lower compressive strength;

• Compressive strength and density of AAM showed dependence on time of irradiation with microwaves, i.e. highest peak being when water and organic compound are almost removed, which was in our case 40 seconds.

According to FTIR self-foaming was a consequence of the degradation of the organic compound, present in the precursor, in alkali media. The pore size in self-foamed samples showed dependence on drying procedure, i.e. with harsher conditions of drying pores were bigger and less uniform in shape due to coalescence of pores.

Self-foaming was not noticed when precursors used was from bigger particles, probably because of larger empty space between bigger particles that do not react with alkali, so escape of gas from the slurry was easier (into the empty space).

Material solidified and dried only under harsher drying conditions and was accompanied by a change of the matrix' surface from smooth to rough with clearly visible quartz particles from a ground precursor in it. Change of the matrix is according to FTIR and EDXS consequence of the removal of an organic compound.

According to EDXS analysis, common ASN did not form since areas of Al and Si were dislocated, and Na was present mostly on the surface of quartz (Si) particles.

ACKNOWLEDGMENTS

REFERENCES

[1] F. Škvára, Alkali Activated Material - Geopolymer, (2007) 16.

[2] M.C. Bignozzi, S. Manzi, I. Lancellotti, E. Kamseu, L. Barbieri, C. Leonelli, Mix-design and characterization of alkali activated materials based on metakaolin and ladle slag, Applied Clay Science. 73 (2013) 78–85. https://doi.org/10.1016/j.clay.2012.09.015.

[3] J. Němeček, V. Šmilauer, L. Kopecký, Nanoindentation characteristics of alkali-activated aluminosilicate materials, Cement and Concrete Composites. 33 (2011) 163–170. https://doi.org/10.1016/j.cemconcomp.2010.10.005.

[4] T. Glasby, J. Day, R. Genrich, D.J. Aldred, EFC Geopolymer Concrete Aircraft Pavements at Brisbane West Wellcamp Airport, (2015) 9.

[5] HASSELL | Project - University of Queensland Global Change Institute, HASSELL Studio. (n.d.). https://www.hassellstudio.com/en/cms-projects/detail/the-university-of-queensland-global-change-institute/ (accessed November 13, 2019).

[6] A. Hajimohammadi, T. Ngo, P. Mendis, A. Kashani, J.S.J. van Deventer, Alkali activated slag foams: The effect of the alkali reaction on foam characteristics, Journal of Cleaner Production. 147 (2017) 330–339. https://doi.org/10.1016/j.jclepro.2017.01.134.

[7] A. Hajimohammadi, T. Ngo, P. Mendis, J. Sanjayan, Regulating the chemical foaming reaction to control the porosity of geopolymer foams, Materials & Design. 120 (2017) 255–265. https://doi.org/10.1016/j.matdes.2017.02.026.

[8] Burkhard Walther, Bernhard Feichtenschlager, Shengzhong Zhou, Self-foaming Geopolymer Composition COntaining Aluminum Dross, US 9,580,356 B2, 2017.

[9] R.A. Fletcher, K.J.D. MacKenzie, C.L. Nicholson, S. Shimada, The composition range of aluminosilicate geopolymers, Journal of the European Ceramic Society. 25 (2005) 1471–1477. https://doi.org/10.1016/j.jeurceramsoc.2004.06.001.

[10] A. Rincón Romero, N. Toniolo, A. Boccaccini, E. Bernardo, Glass-Ceramic Foams from 'Weak Alkali Activation' and Gel-Casting of Waste Glass/Fly Ash Mixtures, Materials. 12 (2019) 588. https://doi.org/10.3390/ma12040588.

[11] Y.-L. Wei, S.-H. Cheng, G.-W. Ko, Effect of waste glass addition on lightweight aggregates prepared from F-class coal fly ash, Construction and Building Materials. 112 (2016) 773–782. https://doi.org/10.1016/j.conbuildmat.2016.02.147.

[12] G.S. Cole, Microwave Core Process, 4331197, n.d..

[13] Shell Mold Casting, (n.d.). https://thelibraryofmanufacturing.com/shell_mold_casting.html (accessed November 14, 2019).

[14] F. Czerwinski, M. Mir, W. Kasprzak, Application of cores and binders in metalcasting, International Journal of Cast Metals Research. 28 (2015) 129–139. https://doi.org/10.1179/1743133614Y.0000000140.

[15] L. Punathil, T. Basak, Microwave Processing of Frozen and Packaged Food Materials: Experimental, in: Reference Module in

UP

Food Science, Elsevier, 2016. https://doi.org/10.1016/B978-0-08-100596-5.21009-3.

[16] D.S. Deore, G.B. Chaudhari, A.G. Chaturvedi, S.U. Gunjal, A studay of core and its types for casting process, (2015) 11.

[17] D. Agrawal, Microwave sintering of metal powders, in: Advances in Powder Metallurgy, Elsevier, 2013: pp. 361–379. https://doi.org/10.1533/9780857098900.3.361.

[18] M. Willert-Porada, Simultaneous use of different high frequency energy sources for material processing, in: Novel Materials Processing by Advanced Electromagnetic Energy Sources, Elsevier, 2005: pp. 99–104. https://doi.org/10.1016/B978-008044504-5/50020-9.

[19] M. Stachowicz, K. Granat, D. Nowak, Application of microwaves for innovative hardening of environment-friendly water-glass moulding sands used in manufacture of cast-steel castings, Archives of Civil and Mechanical Engineering. 11 (2011) 209–219. https://doi.org/10.1016/S1644-9665(12)60184-8.

[20] R.T. Hitchcock, Radio-frequency and microwave radiation, 3rd ed, American Industrial Hygiene Association, Fairfax, Va, 2004.

[21] M. Stachowicz, K. Granat, Ł. Pałyga, Effect of Sand Wetting on Physically Hardened Moulding Sands Containing a Selected Inorganic Binder. Part 2, Archives of Foundry Engineering. 16 (2016) 79–84. https://doi.org/10.1515/afe-2016-0007.

[22] H.S. Mansur, C.M. Sadahira, A.N. Souza, A.A.P. Mansur, FTIR spectroscopy characterization of poly (vinyl alcohol) hydrogel with different hydrolysis degree and chemically crosslinked with glutaraldehyde, Materials Science and Engineering: C. 28 (2008) 539–548. https://doi.org/10.1016/j.msec.2007.10.088.

[23] Y. Chen, C. Zou, M. Mastalerz, S. Hu, C. Gasaway, X. Tao, Applications of Micro-Fourier Transform Infrared Spectroscopy (FTIR) in the Geological Sciences—A Review, International Journal of Molecular Sciences. 16 (2015) 30223–30250. https://doi.org/10.3390/ijms161226227.

[24] B.L. Mojet, S.D. Ebbesen, L. Lefferts, Light at the interface: the potential of attenuated total reflection infrared spectroscopy for understanding heterogeneous catalysis in water, Chemical Society Reviews. 39 (2010) 4643. https://doi.org/10.1039/c0cs00014k.

[25] M. Pavlin, B. Horvat, A. Frankovič, V. Ducman, Mechanical, microstructural and mineralogical evaluation of alkali-activated waste glass and stone wool, Ceramics International. (2021) S0272884221004168. https://doi.org/10.1016/j.ceramint.2021.02.068.

7

Marija Jelčić Rukavina, Ana Baričević, Marijana Serdar, Martina Grubor

Study on mechanical and durability properties of concrete with RTPF after high temperature exposure

STUDY ON MECHANICAL AND DURABILITY PROPERTIES OF CONCRETE WITH RTPF AFTER HIGH TEMPERATURE EXPOSURE

M. Jelčić Rukavina, A Baričević, M. Serdar, M. Grubor

University of Zagreb, Faculty of Civil Engineering, Department of Materials
Fra Andrije Kacica Miosica 26, 10 000 Zagreb
e-mail: marija.jelcic.rukavina@grad.unizg.hr

SUMMARY: This paper presents the results of an experimental study conducted to evaluate the effect of recycled tyre polymer fibres (RTPF) on the mechanical and durability properties of concrete after high temperature exposure as an alternative to polypropylene fibres (PPF) for spalling mitigation. For this purpose, three different concrete mixes were tested: conventional concrete without fibres and two mixes with 2 kg/m^3 of RTPF and PPF respectively. After one year of curing, the specimens were tested under ambient conditions and after exposure to a predefined elevated temperature of up to 500°C with respect to compressive strength, modulus of elasticity, UPV and water absorption. The results obtained in this study lead to the important conclusion that the addition of RTPFs in an amount of 2 kg/m^3 can be used as a substitute for PPF to prevent explosive spalling in heated concrete, but without further degradation of the mechanical and durability properties that may be caused by their melting.

KEY WORDS: recycled tyre polymer fibres (RTPF), polypropylene fibres (PPF), residual properties

1   INTRODUCTION

The most widely used technological solution to prevent concrete spalling at high temperature exposure is the addition of low melting point fibres, such as polypropylene fibres (PPF), which is well documented in both scientific and technical literature [1]–[4]. In EUROCODE 2 [5], only the amount of PPF (2 kg/m^3) is proposed, without specifying the required dimensions. However, studies in this field have shown that the PPF content in concrete to reduce the risk of explosive spalling is usually between 1 and 3 kg/m^3 of concrete, depending on several factors, the most important being the severity of the fire, the moisture content, the permeability of the concrete and the dimensions of the PPF [1], [6]. During heating, the PPF melt at temperatures of 160-170°C and evaporate at a temperature of about 340°C, thus increasing permeability due to the formation of capillary pores as the fibres melt. The increased permeability is the main factor that mitigates spalling. However, despite the addition of PPF to the concrete, high temperatures can severely affect the mechanical and durability properties of the concrete. Therefore, after the fire is extinguished, the post-fire properties of the concrete are important parameters for estimating the residual load-bearing capacity of the reinforced concrete structure to be rehabilitated for further use in the future.

As part of the FP7 project - *Innovative Reuse of All Tyre Components in Concrete (Anagennisi)*, one of the tasks was to identify suitable applications for recycled tyre polymer fibres in cement composites. Studies conducted so far showed that RTPF can be used as PPF substitutes to reduce autogenous and plastic shrinkage in different types of concrete [7] – [11]. Furthermore, the results of the studies [12]–[14] showed that the melting of the crystalline part of the polymers containing the studied polymer fibres occurs in the temperature range of 210 ºC to 260 ºC and the addition of RTPF to the concrete mix in an amount equal to or exceeding 2 kg/m^3 has the potential to prevent the spalling of the concrete during the exposure to ISO and hydrocarbon fires. The aim of the study was to evaluate the behaviour of concrete with an addition of 2 kg/m^3 of RTPF after high temperature exposure. Therefore, the mechanical (compressive strength and modulus of elasticity) and durability (UPV and capillary absorption) properties were tested before and after exposure to temperatures of 500°C. The results obtained are compared with those of conventional concrete and concrete with PPF.

2 EXPERIMENTAL PROGRAME

2.1 Concrete production

Table 1 shows the proportions of the constituents in the mixes studied. The absolute volume method was used to design the concrete mixes, keeping the water-cement ratio constant at 0.46 with 370 kg/m^3 cement and 170 l/m^3 water. Superplasticizer was added while mixing the concrete to achieve consistency class S4 (160 - 210 mm). The study included the following concrete mixes:

– reference mix of normal concrete (referred to as PC in Table 1)

– mix containing 2 kg of monofilament polypropylene fibres (PPF) per m^3 of concrete (referred to as 2PP in Table 1)

– mix containing 2 kg of cleaned RTPF per m^3 of concrete (referred to as 2RTPF in Table 1).

Table 1: Mix designs per m^3 of concrete

Components (kg/m^3) / Mix ID	PC	2PP	2RTPF
Cement	370		
Water	170		
Water/cement	0.46		
Superplasticizer	2.20	1.70	1.67
PP	-	2	-
RTPF	-	-	2
Aggregate 0/4	899	878	878
Aggregate 4/8	347	344	344
Aggregate 8/16	590	602	602
Fresh concrete properties			
Mass per unit volume (kg/m^3)	2390	2379	2359
Air content (%)	1.5	2.3	3.0
Slump test (mm)	175	180	175

All the studied mixes were prepared using CEM II/B-M (S, V) 42.5 N, crushed limestone as aggregate with a maximum particle size of 16 mm and polycarboxylic ether hyperplasticizer, to achieve the targeted workability of the mixes. Two types of polymer microfibers were used for this study: commercial PPF and RTPF obtained from a Croatian tire recycling company - Gumiimpex GRP, whose properties are presented in Table 2.

Table 2: Properties of microfibers [7]–[11]

Type of fibers	Length (mm)	Diameter (µm)		Melting point (ºC)	Density (g/cm3)	Composition
PPF	6	approx. 32 µm		160-170	0.91	*100% PP
RTPF	9.5 ± 4.6	type 1	30.1 ± 2.0	210-260	1.32	**Approx. 60% PET, 25% PA 66 and 15% of PBT
		type 2	20.2 ± 1.7			
		type 3	12.4 ± 1.8			

*PP – Polypropylene; **PET – poly(ethylene-terephthalate), PA 66 – polyamide 66, PBT – poly(butylene-terephthalate)*

Concrete was mixed in a laboratory mixer with a maximum volume of 60 L according to the standard procedure for mixing concrete. For mixes containing fibres, the aggregates and fibres were mixed first to ensure good dispersion of the fibres.

Two types of specimens were prepared:

1. cylindrical specimens with dimensions Ø = 75 mm and L = 225 mm (i.e. slenderness equal to 3). Although non-standard specimen dimensions were chosen, they comply with RILEM recommendations for high-temperature testing [15]–[17] , which recommend a length-to-diameter ratio (slenderness) between 3 and 4 and a specimen diameter greater than 4 times the largest aggregate size (in this case 16 mm).

2. cylindrical specimens with dimensions Ø = 75 mm and L = 50 mm to determine the residual capillary absorption.

2.2 Heating procedure

Temperature exposure was performed according to the recommendations of RILEM Technical Committee [21]. The specimens were exposed to three different temperature cycles using an electric furnace (with T_{max} = 1400°C). The temperature cycle consisted of the following steps:

1. Heating at a rate ΔT/Δt of 2°C/min to the target temperature (200°C, 300°C and 500°).
2. Holding the target temperature until it was reached in the middle of the specimens (approximately 3 hours).
3. Slowly cooling to ambient temperature in a closed furnace to avoid thermal shock and subsequent micro-cracking of the concrete material.

The slow temperature rise was chosen to avoid explosive spalling and high temperature gradients in the samples, and thus severe microcracking, which would affect the experimental results. For each target temperature, seven specimens from the same mix were subjected to a temperature cycle (Figure 6a), with one specimen used to monitor the temperature at its centre. After cooling, the specimens were left at normal laboratory conditions (T=20-25°C; R.H.=50-70%) until testing, one week after cooling.

2.3 Testing methods

The residual properties of the thermally treated specimens were determined 7 days after cooling to room temperature, when the greatest decrease was expected according to Hertz [18] and the following test methods were used:

− Compressive strength was determined in accordance with the RILEM recommendation for compressive strength testing at high temperatures [16], using a hydraulic Toni Technik testing machine with a capacity of 3000 kN and an applied load velocity of 0.5 MPa/s.

− Static modulus of elasticity was determined in accordance with the RILEM recommendation for high temperature elastic modulus testing [17] using the same equipment as for compressive strength.

− Ultrasonic pulse velocity (UPV) was measured along the longitudinal direction of the cylinder according to HRN EN 12504-4 [19]. The tests were performed using a TICO Proceq UPV tester with transducers of 54 Hz.

− The capillary absorption test was performed according to HRN EN 13057 [20] to determine the effect of fibres melting on the concrete structure. After recording the dry weight of each specimen, one side was partially immersed in water. The mass increase was recorded at fixed time points, i.e. 0.2, 0.5, 1, 2, 4 and 24 h, each using a with a precision of 0.001 g. The same time schedule was used for the unheated samples. The water absorption coefficient was calculated from the slopes of the abscissa of water absorption against the square root of time.

3 RESULTS AND DISCUSSION

3.1 Mechanical properties

Figure 1a shows the mean and standard deviation of the initial and residual compressive strength, while Figure 1b shows the relative residual compressive strength of the tested mixes as a function of heating temperature (200, 300 and 500°C). The initial compressive strength after one year ranged from 61 for 2PP to 67 MPa for the mixture PC. This means that the addition of 2 kg/m^3 RTPF to the fresh concrete mix decreases the initial compressive strength by 4.7%, while 2 kg/m^3 PPF decreases the compressive strength by 8.7%. The comparison of relative strength from Figure 1b shows that mixes with microfibers (both PP and RTPF) have slightly higher compressive strength (up to 12%) compared to the plain mix after being exposed to all target temperatures.

Figure 2a shows the mean and standard deviation of the initial and residual modulus of elasticity, while Figure 2b shows the relative residual modulus of elasticity of the tested mixes as a function of heating temperature (200, 300 and 500°C). The initial modulus of elasticity of the tested mixes ranged from 39.74 GPa for 2RTPF up to 43.04 GPa for the mix PC. Compared to plain concrete mix, PC, the addition of PPF negligibly decreased modulus of elasticity for 0.5%, while the addition of RTPF decreased the modulus of elasticity for 7.6%. Figure 2b shows that the addition of 2RTPF had the most favourable effect on the modulus of elasticity compared to the other mixes tested after being exposed to all target temperatures.
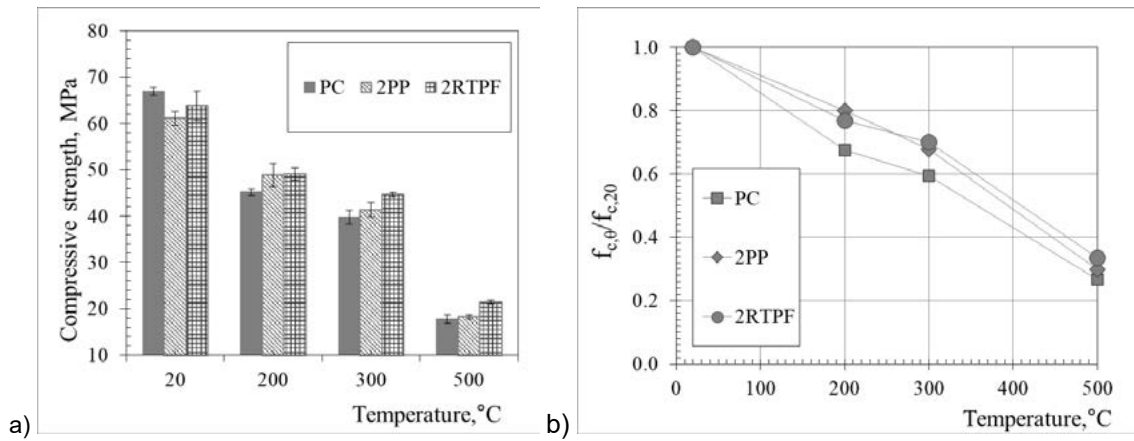
Figure 1 Residual compressive strength vs temperature a) mean and b) relative values
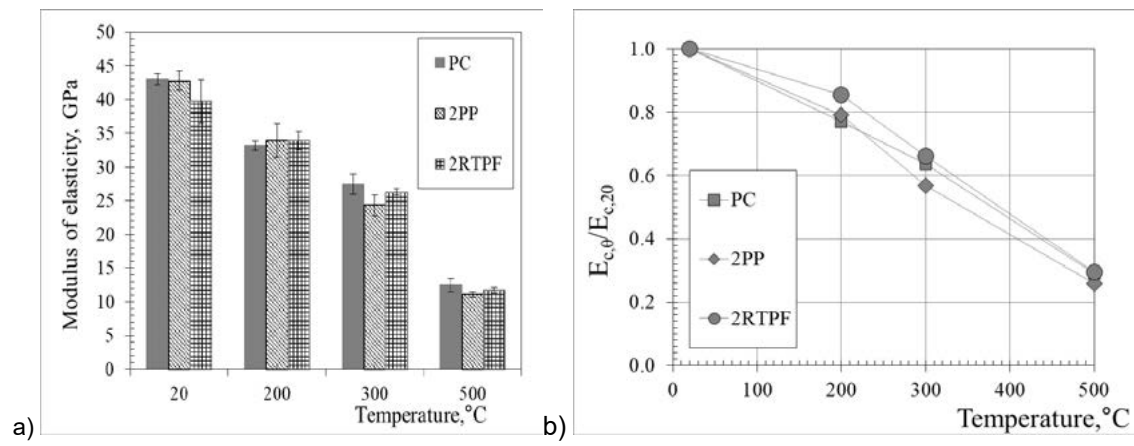
Figure 2 Residual modulus of elasticity vs temperature a) mean and b) relative values

3.2 Durability properties

The initial and residual UPV values after exposure to temperatures from 200°C to 500°C for the tested concretes are shown in Figure 3a. The decrease in UPV values may indicate cracking and an increase in porosity as a result of exposure of the concrete material to high temperatures. The initial values of UPV, which are higher and around 5 km/s, indicate good initial quality of all tested mixes according to [21]. Compared to plain mix, slight variations in the initial UPV values (up to 3.2%) are observed in the presence of microfibers. The relative UPV value as a function of temperature has been plotted in Figure 2b. Throughout the observed temperature range, the results are very similar (the difference is less than 5%). This observation leads to the conclusion that melting of microfibers (both PPF and RTPF) in low volume percentages (up to 0.22%) does not cause further increase in crack occurrence.
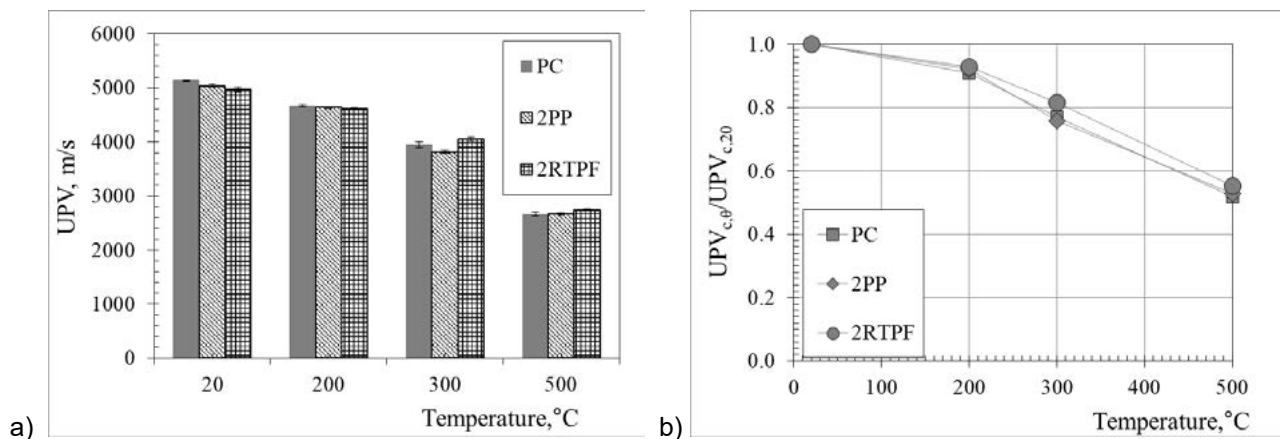
Figure 3 Residual UPV of tested concrete a) mean and b) relative values

In Figures 4a-4b, capillary absorption over time was observed as a function of weight gain at different exposure temperatures. From Figure 4a, it can be seen that the addition of polymer fibres (both PPF and RTPF) had a positive effect on capillary absorption. After treatment at temperatures of 200 and 300°C, a similar behavior can be observed between the mixes. After exposure to 500°C (Figure 4d), the results showed a similar behavior for mixes PC and RTPF. Furthermore, for mix 2PP, it can be seen that the total amount of capillary pores did not change, but the capillary absorption coefficient (considered as the slope of the plotted curve) of the concrete with polypropylene fibres, 2PPF was higher compared to other tested mixes.
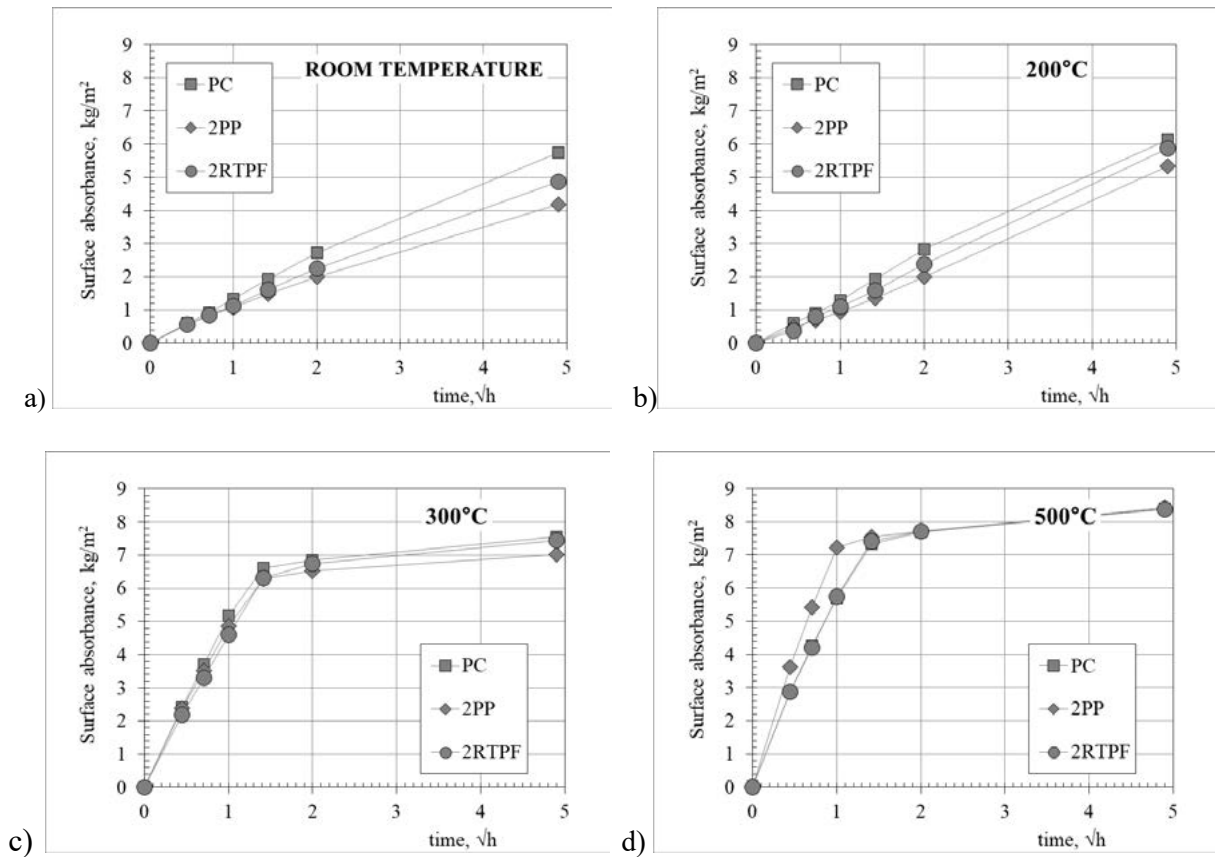
Figure 4 Changes in capillary absorption of PC, 2PP and 2RTPF concrete at a) room temperature and after exposure to temperatures b) 200°C, c) 300°C and d) 500°C

4   CONCLUSIONS

In this study, concrete mixes containing recycled tyre polymer fibres (RTPF) were evaluated in respect to residual properties after high temperature exposure up to 500°C. The obtained results were compared with those of plain mix and mixes containing polypropylene fibres (PPF) which are normally used in concrete to mitigate explosive spalling in case fire.

The results obtained in this study lead to the important conclusion that the addition of RTPF in an amount of 2 kg/m^3 can be used as a substitute for PPF to prevent explosive spalling in heated concrete, but without further degradation of the mechanical and durability properties that may be caused by their melting.

REFERENCES

[1] Khoury, G.A., Willoughby, B.: Polypropylene fibres in heated concrete. Part 1: Molecular structure and materials behaviour, *Mag. Concr. Res.*, Vol. 60 (2008), No. 2, pp. 125–136, ISSN 0024-9831

[2] Hager, I., Mróz, K.: Role of Polypropylene Fibres in Concrete Spalling Risk Mitigation in Fire and Test Methods of Fibres Effectiveness Evaluation, *Materials*, Vol. 12 (2019), No. 23, pp. 1-20, ISSN 1996-1944

[3] Khoury, G. A.: Polypropylene fibres in heated concrete. Part 2: Pressure relief mechanisms and modelling criteria, *Mag. Concr. Res.*, Vol. 60 (2008), No. 3, pp. 189–204, ISSN 0024-9831

[4] Zeiml, M., et al: How do polypropylene fibers improve the spalling behavior of in-situ concrete?, *Cem. Concr. Res.*, Vol. 36 (2006), No. 5, pp. 929–942, ISSN 0008-8846

[5] HRN EN 1992-1-2:2008, Eurocode 2: Design of concrete structures -- Part 1-2: General rules -- Structural fire design (EN 1992-1-2:2004+AC:2008), Croatian Standards Institute: Zagreb, Croatia, 2008.

[6] Zhang, D., Tan, K. H.: Critical Fibre Dimensions for Preventing Spalling of Ultra-high Performance Concrete at High Temperature, Proc. 11th International Conference on Structures in Fire, Lange, D. et. Al (Ed.). pp. 333-341. ISBN 9781742723433, Brisbane, Australia, 30 Nov - 2 Dec 2020, The University of Queensland, Brisbane, Australia, (2020)

[7] Serdar, M. et. al.: Shrinkage Behaviour of Fibre Reinforced Concrete with Recycled Tyre Polymer Fibres, *International Journal of Polymer Science*, Vol. 2015 (2015), Article ID 145918, pp 1-9, ISSN 1687-9422

[8] Baricevic, A. et. al.: Effect of polymer fibers recycled from waste tires on properties of wet-sprayed concrete, *Constr. Build. Mater.*, Vol. 176 (2018), pp. 135–144, ISSN 0950-0618

[9] Baričević, A.: Influence of recycled tire polymer fibers on concrete properties, *Cem. Concr. Compos.,* Vol. 91 (2018), pp. 29–41, ISSN 0958-9465

[10] Grubor, M. et. al: Effect of recycled tire polymer fibers on autogenous deformation of self-compacting concrete, *RILEM Tech. Lett.*, Vol. 5 (2020), pp. 33–40, ISSN 2518-0231.

[11] Grubor, M., Volume deformations of cement composites with recycled tyre polymer fibers, PhD thesis, University of Zagreb Faculty of civil engineering, Zagreb, (2020).

[12] Figueiredo, F. P. et. al.: Effects of Recycled Steel and Polymer Fibres on Explosive Fire Spalling of Concrete," *Fire Technol.*, 55(2019), No. 2, ISSN 0015-2684

[13] Figueiredo, F. P. et. al.: Fire Protection of Concrete Tunnel Linings with Waste Tyre Fibres, *Procedia Eng.*, Vol. 210 (2017), pp. 472–478, ISSN 1877-7058

[14] Figueiredo, F. P. et al.: Recycled tyre polymer fibres to mitigate heat-induced spalling of concrete, Proceedings from the 5th International Workshop on Concrete Spalling. Proceedings from the 5th International Workshop on Concrete Spalling due to Fire Exposure, Bostrom, L., McNamee, R.J. (Ed.), pp. 359-364, ISSN 0284-5172, Borås, Sweden, 12-13 Oct 2017, RISE Research Institutes of Sweden, Borås (2017)

[15] RILEM Technical Committee: Recommendation of RILEM TC 200-HTC: Mechanical concrete properties at high temperatures—modelling and application, Part 1: Introduction - General presentation, *Mater. Struct*, Vol. 40 (2007), No. 9. pp. 841–853, ISSN 1359-5997

[16] RILEM TC 129 MHT: Test methods for mechanical properties of concrete at high temperatures - Compressive strength for service and accident conditions, *Mater. Struct.*, Vol. 28 (1995), No. 7, pp. 410–414, ISSN 1359-5997

[17] RILEM TC 129-MHT: Test methods for mechanical properties of concrete at high temperatures - Modulus of elasticity for service and accident conditions, *Mater. Struct.,* Vol. 37 (2004), pp. 139-144, ISSN 1359-5997

[18] Hertz, K. D.: Concrete strength for fire safety design, *Mag. Concr. Res.*, Vol. 57 (2005), No. 8, pp. 445–453, ISSN 0024-9831

[19] HRN EN 12504-4:2004, Testing concrete -- Part 4: Determination of ultrasonic pulse velocity (EN 12504-4:2004), Croatian Standards Institute: Zagreb, Croatia, 2004.

[20] HRN EN 1305:2003, Products and systems for the protection and repair of concrete structures -- Test methods -- Determination of resistance of capillary absorption (EN 13057:2002), Croatian Standards Institute: Zagreb, Croatia, 2003.

[21] Neville, A., *Properties of concrete*, 4th Edition. Pearson Education, ISBN 9780582230705, England, (1995)

8

Ashfaque Ahmed Jhatial, Ivana Vladić Kancir, Marijana Serdar

Comparative study of selected properties of three binders: blended portland cement, calcium sulfoaluminate cement and alkali activated material based concrete

CoMS_
2020/21

COMPARATIVE STUDY OF SELECTED PROPERTIES OF THREE BINDERS: BLENDED PORTLAND CEMENT, CALCIUM SULFOALUMINATE CEMENT AND ALKALI ACTIVATED MATERIAL BASED CONCRETE

Ashfaque Ahmed Jhatial [1], Ivana Vladić Kancir [1], Marijana Serdar [1]

[1] Department of Materials, Faculty of Civil Engineering,
University of Zagreb, 10000 Zagreb, Croatia.
e-mail: mserdar@grad.hr

SUMMARY: The dependency on cement as the main binder in the manufacturing of concrete has increased the demand for cement. Though it is vital for construction, it has a significant carbon footprint as during its production, high energy is consumed, and greenhouse gases are emitted. According to recent studies, the cement industry currently contributes to approximately 10% of total global CO_2 emissions. To reduce the adverse effects, research has been ongoing following the principles of sustainability, to produce eco-friendlier alternative binders for the construction. In this experimental work, a comparative study was conducted on concrete prepared with calcium aluminate cement (CSA), Alkali-Activated Binder (AAM) and a reference blended Portland cement (PC). To evaluate the binders for potential utilisation, the compressive strength, capillary absorption, chloride diffusion and drying shrinkage were determined. The results indicated that CSA, though had higher chloride diffusion than PC on 28 days, this difference reduced on 56 days. At the same time, the difference between chloride diffusion of AAM and PC was exponential. The capillary absorption results indicated that both CSA and AAM achieved higher capillary absorption than PC. The drying shrinkage over time of CSA and PC were almost identical, whereas for AAM the shrinkage was much higher than PC and CSA at all tested ages of concrete. It was observed from the compressive strength that CSA achieved higher early age strength and similar 28-days strength as PC while the AAM showed significant difference at different ages. Based on the results obtained, it is pointed out that, if alternative binders are to be used in concrete structures, their different properties compared to PC should be considered during preliminary design of concrete in structures.

KEY WORDS: Alkali Activated Material; Calcium Sulfo-aluminate Cement; Durability; Transport Properties; Sustainable Concrete.

1   INTRODUCTION

Ever since the invention of cement and utilisation of concrete as a building material, the demand for these materials has been growing. Nowadays, concrete is the preferred building material in the world, and cement has been used as the sole binder to produce concrete. Though concrete has enabled human beings to construct marvellous structures and made life more comfortable, the environment, however, has been dramatically impacted by mortar and concrete productions. The natural resources are being depleted while significant pollution (CO_2 emissions) is being generated during the production of cement. According to [1], currently, the cement industry is contributing approximately 10% towards the total global CO_2 emissions, this vast amount originates from fossil fuel combustion and limestone thermal decomposition.

Furthermore, a recent study has pointed out that to produce a single tone of cement, approximately 0.9 kg CO_2 [2] is released into the atmosphere. With an annual production of cement is estimated to be 3.5 billion tonnes, this amounts to 3.15 billion tonnes of CO_2 being released into the atmosphere every year [3]. This release of CO_2 severely damages the ozone layer which ultimately causes climate change, and with the ever-growing demand for cement/concrete, the contribution of cement toward global anthropogenic CO_2 emissions is expected to increase further.

Such a vast contribution to the negative impact on the environment has stimulated researchers toward the development of innovative concretes [4], following the principles of sustainability. Several approaches and methods have been suggested to reduce the CO_2 emissions caused by the concrete and mortars during their life cycle. Some of these approaches include the substitution of currently used materials by industrial by-products, enhancing the durability aspects

UP

of concrete so that the maintenance costs are reduced, use of low-CO$_2$ emitting Portland cement and development of innovative alternative binders [5].

Amongst non-Portland clinker cement, Calcium Sulfoaluminate (CSA) has developed a significant interest in the international cement research community. This interest is not just due to the technical properties of CSA cement such as high early age strengths and rapid hardening [6], but also due to its contribution to environmental sustainability. CSA cement is produced based on two clinker types, namely, sulphoaluminate belite clinker and ferroaluminate clinker, in which the calcium sulphate is added in different amounts. Lower temperature and limestone are required during the production of CSA cement, which significantly reduces the thermal input while restricting the release of CO$_2$ by the kilns. Though bauxite, limestone and calcium sulphate are the raw materials which are used in the production of CSA cement, there exists the possibility that these raw materials can be substituted with industrial waste materials [6], this possibility adds significant value to the eco-friendly features that CSA cements portrait.

Alkali activated materials (AAMs) are innovative binders [7] obtained by the chemical reaction between the solid aluminosilicate (precursor) and alkali metal source (activator) [8]. The benefit of AAMs is that there exist many potential precursors to use, such as fly ash, slags, red mud and calcined clay while the activator is a soluble substance which produces alkali metal cations that raises the pH value and accelerates the dissolution of precursors. Besides this, it has been estimated that the AAMs can reduce the CO$_2$ emissions; the reduction can vary from 26% to 80% compared to Portland cement with the same characteristics [9]. This is possible due to the total omission of cement in which limestone must be calcinated at relatively high temperatures and utilisation of industrial by-products which have been calcined at lower temperatures. The utilisation of AAMs in construction is also due to enhanced properties compared to PC such as higher strengths, resistance to acid and fire, lower thermal conductivity and variation in setting time.

The understanding of the effect of different binders on the properties of concrete is necessary to ensure their utilisation in the construction industry. This work aimed to compare concrete manufactured with three different binders. A comparative study was conducted on specimens prepared with CSA (with and without fly ash), AAM (fly ash/slag blend), and a reference blended Portland cement (PC). To evaluate the binders for potential utilisation following properties were considered: compressive strength, capillary water absorption, chloride migration and drying shrinkage. In addition to macroscopic properties, thermogravimetric analysis (TGA) was performed on aged samples to investigate types of hydration products.

2 RESEARCH METHODOLOGY

2.1 Materials and Mixes

This study investigated specimens made of AAM, two different Calcium Sulfoaluminate cement (without and with fly ash), and blended Portland cement (PC), herein, they were designated as AAM, CSA1 and CSA2 and PC respectively. To produce the PC, CEM II/B-S 42.5 N type cement was used, while for both CSA1 and CSA2, a CSA-based rapid set cement was used. Glenium ACE430 superplasticiser based on polycarboxyl ether was used in PC and CSA mixtures, while for CSA mixes BASF delvocrete stabiliser was also used. In order to manufacture the AAM, fly ash and slag were used as precursors, while the activating solution was prepared with sodium hydroxide (NaOH) and sodium silicate (water glass of Mr 122.06). The mix proportions of all four mixes are tabulated in Table 1.

Table 1: Mix proportions of different binder systems to produce 1m^3 concrete

System	Binders (kg)				Aggregates (kg)				Activator		Admixtures		Water (litres)
	CEM II	CSA	Fly Ash	Slag	0–4 mm	4–8 mm	8–11 mm	11–16 mm	Na$_2$SiO$_3$	NaOH	Glenium ACE430	Delvocrete	
PC	370	---	---	---	884	133	379	436	---	---	3	---	155
CSA1	---	370	---	---	884	133	379	436	---	---	2.96	2.59	155
CSA2	---	314.5	55.5	---	884	133	379	436	---	---	2.20	2.52	155
AAM	---	---	340	85	952	319	531		137.5	54.7	---	---	28.6

The PC and CSA concrete specimens were prepared following the procedure for reference concrete according to BS EN 206:2013+A1:2016 [10]. To prepare AAM concrete, the alkali solution was prepared 24 h before casting and cooled at room temperature (T = 20±1°C), to enhance the polymerisation process. Following the recommendations of RILEM TC

247-DTA [11] , fly ash, slag and aggregates were dry mixed for 1 min, afterwards, the activating solutions (water glass and NaOH) were added into the blend and mixed for 6 min. The mixing was paused for 1 min and mixed again for 1 more min.

2.2 Methods

Cube specimens of 15 x 15 x 15 cm dimension were prepared to determine the compressive strength. Samples for a compressive strength were cured in a humid chamber, except specimens from AAM, which were cured at RH = 50±5% and T = 20±1°C for 7 days and then kept at RH = 90±5% and T = 20±1°C until testing. Drying shrinkage was measured on three prism specimens, of dimension 10 x 10 x 40 cm. The specimens were exposed to thermo-hygrometric conditions such that the specimens can deform freely. The first measurement was made 72 ± 0.5 h after the specimens were prepared and every 7 days afterwards. The water capillary absorption was measured according to RILEM 116 [12]. The test equipment consists of a canister with a rod, a sponge to remove surface water, an accuracy scale d = 0.01 g and a stopwatch. Before the capillary test, the samples were cured in water for 28 days, then dried for 7 days in an oven at 105 °C, and then stored in a chamber with constant relative humidity until the capillary absorption test itself. Samples were coated with epoxy resin 24 hours before testing to allow water to be absorbed through only one surface of the sample. The initial mass was measured immediately before each test. Water is then added to the sample tub. The time when the samples are exposed to water is recorded, and the mass of each sample is measured at 10 min, 1 h, 4 h and 24 h intervals. From the obtained results, the water absorption coefficient was calculated. Chloride migration coefficient was measured according to NT Build 492 [13].

The samples were 50 mm high and 100 mm in diameter. Before testing, samples were saturated with $CaOH_2$ solution under vacuum. During testing, samples were placed between cathode tank filled with 10% NaCl solution and the anode cell filled with NaOH solution, with impressed voltage passing through the sample. During the test the temperature was maintained in the range of 20°C to 25°C. TA instruments TGA 55 was used to conduct the thermogravimetric and derivative thermogravimetric (TG-DTG) analyses on one-year hardened specimens. The specimens were ground into power, and test samples of 50 mg were used for measurement. Powder samples were heated from 30 to 900 °C at a heating rate of 10 °C per min in a nitrogen atmosphere.

3 RESULTS AND DISCUSSION

3.1 Compressive Strength

Figure 1 shows the average compressive strength of three specimens for all mixes over different curing ages. The results show that after 7 days CSA1 concrete has the highest strength, which is to be expected since it has been demonstrated in the literature that CSA cement concrete has a faster strength gain [14]. However, after 28 and 56 days, the PC has the highest strength. Though the results obtained did not correlate to the findings of Dachtar [15], but at least showed that the strengths of CSA1 and PC were of approximate magnitudes. As for CSA2, it exhibited constant lower strength at all stages; this could be associated with the addition of fly ash content, as previously shown by Martin and Winnfield [16]. The strength gain of the AAM system was slower during the first 7 days, compared to other mixes, but faster between day 7 and day 28. Higher-strength gain and final strength of AAM mix were expected, when using blended precursor (fly ash and slag) [17].

3.2 Capillary Water Absorption

The capillary water absorption coefficient for all binder systems is tabulated in Table 2. The binder systems will uptake water at a faster rate and will contain a higher fraction of pores with larger diameters when the capillary water absorption coefficient is higher [7]. Both CSA2 and AAM exhibited the highest coefficient value compared to other systems, which may be attributed to the pore distribution being characterised by a higher fraction of pores with large diameters. The water capillary absorption of PC was approximately 70% lower than both CSA2 and AAM and 58% than CSA1.
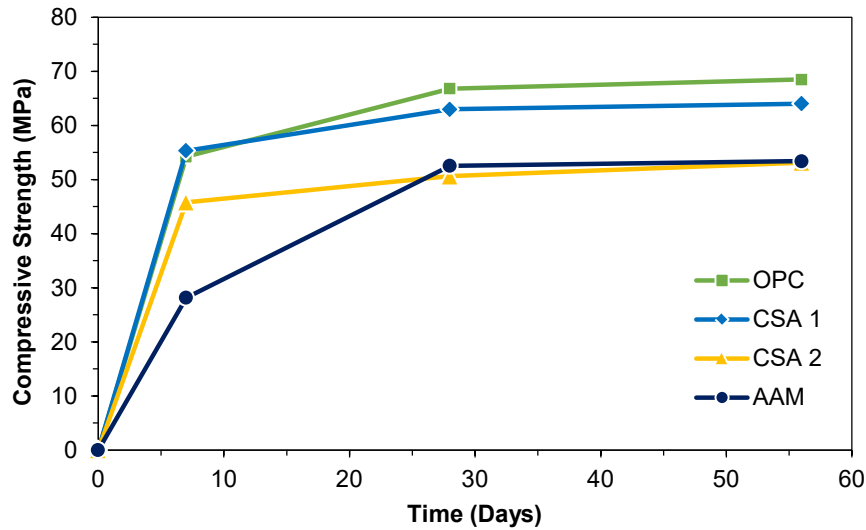
Figure 1: Strength development of different binder systems over time

Both CSA mixes and PC exhibited low water absorption (<3%), whereas the AAM mix exhibited water absorption more than 3%. Figure 2 gives the water absorbed per unit area (Qi) by all mixes at 28 days and 56 days. It can be observed that the trend of AAM is different than the other three mixes, as it absorbs significantly more water during the initial time and reaches saturation earlier. Both CSA mixes showed similar Qi trend, of a near-linear incline whereas the PC mix exhibited a parabolic Qi trend.

Table 2: Capillary absorption coefficient of different binder systems after 28- and 56-days curing

Mix	Capillary absorption coefficient [kg/m^{2}h$^{1/2}$]		Water Absorption %	
	28 Days	56 Days	28 Days	56 Days
PC	0.1	0.07	0.54	0.45
CSA1	0.24	0.25	1.11	1.19
CSA2	0.36	0.36	1.69	1.99
AAM	0.36	0.36	3.41	3.99
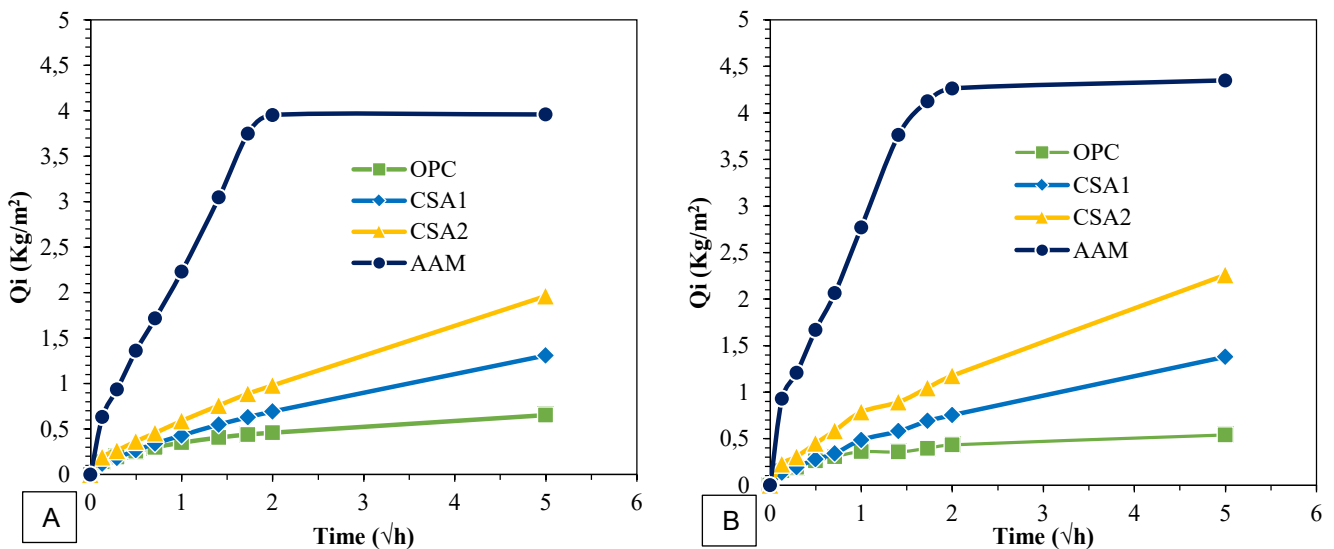
Figure 2: Water absorbed per unit area at **(A)** 28 days **(B)** 56 days.

3.3 Drying Shrinkage

The drying shrinkage is the result of the loss of water present in capillary pores of the concrete. Drying shrinkage occurs when the concrete systems are exposed to environmental conditions in which the relative humidity is less than 100%, and the shrinkage continues until the internal relative humidity of concrete syncs with the external humidity conditions [18]. The pressure is developed when the water starts to leave the small capillary pores, and this pressure may cause the pores to collapse, resulting in macroscopic volume change referred to as drying shrinkage.

The drying shrinkage of all four systems is illustrated in Figure 3. It has been reported that the shrinkage of concrete with CSA is less than that of PC [19]. This similar trend is also observed by CSA1, which exhibited lower drying shrinkage than PC, while the CSA2 which partially incorporated fly ash content further reduced the drying shrinkage. As for AAMs, according to the literature, the shrinkage of fly Ash-based AAMs should be less than that of PC because the water contained in the pores is generally free water which does not cause shrinkage during evaporation. Though the AAM in this study exhibited significantly higher drying shrinkage compared to PC, this increased drying shrinkage can be attributed to the use of slag as a precursor in AAM, which may be due to the larger proportion of smaller diameter pores that cause higher stresses during evaporation of water and thus increased shrinkage [20]. Additionally, in AAM systems, more exist as interstitial water within the gel rather than bound water within hydration products; hence the loss of unbound water over time leads to significant drying shrinkage [21].
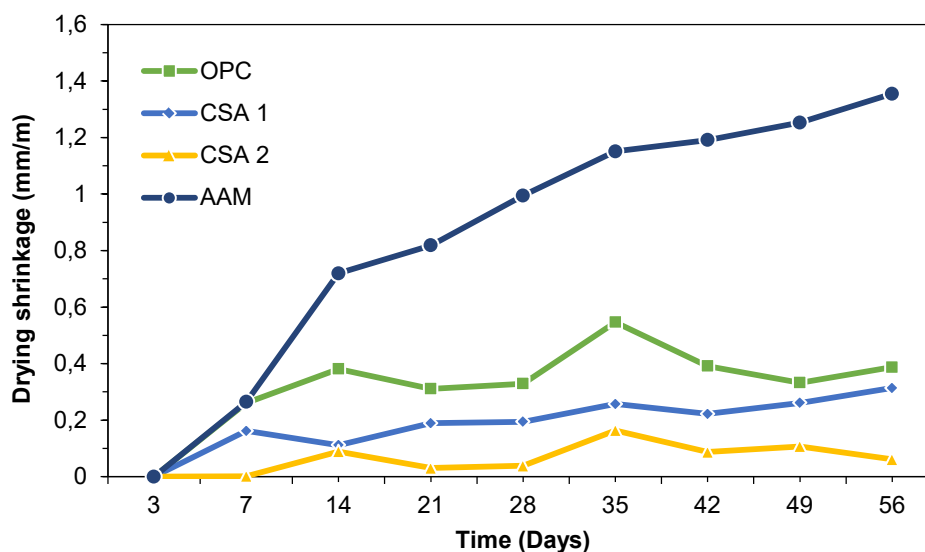
Figure 3: Drying shrinkage of different binder systems at different ages

3.4 Chloride Migration

The chloride diffusion is used to predict of the service life of reinforced concrete structures, as any concrete system can resist the penetration of chloride ions [22], which could severely damage the interior by rusting the reinforcement. The chloride diffusion of all binder systems at 28 and 56 days is illustrated in Figure 4, from which it can be seen that for 28 days, the chlorides passed through the entire samples of CSA1, CSA2, while PC exhibited much better resistance to chloride penetration with a diffusion coefficient of 6.92×10^{-12} m^2/s. For CSA1 the diffusion coefficient was more than double of PC, 14.73×10^{-12} m^2/s and significantly much higher for CSA2 24.68×10^{-12} m^2/s. The CSA1 and CSA2 exhibited improved chloride resistance at 56 days, where the diffusion coefficient was 5.92×10^{-12} m^2/s and 9.42×10^{-12} m^2/s respectively. These results suggest that CSA based concrete will improve their resistance to chloride penetration while it gets older. The results obtained for CSA1 correlate to the findings by Jen et al. [23] for a ratio $C\overline{S}$: $C4A3\overline{S}$ equal to 0.
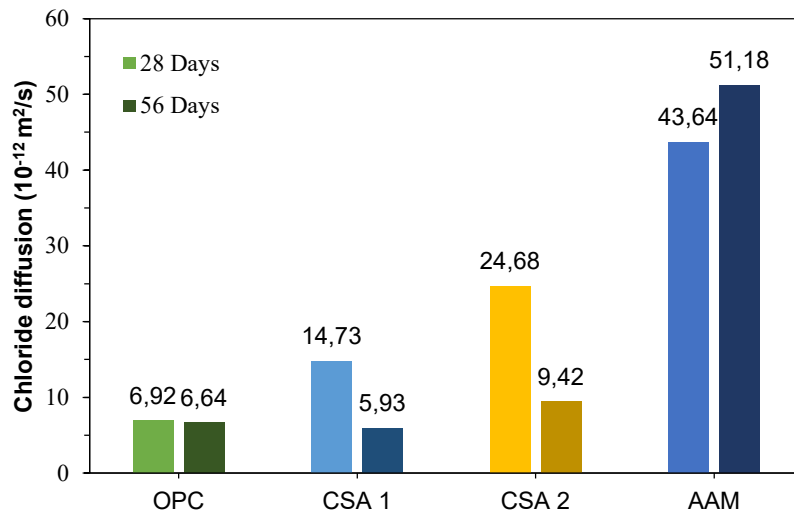
Figure 4: Chloride diffusion of different binder systems at 28 days 56 days.

Contrary to other mixes, AAM showed significantly low chloride resistance with diffusion coefficients of 43.6 x 10^{-12} m^2/s, compared to PC mixture with a diffusion coefficient of 6.92 x 10^{-12} m^2/s at 28 days. Furthermore, AAM showed no improvement in its resistance to chloride ability, in contrast, the diffusion coefficient was increased to 51.18 x 10^{-12} m^2/s when tested at 56 days. At the start of the NT BUILD 492 test, the current released for AAM samples was much higher than in the case of PC concrete. The voltage used for the duration of the test was determined according to the norm with respect to the read-out current. The higher electrical current that passed through the sample significantly affects the diffusion coefficient results. The conductivity of the AAM sample in such a test depends on the activator module representing the SiO$_2$ / Na$_2$O ratio. It has been shown that by increasing the modulus of the activator, i.e. the SiO$_2$ content in the system, the conductivity of the sample decreases. Also, by increasing the modulus, the proportion of NaOH components in the activator also decreases, which means a decrease in the concentration of ions in the pore solution that promotes conductivity [24]. Although this specific AAM sample showed significantly higher current conductivity, this is not necessarily related only to their ability to resist chloride penetration, but also reflect the concentration and composition of free ions present in the pore solution [24].

3.5 Thermogravimetric Analysis

The TG analysis was used to evaluate the composition of hydration products of approximately one-year-old concrete. By monitoring the mass change during the heating of samples, the fraction of different reaction products can be evaluated. According to Scrivener et al. [25], various hydration products can be observed and identified from TGA curves with certain temperature ranges, namely:

1. Gypsum (CaSO$_4$·2H$_2$O) loses its water at around 100 to 140°C to hemihydrate (CaSO$_4$·0.5H$_2$O) and at 140 °C to 150 °C to anhydrite (CaSO$_4$)
2. Calcium silicate hydrate (C-S-H) show water loss temperature of 50 °C to 600 °C
3. Monocarbonate (4CaO·Al$_2$O$_3$·CO$_2$·11H$_2$O) can be observed between 60 °C and 200 °C
4. Monosulfate (4CaO·Al$_2$O$_3$·SO$_3$·12H$_2$O) can be observed between 250 °C and 350 °C
5. Portlandite (Ca(OH)$_2$) dehydroxylates (Ca(OH)$_2$ → CaO + H$_2$O) between 400 °C to 500 °C
6. Calcite (CaCO$_3$), between 600 and 800°C
7. According to Figure 5, which presents the thermogravimetric curves, the first decline in weight is associated with the dewatering process at the temperature of 67 ^{o}C for PC system and CSA1, while for CSA2 this decline peak was at 81 ^{o}C (number 1 zone). As for the AAM system, the endothermic peak was at 83 ^{o}C. This first zone is associated with the dehydration of free water and C-S-H from hydrated matrix [26]. For PC system this peak indicates that C-S-H and ettringite are formed. For CSA systems, the peak indicates the presence of hemi- and mono-carbonates and ettringite. The endothermic peak of AAM may be due to potential formation of additional C-S-H; this may be attributed to the blend of fly ash and slag. The second decline occurs between 120 and 270 °C (number 2 zone). In this zone, CSA systems exhibit peaks at 227 ^{o}C, which indicate the monosulfate. The third decline (number 3 zone) was observed at 432 ^{o}C, which indicates Portlandite. This peak was only exhibited by PC system, as it was the only system which consisted Portlandite.
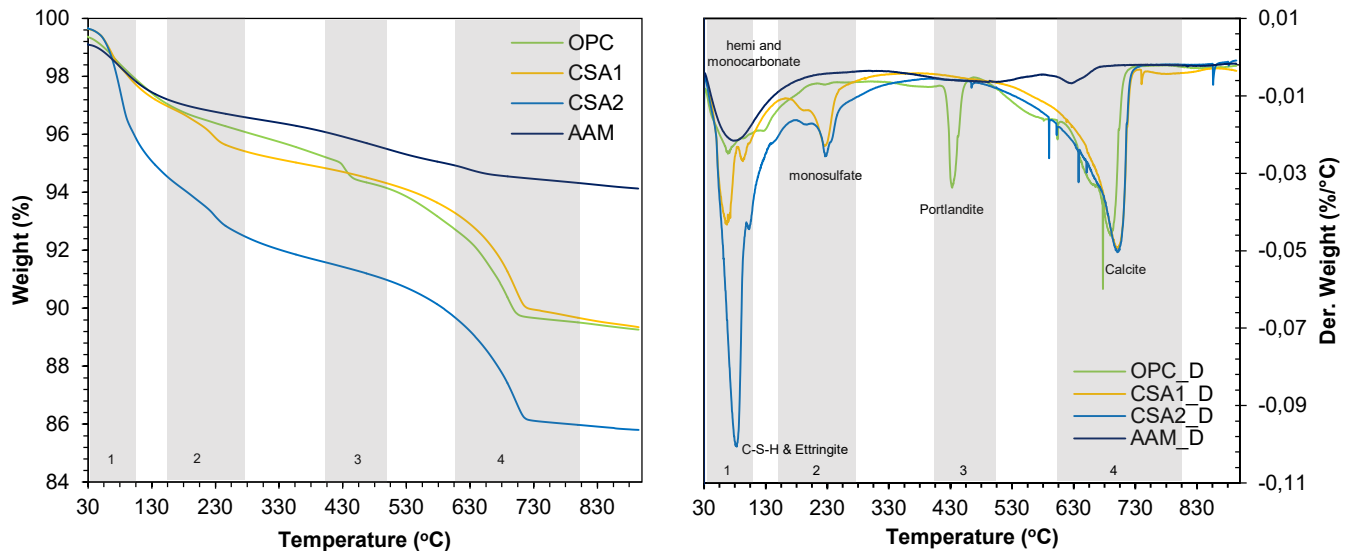
Figure 5: (**A**) TG thermograms and (**B**) DT thermograms for all systems.

Additionally, peaks were observed between 550 and 650 ^{o}C only with PC system which indicated carbonates attributed to carbonation; this could have been produced by external means as the specimens were analysed after one year. The fourth and final peak (number 4 zone) indicate the calcite (aggregate), PC and CSA systems exhibit similar peaks in this zone. The AAM peak at 622 ^{o}C may relate to the decomposition of carbonate, hydrated aluminates and final stage of decomposition of C–S–H [25].

From Figure 5, it can be observed that for PC the main hydration products were C-S-H, ettringite and Portlandite, while for CSA systems, the main hydration products were ettringite, monocarbonate and monosulfate. Significant C-S-H and ettringite was observed by CSA systems, with CSA2 having the maximum C-S-H and ettringite, whereas for AAM, it was lower than PC. Portlandite was only observed in PC system, as well as carbonates formed due to carbonation.

4   CONCLUSIONS

This experimental work was conducted to comparatively study the eco-friendly systems prepared with calcium sulfoaluminate cement (with and without fly ash), alkali-activated material and blended Portland cement. Based on the experimental work presented in this study, several conclusions can be withdrawn about mechanical and durability properties of these mixes. The CSA achieved higher early strength compared to other mixes. However, the ability to achieve higher early strength was highly influenced once fly ash was added in CSA. As for the AAM system, it achieved lower strength compared to other mixes, which may, in this case, be attributed to poor quality of activating solutions. At 56 days PC achieved higher compressive strength than other three systems. Both CSA2 and AAM exhibited the greatest value of capillary absorption coefficient compared to other mixes, which may be attributed to the pore distribution being characterised by a higher fraction of pores with large diameters. The drying shrinkage was lower for CSA cement-based systems compared to PC. Furthermore, the addition of fly ash in the CSA cement system further improved its ability to resist the shrinkage. However, AAM exhibited significantly greater drying shrinkage than PC and CSA systems, which can be attributed to the higher number of pores. High drying shrinkage could be responsible for the induction of microcracks in this system, which could further be responsible for the high permeability of AAM mix prepared within this study. Obtained and presented results highlight the importance of conducting durability studies on alternative binders, to ensure and control the long-term durability of concrete in structures.

ACKNOWLEDGMENTS

REFERENCES

[1] Suhendro, B.: Toward green concrete for better sustainable environment, *Procedia Engineering*. 95: pp. 305 – 320, (2014) doi:10.1016/j.proeng.2014.12.190.

[2] Hasanbeigi, A. et al.: Analysis of energy-efficiency opportunities for the cement industry in Shandong Province, China: A case study of 16 cement plants, *energy*, 35, pp. 3461 – 3473, (2010).

[3] Naqi, A., & Jang, J. G.: Recent progress in green cement technology utilising low-carbon emission fuels and raw materials: A review. *Sustainability*, 11, 537, pp. 1 – 18, (2019).

[4] D'Alessandro, A. et al.: Innovative concretes for low-carbon constructions: A review, *International Journal of Low-Carbon Technologies*, 12(3), pp. 289 – 309, (2017).

[5] Gartner, E., & Hirao, H.: A review of alternative approaches to the reduction of CO2 emissions associated with the manufacture of the binder phase in concrete, *Cement and Concrete research*, 78, pp. 126 – 142, (2015).

[6] Mobili, A. et al.: Calcium sulfoaluminate, geopolymeric, and cementitious mortars for structural applications, *Environments*, 4(3), 64, pp. 1 – 18, (2017).

[7] Provis, J. L.: Alkali-activated materials, *Cement and Concrete Research*, 114, pp. 40 – 48. (2018).

[8] Serdar, M. et al.: Research challenges for broader application of alternative binders in concrete. *Građevinar*, 71(10), pp. 877 – 888, (2019).

[9] Turner, L. K. & Collins, F. G.: Carbon dioxide equivalent (CO2-e) emissions: A comparison between geopolymer and OPC cement concrete, *Construction and Building Materials*, 43, pp. 125 – 130, (2013).

[10] BS EN 206:2013+A1:2016: Concrete. Specification, performance, production and conformity, British Standards Institution, London, UK, (2016)

[11] Provis, J.L. et al.: RILEM TC 247-DTA round robin test: Mix design and reproducibility of compressive strength of alkali-activated concretes. Mater. Struct. 2019, 52, 99 (2019).

[12] RILEM TC 116-PCD: Permeability of Concrete as a Criterion of Its Durability, *Materials and Structure*, 32, pp. 163 – 173, (1999).

[13] NT BUILD 492: Concrete, mortar and cement-based repair materials, chloride migration coefficient from non-steady-state migration experiments. *Nordtest Method 492*, (1999)

[14] Guan, Y. et al.: Experimental study and field application of calcium sulfoaluminate cement for rapid repair of concrete pavements. *Frontiers of Structural and Civil Engineering*, *11*(3), 338-345 (2017).

[15] Dachtar, J.: Calcium sulfoaluminate cement as binder for structural concrete, *Doctoral dissertation*, University of Sheffield) (2004).

[16] Martin, L. H. et al.: Influence of fly ash on the hydration of calcium sulfoaluminate cement. *Cement and concrete research*, 95, pp. 152 – 163, (2017)

[17] Wardhono, A. et al.: The strength of alkali-activated slag/fly ash mortar blends at ambient temperature. *Procedia Engineering*, *125*, 650-656 (2015).

[18] Adams, M. P., & Ideker, J. H.: Volume Stability of Calcium Aluminate Cement and Calcium Sulfoaluminate Cement Systems, *Factors Influencing Conversion and Volume Stability in Calcium Aluminate Cement Systems*, 15, (2014).

[19] Lan, M. Z. et al.: Effect of Anhydrite on the Early Hydration Performance of Rapid Setting and Hardening Belite Sulfoaluminate Cement. In *Materials Science Forum*, Vol. 898, pp. 1990 – 1995, (2017).

[20] Collins, F., & Sanjayan, J. G.: Effect of pore size distribution on drying shrinking of alkali-activated slag concrete. *Cement and Concrete Research*, 30(9), pp. 1401 – 1406, (2000).

[21] Chi, M. & Huang, R.: Binding mechanism and properties of alkali-activated fly ash/slag mortars, Constr. Build. Mater. 40(2013) 291–298.

[22] Lizarazo-Marriaga, J., & Claisse, P.: Determination of the concrete chloride diffusion coefficient based on an electrochemical test and an optimisation model. *Materials Chemistry and Physics*, 117(2-3), pp. 536 – 543, (2009).

[23] Jen, G. et al.: Chloride ingress in a belite-calcium sulfoaluminate cement matrix. *Cement and Concrete Research*, 98, pp. 130 – 135, (2017).

[24] Adam, A.: Strength and durability properties of alkali activated slag and fly ash-based geopolymer concrete, *Doctor of Philosophy (PhD)*, Civil, Environmental and Chemical Engineering, RMIT University, (2009).

[25] Scrivener, K. et al.: (Eds.). (2016). *A practical guide to microstructural analysis of cementitious materials* (Vol. 540). Boca Raton: Crc Press.

[26] El-Didamony, H. et al.: Properties and durability of alkali-activated slag pastes immersed in sea water. *Ceramics international*, *38*(5), 3773-3780 (2012).

9

Naser Kabashi, Mihrie Bajoku

Corrosion- cracking parameter in the concrete structure and impact in reinforced steel bars

CoMS_
2020/21

CORROSION- CRACKING PARAMETER IN THE CONCRETE STRUCTURE AND IMPACT IN REINFORCED STEEL BARS

Naser Kabashi[1], Mihrie Bajoku[2]

[1,2] University of Prishtina, Faculty of Civil Engineering, Department of Materials Sunny Hill n,n, 10 000 Prishtina, Kosovo.
e-mail: naser.kabashi@uni-pr.edu, bajokumihrie@gmail.com

SUMMARY: Concrete structures are under the different environmental conditions, which phenomena will lead to the damages of structure in the time factor. The bridge structures are more attacked, focused on corrosion of steel bars, and with damages of structure elements. Corrosion is caused by many factors of the external environment which, through the protective layer of concrete, reaches the reinforced steel bars in the process caused by the degradation of the concrete in general. The presence of permanent humidity is the permanent factor that involves in the process many other factors from the aggressively of environment substances: chlorine, oxygen, carbon dioxide, sulfates, during the penetration process in concrete. The case study analyzing in this paper is a bridge structure, located in village Drelaj, the region of Rugova, mountains in Kosova. The bridge is at an altitude above 2000m and is under the constant influence of extreme temperature conditions. The methods to be applied in this case are analytical and experimental methods. The analytical method is based on measurements and calculate the depth of corrosion according to ASTM code and calculate the percentage of corrosion according to ACI code. The experimental laboratory method we will determine the corrosion rate with the Corrosion meter instrument. In the end, we will make a comparison between the results achieved, and the proposal for repairing, to increase the bearing capacity.

KEY WORDS: corrosion, environment aggressivity, cracking, concrete, reinforces steel bars.

1. INTRODUCTION

The temperature changed in region Rugova, village of Drelaj, has a major impact on the reinforced concrete structures. In this case study, we are focused in reinforced concrete bridge and behavior under the longtime of constructed and without the maintenance and under the aggressive environmental factors. The study is focused in testing the elements of concrete bridge structures which are more affected by environmental factors. The bridge was built 50 years ago, and in visual inspection are evidenced the damages and degradation of the structure in high level. The geometrical parameters of bridge are: length L = 25.0m ', width B = 7.0m' and span L_0 = 18.0m '. The edge elements of structures are with stone materials, presented in fig.1

Figure 1. Reinforced Concrete Bridge in Drelaj-Peja –photo (25.12.2018)

2. GENERAL CONDITIONS AND DAMAGES OF BRIDGE STRUCTURES

The bridge structure is located in a place where the altitude is very high (over 2000m), and the freeze-thaw cycles, rainfall and water level are main affected factors in degradation process the structures. The level of degradations will lead to the unused structure in very short time, because in many cases is very critical to pass the structures, especially during the winter season. The level of corrosion is very visible and presented in fig.2.

Figure 2.Corrossion process in down part of concrete slab

The concrete protective layer is completely removed and the reinforced steel are completely under environmental aggressive conditions. The structure has been long time under the influence of water, which can be aggressive, acting on the material structure causing harmful effects, such as the impact of aggressive substances in the structure concrete .From the data obtained for the last 10 years from the Ministry of Environment and Spatial Planning, the relative temperature and humidity are presented in table 1, 2 and tab. 3.

Table 1: Maximum temperature (0C) in Peja area

Months	I	II	III	IV	V	VI	VII	VIII	IX	X	XI	XII
Tem.Min(^{0}C)	-8	-2	5	88	17	14	17	18	12	9	2	-1
Tem.Max(^{0}C)	15	22	24	23	32	35	33	35	30	24	24	14

Table 2: Minimum temperature (0C) in Peja area

Months	I	II	III	IV	V	VI	VII	VIII	IX	X	XI	XII
Tem.Min(^{0}C)	-17	-3	-2	0.3	4	7	13	13	4	-2	-2	-9
Tem.Max(^{0}C)	2	14	9	13	17	23	20	21	16	15	11	5

Table 3: Relative humidity (%) max, min, and the average for 10 years in Peja-Drelaj region.

Months	I	II	III	IV	V	VI	VII	VIII	IX	X	XI	XII
Hum. Min.	82	58	48	42	60	78	54	74	71	62	54	66
Hum.max	100	84	90	96	96	92	97	100	100	96	97	98
Hum.aver.	95	73	75	78	73	85	7	86	86	81	81	87

According to the Kosovo Hydro meteorological Institute data, the minimum temperature for ten years in this area is -17^0 C during the January, while the maximum temperature reaches August 35.2^0 C. As temperatures, in this case, can change more, freeze-thaw cycles more to offer any possibility, this question in the construction where we have a loss of mass as well as maintenance is to low and will affected directly in concrete durability [1]. The most affected parts of elements are edge concrete walls and concrete slab I down part or in connection with walls, presented on fig.3.

Figure 3: Degradation concrete elements

This process during which amorphous silicon reacts with the alkali present in the cement, which later in contact with moisture increases its volume. For this reason large internal strains, cracks, diminishing durability characteristics, and also can lead to the Alkalo-Silicate reaction which has degraded the elements of the structure (the soffit part is more damaged).Prerequisites for the formation of alkali-silicate reaction in concrete are:
- Presence of alkali-containing aggregate
- Possibility of alkali content in pores filled with water in concrete.
- Moisture penetration into the concrete.

Another important parameter is carbonation in concrete which is on function of many parameters:

mix Design , Casting the concrete, maintenance ,environment aggressively and other parameters.

Due to the heavy rainfall, the wet concrete has been carbonized for a long time, the penetration of moisture deep into the concrete structure has greatly increased the carbonization of the concrete. During the carbonization process, calcium hydroxide (Ca (OH)$_2$) reacts with CO_2 from the atmosphere and under the action of pH in the atmosphere where the reaction takes place.[2][3]

3. CORROSION MEASUREMENT OF REINFORCEMENT IN CONCRETE WITH CORROSION METER-EXAMINATION OF BRIDGE SECTIONS

In the study case, we are fused in identify the weak points of degradations of concrete, were through the inspections are evidenced the corrosion of reinforced bars in more damages part the concrete. Concept and next step is done using the measurements using the equipment: Corrosion Meter for positions in which the reinforcement is not exposed (separated from the concrete), we have made the measurement with the Corrosion Meter device to identify the most corroded parts of the reinforcement inside the concrete. The testing procedure is based on the colors for rate of the corrosion in display of equipment. For testing procedure it's create the closed electrical circuit by connecting the electrode to reinforced steel and the other fluid-filled electrode to the Corrosion meter. The testing of concrete elements of bridge structures we have created a map for typical measurement points. The grids for measurements are sign at a distance of 15 cm from one point to another. The following positions are evaluate using the measures, presented in fig.4.
1. The inner part of the bridge abutment
2. Section of soffit bridge
3. Front part abutment of the bridge
4. Lateral part abutment of the bridge
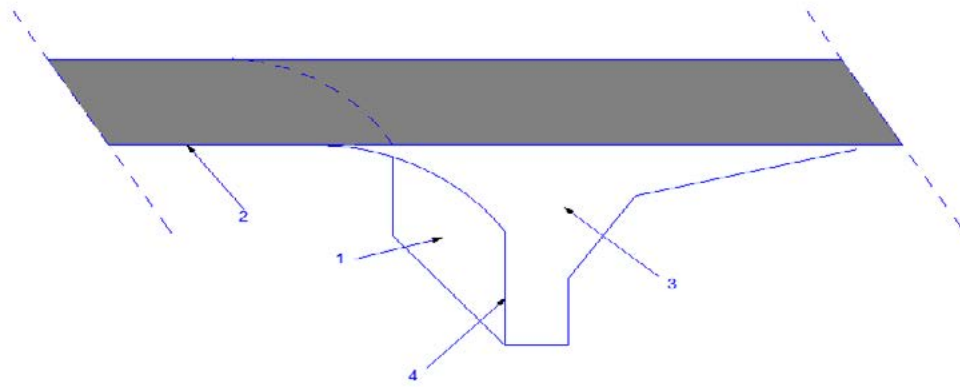
Figure 4. Measurement Positions

3.1.   Review Results

The results of the bridge survey are presented in 4 forms:
   a)   Corrosion Scan
   b)   Cumulative Distribution

The results of the measurements are presented in 2 forms: Below we present the 2 forms of results at the most critical point in the lateral part abutment of the bridge.
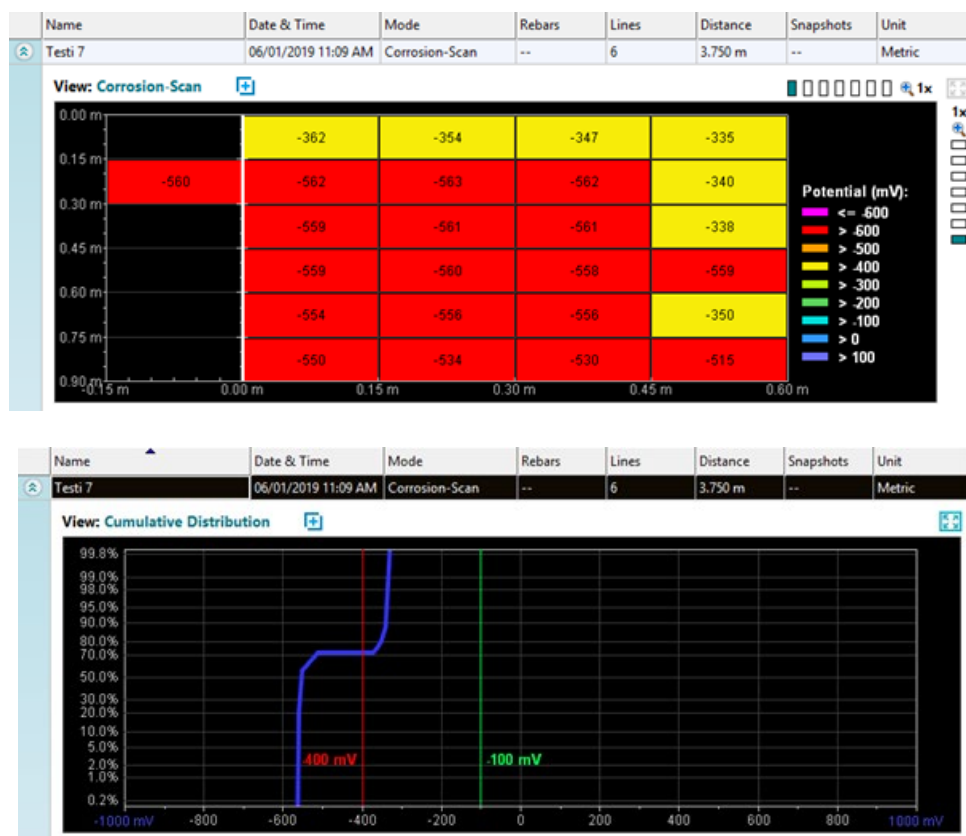
Fig 5 -values of corrosion a function of potential max

The measurements for weak positions in colored form, based on the procedure are presented in fig.6
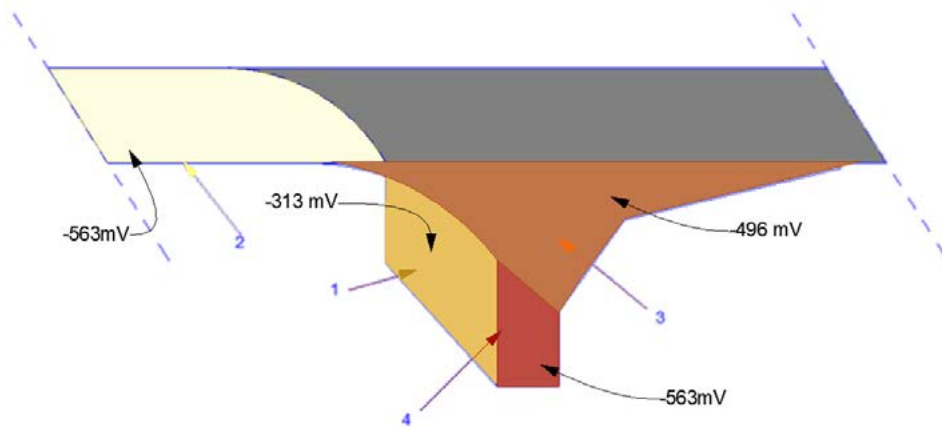
Figure 6. Values of corrosion a function of average values (%)

3.2. Calculation of the reduction of the cross-section of the steel from field measurements

Due to extreme environmental impacts, the structure is in with very high level of degraded and the reinforcement steel is under the influence of aggressive substances In time process the corrosion is increasing process and potentially increased the volume caused numerous cracks which lead to the damages the concrete layer and damages of element of structures. The reinforced steel bars being under the constant influence of the environment and corrosion has reduced its cross-section. From the observations we can see that the concrete layer of the reinforcement has been completely degraded, and the direct measurements of the diameter of reinforced steel bars ø 22 mm. Evaluation of the reinforcement that is on the outside of the damaged structure results in a high presence of corrosion and with this reduction of the diameter from the reinforcement 22mm to 2.2mm, evaluating the direct mesurment method.[4] The reduction of the cross section of the reinforcement is presented in figure 7.

Figure 7. Reduction of armature cross-section caused by corrosion from direct contact with the external environment.

3.2.1. Corrosion rate measurement-ASTM Standard G31 and G1

Based on the ASTM standard for calculating steel bars corroded part is presented in expression (1.0).

$$CR\left(\frac{\mu m}{years}\right) = \frac{K*10^7\ (W_i - W_f)(g)}{A(cm^2)*t(h)*\rho(gr*cm^{-3})} \quad , or \tag{1.0}$$

$$CR\ (mm/years) = K*\frac{W}{\rho A t} \tag{1.1}$$

Were the parameters are:
K-constant with values: K = 534 if CPR is in (mpy) or K = 87.6 if CPR is in mm / years
W-Weight Loss Armor (milligrams)
ρ- density of rebar (gr / cm3)
A-reinforced steel bars surface (cm2)

t-exposure time (hours)[5]

The reduced value from direct measurements using the expression (1.0) results with the reducing the diameter 2.042 mm/50 years.

The reduced value or loss of mass of reinforced steel bars is expressed in table 4, and categorizations based on the EN 12944-2.

Table 4: Corrosion Level Categorization Based on Environmental Impact (EN ISO 12944-2)

Corrosion level categorization	The loss of thickness (cross-sectional reinforcement)/ μm	Examples of the impact of environment
		The impact of outside environment
C1 (Very low)		
C2 (Low)	>1.3-25	Low level of pollution: mainly in rural areas.
C3 (Medium)	>25-50	Urban areas, sulfur dioxide pollution, coastal areas with low salt levels.
C4 (High)	>50-80	Industrial and coastal areas with medium salt levels.
C5 (Very High)	>80-200	Industrial area with high relative humidity, aggressive environment and coastal areas with high salt levels.
CX (Extreme)	**>200-700**	**High-impact coastal areas of salt and industrial areas with extreme humidity and highly aggressive environment.**

According to field measurements done in the steel bar, corrosion has been achieved a reduction of cross section up to 2.2mm or 2200μm based on the above table of EN ISO 12944-2 , than we conclude that our case study belongs to the level of CX corrosion (Level Extreme). While the calculations according to ASTM standard G31 and G1 reduction of cross-sectional reaches 2.04mm or 2200 μm based on the above EN ISO 12944-2 table can conclude that our case study of the level of corroding is CX (level EXTREME).[6]

3.2.2. Calculation of Corrosion Percentage according to ACI-408

The determine of the loss of mass (corrosion mass) is calculate according the ACI-408

The expression for calculating the percentage of steel corrosion is:

$$\%loss\ of\ mass = \frac{w}{\rho A_s l_{corr}} * 100\% \qquad [7] \qquad (2.1)$$

Ku:

w-is the mass loss

As-is the area of steel

lcorr-is the total length of steel that is to be corroded

ρ-is the density of the steel

From the calculations made according to ASTM Standard the percentage of steel corrosion is: $\%\boldsymbol{loss\ of\ mass} = \mathbf{33.5\%\ per\ 50\ years.}$

Results from direct "in situ" evaluations presented the loss of mass the percentage of steel corrosion is: $\%\boldsymbol{of\ loss\ of\ mass} = \mathbf{31.063\%\ per\ 50\ years.}$ **(presented in Table 5)**

Table 5: Calculations and comparison between the ASTM and direct measurements (ENISO 12944-2)

	ASTM Standard	Direct "in situ" evaluations measurements
Rate of corrosion ($\frac{mm}{50vite}$)	2.04	2.2
Percentages of Corrosion ACI-408	33.5%	31.063%

4. RESULTS AND COMPARISON

Below we present the comparison of the results of the measurements performed with the Corrosion Meter equipment in the field at different positions is presented in Figure 8.
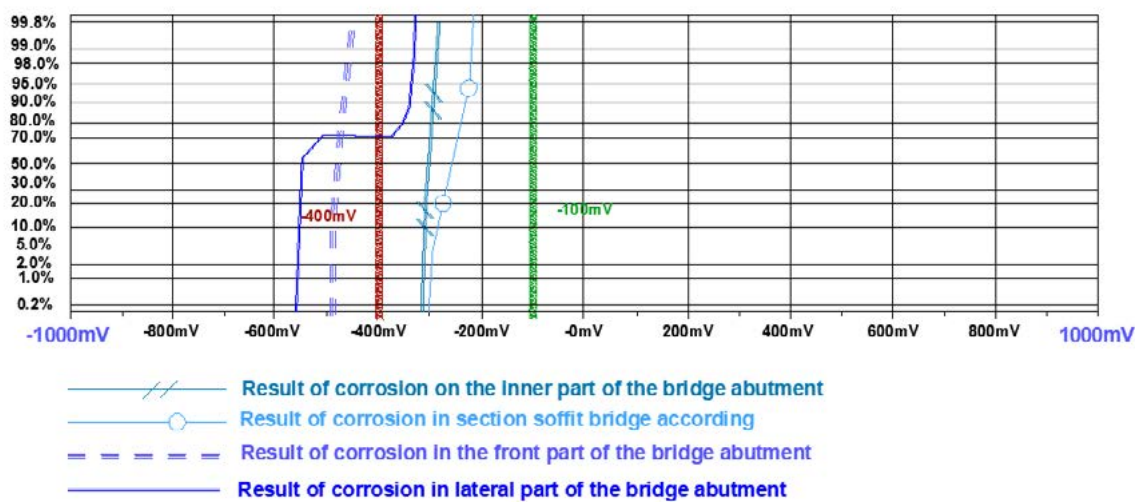
Figure 8. Results of the corrosion rate in specific positions.

5. CONCLUSIONS

From the analysis of the study case, we can conclude:

- Corrosion as a parameter is a function of aggressive parameters resulting in varying degrees of corrosion in different parts.
- The north-facing front results in higher corrosion than the lower-south, the north corrosion values reach> -500mV, while in the southern part the corrosion values are -300mV.
- The north side of the soffit is completely degraded and there is reinforcement detection, whereas in parts where we still have a protective layer the corrosion rate reaches up to -300mV, the south side is very degraded and the protective layer is reduced which has reduced the degree of corrosion (-300mV).
- From field measurements, the steel corrosion rate is 2.2 mm, while according to ASTM calculations the corrosion rate is 2.04 mm.
- According to ACI Standard 408, the corrosion rate for the measured bar (from the same bar we have determined the corrosion rate) the corrosion rate reaches (30-40) %.
- The usability of the bridge structure is directly dependent on the corrosion rate and longevity. In our case, it is questionable, since we have at certain points exceeding the corrosion limits.

Recommendations:
Immediately repairing and retrofitting the bridge structure

REFERENCES

[1] Ministry of Environment and Spatial Planning-Pristina (2019)

[2].Thoft-Christensen "Corrosion and Cracking of Reinforced Concrete"-Danimark (March 2003)

[3]C.M.Hansson, A. Poursaee, S.J.Jaffer "Corrosion of Reinforcing Bars in Concrete"(December 2012)

[4] Lana L. Wong, Sue I. Martin, Raul B. Rebak "Methods to Calculate Corrosion Rates for Alloy 22 from Polarization Resistance Experiments"-Canada (April 3, 2006).

[5] Designation: G1-90 (Reapproved 1999)"Standard Practice for Preparing, Cleaning, and Evaluating Corrosion Test Specimens"

[6] N.Kabashi, "Mirëmbajtja dhe sanimi i strukturave egzistuese"- Prishtina (Octomber 2016).

[7] Kyle Stanish "Corrosion Effects on Bond Strength in Reinforced Concrete" National Library of Canada, Canada, (September, 1997).

10 | Darko Kokot, Alfred Weninger-Vycudil

Assessment of social effects in asset management

ASSESSMENT OF SOCIAL EFFECTS IN ASSET MANAGEMENT

D. Kokot[1], A. Weninger-Vycudil[2]

[1] Slovenian Nationa Building and Civil Engineering Institute, Department of Geotechnics and Infrastructure
Dimiceva ul. 12, 1000 Ljubljana, Slovenia
e-mail: darko.kokot@zag.si

[2] PMS-Consult – Deighton Associates Ltd
Naglergasse 7/9, 1010 Vienna, Austria
e-mail: alfred.weninger@deighton.com

SUMMARY: The transnational European CEDR project ISABELA (Integration of social aspects and benefits into lifecycle asset management) was launched to define a common basis for social impact assessment in asset management. The aim was to define a holistic asset management framework for social key performance indicators (S-KPIs) and to model social benefits in terms of social effects (monetary and non-monetary), social backlog and social risk. These project results are becoming increasingly important in the context of evaluating different maintenance strategies for road infrastructure networks. While decision makers need to present the consequences of their maintenance strategies and policies on both technical and social levels, ISABELA showed how social aspects can be an integrated part in asset management frameworks, how to present social impacts and how to discuss maintenance needs using social aspects. The project aimed to identify clear and justifiable social key performance indicators in combination with existing technical parameters, taking into account different stakeholders and their needs and expectations. To this end, ISABELA considers maintenance aspects such as traffic availability, disturbance and efficiency (travel time, vehicle operating costs, etc.), road safety (fatal and serious accidents related to asset condition), environment (noise, air pollution, natural resources, etc.) and socio economy (asset value, wider social effects, etc.). In addition to the S-KPIs, ISABELA proposed a decision-making process for the selection of appropriate parameters and models, and demonstrated the assessment of social effects with practical examples.

KEY WORDS: Road infrastructure asset management, Social effects, Social risk, Social backlog, Maintenance strategies.

1   INTRODUCTION

Managing our ageing road infrastructure is a major challenge for our society in the 21st century, especially for the Road authorities (RA) who are responsible for these networks. The increasing importance of road infrastructure leads to a growing responsibility in maintaining road infrastructure assets and terms such as availability, safety, sustainability, environmental friendliness, etc. express the expectations of different stakeholders that need to be taken into account. Thus, asset management has become a complex task in which the objective is to find the optimal solution in the form of a balance between the expectations of the different stakeholders and the technical requirements, between the highest possible societal benefits and the always limited financial resources.

Over the last twenty years, many research and development projects have been devoted, in whole or in part, to the analysis of the social impact of the management of road infrastructures, including their operation and maintenance. For example, the development of the HDM system began in the 1970s under the auspices of the World Bank. More recently, a considerable number of European projects have addressed this issue. One of the first, PAV -ECO [1], extended by FORMAT [2], focused specifically on the conceptual development of a framework for cost-benefit analysis and technical models adapted to different contexts or European countries. It quickly became apparent that a key factor in the implementation of this type of analysis by RAs was the development of indicators to characterise the impact of the condition of a road network (in its construction, operation and maintenance phases) on the economic and social activity of the region it affects and, more recently, on the environment.

The COST 354 project [3] sought to identify and propose, at the European level, indicators and indexes to quantify the condition of a network, the first step towards a characterization of the relationship between this condition; the operation -

especially dysfunctions – of road infrastructure; the measures to overcome these dysfunctions; and the effects of both (dysfunctions and remedial measures) on the economy, society and the environment.

While COST 354 focused on technical indicators and indexes, the cornerstone of the overall analysis, a report of the PIARC Technical Committee D1 [4] was mainly interested in identifying indexes (existing or created), called high-level indexes, to measure the social and environmental impacts of road activities. An approach by stakeholders was conducted, which allowed identifying the expectations of these stakeholders regarding the road network, both positive (the need to improve their living conditions) and negative (the fear of deterioration, even temporary, of those). This done, it was possible to propose, when it does not already exist, a scale for assessing the degree of satisfaction or dissatisfaction of each stakeholder, based on combinations of measurable quantities. In continuation of this work, EVITA project [5] went deeply into the construction of indexes to characterize the impact of the roads on the environment, favouring an approach at the road sections level, in particular targeting the impacts on the Society, mainly noise, air pollution and water, removal of non-renewable natural resources (both aggregates and fossil energies). And for its part, the project SBAKPI [6] treated the economic impacts of the operation and maintenance of a network, considered as a whole.

2   ISABELA PROJECT

ISABELA (Integration of social aspects and benefits into life-cycle asset management) aims at defining a holistic asset management framework for social key performance indicators (S-KPIs) and modelling social benefits in terms of social effects (monetary and non-monetary), social backlog and social risk. ISABELA represents a significant extension for life cycle assessment of maintenance strategies. The project closes this gap and makes it possible to include social aspects and benefits in classical asset management.

2.1 Review of stakeholders, and their needs and expectations

The review began with an assessment of stakeholder requirements and expectations and included a literature review of S-KPIs in use and interviews with experts from RAs regarding their current practise and use of S-KPIs. The aim was to review and complete the stakeholder expectations and requirements together with the inventory of available indicators, data, models and methods already available from existing groups/projects.

Five groups of stakeholders were identified: Users, Neighbours, Road Authorities (with subcategories of Road Owners and Road Operators), Financial Institutions and Society.

Users are defined as direct and immediate users, i.e., people (or businesses) who use road infrastructure for transportation and/or commuting, making them the infrastructure's primary service delivery capability. In general, most users expect safe and timely communication between two locations.

Second, the neighbourhood is defined as all households and properties in close proximity to the road infrastructure whose day-to-day functioning is closely related to the performance of an infrastructure. Neighbours may have numerous benefits from their proximity to the road, but they may also be annoyed by traffic noise, maintenance and closures, traffic accidents, and the like.

On the other hand, road authorities and especially road operators certainly tend to provide safe and reliable infrastructure, but in line with budgetary constraints and strategies for the development of a particular area. Therefore, in many cases, the financial aspect can be the crucial one in the asset management of the road network.

Finally, it is a duty of society (defined as both individuals and numerous organisations and associations) to ensure that infrastructure does not have a negative impact on quality of life, ecosystems, cultural heritage, etc.

Obviously, stakeholders agree on many of their expectations - on the importance they attach to the provision of adequate services; however, in order to view the road network asset holistically as a functioning system with many interactions, it is important to consider all requirements in line with all five groups of stakeholders mentioned above when defining future maintenance strategies.

The project group found 30 single stakeholder requirements and expectations from the literature review. However, some of these expectations relate to more than one area, so 63 expectations were eventually identified, of which 15 relate to Users, 11 to Neighbours, 8 to Financial Institutions, 8 to Road Authorities and 21 to Society.

Stakeholder requirements and expectations were grouped into four areas related to the following maintenance aspects: Availability and Disturbance; Road Safety; Environment; and Socio-economics.

2.2 Literature review of socio-economic indicators

In order to respond adequately to stakeholder requirements, road asset managers use a range of indicators that provide a means of measuring, quantifying, comparing and monitoring all aspects of a complex system.

The literature review identified a large number of indicators that relate to four key maintenance aspects. For the "Availability and disturbance" aspect, 16 indicators were identified in five subcategories: Accessibility, Condition, Congestion, Restrictions and Travel Time. For the "Road Safety" aspect, a total of 23 indicators were identified in five subcategories: Accidents, Condition, Overall Safety, Safety Costs, and User Perceptions; most of these indicators were placed in the "Accidents" subcategory. The "Environment" aspect includes 18 indicators divided into five subcategories: Air Quality, CO_2 Emissions, Natural Resources, Noise, and Soil and Water Quality. Finally, for the aspect "Wider socio-economic costs", 45 indicators were identified in the literature, divided into eight sub-categories: Asset Value, Condition, Cost Effectiveness, Environmental Costs, Safety Costs, Wider Socio-economic Costs, Stakeholder Satisfaction and User Costs.

The indicators are derived from the TPs, which provide a certain measure of road asset performance. In this research, an attempt was made not only to define the scope of possible parameters (and derived indicators) capable of covering the widest range of stakeholder expectations, but also to adequately assess the parameters (and indicators) in terms of several objectives. For example, it is important to define indicators with detailed knowledge of mutual interactions and overlaps that adequately address established stakeholder needs, and to assess their degree of objectivity (whether the indicator is based on measurement or estimation), applicability and reliability, assuming timely, non-costly and reliable data sources.

It was found that Availability and Disruption is very important from the perspective of a number of stakeholders and almost directly represents the ability of the infrastructure to provide services to its users. However, infrastructure availability also represents a measure of an operator's efficiency, while disruption can be as important to neighbours as it is to users. It is therefore not surprising that one aspect of availability and disturbance is represented by a number of indicators and parameters. Availability and disturbance- related indicators include five subcategories: Accessibility, Condition, Congestion, Restrictions, and Travel Time.

Road safety is also one of the most important aspects of the overall performance of the road network, affecting users, neighbours, road authorities, but also the whole society. The Road safety category is divided into five subcategories: Accidents, Condition, Overall Safety, Safety Costs and User Perception.

Environmental impacts are still insufficiently considered in asset management, although they are crucial for the quality of life and general well-being of society. There are a large number of indicators in the literature. Environmental impact indicators are divided into the following subcategories: Air Quality, CO_2 Emission, Natural Resources, Noise, and Soil and Water Quality.

Socio-economic indicators include the following sub-categories: Asset Value, Cost Effectiveness, Environmental Costs, Safety Costs, Wider socioeconomic costs, Stakeholder Satisfaction, and User Costs.

2.3 Use of Socio-economic indicators in Road Authorities

The indicators identified in the literature served as the basis for interviews with experts from interested Road Authorities to identify indicators that are either currently in use or that there is interest in using in the development of authorities' asset management programs. Based on these interviews, additional S-KPIs used by authorities were added to the list of indicators.

Most of the identified S-KPIs are not systematically used in the development of asset maintenance programs, and very few of the identified indicators are used by a significant number of road authorities. However, there is considerable interest in implementing and using some of these indicators in the future, particularly those for which data are available in some form within road authorities.

The importance of considering expectations in the area of Road availability and Disturbance in maintenance planning is recognized in all countries, but to varying degrees. The indicators used mostly include some form of condition rating for carriageways and bridges, while other indicators related to accessibility, congestion, availability and travel time are used to a lesser extent.

All countries use some of the S-KPIs related to road safety. The indicators used are mostly related to the number of fatalities, injuries or simply the number of accidents. Based on these data, more complex indicators can be calculated, related to safety costs or frequency of occurrence of accidents. In addition, many authorities use some of the condition parameters to identify appropriate maintenance treatments to achieve certain safety-related levels of these parameters. The S-KPIs for overall safety, safety cost, and user perception are not currently considered significant for maintenance planning by most.

Noise stands out as the most important environmental parameter used by most RDs as a result of implementing the European Noise Directive. Other parameters, such as air quality, CO_2 emissions, environmental costs, natural resources, soil and water quality, do not currently influence planning, but are to some extent part of national legislation. However, as environmental impact is becoming a major issue for all European societies, there is a great interest in the application of the relevant parameters in the future.

Among the parameters related to economics, cost-effectiveness and especially the benefit/cost ratio of maintenance programs seem to be used by most authorities to assess the socio-economic impact of maintenance activities. All other parameters are used to a lesser extent.

3   PROPOSAL OF ISABELA S-KPIS

The focus of the ISABELA project is on indicators that can be applied at the network level (although most of the indicators collected are defined at the project level and then aggregated for use across the network) and that can be related to road maintenance activities. In addition, consideration was given to whether indicators could be monetised and whether there are existing models or whether it was possible to develop models for social benefit, social risk and social backlog.

Therefore, the following main criteria were used as a basis for indicator selection: can the indicator be related to maintenance activities? Is the primary purpose of the indicator to be used for asset management at the network level? Can it be used in existing social benefit models or is it possible to use it for modelling? Is it possible to monetize it?

The following chapters present a brief summary of selected indicators in four main areas: Availability and disturbance, Road Safety, Environment and Socio-economic Impacts, which can be used for socio-economic analysis related to the management of road assets.

3.1 Availability and disturbance

Most Availability and disturbance indicators can be related to travel time to some extent. A functional relationship can be established between the *density of the road network* and the *loss of travel time*. On the other hand, *road availability* is important from the point of view of maintenance and *possibility for detour*. There is also a potential relationship between these two parameters and the importance of the road.

Vehicle operating costs are highly correlated with *road condition*. Travel time at the project level and aggregated at the network level depends on *congestion* caused by maintenance. Therefore, congestion-related indicators can also be related to travel time. *Availability constraints* due to weather are relevant for winter or routine maintenance, but not for construction maintenance.

Three other indicators related to constraints were also considered: due to *load restriction* and *clearance*, and due to the *length of the construction site*. Finally, the aspect of user satisfaction is covered by other indicators (*condition*, *travel time*) in a more objective way.

3.2 Road safety

Road safety indicators include indicators related to accidents, road condition, overall safety and user perception.

Within the Accidents subcategory, indicators are divided into *accidents by impact*, *accidents by user*, and *site-specific accidents*. Within the Condition subcategory, most indicators, such as *longitudinal roughness*, *skid resistance*, *rutting*, and *ravelling*, are routinely collected at the network level for asset management systems. The sub-category Overall safety includes, in addition to the *EuroRAP* score, the *number of tunnels complying with EU safety regulations*.

3.3 Environment

The Environment category includes indicators on air quality, greenhouse gas (GHG) emissions, natural resource use, noise, and soil and water quality.

The air pollution indicator includes emissions of various air pollutants, including *aldehydes*, *sulphur dioxide*, *polycyclic aromatic hydrocarbons*, *CO*, *NOx*, *PM10* and *PM2.5*, and *CO2*. GHG emissions are split into two indicators covering emissions related to *traffic*, and emissions related to *road construction and maintenance activities*.

Similarly, indicators related to natural resource use are divided into those related to *energy consumption* and *materials use*. Noise indicators include *Noise maps*, *Exposure to traffic noise* and *Noise annoyance to humans*. The *Water pollution* index is important from the perspective of salt consumption for winter maintenance. Soil and water pollution indirectly feeds into the evaluation of the *adequacy of the drainage system* and the consequences of road improvement: *Release of hazardous substances due to accidents* and *Emissions of substances that cause acidification*.

3.4 Socio-economic impact

Indicators related to asset value and cost-effectiveness are included in the group of socio-economic effects indicators. This group also includes indicators for *accident costs*, *user costs*, *environmental impact costs*, and costs associated with maintenance activities that reflect *preservation of road investments* and/or *protection of the environment*. All of these indicators are compatible with the expected approach taken in the modelling phase by assuming monetisation of social benefits for various social effects.

One of the remaining indicators for wider socio-economic effects relates to the *contribution of road operations to socio-economic development and employment*.

4   SOCIAL BENEFIT MODELLING

4.1 Decision making process

The selection of appropriate parameters for the specification of Social Key Performance Indicators (S-KPIs) is the first step in the modelling process. For this purpose, the basic requirements from the modelling, the expectations of the stakeholders and which social aspects should be considered have to be matched with the list of indicators and their parameters. The criteria for the selection and assessment process can be summarized by the following questions:

What parameters are needed for the application of the model? Is data available for these parameters at the network level? Is there a correlation between the parameters and the specific social aspect to be addressed? Can the parameters be used to support the expected outcomes and outputs of the modelling?

In principle, the selection of appropriate models and the corresponding S-KPIs should be done by the road authority itself. The ISABELA project does not prescribe the models to be used, nor the indicators to be considered, nor the outputs to be provided to decision makers. Nevertheless, the project provides a practical approach and shows how the modelling

part and the calculation of social effects can be carried out using different indicators.

Regardless of how the specific maintenance program is handled by the road authority, the best level for calculating the social effects is when the individual maintenance projects (usually an accumulation of different maintenance activities on different assets) are defined. In particular, social effects need to be assessed taking into account the different stakeholders and the specific impacts of the maintenance activities as well as the improved asset condition. Each individual maintenance project of a comprehensive maintenance program should be assessed in the same way. Finally, the results can be cumulated over the entire network to reflect the impact at the network level.

As a summary of the study on the processes, the different planning levels, the availability of data and indicators and the models, the recommended approach should be applied at the levels where the maintenance program is defined (by individual maintenance projects) and the results can be cumulated over the whole network.

Thus, ISABELA is a network-level approach for assessment of committed or recommended maintenance programs that takes into account the specifications of maintenance projects and the potential effects of maintenance treatments on societal benefits and drawbacks. However, the recommended approach can also be integrated at other levels to assess asset-specific maintenance treatment strategies (pavement management, bridge management, etc.) and scenarios.

4.2 Modelling social effects

The starting point of the ISABELA approach to social effects modelling is a defined, planned or recommended maintenance program of heavy maintenance (overlay, reinforcement, rehabilitation, etc.) that should be assessed from a social perspective and compared with other options (e.g. do-minimum strategy, routine maintenance strategy). The program can be related to a single asset (e.g., roadway) or to a combination of asset-specific maintenance treatments (cross-asset project). The input parameters can be divided into the following categories: Input parameters describing the maintenance section; Input parameters describing the maintenance project; Input parameters describing the road infrastructure network; Cost rates; and General additional input parameters.

The calculation of the different social effects of a maintenance project is described in detail in the deliverables of ISABELA. The effects, expressed in terms of social savings and social costs, are the basis for the social assessment of each maintenance project. To apply this social valuation to a maintenance project, it is necessary to compare the savings with the costs and obtain a monetary parameter that reflects the total social effects of the maintenance project m. This monetary parameter can be positive or negative. In the case of a positive value, the social savings are higher than the costs; in the case of a negative value, the social costs outweigh the savings. Regardless of the sign, a trade-off between social savings and social costs must be made, as shown in Table 1 below.

Table 1: Balance sheet for the calculation of total social effects of a maintenance project

Category	Social savings (savings in social costs)	Social costs (additional social costs)
Social category X	$savXCST_{s,m}$	$addXCST_{s,m}$
Total social effects	$MSocEff_{s,m}$	

To calculate the total social effects of a maintenance project *m*, the following equations can be applied:

$$SocSAV_{s,m} = \sum_X savXCST_{s,m} \qquad (Eq.\ 1)$$

$$SocCST_{s,m} = \sum_X addXCST_{s,m} \qquad (Eq.\ 2)$$

where:

$SocSAV_{s,m}$ .... social savings of maintenance project *m* on section *s* [€]

$SocCST_{s,m}$ .... social (additional) costs of maintenance project *m* on section *s* [€]

$savXCST_{s,m}$ .... savings in social costs of category (aspect) *X* due to maintenance project *m* on section *s* [€]

addXCST$_{s,m}$................additional social costs of category (aspect) X due maintenance project m on section s [€]

The difference between the savings in social costs and the additional social costs returns the total social effect of the maintenance project m on section s (see Equation 3).

$$MSocEff_{s,m} = SocSAV_{s,m} - SocCST_{s,m} \qquad\qquad\qquad\qquad \text{(Eq. 3)}$$

Two other concepts are proposed by ISABELA to be included in decision making regarding road infrastructure maintenance.

The social maintenance backlog can be defined as the social effects, caused by the failure to meet strategic requirements. It is the difference between the total monetary social effects of the 'target' maintenance strategy, which includes all maintenance activities to meet the strategic requirements and represents the maintenance policy, and the planned maintenance construction programme, e.g. the strategy Do-Minimum. If the total social effects of the planned maintenance construction programme is equal to or higher than the total social effects of the "target" maintenance strategy, a social backlog is zero or non-existent. Note that the "do-minimum" strategy here only meets the minimum requirements, while the "target" strategy is to represent maintenance activities to achieve the strategic requirements of the maintenance policy.

Each maintenance strategy carries some social risk that needs to be assessed and compared with other strategies. This can be done in a qualitative or quantitative way. Basically, social risk can be defined as the expected social consequences in relation to stakeholder expectations in the social domain. Compared to social effects, benefit and backlog, social risk involves an assessment of whether a planned or committed maintenance programme (or strategy) can be implemented under the given social conditions. Mathematically, social risk is evaluated as the product of the likelihood that a predefined maintenance strategy will fail to meet stakeholder expectations and the resulting social consequences, taking into account various uncertainties within the asset management process.

Social risk seeks to imply a better understanding of social effects and responsibilities. Therefore, it is strongly recommended to discuss the definition from a social point of view with relevant experts (risk managers, sociologists, economists, etc.) and adapt it if necessary. As an outcome of ISABELA, this definition of social risk can be used as a starting point for this discussion.

4.3 Practical application

Two different test sites were selected for practical application of the ISABELA models to test the model implementation in existing asset management tools [7]. Here, a summary of the results of the calculations for a section of the A4 motorway (E58 / E60) in Austria is presented.

As an example of the results, Figure 1 compares the social costs and savings for the planned IIP strategy (Infrastructure Investment Program) and the strategy Do-Minimum. It can be seen that both strategies have social costs due to the maintenance projects, but also social savings in safety as a result of the long-term effect of a better pavement condition.
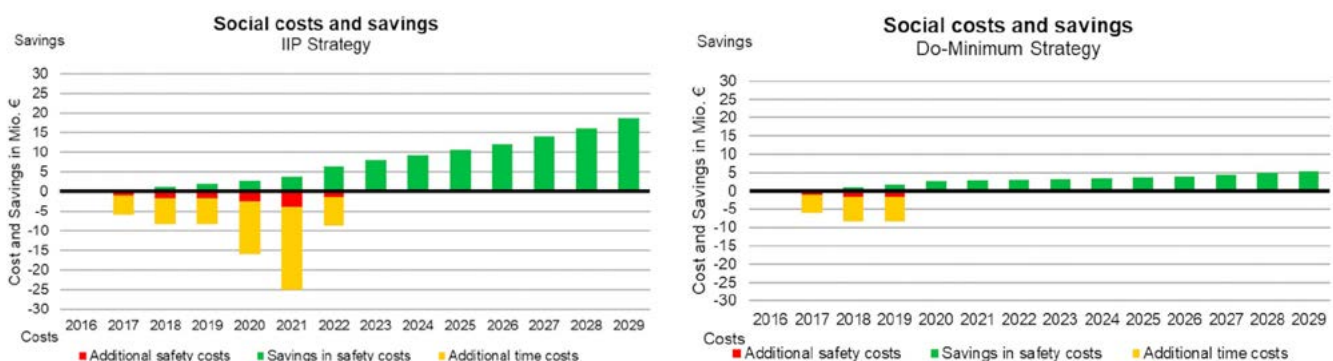

Figure 1: Comparison of social costs and savings for the planned (left) and the Do-Minimum (right) strategy in ISABELA [7]

5   CONCLUSIONS

The study of social performance indicators and models has shown that most social aspects can be covered by simplified approaches, taking into account existing models and available input data and their correlation with expected outputs and outcomes. Most of the models presented in ISABELA are based on simplified relationships between traffic, asset condition and physical or economic effects, which makes them suitable for application in an asset management software solution.

Based on the results of the research and the assessment of the different types of indicators, a procedure for calculating social benefit, social risk and social backlog was developed. A crucial step in the process is the transformation of technical parameters into monetary and non-monetary performance parameters using different models that take into account the different social aspects and stakeholder requirements.

A socio-economic impact analysis can certainly be carried out using the ISABELA models and methodology in most existing asset management systems, provided they meet some requirements derived from the study. However, to perform a reliable and satisfactory socio-economic assessment of their maintenance policy, Road Authorities probably need to collect more socio-economic information (parameters, coefficients...) adapted to their context and take great care in collecting and storing their road data. The results of the socio-economic analysis can be used at different levels depending on the level of application (for individual assets or for maintenance projects) and should be integrated in the decision-making process.

ACKNOWLEDGMENTS

REFERENCES

[1] PAV-ECO, Economic Evaluation of Pavement Maintenance, Final report of PAV-ECO Project for EC-DG-VII RTD Programme, (1999), Available from https://trimis.ec.europa.eu/sites/default/files/project/documents/pavecofrep.pdf Accessed: 2021-03-12

[2] FORMAT, Fully Optimised Road Maintenance, Final report of FORMAT Project for 'Competitive and Sustainable Growth' Programme (1998-2002), (2005), Available from https://trimis.ec.europa.eu/sites/default/files/project/documents/20090917_162005_61131_FORMAT%20-%20Final%20Technical%20Report.pdf Accessed: 2021-03-12

[3] COST 354: Litzka, J., Leben, B., La Torre, F., Weninger-Vycudil, A., de Lurdes Antunes, M., Kokot, D., Mladenović, G., Brittain, S., Viner, H.: The Way Forward for Pavement Performance Indicators Across Europe, COST Action 354 Performance Indicators for Road Pavements Final Report, (2008), Available from http://cost354.zag.si/fileadmin/cost354/1fr/COST354_FinalReport_05062008.pdf Accessed: 2021-03-12

[4] High Level Management Indicators, PIACR Committee D1 Road Asset Management, (2011), Available from https://www.piarc.org/ressources/publications/8/18287,2012R22-EN.pdf Accessed: 2021-03-12

[5] EVITA, Environmental Performance Indicators for the Total Road Infrastructure Assets Available from http://se-kpi.fehrl.org/?m=49&id_directory=7106 Accessed: 2021-03-12

[6] SBAKPI, Strategic Benchmarking and Key Performance Indicators, Available from http://se-kpi.fehrl.org/?m=49&id_directory=7909 Accessed: 2021-03-12

[7] ISABELA - Integration of social aspects and benefits into life-cycle asset management, (2017), Research project under the CEDR transnational research program 2014, Conference of European Directors of Roads (CEDR)

11

Ivana Lipoščak, Dubravka Bjegović, Mario Ille, Ana Baričević, Boris Mikšić

Migratory corrosion inhibitors technology for improving durability of europe's bridges infrastructures

MIGRATORY CORROSION INHIBITORS TECHNOLOGY FOR IMPROVING DURABILITY OF EUROPE'S BRIDGES INFRASTRUCTURES

Ivana Lipoščak[1], Dubravka Bjegović[2], Mario Ille[3], Ana Baričević[4], Boris Mikšić[5]

[1]Cortec Corporation
Ivana Lučića 5, 10000 Zagreb, Croatia
e-mail: iliposcak@cortecvci.com

[2,4]University of Zagreb Faculty of Civil Engineering
Kačićeva26, 10000 Zagreb, Croatia
e-mail: dubravka@grad.hr, abaricevic@grad.hr

[3]Institut IGH, Zagreb
Janka Rakuše 1, 10000 Zagreb, Croatia
e-mail: mario.ille@igh.hr

[5]Cortec Corporation
4119 White Bear Parkway, St. Paul, MN 55110 U.S.A.
e-mail: boris@cortecvci.com

SUMMARY:

Bridges are of vital importance to the European infrastructure network. Due to its significance in the political economy, the demand for sustainable is emphasized, which means very advanced, economical, environmentally friendly, and long-lasting constructions. Now, the European market is dominated by concrete bridges. A survey on condition assessment of European bridges showed that 1/3 of the bridges has symptoms of deterioration, with carbonation and/or chloride induced steel corrosion as main degradation mechanisms. Accordingly, significant resources are put in the maintenance of such bridges often at higher costs and prior then planned.

By using migration inhibition technology in severely corrosive environments, structures can have a stronger resistance to corrosion and therefore longer durability. Increased durability means fewer repairs, enhanced structural integrity and a longer service life, all leading to greater sustainability. This paper presents a review of the present status of migratory corrosion inhibitors technology that is to be used regarding improving durability design of new and existing structures. The focus is placed on the European scenario and on the most widespread deterioration mechanisms: steel corrosion induced by chlorides (very frequent in marine environments or in cold regions where deicing salts are applied) or by carbonation.

This paper includes some analyses of concrete bridges; service life assessment, including comments on life-cycle costs; and concludes with discussion of design options that have been used or have become available recently that might be considered to achieve a service life of 120 years for major concrete bridges.

KEY WORDS: migrating corrosion inhibitors; concrete bridges; durable constructions; service life.

1.0 INTRODUCTION

Service life of 100 years has been used for major bridge and tunnel projects in Europe since the early 1990s.Some European bridges as in Denmark and Sweden, utilized concrete specifications developed to ensure a service life of 100 years. Consultants of these bridges established the following as the basis for the concrete specification requirements:

-the requirements will be based on well-known technology and will secure a service life of 100 years with proper maintenance but without any major repair work.

-the service life period will be the time to be achieved with proper maintenance but without any major repair work. Increasing the service life of major bridges from 75 to 120 or 150 years "without major repair work" would obviously greatly reduce the resources required for a given installation on an annual basis. From this perspective, sustainable development and service life are clearly interrelated.

Traditional approaches for enhancing the service life of bridges used in various codes and specifications such as AASHTO specifications, Eurocodes or British Standards, are mainly in an indirect form, specifying the use of certain details or properties such as cover thickness, maximum crack width, concrete compressive strength, etc.

Recognizing the importance of design for service life has motivated different agencies to undertake new initiatives for developing more formal design approaches for service life, like those used for design for strength. The most notable efforts to develop a scientific approach for service life and durability of concrete elements (covering buildings, bridges, and tunnels) were a series of studies carried out between 1996 and 1999 in Europe for the fédération international du béton (The International Federation for Structural Concrete) published within fib Bulletin 34, Model Code for Service Life Design, (TTD 2006). Bulletin 34, however, only concentrated on addressing concrete service life and durability. The use of recommendations made in Bulletin 34 is believed to be most applicable for concrete in vertical configuration and under compression, such as in substructure columns or sides of concrete box girders. This same debate can also be extended to the use of some of the available commercial and non-commercial programs that use the fundamental concepts stated in Bulletin 34.

One of the missing elements for designing bridges for service life is the framework that would approach the problem in a systematic manner and provide a complete solution in a format that could ensure long lasting bridges. Individual solutions to issues that historically have reduced service life, maintenance plans, retrofit or replacement plans, bridge management, and life cycle cost analysis are all just components of this systematic framework and not the framework itself.

The steps within this framework should start at the design stage and should provide the owner with complete information for ensuring the serviceability of the bridge for a specified target service life. It is important for the plan to be transparent and identify the challenges for the period of specified service life, at the design stage, so that the owner will encounter no surprises.

2.0 CORROSION OF STEEL IN REINFORCED CONCRETE BRIDGES

Faced with rising maintenance costs, many engineers and owners recognize the need to protect existing structures from future corrosion damage. As a result, the use of corrosion mitigation systems to delay the need for future concrete rehabilitation is increasing. Selecting the appropriate corrosion mitigation approach is based on many factors, including the amount and depth of contamination (chloride ingress or carbonation), amount of concrete cracking and concrete damage, severity, and location of corrosion activity (localized or widespread), expected environmental exposure, use and service life of the structure, and the cost and design life of the corrosion protection system.

Chlorides generated or from De-icing salts applied during winter months or marine environment exposed structures penetrate existing cracks and diffuse through the concrete cover to the reinforcing steel, initiating corrosion. Corrosion products exert stresses that can crack the concrete and cause delamination and spalling.

One approach to mitigating the problem is to prevent or minimize chloride penetration of chlorides by minimizing cracking using low permeability concretes, adequate concrete cover over the steel, membranes, sealers, or overlays.

Another approach is to prevent the steel from corroding or to minimize the rate of corrosion through means such as the use of corrosion-resistant reinforcement or cathodic protection or corrosion inhibitors. Depending on the specifics of a project, one or a combination of these approaches may be desirable.

3.0 INFLUENCE OF MIGRATORY INHIBITORS ON SERVICE LIFE OF THE CONCRETE ELEMENTS

Life-cycle costs analyses was done for estimating the lifetime of structure exposed to marine corrosion of Peljesac bridge in Croatia.

Life - 365 [1-6] service life prediction model for concrete structures was used to calculate life-cycle costs for four scenarios of concrete columns construction including: a) ordinary concrete (C40/50), b) ordinary concrete (C40/50) with

sealer, c) ordinary concrete (C40/50) with addition of OCI admixture and d) ordinary concrete (C40/50) with addition of OCI admixture and sealer. Life-365 follows the guidance and terminology in ASTM E-917 Standard Practice for Estimating the Life Cycle Cost of Building System.

3.1 Input parameters for service life prediction

Modelling was performed using annual temperature profile relevant to the location of structure, city of Dubrovnik, Croatia in terms of monthly average temperatures in degrees Celsius. Two exposure conditions were evaluated: marine spray zone and marine tidal zone. Service life prediction was performed on square columns (width 2 m, height 70 m). Reinforcement protective layer (x_d) of 54.5 mm was used, as this is a maximum value of cover that Life-365 allows. Designed service life of the structure is 100 years.

The mix design for the ordinary concrete is presented in Table 1 (4). An average value of the migration coefficient and its standard deviation was determined according to NT BUILD 492 and is equal to D28 = 3.82 x 10-12 ± 0,49 x 10-12 m2/s. For this specific application, a sealer with inhibitor called OCI 2018, a 100% silane concrete sealer containing migrating corrosion inhibitors (OCI), is used. Based on the conducted investigation (5,6), it is recommended to set the propagation time to 20 years and the critical chloride ion content level at 0.18%. Additionally, OCI 2005/2005NS admixture inhibitor was modelled. For OCI the chloride concentration threshold value is increased to 0.18% weight of concrete (5). According to ASTM G109 testing, OCI admixtures slow corrosion rates by 5-13 times compared to a control. Within this prediction a conservative value of 5 times reduction in corrosion was used for modelling and the propagation period was set at 30 years (control with no OCI = 6 years propagation time, a five times reduction would equal 6 years * 5, or 30 years). OCI admixtures have no effect on the diffusion coefficient (D28), the diffusion decay coefficient (m) or hydration values, so they remained the same as for the 1st scenario (7). All data used for the calculations were provided by Cortec® Corporation and are provided in Table 2.

Table 1 Mix design for ordinary concrete (4)

Component	Designation	Amount (kg/m^3)
Cement	CEM II/A-S 42,5 R	380
Aggregate	0/4, 8/16, 16/32 mm	1798
Mineral admixture	MEYCO 610	40
Superplasticizer	REDYPLAST VP 342	6,0

Table 2 Input parameters for service life prediction

Alternative	D_{28} (m^2/s)	m	Hydration (yrs)	Ct (%wt.conc)	Prop (yrs)	Protection
1st	3.82 x 10^{-12}	0.20	25	0.05	6	-
2nd	3.82 x 10^{-12}	0.20	25	0.18	20	Sealer
3rd	3.82 x 10^{-12}	0.20	25	0.18	30	OCI inhibitor
4th	3.82 x 10^{-12}	0.20	25	0.18	30	OCI inhibitor & sealer

3.2 Prediction of service life and life-cycle costs

The results clearly indicate the benefits of additional concrete protection. All alternatives have a longer initiation period and consequently, a longer service life compared to the ordinary concrete mix (1st alternative;(a)) for both exposure conditions. Initiation of corrosion is postponed by 55%, 40% and 48% in marine spray zone conditions and by 63%, 51% and 58% in tidal zone conditions when protection of reinforcement is assured through application of sealer (2nd alternative; (b)), addition of OCI admixture (3rd alternative; (c)) or addition of OCI admixture and sealer (4th alternative; (d)). Prolonged initiation and propagation periods are further reflected in the predicted service life. Application of sealer, incorporation of OCI or OCI and sealer combinations assure prolonged service life of concrete elements by 62%, 66% and 67% in marine spray zone conditions and by 67%, 71% and 73% in marine tidal zone conditions compared to the elements produced with ordinary concrete (1st alternative; (a)). Prolonged service life indicates a longer period before the

concrete needs repairs to achieve its designed service life.
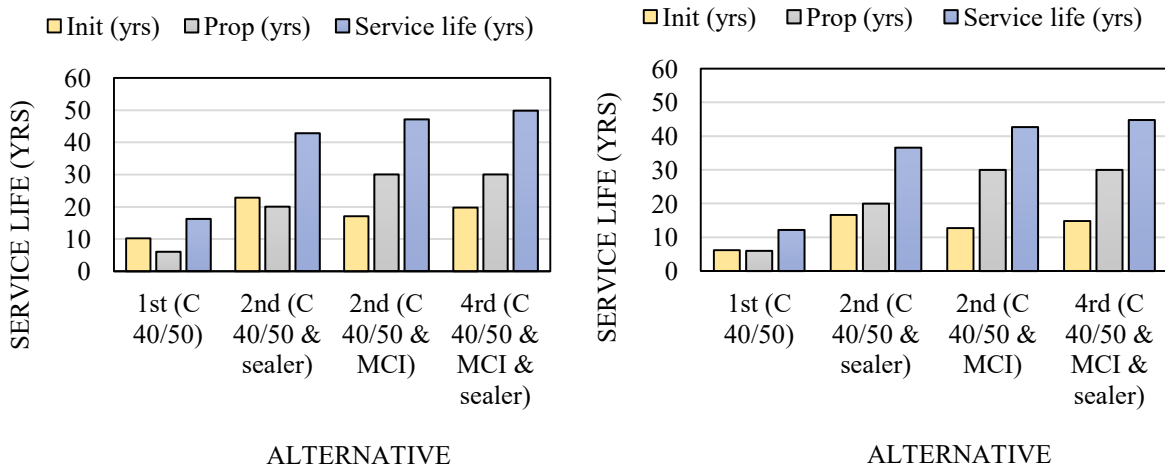
Figure 1 Prediction of the service life for concrete columns exposed to: a) marine spray zone, b) marine tidal zone.

To estimate life-cycle cost, Life-365 follows the guidance and terminology in ASTM E917 Standard Practice for Estimating the Life-Cycle Cost of Building Systems (1). The costs of each alternative consist of the base cost of installing the concrete itself and the cost of concrete repairs throughout the structure's design life. The construction costs are the sum of the basic concrete mix plus the costs of reinforcing and inhibitors. The repair costs are the costs of repairing the structure, starting when the service life of the concretes is reached, it first occurs after the estimated service life and then repeats at fixed intervals for the rest of the study period. Life cycle costs, by alternative & exposure conditions are presented on Figure 2.

Although, initial costs are 7%, 11% and 17% higher for the 2nd, 3rd and 4th alternative, the life-cycle costs are 25%, 24% and 23% in marine spray zone conditions and by 17%, 24% and 23% in marine tidal zone conditions lower compared to the 1st alternative.

Prolonged service life is reflected through reduced costs as the number of repairs is reduced during predicted service life.
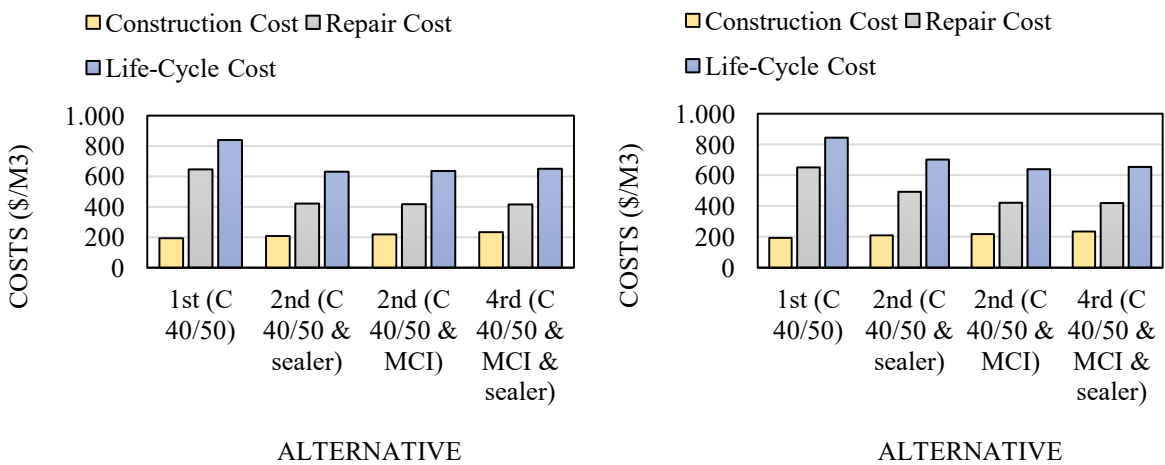

Figure 2 Life cycle costs for concrete columns exposed to: a) marine spray zone, b) marine tidal zone.

4.0 CONCRETE BRIDGES REPAIRED BY UTILISING OCI TECHNOLOGY

4.1 Krk bridge, Croatia

At an annual cost of around €1 million for regular and extra maintenance, the 1.43 km long bridge requires constant monitoring and maintenance due to its sensitivity. If only one year of maintenance is skipped it is later harder and more expensive to repair. For this reason, the entire reinforced concrete structure of the bridge is continuously monitored and maintained, which is crucial if it is to live up of its expected service life. Krk Bridge was built in 1980 and was the longest concrete bridge in the world with the largest range. Apart from the fact that it still imposes on the appearance and range of the large (390 m) and small (244 m) arch (Figure 3), since the bridge is designed and constructed with a minimum protective layer of concrete (2.5 cm), the aggressive effect of the marine environment has caused great damage.

Figure 3. Krk bridge

Testing and inspections from 1993 to 2001 showed that damage of the piers and cracks had reached a level where the mechanical stability of the bridge sections were compromised (Figure 4).
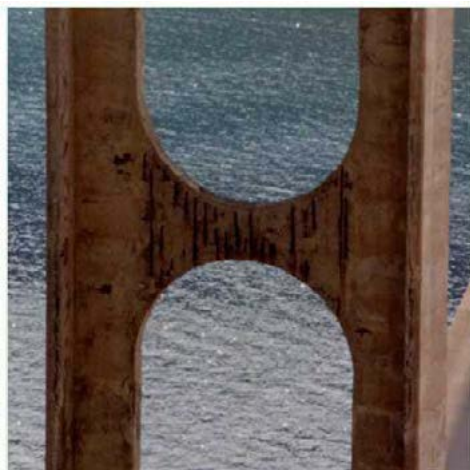
Figure 4. a) cracks on the pillar in 1993.;   b) loosening of the flange edges and widening of the cracks 2001.

The shown cracks significantly facilitate the penetration of chlorides through the damaged and insufficient protective concrete cover, and the process of corrosion of the reinforcement is faster and more intense. The interaction of dynamic influences, concrete creep and the action of an aggressive environment is a major cause of this condition.

Until now, the lower parts of the arches (up to 25 m above sea level), supports, columns, pedestrian corridors of the Krk Bridge were restored and protected from the chloride corrosion, where the concrete cover was reconstructed (partially or completely) and chloride impermeable polymer coating applied.

However, for the remaining larger upper part of the reinforced concrete bridge structure (about 40,000 m2 of arches over 25 m above sea level and overseeing the pavement structure) this would be difficult for several objective reasons. These are much thinner structural elements (thicknesses of a significant portion of 11 to 13 cm) on which the existing concrete cover would be difficult to hydrodemolize, and its thickening would give a significant additional load (about 1,000 tons for only 1,0 cm of widening).

An examination of the condition of the material of the upper parts of the reinforced concrete structure of the small arch bridge, carried out in May 2010 [7] IGH Test Report No. 2122-20-B-129/10, found that these upper parts did not reach above the critical concentration of chloride in the reinforcement zone, so in that case it is not necessary to reconstruct the protective concrete cover.

Therefore, the design solution for the repair and protection of this upper part of the structure was changed to only a chloride-impermeable permanently elastoplastic polymer coating, which is applied to a well-cleaned surface impregnated with organic penetrating corrosion inhibitor, OCI.

Results obtained from monitoring of current condition, installed few years ago are not presented and taken in the time when this paper was done [8-15].

4.2 Maslenica bridge, Croatia

The Maslenica Bridge in Croatia (Figure 5.) is one of the largest bridges of its type with an arc of 200 meters in diameter. Because of the aggressive environment of changing temperatures, constantly fluctuating humidity, and strong wind containing salt from seawater, reinforcing steel had started to corrode, causing concrete spalling. To restore the bridge and prevent future corrosion from happening, all spalling concrete was water-blasted off, along with dirt and corrosion on the rebar.

Figure 5. Maslenica bridge

Tests showed that the concentration of chloride on the columns and foundations of the arch is increased relative to other parts of the structure as well as the visible damage patterned by the corrosion of the reinforcement, which is primarily visible on the heel columns.
Two types of repair were designed depending on the damage of the reinforced concrete structure,
and respectively on chloride saturation and the measured electropotentials on the reinforcement (they gave measured values in the areas of low and medium corrosion risk (from -50 to -350 mV) or are in the area of high and high corrosion risk (from -350 mV to -500 mV and above), (Table 3).

Half cell potentials Cu/CuSO$_4$ (mV)						
(x,y)	1	2	3	4	5	6
1	-470	-425	-370	-375	-355	-375
2	-470	-405	-385	-355	-345	-350
3	-470	-465	-400	-370	-345	-350
4	-415	-415	-380	-360	-360	-335
5	-440	-395	-385	-365	-350	-350

Table 3: Table of measured values of half-cell potentials for the base of arc K1 and criterion according to ASTM

OCI - rust primer was brushed on exposed rebar to passivate the metal from further corrosion, and OCI surface treatment was applied to the entire concrete structure using an airless sprayer to prevent any potential corrosion that was not apparent.OCIs are based on amine technology. They are classified as mixed inhibitors, meaning they affect both anodic and cathodic portions of a corrosion cell. OCI is applied in many forms including as a concrete admixture or a topical treatment. It moves as a liquid through the concrete matrix via capillary action and migrates in a vapor phase throughout the concrete pore structure. When OCI encounters embedded metals, it has an ionic attraction to it and forms a protective molecular layer. This film prevents corrosive elements from further reacting with the reinforcement and reduces existing corrosion rates, greatly extending concrete service life.

4.3 Frederikssund bridge, Denmark

There are many current cases of using organic corrosion inhibitor technology in projects around the Europe such as erecting the new Frederikssund bridge in Denmark (Figure 6). The aim was to replace the old bridge built in 1935 by providing an alternative to the only currently active bridge over the fjord. The project includes design & construction of an 8-km-long dual-carriageway highway, comprehensive of a bridge over the Roskilde Fjord. OCI where used for corrosion protection of PT concrete segments.

Figure 6. Frederikssund bridge

5.0 STRATEGIES FOR ADDRESSING CORROSION

Because of the magnitude of the corrosion problem, both the public and private sectors have ongoing activities aimed at reducing or eliminating corrosion damage to concrete structures. While many technologies and materials have been developed for prevention and repair of corrosion-induced damage, the challenge is to select durable, cost effective technologies and materials from the numerous choices available.

Durability and desired service life must be considered during design. In the case of new structures, it is desirable to

avoid, prevent, or delay the initiation of corrosion using low permeability concretes, proper precautions against cracking and other corrosion-prevention techniques. For existing structures, the condition of the structure should be evaluated to determine if it is corroding or not. If the structure is corroding and the chloride content is high in the concrete, the contaminated concrete is removed; if rust is forming on the surface of the reinforcement, it is cleaned or removed and overlaid with a low permeability concrete overlay. If the existing structure is not corroding, some of the techniques used on new structures, such as applying sealers and membranes, corrosion inhibitors surface treatments, may also be used on the existing structure.

Many strategies have been used successfully to improve the corrosion resistance and durability of new structures. These include: the use of low permeability concrete; use of increased concrete cover; use of improved construction methods such as curing to minimize cracking, use of corrosion-resistant reinforcement, use of corrosion inhibitors to increase the corrosion initiation threshold, use of membranes, coatings, and sealers, and use of improved design details to keep elements dry and to prevent exposure to chlorides. Each of these methods can be effective if it significantly extends the time for corrosion to initiate. In many cases it is preferable to employ more than one technique as this will generally reduce the overall risk of corrosion.

6.0 CONCLUSION

It appears that a fundamental change in approach is necessary in EU practice to achieve the goals of extended service life and a sustainable bridge infrastructure. Reaching these goals involves incorporating details in the design process necessary for extended service life.

Extended service life of major bridges is recommended even if some marginal increase in initial cost is required. LCC analysis of concrete structures are beneficial during design phase to ensure the best choice of suitable materials, technologies, and maintenance techniques.

OCI surface treatments used for repair have been tested extensively and shown to reduce corrosion rates significantly even in the presence of existing chlorides and carbonation. Previous studies have established the benefits of using migrating corrosion inhibitors, the importance of good concrete, and the significance of the ingredients used to make the concrete [16].

Concrete strength for reinforced concrete structures exposed to maritime conditions is just supporting factor, but not the decisive parameter for durability of the construction. For these structures' durability criteria is of the bigger importance and should be included in structural design. Concrete durability depends on many parameters and beside structural design, the attention should be directed also on the concrete mix design including corrosion protection, technology of the concrete production, building process and good-quality workmanship. All the structures in the maritime conditions should be monitored during their service life, to avoid high repair costs. But it is important to underline that the corrosion rate values are very dependent on the environmental conditions and the area on which the current is applied. Different temperature and humidity conditions have a great influence on the measured corrosion rate values [17]. It is essential to combine the on-site corrosion rate measurements with other NDT methods to determine the concrete integrity and state of the reinforcement. [18].

Development of an Eurocodes, national codes, and concrete guidelines specification, with specific service life periods would be beneficial to bridge infrastructure sustainability in Europe.

REFERENCES:

[1] Life-365 Service Life Prediction Model and Computer Program for Predicting the Service Life and Life-Cycle Cost of Reinforced Concrete Exposed to Chlorides, Version 2.2.3, September 28, 2018, Life-365 User manual. http://www.life-365.org/download/Life-365_v2.2.3_Users_Manual.pdf/24.02.2019.

[2] Average monthly temperatures for the Dubrovnik area.

http://meteo.hr/klima.php?section=klima_podaci&param=k1&Grad=dubrovnik/24.02.2019.

[3] Vice Perić, Propisivanje koeficijenta difuzije kao indikatora trajnosti tijekom projektiranja konstrukcija na osnovu svojstava, Sveučilište u Zagrebu Građevinski fakultet, mentor: prof.dr.sc. Dubravka Bjegović, Zagreb, 2012.

[4] Kevin A. MacDonald, Guidance for use in penetrating corrosion inhibitors, Beton Consulting Engineers, 2014.

[5] TCG, Tourney Consulting Group, USBR M-82 Evaluation of Surface Treatments, TCG Project # 14104, 2016.

[6] LIFE-365 Service life prediction model for concrete structures basic input instructions - OCI admixtures in the model, Cortec

[7] Izvještaj o ispitivanju IGH broj 2122-20-B-129/10

[8] D. Bjegovic and B. Miksic, "Migrating Corrosion Inhibitor Protection of Concrete," MP, NACE International, Nov. 1999.

[9] Oslaković, S.; Bjegović, D.; Radić, J. Case study: LCC analysis for Krk Bridge. In Tailor Made Concrete Structures: New Solutions for Our Society, Proceedings of the International FIB Symposium 2008, Amsterdam, The Netherlands, 19–21 May 2008; Walraven, J.C., Stoelhorst, D., Eds.; CRC Press: Boca Raton, FL, USA, 2008; pp. 1005–1007. ISBN 978-0-415-47535-8. [Google Scholar]

[10] Beslac, J. 2003. Maintenance of the Krk bridge, IGH, Zagreb. (in Croatian)

[11] EU – Brite EuRam III. 2000. DuraCrete Final Technical Report, Probabilistic Performance Based Durabillity Design of Concrete Structures, Document BE95- 1347/R17.

[12] FIB, 2007. Concrete Structure Management –The Owners' Guide to Good Practice, fib Bulletin (in press).

[13] Matthews, S.L. 2007. Concrete Structure Management – A whole-life Issue for Owners, fib Symposium Concrete Structures – Stimulators of Development, Cavtat, Croatia, 661–668.

[14] Sram, S. 1981. Execution of the Krk bridge, Građevinar 33, 2, 77–106 (in Croatian).

[15] Stojadinovic, I. 1981. Project of the bridge mainland -island Krk, Građevinar, 33, 2, 57–76 (in Croatian).

[16] B. Bavarian and L. Reiner, "Migrating Corrosion Inhibitor Protection of Steel Rebar in Concrete," Materials Performance, 2003.

[17] Klinghoffer, O., Frølund, T., Poulsen, E.: Rebar Corrosion Rate Measurements for Service Life Estimates, ACI Fall Convention 2000, Toronto, Canada, Committee 365 "Practical Application of Service Life Models"; http://www.germann.org/;

[18] Bjegovic, D., Mikulic, D.; Sekulic, D.: Non-Destructive Corrosion Rate Monitoring for Reinforced Concrete Structures; 15th World Conference on Non-Destructive Testing; Rome, Italy, October 2000, pp. 642-652

12

Kiran Ram, Matea Flegar, Marijana Serdar

Effect of chemical admixtures on corrosion behaviour of structural steel in mortar: comparison between standardized and alternative method

EFFECT OF CHEMICAL ADMIXTURES ON CORROSION BEHAVIOUR OF STRUCTURAL STEEL IN MORTAR: COMPARISON BETWEEN STANDARDIZED AND ALTERNATIVE METHOD

[1]Kiran Ram, [1]Matea Flegar, and [1]Marijana Serdar

[1]Department of Materials, Faculty of Civil Engineering,
University of Zagreb, 10000 Zagreb, Croatia.
e-mail: marijana.serdar@grad.unizg.hr

SUMMARY: Nowadays, corrosion of steel rebars is the most destructive durability issue in RCC structure. There are number of reasons behind this issue including chloride ingress and carbonation. In this study, the effect of two different type of admixtures (set retarder and water repellent) on corrosion resistance of steel in mortar system was investigated by method standardized in EN 480-14. In order to know the efficiency of standard procedure, another set of specimens were casted and assessed by an alternative corrosion detection method. All the specimens were exposed to 3.5% NaCl and saturated Ca(OH)2 solution and the corrosion activity monitored regularly. In standard method, corrosion activity was evaluated by measuring the maximum current density values during potentiostatic polarization. After detection of the corrosion, specimens were opened and checked to confirm the corrosion by visual observation. In the alternative method, corrosion was monitored for a specific period by linear polarization method.

KEY WORDS: admixtures, corrosion, mortar, maximum corrosion current density, linear polarization method

1 INTRODUCTION

In recent years, reinforced concrete structures do not always achieve their expected service life due to corrosion of the steel bars [1]. Reinforced concrete structures experience corrosion due to several reasons such as insufficient cover thickness, severely exposed conditions, ingress of ions (CO_2 or Cl^-). Apart from these causes, the chemical admixtures used for different purposes in the concrete may increase the risk of corrosion initiation of rebars. For instance, admixture having a very low pH value might destroy the passivation of steel bars and thus cause corrosion initiation [2]. Additionally, some chemical admixtures can contain a significant amount of chlorides that could de-passivate the steel in concrete [3]. Consequently, the susceptibility of corrosion due to any chemical admixture must be checked before its use in cementitious systems.

Usually, chemical admixture producers rely on a standard procedure EN 480-14 to prove their product would not initiate the corrosion activity on rebars. This method evaluates the maximum current density that occurred between 1h and 24h during potentiostatic polarization of specimen exposed to sat. $Ca(OH)_2$ solution [4]. The work presented here gives an insight into how two different methods are suitable to check the corrosion activity for newly developed admixtures. This study aimed to compare the corrosion probability interpretation of two different types of admixture by EN 480-14 method (standardized method) and an alternative method, adopted from Šoic et al. [5]. Specimen preparation, exposure conditions, and test equipment were maintained the same for two methods to get a comparable output.

2 MATERIALS AND METHODS

2.1 Materials and mix design

In this study, three categories of specimens were prepared. The first set was control specimen without admixtures, the second set of specimens were made with water proofing admixture (AD1) and the third set was prepared with fast setting admixture (AD2). Control specimen and AD1 specimens were made with water/binder 0.50. For fast setting admixture, the w/b ratio was 0.55 according to the clause in EN 480-14:2007. In the case of AD2, all the ingredients were kept below 5^0C and admixture was added only 15 seconds before the end of mixing, to get enough time for workability and preparation of specimens. Besides, the water content was reduced for AD1 and AD2 mixes (both in liquid form) with an equivalent amount of water present in the admixture, to maintain the constant w/b for all three combinations. Technical details of admixtures AD1 and AD2 and mix details are given in Table 1 and Table 2, respectively.

Table 1 Physical properties of admixtures AD1 and AD2

Property	AD1 (Water repellent admixture)	AD2 (Fast setting admixture)
Visual appearance	White liquid (92% water)	Transparent yellow liquid (51% water)
Density at 20^0C	0.98 g/cm^3	1.43 g/cm^3
pH value	9±1	3±1
Chloride content	≤0.1%	≤0.1%
Alkali content	≤2.0%	≤1.0%

Table 2 Mix details

Materials	Control	AD1	AD2
Cement	1488.59	1488.59	1488.59
Water	744.3	734.71	803.54
Aggregate (0-4 mm)	4465.68	4465.68	4465.68
Admixture	-	10.42	29.92

2.2 Electrodes and exposure conditions

A three-electrode system was used for corrosion monitoring in entire study. For standardized method, three cylindrical mortar specimens were used with 10 mm embedded steel rod prepared according to standard EN 480-14, Figure 1 a). In alternative method, 4 mm thick well-polished (to avoid the irregularities from the surface) steel plates were used instead of steel rod. On them, plastic molds were glued and isolated, in which mortar was poured, as shown in Figure 1 b). Graphite and standard calomel electrode (SCE) were employed as counter electrode and reference electrode respectively. In both approaches, there were two exposure condition maintained - sat. Ca (OH)$_2$ solution (passive conditions) and 3.5% NaCl solution (aggressive conditions).

2.3 Test methods

Compressive strength and chloride migration coefficient were determined according to the standard EN-197 [6] and NT Build 492 [7] respectively. Three specimens were prepared according to the standard and tested after 28 days of curing. For corrosion susceptibility testing, two different approaches were adopted. In standardized method, three specimens of each mix were vertically immersed in sat. Ca (OH)$_2$ solution and 3.5% NaCl solution for 24 hours and then connected with Bio-Logic SA multichannel potentiostat as described in EN 480-14:2007. A potential of -256 mV (vs SCE) was applied across the specimen and current measured for 24 hours. For each test specimen, surface area of steel rod was calculated and the maximum current between 1h and 24h noted. After the testing, all the steel rods were taken out and checked for corrosive spots by visual inspection. In alternative method, specimens with steel plates were cured for 7 days with water and then exposed to the same exposure condition as in first approach. Specimens were continuously monitored using linear polarization method in cycle of 7 days. The open circuit potential was first measured for 15 minutes (OCV) and then steel was polarized in the range of -20 mV to +20 mV from OCV with scan rate of 0.166 mV/s. Solution has been changed regularly in order to maintain the same exposure condition throughout the test.

(a) **(b)**
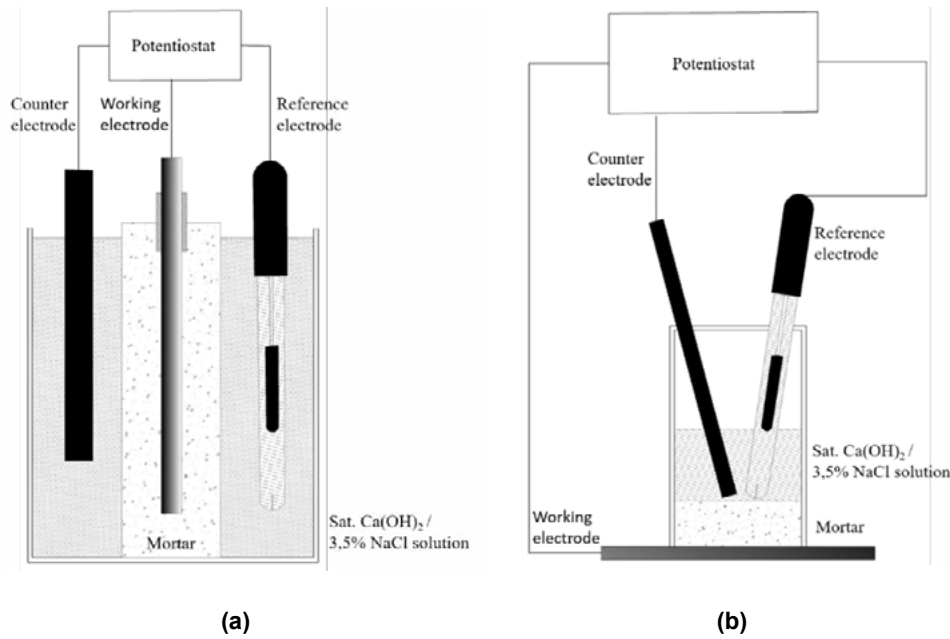
Figure 1 Schematic test set up two testing approaches a) Standardized method, b) Alternative method

3 RESULTS AND DISCUSSION

3.1 Compressive strength

Figure 2a is showing the flow diameter of each mix and Figure 2b and Figure 2c the compressive strength and chloride migration coefficient of three different mixes after 28 days of curing. Both AD1 and AD2 mixes have lower strength compared to control mix. At the same time, these mixes have higher workability, compared to control mix. Lower strength of mixes AD1 and AD2 can therefore be explained with the bigger amount of effective water available in the mix. Regardless of the lower strength, mix AD2 showed better resistance against chloride migration.


(a)

(b) **(c)**
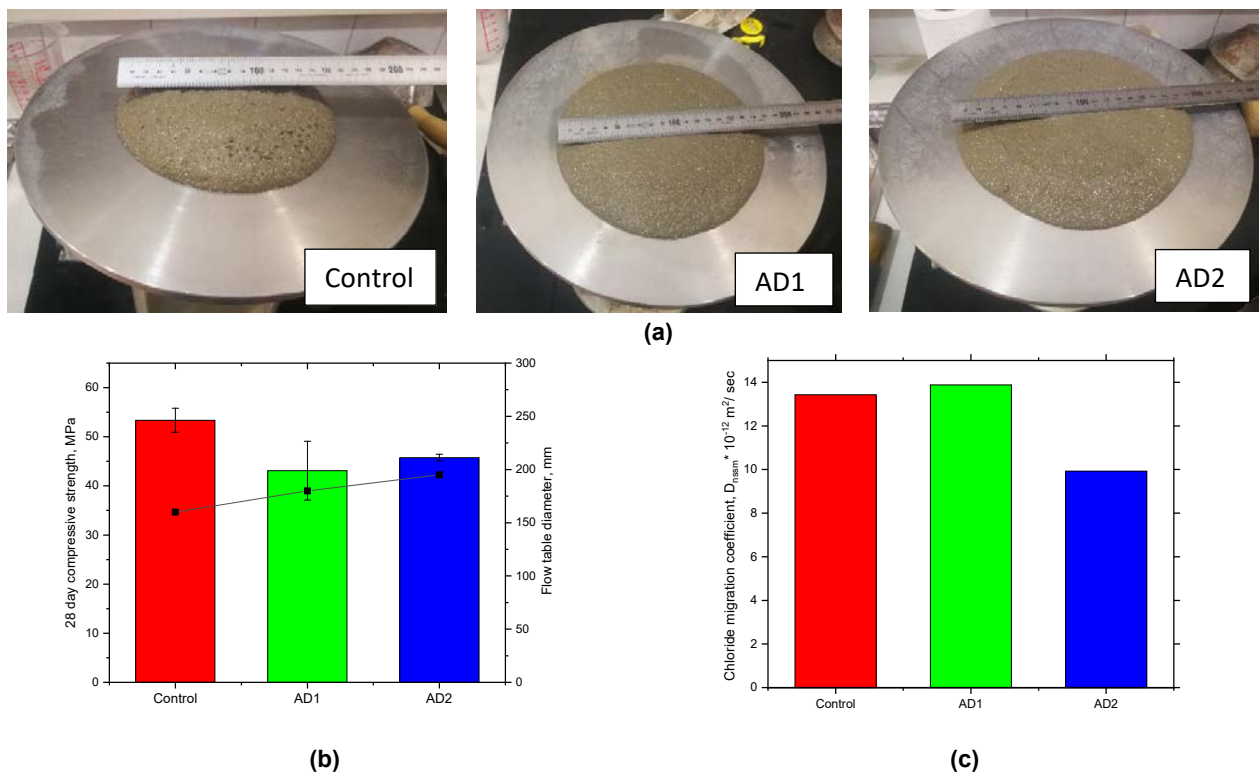
Figure 2 a) Flow table result of each mix, b) 28-day compressive strength and flow table diameter of each mix c) 28-day chloride migration coefficient of each mix

3.2 Corrosion susceptibility according to EN 480-14

Figure 3 a) and b) shows the current density results of all specimens from 1h and 24h of potentiostatic polarization in sat. Ca (OH)$_2$ solution and 3.5% NaCl solution respectively. Here, it is evident that the control specimen was showing very high current density compared to specimens with AD1 and AD2. However, the specimens exposed to sat. Ca (OH)2 has been gradually passivated and got a stable position at the end of the testing period. Therefore, none of the specimens were showing corrosion probability during the test period when exposed to sat. Ca (OH)$_2$ solution.

Figure 3b shows the current density of specimens which were exposed to simulated aggressive condition. From the graphs, it is evident that current densities of steel exposed to chloride environment were much higher than those exposed to passive environment in the case of all three mixes. Table 2 shows the average of maximum current density of both cases. Maximum current density of control specimens in aggressive condition was nearly 4 times larger than that of passive condition, AD1 exhibited nearly 9 times and of AD2 nearly 14 times. In the case of both passive and aggressive exposure, current densities of steel in mixes AD1 and AD2 were higher compared to control mix, indicating that tested chemical additions do not increase the corrosion susceptibility, rather they even decrease it. Results also indicate that, even though the tests are performed 24 hours after curing and only last for 24 hours, it was possible to differentiate passive from aggressive exposure conditions. Additionally, the steel rods took out after the test duration and checked the localized corrosion. But there was no sign of any corrosion spots due to the short span of testing time.


(a)   (b)
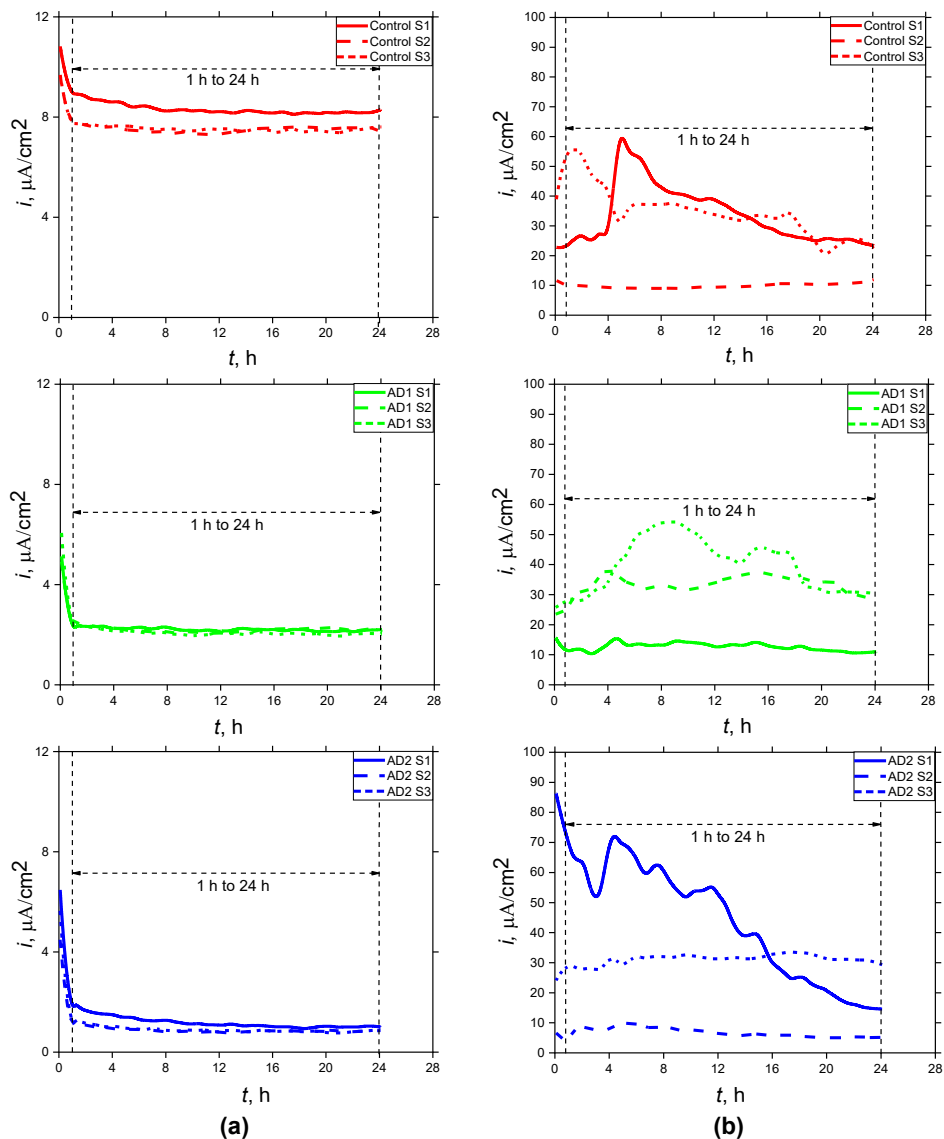
Figure 3 Current density values from EN 480-14 method and specimen exposed to a) Sat. Ca (OH)$_2$ b) 3.5% NaCl solution

Table 2 Maximum current densities of specimens

	Max. current density, i_{max} (µA/cm^2)	
Specimen	Exposed to Sat. Ca (OH)$_2$ solution	Exposed to 3.5% NaCl solution
Control	10.17±2.55	44.89±26.8
AD1	4.56±0.115	37.42±18.80
AD2	3.16±0.22	42.51±32.56

3.3 Corrosion monitoring by alternative method

Figure 4 shows the open circuit potential (E_{ocv}), corrosion current (i_{corr}), and polarization resistance (R_p) of specimens in each stage of test. While considering E_{OCV} of specimens, specimens were showing less than -100 mv after 4 cycles in passive exposure conditions. Therefore, specimens were getting a passivation after some days of exposure in sat. Ca (OH)$_2$ solution. On the other hand, potential of all specimens in aggressive exposure conditions was significantly lower (around -300 mV) over entire duration compared to passive exposure conditions, which is attributed to the presence of chlorides [8,9]. However, corrosion current and linear polarization resistance are not exhibiting the same trend as OCV and showing similar range of values in both exposure condition. Despite this, corrosion current and linear polarization resistance is conveying the specimens were stable in both conditions and less prone to corrosion activity.
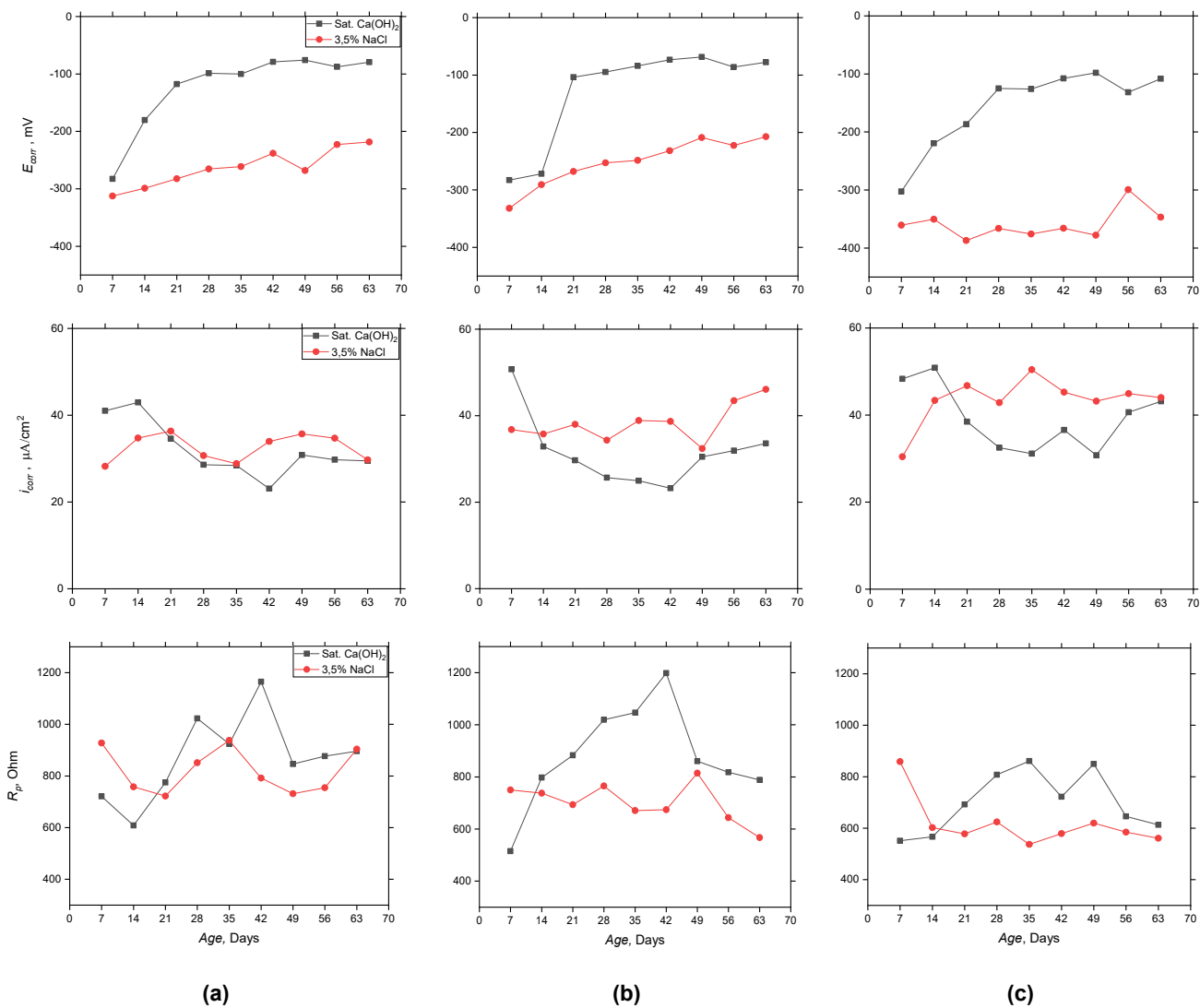

Figure 4 Open circuit potential (E_{ocv}), current density i_{corr} and polarization resistance R_p obtained using alternative method for a) Control specimen b) AD1 specimen and c) AD2 specimen

4   CONCLUSIONS

The present study aimed to compare standardized method for evaluating corrosion susceptibility according to EN 480-14 to the alternative method, suggested by Šoic et al. [5], based on EN ISO 16773 standard for protective coatings on the steel. The specimens with chemical admixtures were prepared and exposed to passive (sat. Ca $(OH)_2$ solution) and aggressive (3.5% NaCl solution) exposure conditions to compare these methods. The idea was to evaluate whether the two methods can detect the corrosion possibility between different mixes and different exposure conditions.

When using the standardized method, the specimens exposed to aggressive conditions were showing high corrosion activity and were stable in passive conditions. Mixes with admixtures, both water repellent and fast setting admixture, were showing lower corrosion activity in aggressive environment and higher passivity in passive environment. Since testing is performed after 24 hours of curing and lasting only 24 hours, it was possible to detect differences in corrosion behavior between different mixes and between different exposure conditions. In the alternative method, all the specimens were showing similar trends in both types of exposure. The difference between exposure conditions was strongly detectable only from values of corrosion potential. In the case of corrosion current and polarization resistance, specimens were showing similar behavior in both exposure conditions and for all three mixes. Gradually, there was a certain increase in current densities and a decrease in polarization resistance for AD1 and AD2 compared to the control mix in aggressive exposure. Therefore, it seems that for this specific method longer exposure times are needed to obtain results.

Based on the results of this study, it can be concluded that the main benefit of standardized method is that it is fast and was able to detect differences between mixes and conditions. The main disadvantages of this method, the results are only qualitative and comparative, and there is no recommendation on interpreting the result based on the maximum current density value. Also, the test could not give long term effect of these admixtures. On the other side, the alternative method gives quantitative results, which can be transferred into engineering units (such as micrometers of steel lost due to corrosion), but the method requires more time to obtain results indicating corrosion susceptibility.

5   REFERENCES

[1] Ahmad, S., 2003. Reinforcement corrosion in concrete structures, its monitoring and service life prediction-a review. *Cement and concrete composites*, *25*(4-5), pp.459-471.

[2] Huet, B., L'Hostis, V., Miserque, F. and Idrissi, H., 2005. Electrochemical behavior of mild steel in concrete: Influence of pH and carbonate content of concrete pore solution. *Electrochimica Acta*, *51*(1), pp.172-180.

[3] Ormellese, M., Berra, M., Bolzoni, F.A.B.I.O. and Pastore, T., 2006. Corrosion inhibitors for chlorides induced corrosion in reinforced concrete structures. *Cement and concrete research*, *36*(3), pp.536-547.

[4] EN 480-14:2007. Admixture for concrete, mortar and grout – Test methods – Part 14: Determination of the effect of corrosion susceptibility of reinforcing steel by potentiostatic electro-chemical test. 2007

[5] Šoić, I., Martinez, S., Lipošćak, I. and Mikšić, B., 2018. Development of method for assessing efficiency of organic corrosion inhibitors in concrete reinforcement. *Građevinar*, *70*(05.), pp.369-375.

[6] EN 196-1:2016 Methods of testing cement. Determination of strength

[7] NT BUILD 492. Concrete, mortar and cement-based repair materials, chloride migration coefficient from non-steady-state migration experiments. *Nordtest Method 492*, (1999)

[8] Saremi, M. and Mahallati, E., 2002. A study on chloride-induced depassivation of mild steel in simulated concrete pore solution. *Cement and Concrete Research*, *32*(12), pp.1915-1921.

[9] Itagaki, M., Tagaki, M. and Watanabe, K., 1996. Active dissolution mechanisms of iron using EIS with channel flow double electrode. Influences of chloride and fluoride ions. *Electrochimica acta*, *41*(7-8), pp.1201-1207.

13 | **Darja Rant, Mateja Štefančič, Vesna Z. Serjun, Mateja Golež**

Mud from the Sitarjevec mine as a pigment for textile printing

UP

MUD FROM THE SITARJEVEC MINE AS A PIGMENT FOR TEXTILE PRINTING

Darja Rant[1], Mateja Štefančič[1], Vesna Z. Serjun[1] and Mateja Golež[1]

[1]Slovenian National Building and Civil Engineering Institute, Department of Materials, Laboratory for stone, aggregates and recycled materials
Dimičeva ul. 12, 1000 Ljubljana, Slovenia
e-mail: darja.rant@zag.si

SUMMARY: The Sitarjevec mine, located near the town of Litija (Central Slovenia), is recognized by the strong yellow colour of its dripstone structures and mine mud deposits. The mine mud, composed predominantly of goethite, accumulates on the ground of the mine shafts as the result of the interaction between percolating underground water, iron ore minerals and microorganisms. Since the accumulation of limonite mine mud is an ongoing process, larger quantities of mud have been deposited in the mine shafts since its closure. These deposits present a real threat of unleashing a mine mud spill on the town of Litija. Such a scenario has already previously occurred. In order to find new potential routes for recycling larger quantities of this mine mud, the present research work was performed to assess the use of mine mud as a pigment in the dye industry. In the first stage, the chemical (XRF) and microstructural (SEM) characteristics of the mine mud were defined together with the identification of its phase composition (XRD), particle size distribution and specific surface area (BET). Furthermore, the pigment was used to colour textile printing paste on a laboratory scale. To define the most appropriate quality of textile prints the rheological response of the various textile printing paste samples was investigated in terms of their plastic viscosity, indicating their suitability for use in textile printing. Test prints were conducted, and the properties of leaching and fastness in the prints were assessed.

Keywords: mine mud, recycling, pigment, printing paste, textile, rheology

1   INTRODUCTION

The Sitarjevec mine, located in the town of Litija, Slovenia, was first mentioned in the 16th Century. It is presumed, however, that mining in this area was present as early as 4000 years B.C. Until 1965, when the mine was closed, it represented one of the largest and richest ore deposits in Slovenia. The main ores were lead, mercury, zinc, copper, iron and barite [1]. About two decades ago, monitoring of the formation of speleothems – stalactites, stalagmites, drapery and straws – which formed in the shafts following the closure of the mine, began. They are recognized as one of the fastest-growing dripstone speleothems worldwide [2].

The mine is also recognized because of the strong yellow colour of the deposits. The mine mud – deposits of Fe-rich residue, composed predominantly of goethite – gathers in the mine shafts due to the interaction between percolating underground water, iron ore minerals, and microorganisms. This mud has been recognized as a source of ochre pigment [3].

The large quantities of mine mud and underground water present a real threat to the old historical centre of Litija. As drainage of the acid mine water from the shafts of the abandoned mine has gradually been limited, it is estimated that more than 6000 cubic meters of acid mine water has accumulated in the mine over the last few decades. Accidents related to outbursts of mine mud occurred in Litija in 1895 and 1932 [4]. As stated by Kirby et al. [5], the utilization of material that is currently considered to be an environmental contaminant could present a financial benefit in the remediation of mine drainage, as well as help avoid additional environmental disturbances due to the mining of Fe-bearing minerals.

Furthermore, for the purposes of adventure tourism, the mine mud must be cleaned from the shafts, making it a waste material. At the end of the year 2017, the Municipality of Litija opened 100 m of the export shaft to the public. Since then they have renovated a further 300 m of mining shafts for museum exhibitions and guided tours. Sitarjevec mine evidently has potential as a natural science and outdoor history classroom to become the main tourist attraction in the town of Litija. Additionally, opportunities for further potential applications to exploit the substantial quantities of mud from the mine are being investigated, such as its use as a sustainable, natural colouring agent – a pigment for textile printing. Accordingly, the physical properties and chemical and mineralogical composition of the pigment found in the mine have been analysed

and are presented in this work.

New products for tourists at the Sitarjevec mine, such as protective clothing for visitors and tourist guides, have been designed. Designs include patterns printed on textiles using pigment from the mine. During the printing process pigment needs to be mixed into an adequate medium – printing paste – to be transferred and fastened to textiles.To achieve textile prints of an appropriate quality, the rheological response of the various samples of printing paste was investigated in order to find the composition of printing paste most suitable in terms of its visco-elastic properties – apparent viscosity, yield stress, shear modulus, and structural recovery – to be satisfactorily printed on textile. The fastness properties of the prints were also investigated.

The ochre pigment from the mine is assumed to be primarily composed of the mineral goethite (α-FeOOH), which is a major component of many ores, sediments, and soils, and one of the most thermodynamically stable iron oxides [6]. Goethite can be found in both humid and semiarid regions and also appears as the weathering product of various iron-containing rocks. Naturally occurring goethite collected from mines or other iron ore deposits has been characterized in terms of its chemical and mineralogical composition and temperature dependent transformations in order to assess potential applications for its use in various industrial processes, for technological purposes [7], as a colouring agent in art [8,9,5], for glazed ceramics [10], and for purposes of conservation and restoration [11].

To the best of the authors' knowledge, iron ore deposits such as mine mud from the Sitarjevec mine have been scarcely researched in terms of their potential application in textile printing. Onar Camlibel et al. [12] were successful in showing the antibacterial, UV protection, flame retardancy and colouration properties of iron ores as additives in the coating of textile surfaces.

The objective of this study was to characterize the ochre pigment from the Sitarjevec mine, assess its suitability in the field of textile printing, and present possibilities regarding the use of natural material from the mine, recognized for its visible characteristic i.e. colour, as a pigment for printing on textile souvenirs.

2 MATERIALS AND METHODS

2.1 Material collection and preparation

Mine mud was collected from the main shaft at the Sitarjevec mine. It was filtered through a sieve with holes of 0.63 mm to remove any larger pieces, dried, annealed for two hours at nine different temperature (150, 200, 250, 300, 550, 800, 900, 1000, 1100 °C), ground, and then passed through a sieve with openings of 0.063 mm. Annealing temperatures were chosen on the basis of the variation of the colours obtained due to exposure of the pigment to different temperatures. A change in colour is apparent at ambient temperatures up to 300 °C. Above this temperature, the colour of the annealed samples remains similar up to a temperature of 800 °C. After exceeding this temperature, differences in colour become visible once again.

For the purposes of textile printing, the particle size distribution of the pigment particles should be in the range between 0.2 µm and 1 µm [13]. To achieve particles with an appropriate particle size distribution, the natural pigment was micronized at Cinkarna Celje, using a pilot 8'' jet mill/ micronizer equipment.

2.2 Mixture design

The mix design of the printing pastes was adjusted based on preliminary test prints performed with the ground pigment and various commercially available textile printing pastes. Six mixes were shortlisted, incorporating micronized ocher pigment, demineralized water, and two commercially available textile printing pastes, Printperfekt Lac 110 Neu (Bezema, Switzerland) and Elastil Coprente FG (Minerva, Italy), with high covering properties. The series including Printperfekt Lac 110 Neu and Elastil Coprente FG printing paste were denominated PP and EC, respectively. The composition of each of the mixtures is presented in Table 1.

The selection of the most suitable mixture from the set of printing paste samples investigated was based on several criteria, namely: (1) the ability of the printing paste to maintain stable rheological properties similar to the reference printing paste after the addition of the dry micronized pigment and, in some cases, water (2) the environmental acceptability of the material, (3) the ease of printing and properties of fastness, and (4) the similarity of the print colour to the colour sensation in the main shaft of the Sitarjevec mine.

Table 1: Mixture composition of the printing paste samples investigated

Sample ID		Mixture composition			
		PP (%)	EC (%)	Micronized pigment (%)	Water (%)
PP series	PP	100	-	-	-
	PP5bV	95	-	5	-
	PP5V5	90	-	5	5
	PP5V10	85	-	5	10
EC series	EC	-	100	-	-
	EC20bV	-	80	20	-
	EC20V5	-	75	20	5
	EC20V30	-	50	20	30

Furthermore, a water- and oil-repellent finishing agent (Dynasilan F8815) was used on the samples in the finishing process before carrying out the leaching and fastness tests.

2.3 Methods

The ochre pigment was characterized in terms of its physical properties, and its chemical and mineralogical composition.

The morphological features of the pigment particles were examined using a scanning electron microscope JSM-5500LV (JEOL, Tokyo, Japan).

The particle size distribution of the ground and micronized pigment sample was determined using an SYNC laser diffractometer (Microtrack MRB, Verder Scientific GmbH & Co. KG, Germany). The material was dispersed in isopropyl alcohol in a container on the FLOWSYNC unit for wet measurements.

The mineralogical composition of the pigment was analyzed by X-ray powder diffraction (XRD) on both the natural and the annealed samples. Powder diffraction data were collected using CuKα radiation on an Empyrean diffractometer (PANalytical, Almelo, The Netherlands) operated at 45 kV and 40 mA. The measurements were made in flat-plate Bragg–Brentano θ–2θ geometry over an angular range of 8 to 70 °2θ using a step size of 0.02 °2θ and an accumulated time per step of 100 s. The resulting diffraction pattern was analyzed using HighScore Plus (PANalytical, Almelo, The Netherlands) powder diffraction analysis software.

The specific surface area of the natural and annealed pigment samples was determined by nitrogen gas sorption using ASAP 2020 equipment (Micromeritics, Norcross, Georgia). The samples were evacuated at a temperature of 105 °C and an evacuation rate of 0.67 kPa/s until a final vacuum of 2 Pa was achieved. The specific surface area was determined following the method proposed by Brunauer, Emmet, and Teller (SSA_{BET}).

For chemical analysis, the samples were prepared in triplicate as fused beads with a diameter of 40 mm and height of 3.6 mm. The chemical composition of the pigment was measured with a Perform'X ARL (Thermo Fischer, Madison, WI, USA) wavelength dispersive X-ray fluorescence spectrometer (WD XRF). UniQuant™ software was used to determine the major and minor oxides present in the sample.

Loss on ignition of the pigment was determined according to SIST EN 15169 (2007). The dried sample was placed in an oxidizing muffle furnace for 2 hours at 1000 °C and cooled to room temperature in a desiccator before being weighed. The change of mass after this step was recorded as LOI (Loss On Ignition).

Investigation methods were carefully selected in order to find a printing paste/ pigment mixture with technical characteristics (printing characteristics and fastness) similar to the reference printing paste and proof of its environmental inertness.

Measurements of the rheological behaviour of the printing paste mixtures were performed on an MCR 302 (Anton Paar GmbH, Austria). Tests including the amplitude sweep test, the creep test, the flow behaviour test and the ORO test were performed in order to derive the structural recovery of the samples being investigated. RheoCompass™ V1.20.493 (Anton Paar GmbH, Austria) software was used for data processing. Homogenization of components within the printing paste samples was executed with an ULTRA-TURRAX® homogenizer (IKA®-Werke GmbH & Co. KG, Germany) for 3 min at 600 rpm.

Analysis of the environmental impact of the pigment mixed into the printing paste was performed based on the results of the leaching test. In the textile printing process, pigment particles, which potentially contain toxic elements, were mixed into the printing paste, and pigment mixtures were printed on cotton fabric in a rectangular pattern. The leaching test was performed according to SIST EN 1744-3 (2002), using demineralized water as a leaching solution. The ratio of the dry mass of printed samples to the volume of leaching solution was 1:10. Samples were prepared in three different ways: (1) the textile was printed with printing paste (PrP), (2) the textile was printed with printing paste and pigment (PrP&P), (3) the textile was printed with printing paste and pigment, then after the fixation process it was subjected to the water- and oil-

repellent finishing process (PrP&P&F). The application of the water- and oil-repellent finishing was considered necessary to minimise moisture uptake and soiling of the protective clothing. Chemical analysis of the leachate was performed according to SIST EN ISO 17294-2 (2017). The total content of elements, including As, Ba, Cd, Co, Cr, Cu, Hg, Mo, Ni, Pb, Sb, Se, and Zn, was determined by inductively coupled plasma mass spectrometry (ICP-MS). The Cl^- and SO_4^{2-} content in the leachates was determined by UV/Vis spectrophotometry according to ISO 15923-1:2013. The content of F^- in the leachates was determined according to the SPADNS method (Macherey Nagel, cat. no. 918 142).

Colour fastness to artificial light, to washing (40 °C) and to dry and wet rubbing were tested in order to assess the compatibility of the pigment with the printing paste and to determine the suitability of the pigment for the purpose of printing. Tests were conducted according to ISO 105-B02, SIST EN ISO 20105-C01 and SIST EN ISO 105-X12, respectively. Fastness properties were tested on the PrintPerfekt Lac 110 Neu printing paste with the addition of 5 wt.% of pigment (PP5bV).

3 RESULTS AND DISCUSSION

3.1 Material characterization

Scanning electron microscope images of the ground pigment particles revealed that the particle size distribution (PSD) was in the range of nano- and micro-sizes, and some aggregates were also found. The PSD showed that all particles were smaller than 35 μm. The median particle sizes D_{90}, D_{50} and D_{10}, based on a volume distribution, were determined to be 12.49 μm, 1.48 μm and 0.34 μm, respectively. The PSD range of the investigated pigment was thus more than 30 μm, which, according to the criteria that determine the color of the pigment, is a wide distribution given the impact it has on the colour intensity of the pigment and all subsequent applications. According to Jones [14], decreasing the PSD range increases the purity of the colour and its brilliance.

Figure 1 shows XRD patterns obtained at the various annealing temperatures. It confirms that the natural pigment is of high purity under standard conditions, and that it is composed of the mineral goethite. The XRD patterns in Figure 1 show that goethite is stable up to approximately 200 °C. By increasing the temperature beyond 250°C peaks representative of hematite started to become distinguishable from the background, confirming the thermally-induced phase transformation [15].

The BET specific surface area (SSA_{BET}) results are consistent with the XRD results, showing an increase in the SSA_{BET} from 119,2 m^2/g to the maximum of 151,6 m^2/g when the temperature increased to 250 °C, which is ascribed to the formation of slit-shaped micropores as a result of the dehydroxylation of goethite and the formation of hematite. A substantial decrease to 47,7 m^2/g is then evident at 550 °C, followed by a continuous reduction in the specific surface area as annealing temperature increased, as internal and interparticle sintering occurred [16,17].
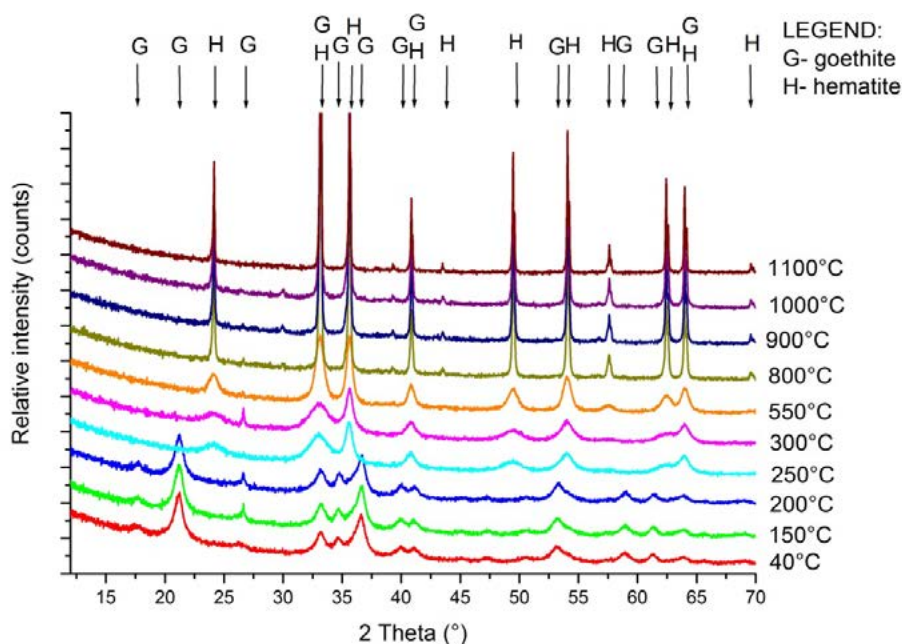

Figure 1: XRD patterns of an investigated sample of pigment annealed at different temperatures

The chemical composition of the pigment sample is presented in Table 2. The contents of Fe_2O_3, SiO_2 and Al_2O_3 were 72.32 %, 2.27 % and 1.20 %, respectively. The presence of oxides other than Fe_2O_3 shows the presence of impurities coming from the surrounding base rock. The loss on ignition (LOI_{1000}) was 22.47 %, indicating the thermal decomposition of phases present in the sample. The LOI_{1000} results mostly from dehydration, i.e., the loss of water adsorbed on the outer and inner surfaces of minerals, and dehydroxylation, i.e., the loss of chemically bound water [16]. The XRD data confirms that the dehydroxylation of goethite occurred efficiently at temperatures higher than 550 °C, as shown in Figure 1.

Table 2: Chemical composition of the natural pigment

Parameter	Content (wt.%)	Std. Dev. (wt.%)
Na_2O	0.59	0.036
MgO	0.27	0.017
Al_2O_3	1.20	0.060
SiO_2	2.27	0.080
K_2O	0.14	0.008
CaO	0.09	0.006
MnO	0.10	0.006
Fe_2O_3	72.32	0.150
ZnO	0.29	0.019
Other oxides*	0.27	0
LOI	22.47	0.022

*total content of other oxides in traces

3.2 Textile printing pastes

The results of particle size analysis of the micronized natural pigment sample showed a PSD range of between 0.0860 µm and 7.78 µm. The median particle sizes D_{90}, D_{50} and D_{10}, based on a volume distribution, were determined to be 1.74 µm, 0.5 µm and 0.19 µm, respectively. The PSD range of the pigment particles following micronization is appropriate for textile printing [13].

As there is a lack of comprehensive work about screen printing [18], further research is needed to define the appropriate mix of printing paste, pigment, and potentially water to achieve a printing paste with acceptable printability, as determined from its rheological response. The rheological properties measured, including loss (G') and storage (G'') modulus, the loss factor ($\tan\delta$), the limit of the viscoelastic region (γ_L), flow point (τ_f), static (τ_{sy}) and dynamic (τ_{dy}) yield stress and apparent viscosity (η), are presented in Table 3. In the PP-based printing paste samples all four materials behave as a viscoelastic solid, as G' > G'', within the limit of the viscoelastic (LVE) region. The loss factor was $\tan\delta < 1$, of the order 2×10^{-1}, for all the samples examined, meaning that their structure resembled that of a gel in the LVE region. The flow point was similar for samples PP and PP5bV, at approximately 60 Pa, while it decreased by a factor of three in the PP5V10 sample. The addition of water substantially decreased the flow point (Table 3) and the structural strength of samples PP5V5 and PP5V10 in comparison to the reference sample PP, which can be seen from the decreasing values of G' and G''. The data in Table 3 also show that the viscous behaviour of the PP and PP5bV samples is similar, with only a slight reduction in values of dynamic yield stress and apparent viscosity at shear rates of 1, 10 and 50 s^{-1}. This reveals that, up to 5 wt.%, the addition of pigment does not significantly influence the flowability properties in comparison to the reference sample PP. In contrast, when water is added, as in the PP-based printing paste samples PP5V5 and PP5V10, the dynamic yield stress and apparent viscosity are substantially altered.

Table 3: Rheological parameters of the PP-based printing paste series

Sample ID	Storage modulus within the LVE, G' (Pa)	Loss modulus within the LVE, G" (Pa)	Loss factor, tanδ (-)	Limit of the viscoelastic region, γ_L (%)	Flow point, τ_f (Pa)	Static yield stress, τ_{sy} (Pa)	Dynamic yield stress, τ_{dy} (Pa)	Apparent viscosity, η, at shear rate 1 s^{-1} (Pa.s)	Apparent viscosity, η, at shear rate 10 s^{-1} (Pa.s)	Apparent viscosity, η, at shear rate 50 s^{-1} (Pa.s)
PP	2318	444	0.192	0.002	62	21.45	38.72	73.4	14.70	5.72
PP5bV	2350	561	0.239	0.002	60	19.21	41.77	78.5	15.30	4.53
PP5V5	1380	343	0.249	0.002	43	13.78	27.78	51.87	10.09	3.80
PP5V10	523	136	0.260	0.003	17	5.89	12.04	23.38	4.78	1.88

Additionally, tests of structural recovery showed that the structure of the PP-based printing paste samples recovers quickly in all four samples under investigation, after approximately 12 to 18 s. Samples with the addition of water, i.e. PP5V5 and PP5V10, tended to recover faster than the reference printing paste PP or the printing paste with only the addition of pigment, PP5bV, but the 6 s difference is supposed to be insignificant in real applications.

Results for the EC series of printing paste samples showed that a more substantial amount of pigment is needed in order to achieve the colour required, as the EC printing paste covers the pigment colour more effectively than the PP printing paste (Figure 2). Furthermore, significant dilution of the EC printing paste was needed for a comparable rheological response to be achieved in samples incorporating the pigment, which was shown to compromise the properties of the EC printing paste. The PP printing paste performed better, both in terms of colour and rheological behaviour, especially in the case where only 5 wt.% of pigment was added (sample PP5bV).

Figure 2: Photograph of samples, printed with printing paste Printperfekt Lac 110 Neu (5 wt.% of pigment) – PP5bV, and Elastil Coprente FG (20 wt.% of pigment) – EC20bV, showing the differences in colour and quality of the print

Printed textiles are known for their potentially hazardous effects during both production and use. A study of a total of 52 samples of textiles found the toxicity of printed cotton and cotton/linen textiles to be significantly higher than those that were unprinted [19]. The results of the leaching test show that the values of most of the heavy metals were lower in the PrP&P sample compared to the PrP sample. The only two parameters where values of the leachate were higher from the PrP&P sample compared to the PrP sample were Ba and sulphate. With the finishing process, most of the values of the PrP&P leachate decreased, the exceptions being Ni, Zn and sulphate.

Taking into consideration the legislation regarding the discharge of waste water into waters with a drainage area smaller than 10 km^2 [20], the most critical parameters in the leachate of all three samples were the concentrations of As, Co, fluoride and sulphate. As exceeded the limit value in the PrP leachate; Co exceeded the limit value in both the PrP and PrP&P leachate, but the value decreased to a satisfactory concentration (i.e. below the limit) when the finishing process was applied; fluoride exceeded the limit value in all three samples; and sulphate is at the legislation limit in the PP&P leachate and exceeds the limit in the PrP&P&F leachate. For situations where the drainage area is larger than 10 km^2, concentrations of all the elements fall far below their respective limit values.

Table 4: Colour fastness properties of the samples printed with PP printing paste, with and without water- and oil-repellent finishing

Analysis	Visual assessment			
	Grey scale fastness grade of the printed sample (no finishing)		Grey scale fastness grade of the printed sample with finishing	
Colour fastness to artificial light	5		5	
Colour fastness to washing	5		5	
Colour fastness to rubbing	dry	wet	dry	wet
	4	1	4	4

Colour fastness to artificial light and washing was excellent in both samples, with or without the water- and oil-repellent finishing (Table 4). Colour fastness to dry rubbing was good in both samples, but in the case of the untreated samples (without finishing) the colour fastness to wet rubbing is poor. A possible reason for the inadequate wet rubbing properties is the concentration of pigment added as dry matter. Adding pigment to the printing paste in a concentration of 5 % could be exceeding the ability of the binder in the printing paste to crosslink on the textile. According to other authors [21,22], this property is most compromised when subjected to wet rubbing. The process of finishing significantly improved the colour fastness of the samples to rubbing under wet conditions.

4   CONCLUSIONS

The potential for mine mud from the Sitarjevec mine to be used as a pigment for textile printing was proven. After the characterization of mine mud, both natural and annealed, the research focused on the natural pigment. It was shown that a small quantity of pigment (5 % / printing paste), creating a print similar in colour to the colour sensation of the mine mud in its original whereabouts, mixed into the appropriate printing paste has an insignificant effect on the rheological properties of the mix. The printing paste sample PP5bV, which was composed of PP and 5wt.% pigment, without the addition of water, behaves similarly to the reference printing binder PP in terms of the rheological parameters measured. Based on the rheological examinations performed soon after mixing, this mixture composition should, therefore, achieve satisfactory results during the printing process.

The leaching results show that elements in the pigment, crosslinked in the printing paste, do not present any additional environmental hazard. Not only are the pigment and printing paste well crosslinked, in most cases the concentrations of elements in the leachate from the PrP&P sample are even lower than in the leachate from the PrP sample. .

The fastness properties of the printed samples are good, especially in those that had been treated with the water- and oil-repellent finishing.

The results of this study represent a basis for further research into the possibilities of printing using pigment from the Sitarjevec mine. More detailed research regarding the rheological behaviour is expected, including the addition of some auxiliaries, with additional fastness tests.

ACKNOWLEDGMENTS

REFERENCES

[1] Zarnik, B. et al.: Predstavitev rudnika Sitarjevec, Rudnik Sitarjevec – odkriti zaklad, Proceedings of 1st Expert symposium on Sitarjevec Mine and meeting of mining towns, Zarnik, B. et al. (Eds.), 44-46, ISBN 978-961-94521-0-3, Litija, september 2018, Občina Litija, Litija, (2018).

[2] Jeršek, M. et al.: Vpliv bakterij na rast limonitnih kapnikov v rudniku Sitarjevec pri Litiji, Rudnik Sitarjevec - odkriti zaklad, Proceedings of 1st Expert symposium on Sitarjevec Mine and meeting of mining towns, Zarnik, B. et al. (Eds.), 22-25, ISBN 978-961-94521-0-3, Litija, september 2018, Občina Litija, Litija, (2018).

[3] Golež, M. et al.: Znanstveno-umetniški potenciali rudnika Sitarjevec, Rudnik Sitarjevec – odkriti zaklad, Proceedings of 1st Expert symposium on Sitarjevec Mine and meeting of mining towns, Zarnik, B. et al. (Eds.), 44-46, ISBN 978-961-94521-0-3, Litija, september 2018, Občina Litija, Litija, (2018).

[4] Herlec, U. et al.: Ogroženost področja rudnika Sitarjevec zaradi možnosti izbruhov ujete rudniške vode, Book of abstracts of 2. Slovenian geological congress, Režun, B. et al. (Eds.), 140, ISBN 961-90141-5-4, Idrija, september 2006, Rudnik živega srebra v zapiranju, Idrija, (2006).

[5] Kirby, C.S.; Decker, S.M. & Macander, N.K.: Comparison of color, chemical and mineralogical compositions of mine drainage sediments to pigment, *Environmental Geology*, 37 (1999) 3, 243-254. DOI: 10.1007/s002540050382

[6] Cornell, R.M. & Schwertmann, U.: *The Iron Oxides: Structure, Properties, Reactions, Occurences And Uses*, Wiley-VCH Verlag GmbH & Co. KGaA, 2003, Print ISBN 9783527302741, Online ISBN 9783527602094, |DOI:10.1002/3527602097

[7] Gialanella, S. et al.: On the goethite to hematite phase transformation, *Journal of Thermal Analysis and Calorimetry*, 102 (2010) 3, 867–873. DOI: 10.1007/s10973-010-0756-2

[8] Cavallo, G. & Zorzin, R.: Preliminary data on the yellow ochers at the mine of Via Tirapelle in Verona (Italy), *X-Ray Spectrometry*, 37 (2008) 4, 395-398. DOI: 10.1002/xrs.1018

[9] Frost, R.L.; Ding, Z. & Ruan, H.D.: Thermal analysis of goethite, *Journal of Thermal Analysis and Calorimetry*, 71 (2003) 783–797. DOI: 10.1023/A:1023365923961

[10] Pereira, O.C. & Bernardin, A.M.: Ceramic colorant from untreated iron ore residue, *Journal of Hazardous Materials*, 233-234 (2012) 103-111. DOI: 10.1016/j.jhazmat.2012.06.057

[11] Gil, M. et al.: Limewashing paintings in Alentejo urban heritage: pigment characterization and differentiation by WDXRF and XRD. *Applied Physics A*, 90 (2008) 1, 49–54. DOI: 10.1007/s00339-007-4252-x

[12] Onar Camlibel, N. et al.: Antibacterial, UV protection, flame retardancy and coloration properties of cotton fabrics coated with polyacrylate polymer containing various iron ores, *The Journal of The Textile Institute*, 109 (2018) 11, 1424-1433. DOI: 10.1080/00405000.2018.1423937

[13] Mikuž, M. et al.: *Primerjalna študija parametrov tiskanja in dezeniranja v procesu brizgalnega in filmskega tiska tekstilij s pigmentnimi barvili*, Dissertation, Ljubljana, (2006).

[14] Jones, T.S.: *Iron Oxide Pigments (in Two Parts): 1.Fine-particle iron oxides for pigment, electronic, and chemical use*, United States Department of the Interior, Bureau of Mines, ISSN 1066-5544, Michigan (1978).

[15] Walter, D.; Buxbaum, G. & Laqua, W.: The Mechanism of the Thermal Transformation From Goethite to Hematite, *Journal of Thermal Analysis and Calorimetry*, 63 (2001) 733–748.

[16] Liu, H. et al.: Thermal treatment of natural goethite: Thermal transformation and physical properties, *Thermochimica Acta*, 568 (2013) 115-121. ISSN 0040-6031. DOI: 10.1016/j.tca.2013.06.027

[17] Saito, G. et al.: Optimization of the Dehydration Temperature of Goethite to Control Pore Morphology, *ISIJ International*, 56 (2016) 9, 1598–1605.

[18] Forte Tavčer, P. et al.: Optimiziranje tiskanja tkanin z uporabo statističnega programa za načrtovanje poskusov, *Tekstilec*, 52 (2009) 1–3, 7–23.

[19] Dave, G. & Aspegren, P.: Comparative toxicity of leachates from 52 textiles to Daphnia magna, *Ecotoxicology and Environmental Safety*, 73 (2010) 7, 1629-1632. ISSN 0147-6513. DOI: 10.1016/j.ecoenv.2010.06.010

[20] Official Gazette of R.S.: *Decree on the Emission of Substances and Heat when Discharging Waste Water into Waters and the Public Sewage System*, Nos. 64/12, 64/14 and 98/15 (2012).

[21] Forte Tavčer, P.; Ahtik, J. & Godec, M.: Lastnosti fosforescenčnih pigmentov, tiskanih na tkanino, *Tekstilec*, 59 (2016) 3, 226-236. DOI: 10.14502/Tekstilec2016.59.226-236.

[22] Bračko, S. et al.: Impregnation dyeing of cotton/polyester spun yarn mixture with photoluminescent pigments, *Tekstil ve Konfeksiyon*, 21 (2011) 1, 58–64. ISSN 1300-3356.

14

Tvrtko Renić, Ivan Hafner, Tomislav Kišiček

Ductility of hybrid FRP – steel reinforced concrete sections

DUCTILITY OF HYBRID FRP – STEEL REINFORCED CONCRETE SECTIONS

Tvrtko Renić[1], Ivan Hafner[2] and Tomislav Kišiček[3]

[1] University of Zagreb Faculty of Civil Engineering, Zagreb, Croatia
Fra Andrije Kačića Miošića 26, 10 000 Zagreb
e-mail: tvrtko.renic@grad.unizg.hr

[2] University of Zagreb Faculty of Civil Engineering, Zagreb, Croatia
Fra Andrije Kačića Miošića 26, 10 000 Zagreb
e-mail: ivan.hafner@grad.unizg.hr

[3] University of Zagreb Faculty of Civil Engineering, Zagreb, Croatia
Fra Andrije Kačića Miošića 26, 10 000 Zagreb
e-mail: tomislav.kisicek@grad.unizg.hr

SUMMARY: Reinforced concrete is a widely used structural material. Usually, steel is the material used for reinforcing elements. Most important problem with using steel is the fact that it is susceptible to corrosion, which significantly affects durability of a structure. Fiber reinforced polymer (FRP) materials can be used instead of steel to avoid corrosion. FRP can either be used for repair of existing, or design of new structures. Different materials can be used to form FRP reinforcement, each having their own modulus of elasticity and strength, but all of them behaving elastically until failure. Usually, stiffness of steel is greater than stiffness of FRP bars, making FRP reinforced elements more sensitive to deflections. Hybrid FRP – steel reinforced members mitigate insufficiencies of both elements reinforced only with steel and elements reinforced only with FRP. Behaviour of hybrid reinforced members depends on not only the amount of each type of reinforcement, but also on its distribution inside a section. Since ductility of sections is important for overall structural response, a more detailed analysis of ductility is given in this paper. Different concrete sections with the same bending moment capacity are analysed. Only rectangular sections under bending moment are considered in this paper. Concrete class, width and height are all kept the same, while the rebar material, amount and layout are varied. Bending moment – curvature diagrams are obtained and compared with each other, as well as section stiffnesses.

KEY WORDS: hybrid reinforcement, reinforced concrete, ductility, bending moment – curvature diagram

1 INTRODUCTION

Concrete structures are traditionally reinforced with steel rebars which tend to corrode and cause durability problems. As a shift occurs from building new to maintaining the existing structures, need for a non-corroding reinforcement arises. Fiber reinforced polymer (FRP) reinforcement doesn't corrode which makes it more durable than steel. This is important not only in the design of new structures, but also for the repair of existing ones. Usually rebars are used in new structures, while FRP bands are used in the repair of existing structures, but that doesn't have to be the case. In this paper only rebars are considered.

One additional advantage of non-metallic reinforcement is the fact that it's nonmagnetic which can be useful in certain situations. FRP has some disadvantages as well, most notably the fact that it is a nonductile material that has a lower modulus of elasticity than steel. This leads to much larger deflections and less shear strength than beams reinforced with steel for similar cross sections [1]. Due to large expected deflections, they may govern design requiring a larger amount of reinforcement, than is necessary for ULS, to control the deflections. Similar problem arises regarding the crack width which is also larger for FRP reinforced elements. Additional problem is the limited availability of curved or shaped reinforcement bars used for shear or torsion reinforcement. Strength of FRP is greater than strength of steel causing significant differences in strength to stiffness ratio between the two materials. This has a significant impact on the distribution of stresses along the section [2]. Design of sections reinforced with FRP is mostly based on the same principles that were developed for steel reinforced sections like the fact that plane sections remain plane and no

significant bond slip takes place. Former depends on the latter since high bond demand around the crack can lead to bond slip and higher deformations.

Flexural capacity of FRP reinforced section can either be controlled by concrete crushing or reinforcement rupture, since no yielding of rebars is possible. Although both types of failure are brittle and generally undesirable, sections are usually designed to achieve failure by concrete crushing rather than rupture of rebars. This is achieved by over-reinforcing a section [2]. If flexural overstrength is achieved, codes of practice do not provide information about the failure mode that will actually occur first and at which load level [2].

To avoid disadvantages of both steel and FRP, hybrid reinforcement may be implemented. Behaviour of hybrid reinforced elements is somewhere between pure FRP and pure steel elements. Instead of separate steel and FRP rebars, a combined hybrid rebar may be used [3], but it is less common. Hybrid sections can be achieved with combining different types of FRP [4]. Although behaviour of members reinforced with FRP has been researched extensively [1], [2], [4] – [12], limited theoretical and experimental data exists on hybrid FRP-steel elements [13] – [21]. Using hybrid systems ensures higher ductility than using pure FRP reinforcement, but it's unclear how to ensure ductility comparable to that of conventional steel reinforced elements [18]. To avoid corrosion obviously location of each bar needs to be considered. Corner steel bars should be replaced with FRP bars to ensure durability [19]. Ratio of steel to FRP reinforcement, as well as location and distribution of rebars influences the behaviour of a hybrid section. Because of that, an analysis was carried out in this paper to determine ductility of a section with different arrangements of steel and FRP rebars and their influence on stiffness. Although some research exists on the topic [15], [16], [22], it only covers some specific situations so further analysis needs to be done.

2   SECTION BEHAVIOUR AND MODELLING ASSUMPTIONS

Geometry of a rectangular section and strains, as well as symbols used are shown in figure 1.
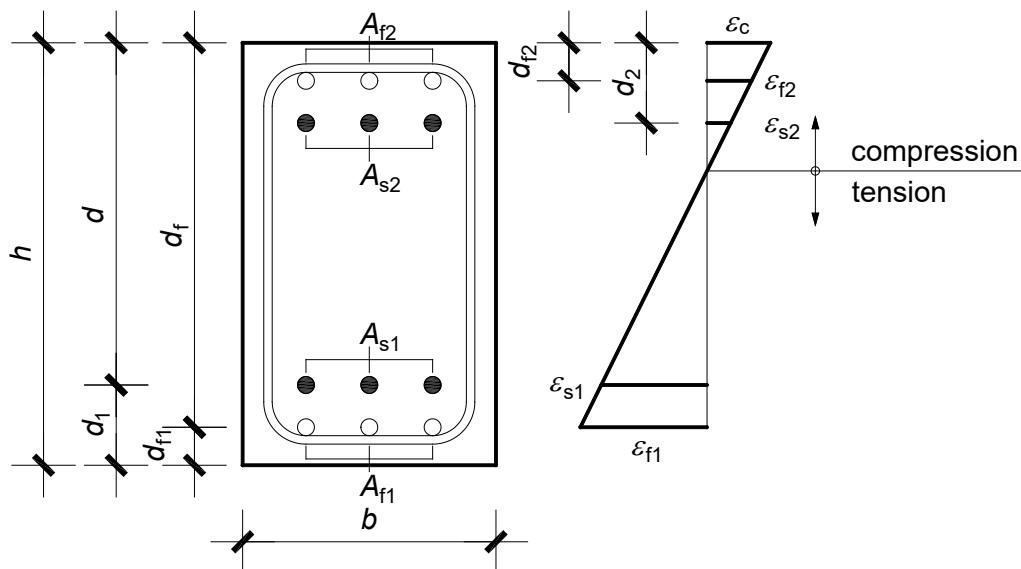
Figure 1: Section geometry and strains

Several modes of failure of hybrid section under bending can occur:

1) concrete crushing before the steel yields and FRP ruptures   ($\varepsilon_c = \varepsilon_{cu2}$; $\varepsilon_{s1} < \varepsilon_{yk}$; $\varepsilon_{f1} < \varepsilon_{fu}$)
2) concrete crushing after the steel yields, but before FRP ruptures   ($\varepsilon_c = \varepsilon_{cu2}$; $\varepsilon_{s1} \geq \varepsilon_{yk}$; $\varepsilon_{f1} < \varepsilon_{fu}$)
3) Steel ruptures followed by concrete crushing before the FRP ruptures   ($\varepsilon_c = \varepsilon_{cu2}$; $\varepsilon_{s1} = \varepsilon_{su}$; $\varepsilon_{f1} < \varepsilon_{fu}$)
4) Steel ruptures followed by FRP rupture before the concrete crushing   ($\varepsilon_c < \varepsilon_{cu2}$; $\varepsilon_{s1} = \varepsilon_{su}$; $\varepsilon_{f1} = \varepsilon_{fu}$)
5) FRP ruptures followed by concrete crushing before the steel yields   ($\varepsilon_c = \varepsilon_{cu2}$; $\varepsilon_{s1} < \varepsilon_{yk}$; $\varepsilon_{f1} = \varepsilon_{fu}$)
6) FRP ruptures followed by concrete crushing before the steel ruptures   ($\varepsilon_c = \varepsilon_{cu2}$; $\varepsilon_{s1} < \varepsilon_{su}$; $\varepsilon_{f1} = \varepsilon_{fu}$)
7) FRP ruptures followed by steel rupture before the concrete crushing   ($\varepsilon_c < \varepsilon_{cu2}$; $\varepsilon_{s1} = \varepsilon_{su}$; $\varepsilon_{f1} = \varepsilon_{fu}$)
8) FRP ruptures at the same time as concrete crushing before the steel ruptures   ($\varepsilon_c = \varepsilon_{cu2}$; $\varepsilon_{s1} < \varepsilon_{su}$; $\varepsilon_{f1} = \varepsilon_{fu}$)

Where:
ε_{cu2}	ultimate concrete compressive strain
ε_{yk}	characteristic yield strain of steel reinforcement
ε_{su}	ultimate steel strain at rupture
ε_{fu}	ultimate FRP strain at rupture

Failure number 8 is called a balanced failure for hybrid elements where crushing of concrete and FRP rupture occur at the same time [16], [17]. While some other types of failure may be possible, they are less probable. Out of the 8 presented here, failure types 1 and 5 seem the least probable. Failure number 2 seems like the most acceptable design choice [16]. This is also proposed in [6]. To achieve that type of failure, based on the analysis made in [16] limits of the amount of FRP reinforcement were given. Additional research should be made, and equations revised if they were to be used in the codes. Ultimate strains and yield strain depend on the material used. Some analytical [16] and numerical [22] procedures were proposed recently for assessment of hybrid element behaviour, but variation of reinforcement location along the height was not considered in either paper. Influence of axial force, as well as the distribution of reinforcement and their different arrangement were not considered in either [16] or [22]. Different arrangements of reinforcement along the height of a section and axial force were considered in [15], but only numerical procedure with no equations was given. Using nonlinear time history analysis, they determined hysteresis loops and compared different reinforcement distributions. It was shown that walls with steel reinforcement near the ends and FRP reinforcement near the middle of the wall were as good at dissipating energy as their conventional steel reinforced counterparts but had a greater self-centring behaviour. This may lead to the development of improved seismic resisting systems. The question remains as how to implement this into the codes, i.e. how to ensure that hybrid sections have the required ductility since rebar arrangement and the ratio of steel to FRP reinforcement can significantly influence the behaviour.

Bending moment – curvature diagrams describe the behaviour of a concrete section. It is defined by a few characteristic points:

- Forming of a crack $(M_{cr} – 1/r_{cr})$
- Yielding of steel $(M_y – 1/r_y)$
- Rupture of either steel of FRP $(M_r – 1/r_r)$
- Cross section failure $(M_u – 1/r_u)$

Depending on the type of failure discussed before, some of these points may not exist for a given cross section. Only a brief theoretical overview is presented here, detailed background of defining a bending moment – curvature diagram for pure steel reinforced sections can be found in [23]. Internal forces, stresses and strains at different characteristic points are shown in figure 2. The failure shown is failure number 6 because all the characteristic points are visible.
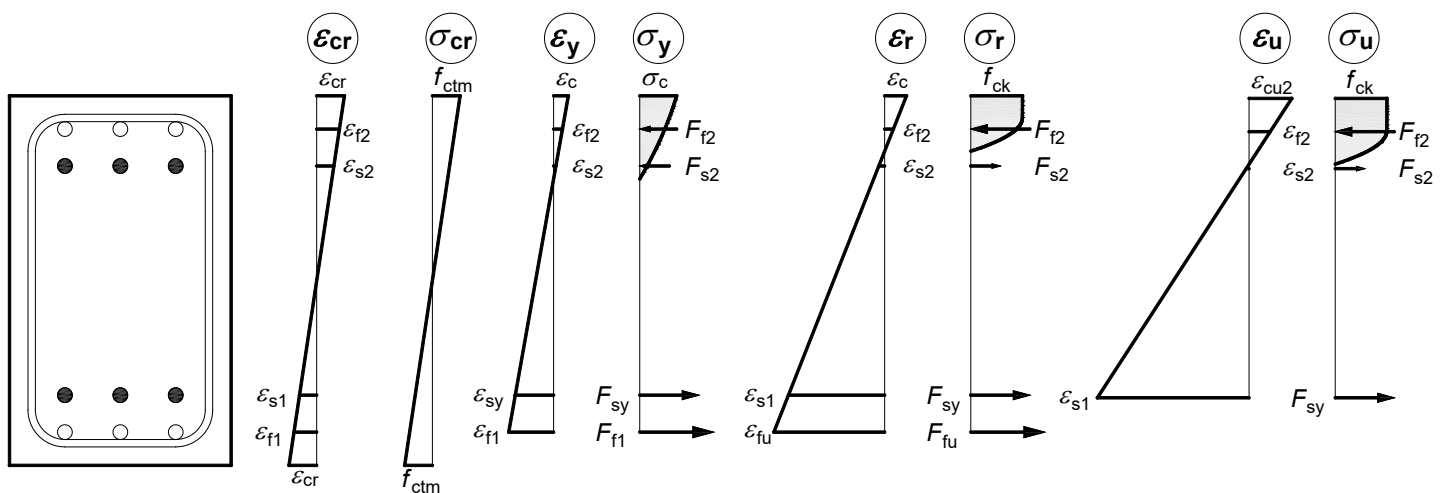
Figure 2: Strains and internal forces for specific points of bending moment – curvature diagram

In figure 2 f_{ctm} is mean tensile strength of concrete, F are forces and f_{ck} is characteristic compressive strength of concrete. In this specific example, steel at the top of the section changed signs between the point of lower steel yielding and lower FRP rupturing. Depending on the geometry of a section, amount of reinforcement, their ratio and location along the location of the neutral axis changes for each of the specific points and with it the sign of some forces might change.

Bending moment – curvature diagram for a situation shown in figure 2 is drawn in figure 3.
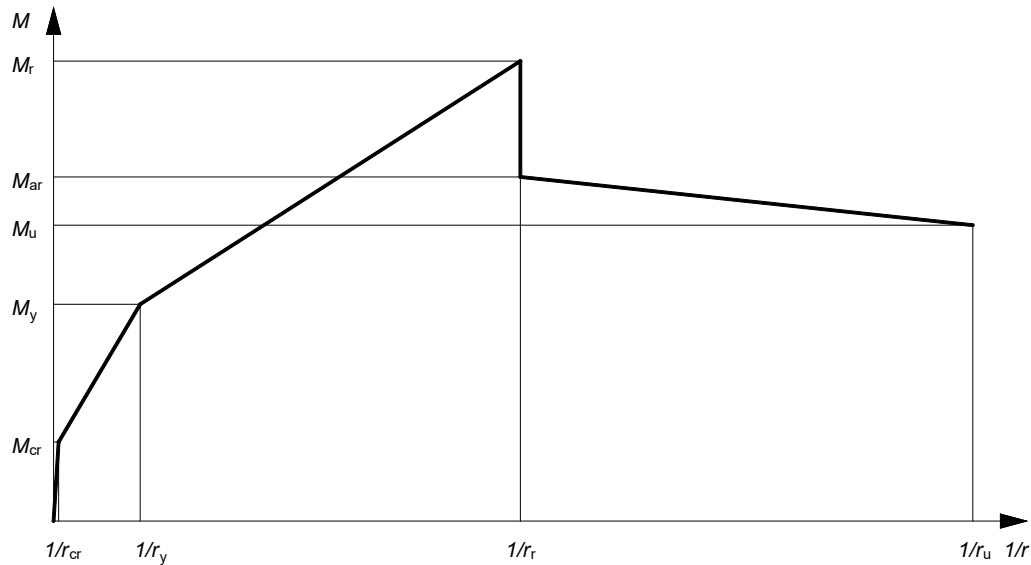
Figure 3. Bending moment – curvature diagram for failure mode 6

Rupture of FRP causes a jump in diagram as can be seen in figure 3. Bending moment before rupture is denoted as M_r, while bending moment after rupture is denoted M_{ar}. If no steel existed, failure would occur at curvature $1/r_r$ (although numerically, this point would have a slightly different value without steel) so it can clearly be seen from figure 3 that adding steel to an FRP section increases the curvature capacity of a section. It can also be seen from the figure 2 that the location of reinforcement will influence the behaviour of the section because forces in rebars depend on their vertical position inside a section. Ductility changes with location of each reinforcement, and so does the stiffness of the section. Location of rebars was varied and ductility calculated as $\mu_\varphi = (1/r_u) / (1/r_y)$. Stiffness variation was also calculated for different rebar locations.

2.1 Modelling procedure

Cross section considered in this paper is rectangular with parameters shown in figure 1. Variation of reinforcement location along the height is considered by varying the distances d_1, d_2, d_{f1} and d_{f2}. Only one row of reinforcement is considered in tension and one in compression for both steel and FRP. If more rows are required, for calculation they may be substituted with one row which gives the same resultant tensile force. Steel reinforcement can be either above or below the FRP. Only rectangular cross sections are considered and positive bending moment (bottom part of the section is in tension). There is no difference in the way moment – curvature diagram is calculated when negative moment acts on a section because the section is rectangular. Procedure for determining bending moment – curvature diagrams, as presented earlier, is adopted from [23], but some changes were made. Procedures for considering axial force, T shape of sections, as well as multiple rows of reinforcement of different characteristics were added to an already existing program. Although some of these additions were not used in this paper, they might prove themselves useful in further research. Material properties used in this paper are presented in table 1. Concrete and steel properties were taken from Eurocode HRN EN 1992-1-1 [24] and FRP properties were taken from *fib* bulletin 40 [25]. The only modification made in this paper is that strength is calculated from modulus of elasticity and ultimate strains, instead of being taken directly from [25]. The reason is that values given there do not match exactly. Concrete is modelled with parabola-rectangle diagram and steel with bilinear elastic-perfectly plastic diagram in accordance with HRN EN 1992-1-1 [24]. FRP is modelled as linear until rupture. Plane sections are assumed to remain plane after bending and no slippage of any reinforcement is considered. Tension strength of concrete is disregarded. Only flexural behaviour is considered, and it is assumed that no other type of failure will occur (such as shear failure). Influence of stirrups on the confinement of concrete is not considered. It is considered in this paper that when the concrete crushes, failure has occurred. This assumption, as well as other assumptions made in this paper are usually considered in design of pure steel and pure FRP reinforced sections. Influence of axial force on ductility was not considered in this paper.

Table 1. Material properties used in this paper

Material	Concrete C25/30	Steel B500B	Carbon FRP (high strength)	E-glass FRP
characteristic strength [N/mm^2]	25	500	2640	1738
Young modulus [N/mm^2]	31476	200000	240000	72400
yield strain [‰]	-	2,5	-	-
ultimate strain [‰]	3,5	50	11	24

3 RESULTS

3.1 Variation of ductility with rebar distribution

Reinforcement ratio was kept constant at $\rho_1 = \rho_2 = \rho_{1f} = \rho_{2f} = 0,005$ where ρ_1 is tension steel reinforcement ratio, ρ_2 is compression steel reinforcement ratio, ρ_{1f} is tension FRP reinforcement ratio, ρ_{2f} is compression FRP reinforcement ratio. All the reinforcement ratios are calculated with larger value of d and d_f. Only tension steel and FRP reinforcement's position was varied, compression steel and FRP were held at constant height, i.e. $d_2/h = 0,1$ and $d_{f2}/h = 0,1$ for simplicity. Width of rectangular section used in calculation was 30 cm and height 50 cm.

Table 2. Calculated ductilities for different positions of tension reinforcement

d_1/h	d_{f1}/h	d_2/h	d_{f2}/h	μ_{CFRP}	μ_{GFRP}
0,1	0,1	0,1	0,1	2,98	4,57
0,2	0,1	0,1	0,1	2,52	3,95
0,3	0,1	0,1	0,1	2,06	3,33
0,4	0,1	0,1	0,1	1,58	2,70
0,5	0,1	0,1	0,1	1,05	2,07
0,1	0,2	0,1	0,1	3,26	4,85
0,2	0,2	0,1	0,1	2,92	4,45
0,3	0,2	0,1	0,1	2,42	3,77
0,4	0,2	0,1	0,1	1,90	3,08
0,5	0,2	0,1	0,1	1,35	2,39
0,1	0,3	0,1	0,1	3,59	5,18
0,2	0,3	0,1	0,1	3,23	4,75
0,3	0,3	0,1	0,1	2,85	4,31
0,4	0,3	0,1	0,1	2,28	3,55
0,5	0,3	0,1	0,1	1,69	2,78
0,1	0,4	0,1	0,1	4,00	5,56
0,2	0,4	0,1	0,1	3,60	5,10
0,3	0,4	0,1	0,1	3,19	4,63
0,4	0,4	0,1	0,1	2,76	4,13
0,5	0,4	0,1	0,1	2,11	3,27
0,1	0,5	0,1	0,1	4,52	6,02
0,2	0,5	0,1	0,1	4,07	5,52
0,3	0,5	0,1	0,1	3,61	5,01
0,4	0,5	0,1	0,1	3,14	4,48
0,5	0,5	0,1	0,1	2,65	3,91

It is clear from the results shown in table 2 that vertical position of reinforcement influences the ductility of a section. This happens because strain in reinforcement changes with the change of its position. Mode of failure could change for different position and ratio of reinforcement which would imply a change of ductility. Second mode of failure (as described in section 2 of this paper) was noted in all cases shown in table 2. Bending moment – curvature diagram for this type of failure is shown in figure 4. It differs from the one in figure 3 because no FRP rupture occurs (there's no jump in the diagram). If for example ρ_{1f} is changed to 0,0003 type of failure changes to 6 and with it the ductility. Comparing the values in table 2 it seems that the ductility increases by moving FRP bars away from tension face, and opposite can be said for steel bars. Moving FRP reinforcement towards a middle of a section seems to always increase ductility, but further research needs to be done to validate this assumption. Further research should be done to better understand the change of ductility.
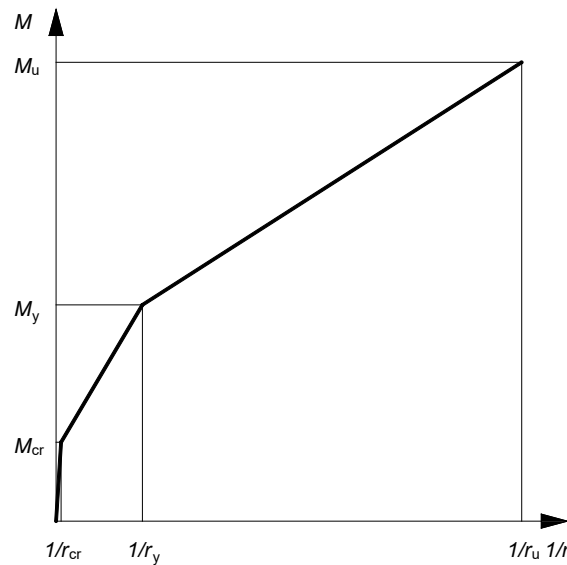

Figure 4. Bending moment – curvature diagram for failure mode 2 occurring in analysis

3.2 Variation of bending stiffness with rebar distribution

In addition to change of ductility, stiffness changes with the location of reinforcement. As stiffness changes with curvature, bending stiffness ($K_b = M/(1/r)$) – curvature ($1/r$) diagram is constructed. Stiffness is calculated as ratio of bending moment and curvature for all of the specific points of a diagram and linearly interpolated in between. For bending moments smaller than cracking moment, stiffness is assumed to be constant. Bending stiffness – curvature diagram is shown in figure 5, but only for the first five inputs in table 2, i.e. only variation of steel along the height was shown, while FRP rebars were held constant at 0,1h distance from tension face. Also, only stiffness of section reinforced with GFRP bars is considered. Both these simplifications were made only for clarity of diagrams presented and same conclusions apply for different locations of rebars and CFRP rebars. In figure 6 steel rebars were held constant at 0,1h distance from tension face and FRP location was varied along the height.

It can be seen from figure 5 that variation of stiffnesses with the change of steel rebar position is significant for the points between cracking of concrete and steel yielding. Ultimate curvature didn't change, while ultimate moment changed slightly.

It can be seen from figure 6 that variation of stiffnesses with the change of FRP rebar position is less significant than with variation of steel. Ultimate curvature changes increases with rebars further away from tension face of the section.

Further analysis should be done to investigate all the influences on stiffness and ductility of hybrid sections. This could lead to better understanding of such a system and could help in code development.
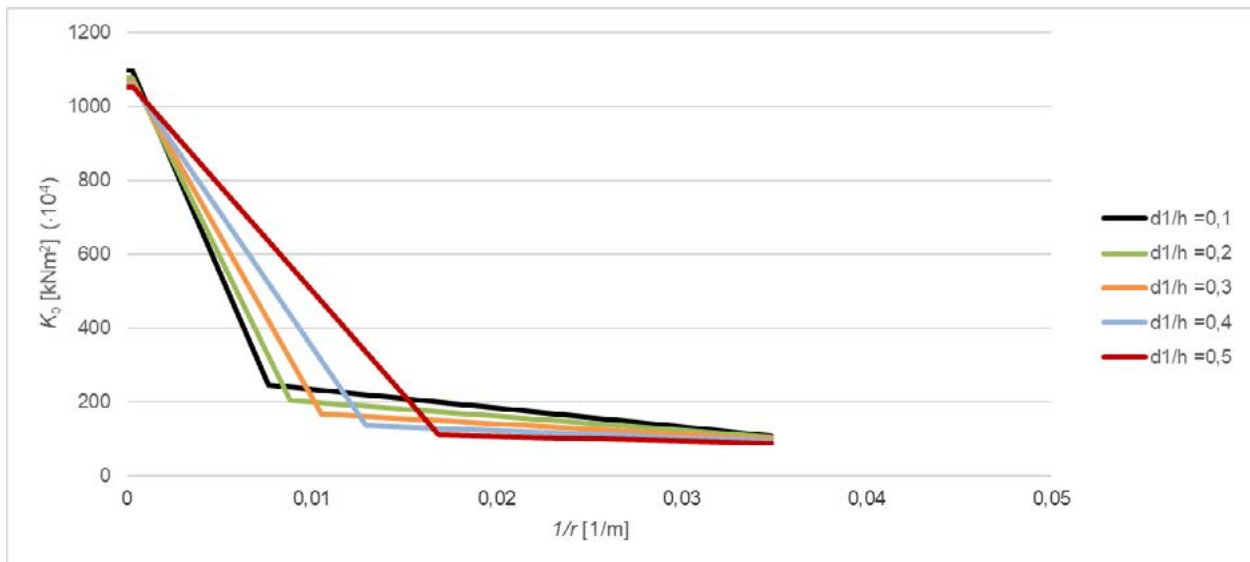
Figure 5. Bending stiffness – curvature diagram with the change of steel location
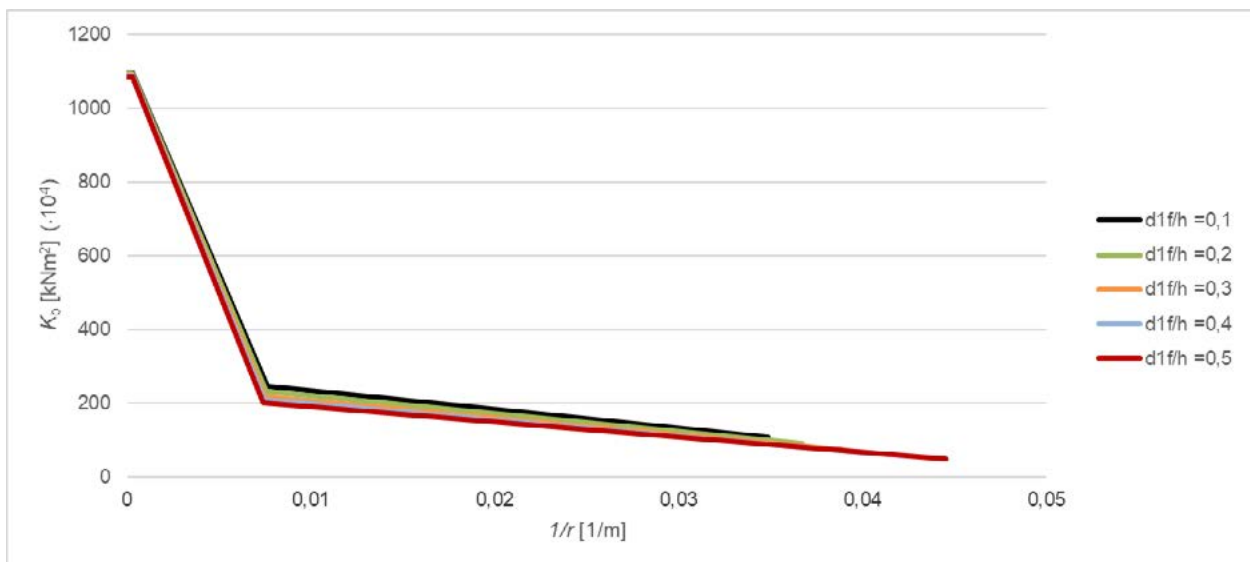

Figure 6. Bending stiffness – curvature diagram with the change of GFRP location

4   CONCLUSION

Hybrid FRP – steel reinforced concrete combines the benefits of both materials and minimises their negatives. Behaviour of hybrid sections needs to be investigated for it to be applicable in the real world. Although much is already known about such elements, further research should be done to understand some of the aspects of behaviour. One of the important aspects is the ductility of a section, another one is stiffness. In this paper ductility and stiffness of hybrid sections with different rebar positioning were analysed. Because failure mode plays an important role in the overall behaviour rebar positioning can prove to be of great importance when determining ductility. It is shown in this paper that the ductility depends on the position of rebars, but further research should be done to fully understand it. Bending stiffness seems to depend more on the location of steel than FRP, but ultimate curvature increases more with the change of FRP location, at least for a specific type of failure.

ACKNOWLEDGMENTS

REFERENCES

[1] Pilakoutas, K. et al.: Design Philosophy Issues of Fiber Reinfored Polymer Reinforced Concrete Structures, *Journal of Composites for Construction*, 6 (2002.) 3, pp. 154–161

[2] Pilakoutas, K. et al.: Design guidelines for FRP reinforced concrete structures, *Structures and Buildings*, 164 (2011.) SB4, pp. 255–263

[3] Harris, H.G. et al.: New Ductile Hybrid FRP Reinforcing Bar for Concrete Structures, *Journal of Composites for Construction*, 2 (1998.) 1, pp. 28–37

[4] Wang, X.; Wu, Z.: Integrated high-performance thousand-metre scale cable-stayed bridge with hybrid FRP cables, *Composites: Part B*, 41 (2010.), pp. 166–175

[5] Ashour, A.F.; Habeeb, M.N.: Continuous concrete beams reinforced with CFRP bars, *Structures and Buildings*, 161 (2008.) SB6, pp. 349–357

[6] Uddin, N. (Ed.): *Developments in fiber-reinforced polymer (FRP) composites for civil engineering*, Woodhead Publishing Limited, 978-0-85709-895-5, Cambridge, UK, (2013.)

[7] Barris, C. et al.: An experimental study of the flexural behaviour of GFRP RC beams and comparison with prediction models, *Composite Structures*, 91 (2009.), pp. 286–295

[8] Pecce, M. et al.: Experimental Response and Code Models of GFRP RC Beams in Bending, *Journal of Composites for Construction*, 4 (2000.) 4, pp. 182–190

[9] Brown, V.L., Bartholomew, C.L.: FRP reinforcing bars in reinforced concrete members, *Materials Journal*, 90 (1993.) 1, pp. 34–39

[10] Toutanji, H.A., Saafi, M.: Flexural Behavior of Concrete Beams Reinforced with Glass Fiber-Reinforced Polymer (GFRP) Bars, *Structural Journal*, 97 (2000.) 5, pp. 712–719

[11] Benmokrane, B. et al.: Glass fibre reinforced plastic concrete structures rebars for concrete structures, *Construction and Building Materials*, 9 (1995.) 6, pp. 353–364

[12] Ashour, A.F.: Flexural and shear capacities of concrete beams reinforced with GFRP bars, *Construction and Building Materials*, 20 (2006.), pp. 1005–1015.

[13] Aiello, M.A., Ombres, L.: Structural Performances of Concrete Beams with Hybrid (Fiber-Reinforced Polymer-Steel) Reinforcements, *Journal of Composites for Construction*, 6 (2002.) 2, pp. 133–140

[14] Dundar, C. et al.: Prediction of load – deflection behavior of multi-span FRP and steel reinforced concrete beams, *Compostie structures*, 132 (2015.), pp. 680–693

[15] Ghazizadeh, S. et al.: Analytical model for hybrid FRP-steel reinforced shear walls, *Engineering Structures*, 156 (2018.), pp. 556–566

[16] Kara, I.F. et al.: Flexural behavior of hybrid FRP/steel reinforced concrete beams, *Compostie structures*, 129 (2015.), pp. 111–121

[17] Lau, D., Pam, J.H.: Experimental study of hybrid FRP reinforced concrete beams, *Engineering Structures*, 32 (2010.) 12, pp. 3857–3865

[18] Pang, L. et al.: Design Propositions for Hybrid FRP-Steel Reinforced Concrete Beams, 20 (2016.) 4, pp. 1–9

[19] Qu, W. et al.: Flexural Behavior of Concrete Beams Reinforced with Hybrid (GFRP and Steel) Bars, *Journal of Composites for Construction*, 13 (2009.) 5, pp. 350–359

[20] Sun, Z. et al.: Experimental study on the flexural behavior of concrete beams reinforced with bundled hybrid steel/FRP bars, *Engineering Structures*, 197 (2019.), pp. 1–9

[21] Yuan, F. et al.: Experimental study on seismic behaviours of hybrid FRP – steel reinforced ECC – concrete composite columns, *Composites Part B*, 176 (2019.), pp. 1–10

[22] Bencardino, F. et al.: Numerical and analytical modeling of concrete beams with steel , FRP and hybrid FRP-steel reinforcements, *Composite Structures*, 140 (2016.), pp. 53–65

[23] Kišiček, T., Sorić, Z.: Dijagram moment savijanja – zakrivljenost za armiranobetonske gredne elemente, *Građevinar*, 55 (2003.) 4, pp. 207–215

[24] HRN EN 1992-1-1:2013, Eurokod 2: Projektiranje betonskih konstrukcija - Dio 1-1: Opća pravila i pravila za zgrade, Zagreb, (2013.)

[25] fib bulletin 40 : *FRP reinforcement in RC structures*, fib, 978-2-88394-080-2 , Lausanne, (2007.)

15

Sebastijan Robič, Aljoša Šajna, Lucija Hanžič, Alisa Machner, Marie Helene Bjørndal, Klaartje De Weerdt, Yushan Gu, Benoit Bary, Rosamaria Lample

Experimental carbonation study for durability assessment of novel cementitious materials

EXPERIMENTAL CARBONATION STUDY FOR DURABILITY ASSESSMENT OF NOVEL CEMENTITIOUS MATERIALS

S. Robič[1], A. Šajna[1], L. Hanžič[1], A. Machner[2,5], M. H. Bjørndal[2], K. De Weerdt[2], Y. Gu[3], B. Bary[3] and R. Lample[4]

[1] Slovenian National Building and Civil Engineering Institute (ZAG), Department of Materials, Laboratory for Concrete
Dimičeva ulica 12, 1000 Ljubljana
e-mail: sebastijan.robic@zag.si

[2] Norwegian University of Science and Technology (NTNU), Department of Structural Engineering
Richard Birkelandsvei 1A, 7491 Trondheim, Norway
e-mail: klaartje.d.weerdt@ntnu.no

[3] The French Alternative Energies and Atomic Energy Commission (CEA)
Université Paris-Saclay, CEA, Service d'Étude du Comportement des Radionucléides, 91191, Gif-sur-Yvette, France
e-mail: benoit.bary@cea.fr

[4] Acciona Construction
28108 Alcobendas, Spain
e-mail: rosamaria.lample.carreras@acciona.es

[5] Technical University Munich, cbm, Professorship for Mineral Construction Materials
Franz-Langinger-Str. 10, 81245 Munich, Germany
e-mail: alisa.machner@tum.de

SUMMARY: The design process of concrete structures is carried out using standards and guidelines, while the durability predictions of concrete structures is supported only with exposure classes and experience-based requirements. To improve durability predictions of the carbonation resistance of concrete, a numerical model is being developed within the Horizon 2020 project EnDurCrete, coupling the rate of carbonation, and the drying rate. To verify the numerical model, an accelerated carbonation study was carried out. Experiments were conducted on mortars incorporating a novel CEM II/C (S-LL) cement, developed within the EnDurCrete project, and a commercially available reference cement CEM II/A-S. EnDurCrete mortars (EnM) and reference mortars (RefM) were prepared with water-cement ratios of 0.6 and 0.5 (denoted with label extensions -06 and -05). Visual assessments and thermogravimetric analysis (TGA) were used to measure the carbonation rates, which were found to be ~1.0 mm day$^{-0.5}$ in EnM-06 and ~0.6 mm day$^{-0.5}$ in RefM-06, while in EnM-05 and RefM-05 the values were ~0.7 and ~0.2 mm day$^{-0.5}$ respectively. Additionally, TGA shows that the initial portlandite (CH) content is ~1.5 wt% in EnM-06 as opposed to ~3.0 wt% in RefM-06. The difference in the initial CH content in the two hydrated binders might explain the difference in their carbonation rate. During the moisture transport experiments a gravimetric method was used to determine mass changes as specimens underwent drying and resaturation with and without CO_2 present. The drying led to a decrease in mass, but in the presence of CO_2 this mass loss was compensated by the mass gain due to uptake of CO_2 during carbonation. The resaturation experiments indicate an increase in the suction porosity in the carbonated samples compared to the non-carbonated samples.

KEYWORDS: Concrete, absorption of water, carbonation, durability assessment, model verification.

1 INTRODUCTION

The design process of concrete structures relies on standards like Eurocode 2 [1], [2] and guidelines like fib Model Code 2010 [3]. The main focus of the existing codes and guidelines is on mechanical performance, which is analysed with advanced structural design models. In contrast, durability related phenomena are addressed mainly through the selection of the exposure classes and experience-based requirements. As a result, concrete durability forecasts are only crude approximations not supported by the sophisticated modelling of concrete degradation over time. The deterioration and maintenance of concrete are having a significant impact on the public sector budget. Maintenance costs and shutdowns of the infrastructure like tunnels, bridges or power plants are particularly important, due to their impact on the wider community.

When concrete is exposed to an aggressive environment with an increased concentration of carbon dioxide in combination with moisture, concrete undergoes a carbonation process. The main process in carbonation of concrete is the reaction of portlandite ($Ca(OH)_2$, commonly denoted CH) with carbon dioxide (CO_2). The reaction products are calcium carbonate ($CaCO_3$) and water (H_2O). This reaction leads to a net mass gain, as the uptake of CO_2 (44 g/mol) leads to a larger mass increase compared to the release of water (12 g/mol). While the products of this chemical reaction are not detrimental to concrete durability per se, the consumption of CH reduces the pH value of the pore solution, which may lead to the corrosion of reinforcement steel. The rate of carbonation is influenced by the curing conditions of concrete and by the climatic and local conditions to which the concrete is exposed. To accurately predict concrete deterioration, a numerical model for concrete carbonation is being developed within the Horizon 2020 project EnDurCrete.

The European Commission and European Construction Industry push to improve and develop technologies that reduce CO_2 emissions as well as energy and material usage in the cement production processes [4]. Many studies attempt to develop environmentally-friendly concrete by reducing Portland clinker content in cement and substituting it with supplementary cementitious materials [5]–[7]. In this manner, the above-mentioned model development is also linked to another aim of the EnDurCrete project namely, the development of low carbon-footprint binders aligned with the new edition of prEN 197-1 [5]. One such novel cement is CEM II/C (S-LL), a low-clinker cement containing high-value industrial by-products. The use of this cement is aiming to create cost-effective sustainable concrete on one hand and high durability concrete, which can withstand exposure to aggressive environments on the other hand. Details of the novel cement CEM II/C (S-LL) developed by *HeidelbergCement* are summarized by Bolte et al. [6].

This study aims to present experimental results of an accelerated carbonation programme conducted on mortar samples incorporating novel CEM II/C (S-LL) binder developed within the EnDurCrete project and to compare it with the performance of mortars prepared with the commercially available cement CEM II/A-S. The specimens underwent accelerated carbonation in the conditioning chamber with controlled CO_2 concentration, temperature and relative humidity. The carbonation rate was assessed by measuring the depth of carbonation over time visually using a pH indicator, and by thermogravimetric analysis (TGA). The impact of carbonation on moisture transport was evaluated by the gravimetric method on specimens exposed to a specific protocol of drying and wetting.

The results of the accelerated carbonation tests will serve for the validation of the numerical model dealing with carbonation processes in concrete namely, the coupling between saturation degree, water transport and carbonation extent. The numerical model simplifies carbonation to the dissolution of one combined Ca phase, which embodies all Ca-based hydrates in the hydrated cement, and the precipitation of the calcite phase [7]. In addition, the results aim to further the understanding of concrete deterioration in a CO_2-rich environment. Consequently, the design of concrete structures in terms of durability will be improved resulting in reduced maintenance costs and shutdowns of the infrastructure caused by the deterioration of concrete due to carbonation.

2   MATERIALS AND METHODS

Concrete used in tunnels is normally designed with a relatively low water/cement (w/c) ratio and therefore measurable carbonation only occurs during long-term exposure. To accelerate the process, mortar mixes used in this study have a higher w/c ratio than usually applied for such structures, namely 0.50 or 0.60 so that measurable carbonation takes place in a reasonable timeframe. Mortar mix designs developed by *HeidelbergCement* are shown in Table 1. Specimens were labelled EnM for EnDurCrete mortar using novel CEM II/C (S-LL) cement and RefM for reference mortar using CEM II/A-S cement. The label extension -05 or -06 was used to denote w/c ratio. The two cements are composite cements blends containing the same type of components namely clinker (K), ground granulated blast furnace slag (S) and limestone filler (LL), however, in different ratios [6] as shown in Table 1.

Mortar prisms measuring 10 cm × 10 cm × 40 cm were cast for this study. The prisms were cured in a humidity chamber with relative humidity (RH) > 95 % at 20 ± 2 ºC for 21 days as per EN 12390-2 [8]. Next, the prisms were wrapped in plastic foil and transported from the casting to the testing facilities where they were cured at 20 ºC up to 76 days. The moisture state of the specimens was checked at this stage using the method described in [9], [10] to confirm that the specimens did not dry out. After curing, the prisms were cut laterally either into thick blocks with dimensions 10 cm × 10 cm × 7 cm or into thin plates with dimensions 10 cm × 10 cm × 2 cm. The thick blocks were used for the carbonation rate measurements, while the thin plates were used for moisture transport experiments.

Table 1: Mortar mix design, stating the mass of components needed for 1 m³ of mortar. EnM and RefM stand for mortar made with EnDurCrete and reference cement respectively, while extensions -06 and -05 denote w/c ratios. The composition of cement is given as wt% of clinker (K), ground granulated blast-furnace slag (S) and limestone (LL). Mortar mix designs and types of cement were provided by *HeidelbergCement.*

Components		K (%)	S (%)	LL (%)	Mass of component per 1 m³ of mortar [kg]			
					EnM-06	**RefM-06**	**EnM-05**	**RefM-05**
Cement	**CEM II/C (S-LL)**	50	40	10	487	/	552	/
	CEM II/A-S	83	13	4	/	487	/	552
Aggregate	**Sand 0/4**				1524	1524	1498	1496
Admixture	**Superplasticizer**				1.5	1.8	3.2	3.8
Water					292	292	264	263

2.1 Carbonation rate

Eight thick blocks of each mix were placed into the carbonation chamber with a temperature of 21 ± 2 ºC, RH 60 ± 10 % and 1 % CO_2 according to EN 13295 [11]. Four blocks were used for the pH-indicator method while the other four were used for the TGA method.

For the pH-indicator method, one block was taken out of the carbonation chamber after 14, 28 and 90 days and, depending on the w/c ratio, either after 146 (w/c 0.60) or 167 days (w/c 0.50) of exposure. It was split perpendicularly to the sawn surface.The carbonation front was visually determined with a ruler on a freshly split surface with dimensions 7 × 10 cm² , which was sprayed with a thymolphthalein pH-indicator solution. Where the mortar is unaffected by the carbonation (pH above 9.3 to 10.5) indicator turns blue while the carbonated surface remains uncoloured.

For the TGA method, the remaining four blocks were used, which were taken out of the carbonation chamber the same day as the blocks for the pH indicator test. The blocks were profile-ground inwards from the sawn surface. The powder extracted from the consecutive layers was used for the TGA measurements using a *Mettler Toledo TGA/DSC3+* device. The amount of CH relative to the ignited mass of the powder ($CH_{ignited}$) at 900 °C was calculated as

$$CH_{ignited} = \frac{w_{400} - w_{550}}{w_{900}} \times \frac{M_{CH}}{M_{H_2O}}$$

where w_{400}, w_{550} and w_{900} refer to the mass of powder at 400, 550 and 900 ºC respectively and M is the molar mass of either CH or water [12]. Since carbonation consumes CH, its content is a measure of the degree of carbonation. The CH content was plotted as a function of the depth from the exposed surface. A detailed description of the experimental set-up can be found in [10].

2.2 Moisture transport

The moisture transport experiment was carried out on the thin plates. It consisted of several stages of conditioning as shown in Figure 1, where stage 1 corresponds to curing described at the beginning of Ch. 2. After 76 days of curing, thin plates were sawn and the plates were organized into two groups, namely group "0 %" and group "3 %" indicating the CO_2 concentration to which groups were exposed in stage 2. Throughout the experiment, the mass of the plates was measured at regular intervals using a balance with accuracy 0.01 g.

In stage 2, the thin plates of the "3 %" group were placed in the carbonation chamber with a temperature of 21 ± 2 ºC, RH 60 ± 10 % and 3.1 % CO_2 according to EN 13295 [11]. The higher CO_2 concentration, compared to 1 % used on the thick blocks in Ch. 2.1, was assumed to have no impact on the type of phases that form during the carbonation process [13]. The thin plates in the "0 %" group were stored in the conditioning chamber with a temperature of 18 – 25 ºC and RH 50 – 65 % at a reduced CO_2 concentration. Soda lime as a CO_2 trap was put under the specimens to capture carbon dioxide and reduce its concentration in the chamber's atmosphere. Stage 2 lasted for 146 days. At the end of stage 2, one plate from each group was split in half and the carbonation depth was measured using a phenolphthalein pH-indicator solution. The rest of the plates proceeded to stage 3.

In stage 3, the remaining plates from both groups were re-saturated. The plates were first saturated by capillary absorption. The water level was gradually increased over several days until the specimens were completely immersed.

Again, the mass of the plates was measured at regular intervals. When they all reached a near to constant mass, they were further saturated by vacuum saturation according to EN 12390-11 [14]. Stage 3 lasted for 63 days.

In stage 4, the specimens were kept in normal atmospheric conditions at 20 ºC and RH 60 %. This stage lasted 33 days. Once the plates reached a constant mass, they were further conditioned at 20 ºC and RH 30 % in stage 5. Upon completion of stage 5 the total porosity of specimens was determined according to SIA 262-1 [15].
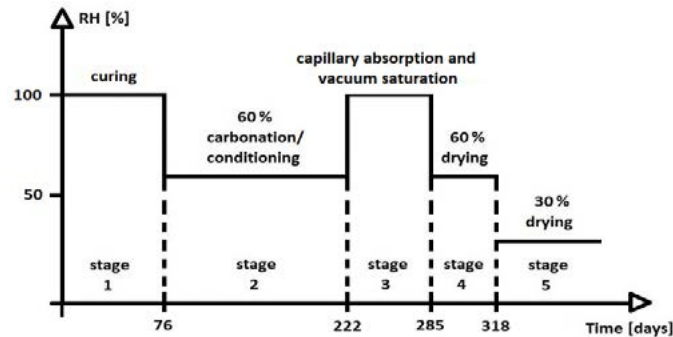

Figure 1: Stages of the moisture transport experiment carried out on the thin plates.

3   RESULTS AND DISCUSSION

The results of the accelerated carbonation study, where carbonation rate was measured by a pH-indicator and by TGA, are presented in Ch. 3.1. Results of both methods are compared and discussed and they are found to have good correlation. Moisture transport results, given in Ch. 3.2, indicate an increase in porosity due to carbonation in specimens with w/c ratio 0.6.

3.1 Carbonation rate

Carbonation depth results assessed visually after spraying the pH-indicator solution on the freshly split surfaces are given in Figure 2 where carbonation depth is plotted against the square root of time. In general, there is a linear relationship between the carbonation depth and the square root of time, therefore a straight line was fitted to the results. It can be seen, that the carbonation rate of ~1.0 mm day$^{-0.5}$ found in EnM-06 is the highest, while RefM-05 has the lowest carbonation rate of ~0.2 mm day$^{-0.5}$. The other two mortars, namely EnM-05 and Ref-06, have approximately the same carbonation rate of ~0.6 mm day$^{-0.5}$. Consequently, after 146 days of exposure, EnM-06 shows a carbonation depth of 13 mm as opposed to the 9 mm measured on RefM-06. Similarly, EnM-05 shows a carbonation depth of 8 mm while only 4 mm was measured on RefM-05. The results thus indicate that a higher w/c ratio leads to a higher carbonation depth. This is expected since higher w/c ratio generates higher porosity of the cement matrix, allowing a faster penetration of CO_2 into the sample [16].

The CH content determined by TGA as a function of depth for the samples prepared with a w/c ratio of 0.6 are shown in Figure 4. In general, the CH content decreases towards the surface where no CH can be detected because all of it was consumed during carbonation reaction. The plateau level of the CH content determined on deeper sections represents the amount initially present in the uncarbonated mortars. The depth at which the CH content equals zero corresponds well to the carbonation depth measured with the visual method and therefore results already shown in Figure 2.

The lower carbonation resistance of the EnDurCrete mortars compared to the reference mortars might be related to the difference in the CH content in the uncarbonated mortar samples (Figure 3). Since less CH is available in the EnDurCrete mortars compared to the reference mortars, these samples have a lower buffer capacity during carbonation. Additionally, Revert et al. [17] have observed that low clinker binders get a coarser porosity upon carbonation enabling faster carbonation rates.

CoMS_
2020/21
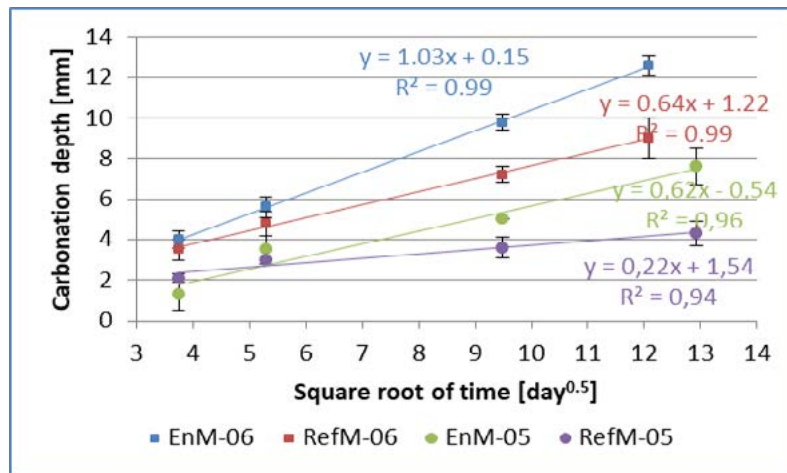
Figure 2: Carbonation depth measured visually after spraying the split samples with a pH indicator plotted against the square root of time. "EnM" and "RefM" stand for EnDurCrete and reference mortar respectively, while extensions "-06" and "-05" refer to water/cement ratios of 0.6 and 0.5. The error bars indicate the variation in the carbonation depth (10 measuring points) measured in one sample for each mortar and exposure time.
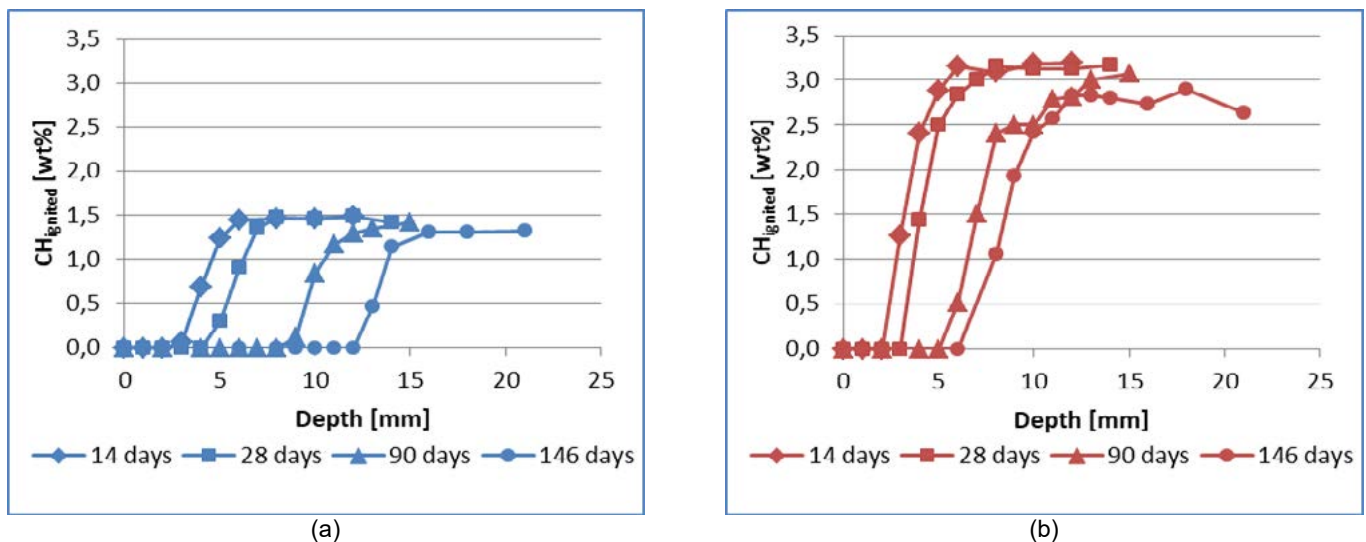

Figure 3: CH content measured with thermogravimetric analysis (TGA) after 14, 28, 90 and 146 days of exposure to accelerated carbonation for (a) EnDurCrete mortar (EnM-06) and (b) reference mortar (RefM-06) both made with w/c ratio of 0.6.

3.2 Moisture transport

The mass changes of the thin plates during the moisture transport experiments are shown in Figure 4 for w/c ratio 0.6 and in Figure 5 for w/c ratio 0.5. The results in both figures are normalised to the initial mass of each plate. The rapid drop of mass at the beginning of stage 2 is probably due to surface drying of the freshly cut samples. The plates in group "0 %" continue to lose mass until equilibrium is reached between 96 and 98 wt% of the initial mass. When looking at the drying profiles of the 0% series, we can see that the RefM-06 seems to dry faster and to a larger extent compared to the EnM-06. Plates in group "3 %", on the other hand, first decrease in mass but start to increase in mass after ~3 days of exposure, at this point the net mass gain due to carbonation (see Ch. 1) compensates for the mass loss due to drying. Sanjuán et al. [18] also report an initial decrease in weight followed by mass gain despite their specimens having been stabilised at 60 % RH before carbonation. The only exception where the mass continues to decrease throughout stage 2 is EnM-06. The decrease or increase in mass in these experiments can give a hint on which of the two mechanisms (drying vs carbonation) has the strongest impact on the weight of the sample. When CO_2 is present, carbonation will cause a weight gain due to the binding of CO_2 in the reaction products. This weight gain will partially counteract the mass loss due to the simultaneous drying. According to Figure 2, the EnM-06 mortar carbonates faster than the RefM-06, however, due to the lower clinker content in the EnM-06 mortar, it has a lower CO_2 binding capacity compared to the RefM-06. This might explain why the EnM-06 mortar does not gain any mass during simultaneous drying and carbonation, whereas the RefM-06 mortar does (stage 2 in Figure 4 and Figure 5).
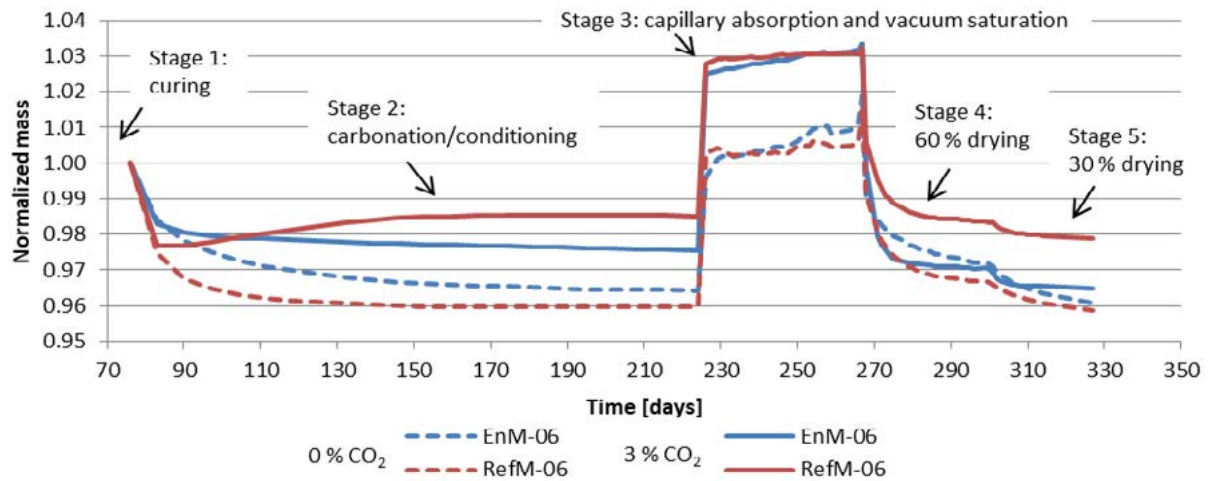
Figure 4: Mass changes during the moisture transport experiment for plates with water/cement ratio of 0.6. In stage 2 one group was exposed to carbonation in 3.1 % CO_2 environment and the other to conditioning in ~0 % CO_2 environment. "EnM" and "RefM" stand for EnDurCrete and reference mortar respectively.
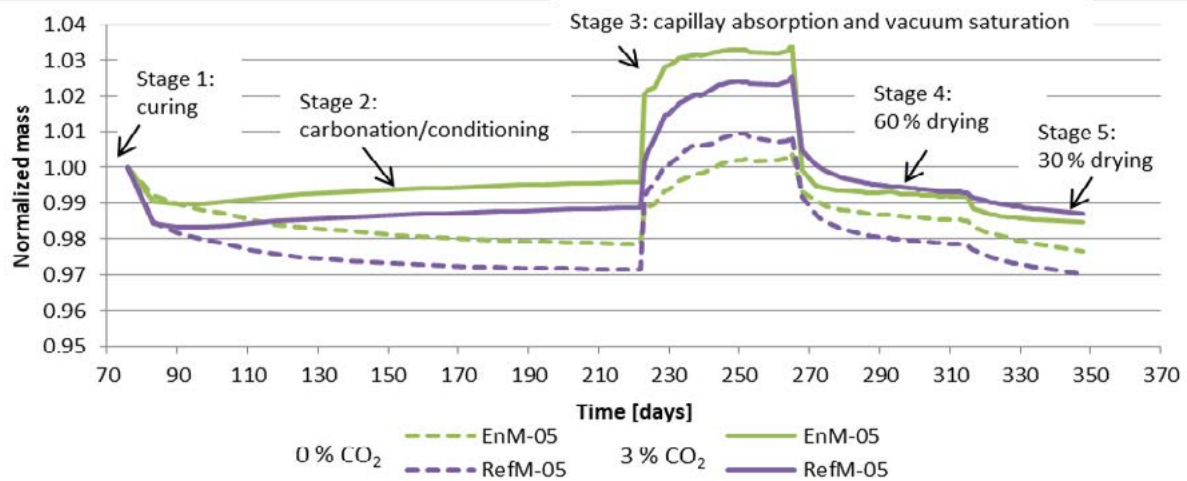

Figure 5: Mass changes during the moisture transport experiment for plates with water/cement ratio of 0.5. In stage 2 one group was exposed to carbonation in 3.1 % CO_2 environment and the other to conditioning in ~0 % CO_2 environment. "EnM" and "RefM" stand for EnDurCrete and reference mortar respectively.

In stage 3, significant differences between groups "0 %" and "3 %" are observed. The uncarbonated plates in the former group absorb significantly less water than carbonated plates in the latter group compared to their starting weight. This indicates an increase in capillary porosity during carbonation compared to the uncarbonated samples. This assumption is confirmed by porosity results shown in Figure 6b where one can see that in "-05" specimens porosity increased for ~2 % due to carbonation which isn't the case for -06 samples

Stages 4 and 5 show gradual loss of mass. For specimens in "0 %" group, the mass at the end of stage 5 (30% RH) is approximately the same as mass at the end of stage 2 (60% RH). Normalised mass (to initial mass) of carbonated specimens is by ~2 % larger than the normalised mass of uncarbonated specimens.

The fact that the EnM-06 and RefM-06 were fully carbonated, corresponds to the plateauing of the carbonated samples in Figure 4 during stage 2, confirming that these samples have reached equilibrium at those conditions. The corresponding curves for the carbonated EnM-05 and RefM-05 samples in Figure 5, do not reach the plateau during stage 2, which agrees with the fact that they haven't been fully carbonated yet as shown in Figure 6.

The degree of carbonation at the end of stage 2 was checked on one thin plate with the pH-indicator method. Plates were considered fully carbonated if the depth of carbonation was equal to half of the plate thickness, that is 10 mm. The

results for plates in groups "3 %" and "0 %" are shown in Figure 6a. Plates in the group "3 %" and w/c ratio 0.6 (EnM-06 and RefM-06) carbonated completely while those with w/c ratio 0.5 carbonated only half the depth in case of EnM-05 and quarter of the depth in the case of RefM-05. This is an undesired outcome since the numerical model calibration is planned to be performed on a fully carbonated material on one hand and completely uncarbonated on the other. The results show that the reduced CO_2 levels in the conditioning chamber were able to limit the carbonation depth of the 0% samples. No carbonation depth was measured on 0% EnM-05 and RefM-05 samples.
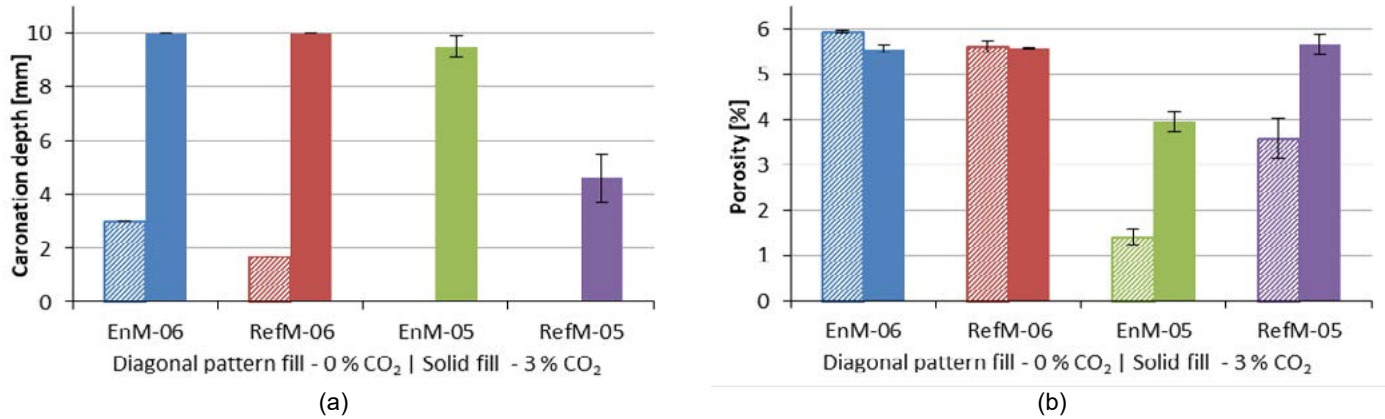

Figure 6: Carbonation depth (a) and total porosity (acc. SIA 262-1) (b) of conditioned specimens after stage 5. Specimens in group "3 %" were exposed to 3.1 % CO_2 atmosphere while specimens in group "0 %" were exposed to the atmosphere with reduced CO_2 content. "EnM" and "RefM" stand for EnDurCrete and reference mortar respectively, while extensions "-06" and "-05" refer to water/cement ratios of 0.6 and 0.5. The error bars indicate the variation in vačues measured on three sample.

4   CONCLUSIONS

An experimental programme was carried out to collect data for verification of numerical model studying (1) rate of carbonation, and (2) impact of carbonation on moisture transport. For the verification of the rate of carbonation model, thick mortar blocks were exposed to accelerated carbonation conditions and the depth of carbonation was measured visually on split samples sprayed with a pH-indicator and on profile-ground specimens using the TGA method. For the model verification, the impact of carbonation on moisture transport was monitored by measuring the mass of thin mortar plates subjected to a specific protocol of conditioning.

The results obtained in this study indicate that the carbonation depth is affected by the amount of clinker in the cement and w/c ratio. The lower the amount of clinker and/or higher the w/c ratio, the higher the carbonation rate is. Carbonation rates were found to be ~1.0 mm day$^{-0.5}$ for EnM-06 and ~0.6 mm day$^{-0.5}$ for Ref-06, while for EnM-05 and RefM-05 carbonation rate was ~0.7 and ~0.2 mm day$^{-0.5}$ when exposed to accelerated carbonation with 1 % CO_2. Results of both methods, namely visual and TGA method, are in fairly good agreement. Additionally, TGA shows that initial CH content is ~1.5 wt% in EnM-06 as opposed to ~3.0 wt% in RefM-06. Based on the results of this study, the lower initial CH content of the EnDurCrete samples might be the reason for the larger carbonation depth.

The moisture transport experiments show that carbonation increases the total porosity, which can facilitate the transport of deleterious substances, and therefore can promote other deterioration processes in addition to corrosion of reinforcement. The results obtained on EnM-06 show that during carbonation at constant RH EnM-06 performs differently compared to other mortars. In contradiction to the results obtained in the carbonation rate experiment, during exposure to the CO_2-rich environment, its mass continued to drop while it exhibited the highest carbonation rate. The decrease or increase in mass shows which of the two mechanisms (drying vs carbonation) has the strongest impact. As an improvement to the experiment protocol authors recommend conditioning specimens at 60 % RH after stage 1 until a constant mass is achieved and then exposing them to carbonation.

The experimental results presented here will be used for verification of mechanistic/generic models developed within EnDurCrete project [7], which can be applied to novel cements with varying compositions. These models aim to improve prediction of concrete durability in a CO_2-rich environment and therefore reduce the maintenance-related costs, particularly in the public infrastructure sector.

ACKNOWLEDGEMENTS

REFERENCES

[1] EN 1992-1-1 Eurocode 2: Design of concrete structures. General rules. Rules for buildings. European Committee for Standardization (CEN), 2014.

[2] EN 1992-2 Eurocode 2: Design of concrete structures. Concrete bridges. Design and detailing rules. London: European Committee for Standardization (CEN), 2008.

[3] P. Beverly and International Federation for Structural Concrete, Eds., fib model code for concrete structures 2010. Berlin: Ernst & Sohn, 2013.

[4] 'Construction | Internal Market, Industry, Entrepreneurship and SMEs'. https://ec.europa.eu/growth/sectors/construction_en (accessed Feb. 05, 2021).

[5] prEN 197-1 Cement. Composition, specifications and conformity criteria for common cements. European Committee for Standardization (CEN), 2018.

[6] G. Bolte, M. Zajac, J. Skocek, and M. Ben Haha, 'Development of composite cements characterized by low environmental footprint', Journal of Cleaner Production, vol. 226, pp. 503–514, Jul. 2019, doi: 10.1016/j.jclepro.2019.04.050.

[7] CEA, 'D4.3 Report on modelling and simulation of materials at mesoscale', D4.3, 2021.

[8] 'EN 12390-2 Testing hardened concrete. Making and curing specimens for strength tests'. European Committee for Standardization (CEN), 2019.

[9] J. Lindgård, E. J. Sellevold, M. D. A. Thomas, B. Pedersen, H. Justnes, and T. F. Rønning, 'Alkali–silica reaction (ASR)—performance testing: Influence of specimen pre-treatment, exposure conditions and prism size on concrete porosity, moisture state and transport properties', Cement and Concrete Research, vol. 53, pp. 145–167, Nov. 2013, doi: 10.1016/j.cemconres.2013.05.020.

[10] M. H. Bjørndal, 'Carbonation resistance of concrete and mortar containing novel low clinker cement', Norwegian University of Science and Technology (NTNU), Trondheim, 2019.

[11] 'EN 13295 Products and systems for the protection and repair of concrete structures - Test methods. Determination of resistance to carbonation'. European Committee for Standardization (CEN), 2004.

[12] A. B. Revert, K. De Weerdt, K. Hornbostel, and M. R. Geiker, 'Investigation of the effect of partial replacement of Portland cement by fly ash on carbonation using TGA and SEM-EDS', Lyngby, Denmark, 2016, pp. 413–422.

[13] M. Thiery, 'Carbonation kinetics of a bed of recycled concrete aggregates: A laboratory study on model materials', Cement and Concrete Research, p. 16, 2013.

[14] EN 12390-11 Testing hardened concrete. Determination of the chloride resistance of concrete, unidirectional diffusion. European Committee for Standardization (CEN), 2015.

[15] SIA 262-1 Concrete structures. Complementary specifications. Swiss Society for Engineers and Architects (SIA), 2013.

[16] S. Boualleg, M. Bencheikh, L. Belagraa, A. Daoudi, and M. A. Chikouche, 'The Combined Effect of the Initial Cure and the Type of Cement on the Natural Carbonation, the Portlandite Content, and Nonevaporable Water in Blended Cement', Advances in Materials Science and Engineering, vol. 2017, pp. 1–17, 2017, doi: 10.1155/2017/5634713.

[17] A. B. Revert, K. De Weerdt, U. H. Jakobsen, and M. R. Geiker, 'Impact of Accelerated Carbonation on Microstructure and Phase Assemblage', Nordic Concrete Research, vol. 59, no. 1, pp. 111–126, Dec. 2018, doi: 10.2478/ncr-2018-0018.

[18] M. A. Sanjuán, C. Andrade, and M. Cheyrezy, 'Concrete carbonation tests in natural and accelerated conditions', Advances in Cement Research, no. 4, p. 10, 2003.

16

Irina Stipanović, Sandra Škarić Palić, Aljoša Šajna, Henar Martin-Sanz, Eleni Chatzi

LCA and LCC assessment of UHPFRC application for railway steel bridge strengthening

CoMS_
2020/21

LCA AND LCC ASSESSMENT OF UHPFRC APPLICATION FOR RAILWAY STEEL BRIDGE STRENGTHENING

Irina Stipanović[1, 2], Sandra Škarić Palić[2], Aljoša Šajna[3], Henar Martin-Sanz[4], Eleni Chatzi[4]

[1] University of Twente, Faculty of Engineering Technology, Enschede, Netherlands. e-mail: i.stipanovic@utwente.nl

[2] Infra Plan konzalting, Zagreb, Croatia, e-mail: irina.stipanovic@infraplan.hr; sandra.skaric@infraplan.hr

[3] Slovenian Nationa Building and Civil Engineering Institute, Department of Materials, Ljubljana, Slovenia, e-mail: aljosa.sajna@zag.si

[4] Department of Civil, Environmental and Geomatic Engineering (IBK), ETH Zurich, Switzerland, e-mail: chatzi@ibk.baug.ethz.ch

SUMMARY: Most of the existing railway steel bridges are nowadays older than 70 years, experiencing serious aging and overload problems. Therefore they either need to be replaced or strengthened to fulfil the increased requirements. The main idea of strengthening existing steel bridges is considering the possibility of adding load bearing deck above the main girders without replacing them. In this particular case study, the original steel structure of the 9m long railway bridge was dismantled and transported to the laboratory for the experimental assessment and development of the new rehabilitation method. Based on the assessment results, a strengthening slab was designed using Ultra High Performance Fibre Reinforced Concrete (UHPFRC) formula. In the life cycle analysis, using LCC and LCA models, the comparison of the application of UHPFRC cast in-situ deck is compared to the bridge replacement solution, which was actually selected method by the owner. The executed solution used also a temporary bridge in order to enable continuous traffic, which has caused very high construction costs. In order to compare different options, we have additionally analysed a solution without a temporary bridge, which created three life cycle scenarios. Most important steps during the construction, exploitation and end-of-life stage have been taken into account and integrated into the LCA and LCC models. Finally the environmental, economy and societal impacts of three solutions were compared over the period of 60 years. The rehabilitation option with UHPFRC deck has shown by far the lowest direct and environmental cost while the user delay costs only after the period of 50 years are not the most convenient for users. Superior characteristics of UHPFRC enabled the optimization of the load bearing deck and by that a very low total used quantity of material resulting in minimum direct and indirect costs.

KEY WORDS: railway steel bridge; UHPFCR; strengthening; LCA; LCC model.

1 INTRODUCTION

EU transport policy provides the challenge to railway infrastructure owners to increase the productivity of existing rail networks, prioritise renewal and optimise new sections to reduce bottlenecks, increase productivity and achieve a switch from transport by road to rail. In its 2011 white paper entitled 'Roadmap to a Single European Transport Area — Towards a competitive and resource efficient transport system' [1], the Commission set the goal of ensuring that the majority of medium-haul passenger transport is carried out by rail by 2050. In the medium term (by 2030), the length of the existing high-speed network should be tripled and a dense rail network in all Member States maintained. In the long term, a European high-speed rail network should be completed. On the other hand European rail infrastructure managers (IMs) are managing ageing rail infrastructure with 95% of the network being built before 1914 [2]. This needs to be achieved at a time when budgets are restricted whilst improving customer satisfaction and dealing with challenges from natural hazards and extreme weather events which are affecting all of Europe. In order to deal effectively with this grand challenge, researchers and professionals need to develop methods to maintain and upgrade the existing rail infrastructure across the whole European railway area. Bridges as critical structures on the transport networks, are usually requiring highest maintenance and/or replacement costs. The problem is particularly rising in railways, where high percentage of bridges were built more than 70 years ago and were not designed for current loads and high speed trains. These are mainly bridges made of hot rolled steel or cast iron, mainly connected by means of rivets. Due to economic and environmental reasons, extending the service life of these structures proves beneficial, in opposite to demolishing or reconstructing them. [3-6]

UP

In the last few decades Ultra-High Performance Fibre Reinforced Concrete (UHPFRC) materials have been increasingly applied for rehabilitation projects of existing bridges, proving itself as a reliable, cost efficient and sustainable alternative against conventional methods, but mostly for strengthening and rehabilitation of concrete structures [7-11]. In this paper the comparison of the application of UHPFRC cast in-situ deck is compared to the standard concrete bridge replacement solution, which was actually selected method by the owner. All steps during the construction, exploitation and end-of-life stage, while taking into account the direct and indirect impacts of technology, duration of works, service life etc. are taken into account and integrated into the Life Cycle Assessment (LCA) and Life cycle cost (LCC)models. Finally the environmental, economy and societal impacts of two solutions are compared over the whole bridge life cycle. The initial research work has been done within the EU research project SMART RAIL. [12, 13] The concept of strengthening steel bridge sections by transforming them into a composite section has been developed earlier [14, 15], while the innovation of this research lies in the use of UHPFRC for the construction of a composite deck.

2 CASE STUDY – RAILWAY STEEL BRIDGE

The case study presented in this paper relates to the Buna bridge, which was a component of to the Croatian Railway network since 1953, until its decommissioning in 2010. It stands as a good example of the steel bridge construction techniques of that period, i.e., steel plates joined by riveted connections. The structure, almost 9 m long, comprises of two main girders of 0.9 m depth, tied to each other every 2.26 m by means of L shape profiles. Diagonal L beams in a zig zag disposition close the lattice on the top, leaving a space of 1.8m between the 81 two girders. Wooden sleepers were directly supported over the bridge without any covering slab. Figure 1 illustrates the configuration of the structure. When a decision was made to replace the steel superstructure of the Buna bridge, the opportunity came up for experimental investigations on a real characteristic example of a steel bridge connected with rivets. Once the bridge was decommissioned, it was transported to laboratory facilities, in order to determine its static and dynamic performance and to find an economical and practical strengthening solution that could prove useful in future projects [13-15].
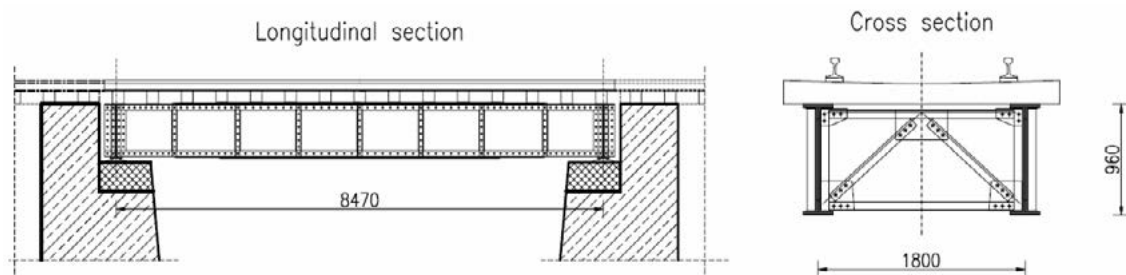

Figure 1: Schematic drawing of the tested steel bridge [12]

Figure 2: Original Buna bridge transported to the laboratory before testing [12, 13]

The main idea of strengthening existing steel bridges is considering the possibility of adding load bearing deck above the main girders without replacing them [4, 12-14]. Composite beams, subject mainly to bending, consist of a steel section acting compositely with a top flange of reinforced concrete. The two materials are interconnected by means of mechanical shear connectors. Converting alone metal section to composite cross-section raises the centre of gravity so that new composite cross-section can carry additional loads. In addition, the concrete deck stiffens upper steel flange and thus eliminates the problem of stability of compressed part of the cross-section (Figure 3).
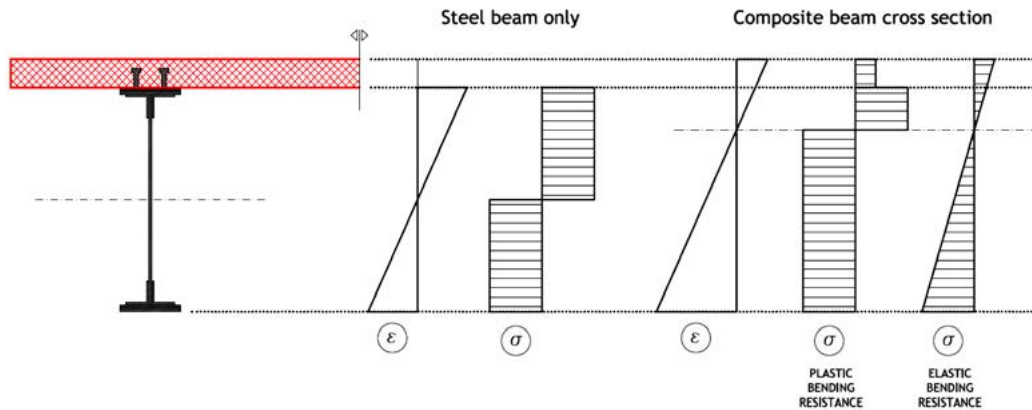

Figure 3: Composite effect shown through diagrams of strain and stresses [12]

The reason for using an UHPFRC for the strengthening of a steel railway bridge, apart from its excellent mechanical properties, is the fact that the deck is not reinforced with a standard reinforcement net, and it is expected that the procedure related to the execution of deck cast in situ will be shorter in relation to the standard reinforced-concrete deck. Therefore, the railway line will be closed to traffic for a shorter period of time, rendering not only economical but further advantages for the users. In addition, the UHPFRC deck height is less than the standard reinforced-concrete deck height, which minimizes problems related to adjustment of the track substructure geometry to the new height of the bridge.

3 LIFE CYCLE ANALYSIS OF UHPFRC REHABILITATION SOLUTIONS

3.1 UHPFRC strengthening solution

Ultra-High-Performance Fibre-Reinforced Concrete (UHPFRC) is a composite material which tends to exhibit superior properties such as advanced strength, durability, and long-term stability compared to conventional concrete. Mechanical properties like compressive and tensile strengths are much higher and this enables slender constructions due to increased capacity of transferring forces. Very dense matrix causes outstanding durability properties and it is shown that the concrete is very resistant to chloride and other chemical attacks and has a high abrasion and fire resistance. [7] It was decided to use the enhanced performance in strength and durability of UHPFRC and cast a deck slab upon the existing steel superstructure of a bridge in the lab. The original steel structure was transported and tested within a laboratory setting prior to the implementation of a cast in-situ UHPFRC deck. Results of these tests can be found in [13-15]. The main objective of strengthening the Buna bridge was converting the existing steel cross section to composite cross-section. This caused rising of the neutral axis, increase of the bearing capacity and finally enables the composite cross section to carry additional loads. In addition, the concrete deck stiffens the upper steel flange and thus reduces or even eliminates the problem of stability of the cross-section. The advantages of UHPFRC particularly valuable for rehabilitation of railway bridges are high strength and ductility, low added dead load, low added thicknesses, i.e. change in the track vertical alignment, extreme durability. [1, 4]

3.2 Rehabilitation process with UHPFRC

In the laboratory the whole process of the strengthening the existing bridge was performed as presented in Figure 4.

a) Steel structure was sandblasted and painted, two rows of steel studs on the upper flange of the steel girders were welded.

b) Formwork was built up

c) minimum secondary reinforcement in transverse direction was deployed and number of sensors were embedded inside the slab,.

d) UHPFRC slab was casted.
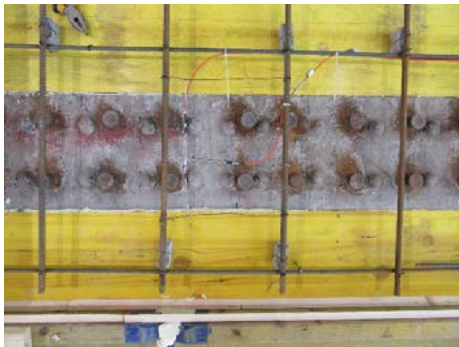
Figure 4: Strengthening process of the steel bridge

For improving the load transfer between the steel girders and the concrete slab, steel studs have been welded on the upper flange of the girders. The commercially available studs (type) were shortened to a length of 55mm, to fit into the concrete slab of designed thickness of 70 mm. Two rows of studs with an axial distance of 100 mm were welded on each girder using standard welding procedure, Figure 5a. The formwork for the slab was set-up as it would be done on-site, i.e. the formwork was supported by the steel girders only, see Figure 2b). The concrete slab was in the transverse direction reinforced with rebars of ϕ12 mm at a spacing of 250 mm, Figure 5c. The reinforcement was placed 2 cm under the designed upper surface of the slab. Finally the UHPFRC was placed, with the thickness of 70 mm. UHPFRC mix was designed using locally available raw materials, dolomite aggregate of maximum size of 4 mm, cement, limestone filler and superplasticizer. The selected concrete mix can be found in [16]. Fresh concrete properties were determined as follows: the slump (acc. EN 12350-2), the air content (acc. EN 13950-7) and the density. The concrete had a slump of 190 mm, air content of 3.3 % and density of 2620 kg/m^3.

3.3 Executed solution with new concrete bridge

The new bridge structure is designed as a composite concrete-steel structure. Seven steel girders IPB 450 are embedded in concrete at a distance of 60 cm with a span of 10.5 m. This will increase the clear opening of the bridge by 1.4 m, so that the new opening will be 8.70 m. The load-bearing structure will be of a total length of 11.80 m and will consist of seven steel girders embedded in a concrete at a distance of 60 cm with the compression slab 15 cm thick on top. The total height of the structure will be 60 cm, as presented in Figure 5. All concrete elements are made of concrete min. class C30 / 37, soft ribbed reinforcement type B500B, and embedded steel girders S235JRG2 [17].
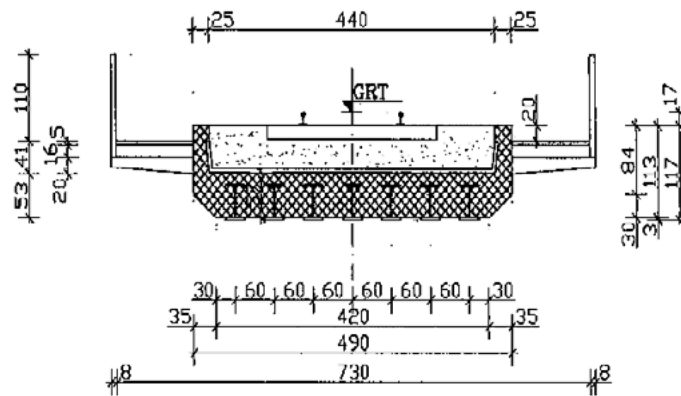
Figure 5: New Buna bridge

4 WHOLE LIFE CYCLE MODEL

The life cycle analysis were performed for three different bridge upgrade scenarios. Since the life cycle analysis are performed for comparative purposes, structural elements and equipment which are the same in different solutions are excluded from the analysis, e.g. substructure, rail equipment, bridge equipment. The life cycle scenarios include rehabilitation works, used materials, delays caused by the rehabilitation project and maintenance works for the 60 year period. The following three options are compared:

- Scenario 1: Old steel bridge is removed and new concrete bridge is constructed with rail traffic redirected on the provisional bridge – This option was actually performed for the rehabilitation work of the Buna bridge on the Croatian Railway network. The works included provisional bridge since the railway line had to be in operation the whole time during performance of rehabilitation works. This scenario includes *I*-shaped steel girders and conventional C30/37 concrete with ballast layer beneath the concrete sleepers and rails. In the life cycle scenario of 60 years regular maintenance, inspections and periodic concrete repair works are included.
- Scenario 2: Old steel bridge is removed and new concrete bridge is constructed with closed rail traffic for one month – The works are the same as in Scenario 1 but without provisional bridge meaning that the rail traffic is closed for one month. This has a large impact on users.
- Scenario 3: Old steel bridge is strengthened with the added UHPFRC slab on top of it – This scenario includes cleaning and painting of the existing steel superstructure, welding of steel studs and casting of thin layer of UHPFRC concrete deck, see Fig. 4.

4.1 Construction costs

The direct construction costs (CC) were retrieved from the original design and actual construction work costs provided by the owner of the bridge. These costs were used for the scenarios 1 and 2. The cost for scenario 3 is based on the cost of UHPFRC concrete installed in the deck in laboratory. Overall calculation of CC begins by first dividing the designed object into separate construction elements. The next step is determining the unit cost of a particular construction element and multiplying it by the amount that that element occurs in the design. This results in the total costs of that particular element in the total object. Doing this for every construction element and summarising these costs will yield the total assigned construction costs.

4.2 Maintenance costs

The maintenance costs will be calculated in a similar manner to the initial construction costs. First the maintenance scenario that most accurately describes the estimated required maintenance over the life cycle of the object has to be determined. This means determining the different necessary maintenance activities, their accompanying frequencies and their estimated unit costs. Next, the unit cost of a certain maintenance activity (AUC_i) is multiplied by the quantity of units related to that activity (Aq_i). The resulting yearly maintenance cost for that activity is attributed to all the years in the life cycle of the object in which that maintenance activity takes place (based on the frequency attributed to that activity). This creates a maintenance schedule with which the total maintenance costs of every year in

the life cycle can be calculated. Summarizing the maintenance costs of every year in the life cycle of the object gives the total nominal maintenance costs of the object. Because the maintenance costs are made in the year the maintenance takes place, the future cash flows have to be discounted to create a present value. The total discounted maintenance costs may be increased by a certain percentage that cover the *unassigned costs*, *indirect costs* and *unassigned object risks* (but not *engineering costs* and *other additional costs*), if that is the owner's practice. For more details please refer to [18].

4.3 User delay costs

The equations used for determining the user delay cost are based on the work of [18, 19]. The total user costs are a summation of the two sub-categories; freight delay costs and passengers delay costs. Because the user costs are made during the life cycle of the bridge, future cash flows will have to be discounted to determine a total present value. The traffic delay costs are the costs that represent the valuable time of the network users itself. This economic value of the user's time is dependent on several factors, namely the type of traffic (passenger vehicle or freight traffic), the amount of persons/cargo per vehicle and the type of cargo/person (business/leisure). The input data for the calculation of traffic delay costs are coming from data provided by the owner of the railway line (0.31€ per min of delay). The traffic delay costs can be then determined as follows:

$$TDC_t = ETT \times ADT_t \times VOT \times N_t \qquad \text{(Eq. 1)}$$

wherein TDC_t is traffic delay costs for year t (€), ETT is extra travel time per type of users (hours), ADT_t is the average daily traffic (separately for freight and for passenger trains) in year t passing the analysed section or bridge in question, VOT is a monetary value for the users time (€/hour), and N_t is the duration of a certain maintenance activity (days).

4.4 Environmental costs

In this case study for the LCA calculations GaBi software was applied. This software allows to estimate the relevant environmental indicators based on the CML-2001 method [20]. Using the 'revealed collective preference method' the environmental costs can then be determined. The environmental impact per kg of material for certain impact category has been determined and then monetized by using the method explained in [21]. The shadow prices are a way of monetizing environmental effects. For an explanation and in-depth discussion the author refers to the report by CE Delft [22] which provides the different environmental effect categories and their corresponding shadow prices are presented.

This is where the method used in this research differs from the framework of the ISO 14040 [23]. Instead of first determining the life cycle inventory (LCI) of one complete product life cycle and then determining the resulting impact via life cycle impact assessment (LCIA), this study first determines the environmental impact of one kg of material as a basic parameter of the model and then uses those values to calculate the total environmental impact by multiplying it with the amount of material present in the construction or maintenance activity. The total environmental costs can then be determined using the unit shadow price for each environmental category. Environmental costs incurred during the life cycle of the bridge are not discounted as recommended by [24].

5 RESULTS

The whole life cycle model takes into account direct and indirect costs, where direct are borne by the owner (construction and maintenance costs), and indirect costs (user delay and environmental costs) are borne by the society. In the case study three different rehabilitation scenarios are analysed as presented before. The aim of the model is to provide to the infrastructure owner the insights into the impacts of different maintenance strategies and enable optimal decision making. In the model input parameters can be changed according to the decisions made. Traffic closures and duration of the maintenance activities are used from the current practice and from the owners experience, and prediction of the future performance is based on the experts judgments and historical data. The graphs in Figure 6 clearly show that choosing different options in the beginning of a structures life cycle have a significant impact on different total costs in all phases. The rehabilitation option with UHPFRC deck (scenario 3) due to its small thickness of 7 cm, has by far the lowest direct and environmental cost while the user delay costs for a longer period of time is also the most convenient for users. Superior characteristics of UHPFRC enable much thinner structural elements and by that a very low total used quantity of material resulting in decreased costs. Scenario 2 where the bridge is closed for rehabilitation works reveals the highest

user delay cost but lower direct and environmental costs since the provisional bridge is not built. Scenario 1 with the provisional bridge has the highest total costs, although the smallest user delay costs since with the solution of provisional temporary bridge no delays were caused.
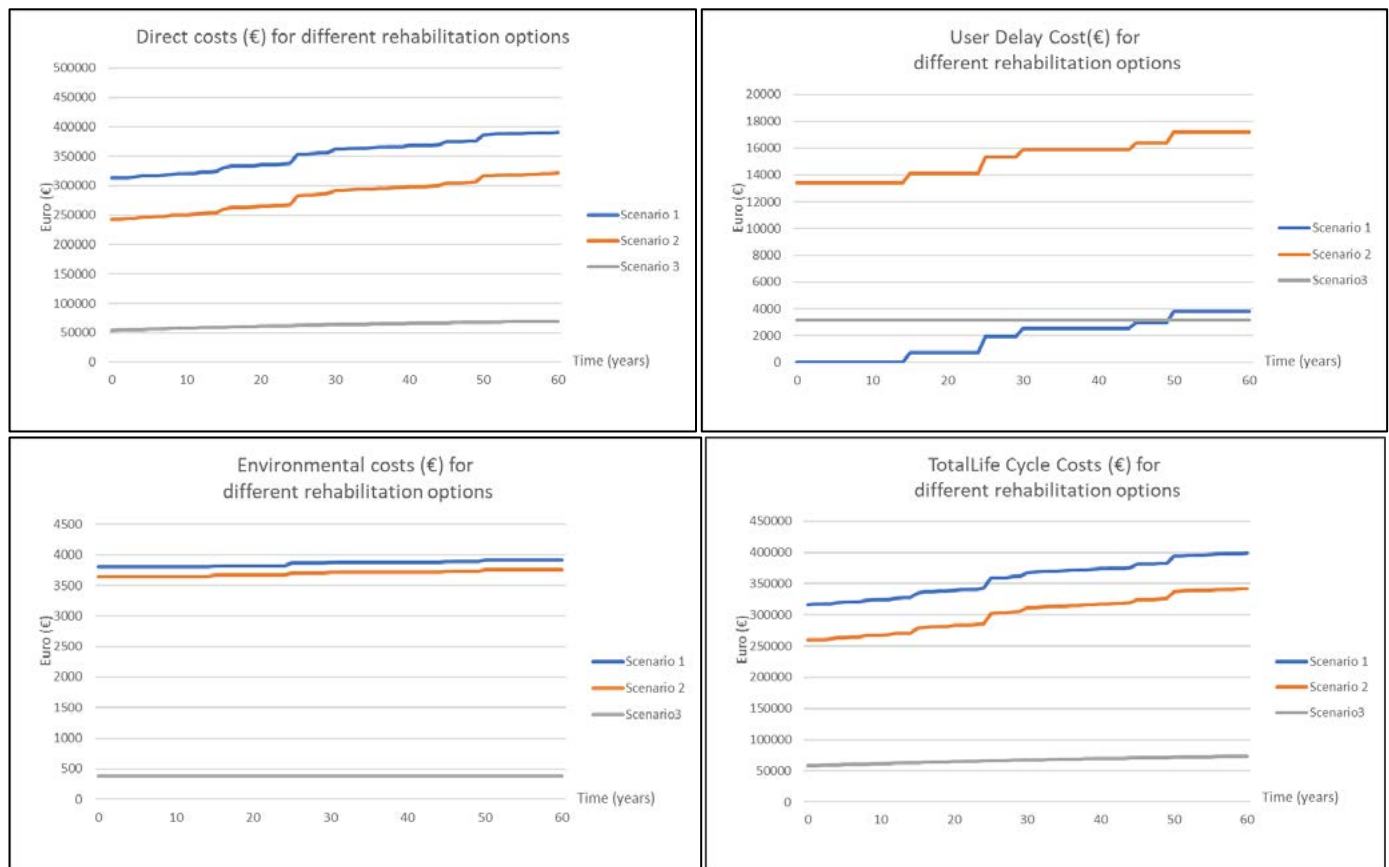

Figure 6: Direct costs, user delay, environmental and total life cycle costs for three different scenarios

6 CONCLUSIONS

In this paper the idea of strengthening existing steel bridge by adding UHPFRC deck, above the main girders without replacing it, has been explored and compared to the conventional solution of replacing the existing bridge with the new one. In this particular case study, the original steel structure of the 9m long railway bridge was dismantled and transported to the laboratory for the experimental assessment and development of the new rehabilitation method. Based on the thorough laboratory static and dynamic assessment, a strengthening UHPFRC slab was designed, satisfying all design requirements and the technological limitations, such as mixing, transporting and casting. In the life cycle analysis, using LCC and LCA models, the comparison of the application of UHPFRC cast in-situ deck is compared to the bridge replacement solution, which was actually selected method by the owner. The executed solution used also a temporary bridge in order to enable continuous traffic. This has caused very high construction costs. In order to compare different options, we have additionally analysed a solution without a temporary bridge, which created three life cycle scenarios. Most important steps during the construction, exploitation and end-of-life stage, while taking into account the direct and indirect impacts of technology, duration of works, service life etc. have been taken into account and integrated into the LCA and LCC models. Finally the environmental, economy and societal impacts of three solutions were compared over the period of 60 years. The rehabilitation option with UHPFRC deck has shown by far the lowest direct and environmental cost while the user delay costs only after the period of 50 years are not the most convenient for users. Superior characteristics of UHPFRC enabled the optimization of the load bearing deck and by that a very low total used quantity of material resulting in minimum direct and indirect costs.

ACKNOWLEDGMENTS

REFERENCES

[1] European Commission, WHITE PAPER Roadmap to a Single European Transport Area – Towards a competitive and resource efficient transport system / COM/2011/0144 final, (2011)

[2] European Railway Agency, Intermediate report on development of railway safety in the European Union, (2013).

[3] McCarron, P. Way Beam Replacement and Bridge Deck Strengthening using Concrete Composite Construction, University of Surrey Department of Civil Engineering, (2005).

[4] Carroll, M. An Investigation into Concrete Composite Strengthening of a Continuous Wrought Iron Railway Bridge using Precast Concrete Deck Slabs, Dissertation, University of Surrey Department of Civil Engineering, (2010).

[5] Network Rail, Railway Bridges Today and Tomorrow, Proceedings of the conference, UK, (2006).

[6] Olofsson, I., Elfgren, L., Bell, B., Paulsson, B., Niederleithinger, E., Sandager, J., Jensen, Feltrin G., Täljsten, B., Cremona, C., Kiviluoma, R., Bien, J. Assessment of European railway bridges for future traffic demands and longer lives – EC project "Sustainable Bridges", Structure and Infrastructure Engineering, Vol. 1, No. 2, pp. 93 – 100, (2005).

[7] Bøhnsdalen Eide M., Hisdal J.M., SINTEF Building and Infrastructure, Ultra High Performance Fibre Reinforced Concrete (UHPFRC) – State of the art, COIN Project report 44, (2012). http://hdl.handle.net/11250/2379433

[8] Brühwiler E, Denarié E. Rehabilitation and Strengthening of Concrete Structures Using Ultra-High Performance Fibre Reinforced Concrete. Structural Engineering International; (2013) 23(4): 450-7.

[9] G. Habert, E. Denarié, A. Šajna, P. Rossi, Lowering the global warming impact of bridge rehabilitations by using Ultra High Performance Fibre Reinforced Concretes, Cement and Concrete Composites, Vol. 38, (2013), pp. 1-11, ISSN 0958-9465, https://doi.org/10.1016/j.cemconcomp.2012.11.008.

[10] Franssen, R., Guner, S., Courard, L., Mihaylov, B., A study on the numerical modelling of UHPFRC-strengthened members, ICCRRR 2018, paper 09001, https://doi.org/10.1051/matecconf/201819909001, (2018).

[11] Sakr, M.A., Sleemah, A.A., Khalifa, T.M., Mansour, W.N. Behavior of RC beams strengthened in shear with ultra-high performance fiber reinforced concrete (UHPFRC), ICCRRR 2018, paper 09002, https://doi.org/10.1051/matecconf/201819909002, (2018)

[12] SMART RAIL FP7 Project, Deliverable 3.3 Rehabilitation of Bridges and Tunnels, Recommendations for the rehabilitation of engineering structures (bridges and tunnels), http://smartrail.fehrl.org/, 2013.

[13] Dzajic, I., Stipanovic Oslakovic, I., Sajna, A. Rehabilitation of steel railway bridges by implementation of UHPFRC deck. Proceedings of the International Conference on Road and Rail Infrastructure CETRA, (2014), Publisher: University of Zagreb, ISSN: 1848-9850.

[14] Martín-Sanz, H., Tatsis, K., Chatzi, E., Brühwiler, E., Stipanovic, I., Mandic, A., Damjanovic, D. & Sajna, A. Towards the use of UHPFRC in railway bridges: the rehabilitation of Buna Bridge, Life-Cycle Analysis and Assessment in Civil Engineering: Towards an Integrated Vision – Caspeele, Taerwe & Frangopol (Eds) © 2019 Taylor & Francis Group, London, ISBN 978-1-138-62633-1, pp. 203-209.

[15] Škarić Palić, S., Damjanovic, D., Stipanović Oslaković, I., Martín-Sanz, H., Košćak, J., Duvnjak, I., Šajna, A. Experimental Investigation of a Steel Railway Bridge Strengthened with UHPFRC Deck Slab, Proceedings of RILEM Conference "Spring Convention and Sustainable Materials, Systems and Structures Conference", (2019), 20 – 22 March 2019, Rovinj, Croatia.

[16] Šajna A., Stipanovic I., Martin-Sanz H., Damjanovic D., 'Rehabilitation of an old steel railway bridge using UHPFRC – material characteristics and casting technology', RILEM International Conference on Sustainable Materials, Systems and Structures, (2019), 20 – 22 March 2019, Rovinj, Croatia.

[17] Railway Design Company (Zeljeznicko projektno drustvo d.d.) Rehabilitation design project Buna bridge, 2010 (in Croatian).

[18] Skaric Palic, Stipanovic (2019) SAFE-10-T Deliverable D2.4 Report on Whole Life Cycle Model, https://www.safe10tproject.eu/publications

[19] Sundquist, H., & Karoumi, R. (2012). Life Cycle Cost Methodology and LCC Tools. ETSI. Retrieved from http://www.etsi.aalto.fi/Etsi3/PDF/TG3/LCC%20Description.pdf

[20] Thinkstep. (2015, April 10). Description of the CML 2001 Method. Retrieved from http://www.gabisoftware.com/support/gabi/gabi-lcia-documentation/cml-2001/

[21] TNO-MEP. (2004, March 8). Toxiciteit heeft zn prijs: schaduwprijzen voor eco-toxiciteit en uitputting van abiotische grondstoffen binnen dubocalc.pdf. Rijkswaterstaat. Retrieved from http://publicaties.minienm.nl/download-bijlage/15533/toxiciteit-heeft-z-n-prijs-schaduwprijzen- voor-eco-toxiciteit-en-uitputting-van-abiotische-grondstoffen-binnen-dubocalc.pdf

[22] CE Delft. (2003, April). Weging in DuboCalc: Toepasbaarheid van de preventiemethodiek. CE Delft. Retrieved from http://www.ce.nl/?go=home.downloadPub&id=72&file=03_7486_13.pdf

[23] ISO 14040:2006 Environmental management — Life cycle assessment — Principles and framework

[24] Hellweg, S., Hofstetter, T. B., & Hungerbuhler, K. (2003). Discounting and the environment should current impacts be weighted differently than impacts harming future generations? The International Journal of Life Cycle Assessment, 8(1), 8–18.

17

Marko Stojanović, Ksenija Janković, Dragan Bojović, Lana Antić, Ljiljana Lončar

Influence of different types of fibers on the ultimate and residual flexural strength of sprayed concrete

INFLUENCE OF DIFFERENT TYPES OF FIBERS ON THE ULTIMATE AND RESIDUAL FLEXURAL STRENGTH OF SPRAYED CONCRETE

Marko Stojanović[1], Ksenija Janković[2], Dragan Bojović[3], Lana Antić[4], Ljiljana Lončar[5]

[1,2,3,4,5]Institute for testing of materials-IMS Institute
Bulevar vojvode Mišića 43, 1100 Belgrade, Serbia
e-mail: ksenija.jankovic@institutims.rs

SUMMARY: The influence of the application of different types of fibres on the flexural strength of beams cut from slabs of sprayed concrete is presented in the paper. Fibres of different materials, shapes and dimensions were used. All types of concrete were made of the same component materials and composition, except the amount of fibres that is varied. Slabs of dimensions 60x60x10 cm were made using a concrete spraying machine. After curing, the beams of 75x125x500 mm were cut from the beams. Flexural strength of the beams was tested according to SRPS EN 14488-3 at the age of 28 days. Based on the test results, depending on the type, shape, amount and distribution of fibres, values of ultimate and residual strengths were analysed. The highest values of ultimate and residual strength at deformations of 0.5-1, 0.5-2 and 0.5-4 mm had sprayed concrete (or shotcrete) with the addition of 40 mm polypropylene fibres.

KEY WORDS: shotcrete, fibres, flexural strength, ultimate and residual strength.

1 INTRODUCTION

Shotcrete has been used as a protective coating of wall masses and soil surfaces that are prone to collapsing for over 50 years now. Before 1990, there wasn't much information related to the mechanical properties of shotcrete in the research papers published in scientific journals, but the academic community saw this material as an opportunity to stabilize the slopes and improve tunnel safety [1].

There are many applications of shotcrete: tunnelling, mining, slope stabilization, concrete repair, etc. It offers several advantages in industrial applications, including good substrate adhesion, the opportunity to dispense with formwork, good compaction, strength that rapidly increases during curing, and ease of application in restricted areas. Different admixtures and additions are used for regulating the required properties of the produced shotcrete [2].

However, meeting the high support requirements for the traditional wet-mix shotcrete technique is difficult, especially under the complicated geological conditions such as large geo stress and high-pressure water pouring causing shotcrete layer cracking and large rebound. Hence, a high performance wet-mix shotcrete has to be made, owning high pumpability and shoot ability and harden characteristics together. That can be performed if the mixture proportions based on the fibre reinforced shotcrete are optimized. Fibres significantly affect shotcrete properties and the addition of fibres to normal shotcrete can improve the toughness or energy absorption capacity efficiently [3-4].

The toughness of fibre reinforced sprayed concrete may be specified either by residual strength or by energy absorption class depending on the test considered to characterize the material, according to SRPS EN 14487-1:2008 [5]. For example, there were four classes of residual strength (Class S1 to S4) defined based on the results from flexural tests of beams that were sawn from sprayed panels with standardized dimensions of 75 x 125 x 500 mm and defined by SRPS EN 14488-3:2006 [6]. In cores extracted from the structure, this procedure is time-consuming, difficult, and not practical. The slab specimen test described in SRPS EN 14488-5:2006 [7] as well as some other tests, also rely on the production of test panels, which must be sprayed separately and are difficult to extract from the structure. The rebound in the panel may be very different from the real structure, so this is an important drawback. Consequently, the composition and the performance in the test panel may be different from the ones found in the structure.

In wet-mix shotcrete technique, fibres are added to the fresh concrete and the mixtures are pumped to a nozzle, where it is accelerated by compressed air so they can be sprayed onto a surface. Setting accelerator is normally added at the nozzle in order to reach the certain stiffness upon arrival on the surface area.

2 EXPERIMENTAL WORK

In this paper, three types of shotcrete were prepared, which were designed with different polypropylene fibres and one control type without fibres. Shotcrete was made with materials that are available in Serbia. Portland cement CEM I 52.5 R, manufactured by CRH - Popovac, was used. The chemical, physical and mechanical properties of the cement are shown in Table 1.

Table 1: Properties of cement CEM I 52.5R, CRH - Popovac

Chemical, %		Physical		Mechanical	
SiO_2	19.51	Specific gravity, kg/m^3	3120	Compressive strength, N/mm^2	
Al_2O_3	5.12	Specific surface, cm^2/g	4180	2 days	34.5
Fe_2O_3	2.53	Standard consistency, %	30.2	28 days	59.5
CaO	63.74	Setting time, min		Flexural strength, N/mm^2	
MgO	2.45	Initial	150	2 days	7.1
Na_2O	0.22	Final	200	28 days	9.9
K_2O	0.71	-	-	-	-
SO_3	2.90	-	-	-	-
Cl^-	0.004	-	-	-	-

Crashed, fractionated stone aggregate with the maximum grain size of 8 mm was used. Specific gravity of fine and coarse aggregates was 2710 kg/m^3 and 2720 kg/m^3 respectively. Water absorption of fine aggregate is 1.2%, and for coarse aggregate it is 0.9%.Polypropylene fibres "Sika fibre PM-39" and "Sika fiber T-40" - Sika, were used in the research. The properties of the fibres are shown in Table 2.

Table 2. Properties of the polypropylene fibres

Properties	Sika fiber PM-39	Sika fiber T-40
Material	Polypropylene 100%	Polypropylene 100%
Design	Monofilament	Monofilament
Specific gravity	0.91 g/cm³	0.91 g/cm³
Equivalent diameter	0.70 – 0.73 mm	0.78 mm
Length	39 mm	40 mm
Aspect ratio	85	67
Alkali resistance	Excellent	Excellent
Tensile Strength	448 MPa	600 MPa
Modulus of elasticity	3600 - 3700 MPa	2500 MPa
Chemical resistance	Excellent	Excellent
Melting point	165°C	160°C
Ignition point	>360°C	590°C

In this research, used Sika admixture: "Sika Techno 20S" superplasticizer, with a specific gravity of 1060 kg/m^3, and the recommended dosage of 0.6 %; "Sigunit L5601AF" set accelerating admixture, with the specific gravity of 1040 kg/m^3, and the recommended dosage of 3.5 %, produced by Sika, were used. Three types of shotcrete samples were made: control concrete without fibres and shotcrete with the addition of 4 kg/m^3 of two types of polypropylene fibres. A "dry process" was used to prepare the basic mix of shotcrete. The shotcrete mixtures were given in Table 3.

Table 3. Mixtures of shotcrete

Materials		Reference without fibres	Sika fibres PM 39	Sika fibres T40
Cement (kg/m3)		420	420	420
Aggregate (kg/m3)	0/4mm – 70%	1066	1066	1088
	4/8 mm – 30%	458	458	583
Mineral supplement - limestone		160	160	160
Superplasticizer (kg/m3)		2.52	2.52	2.52
Set accelerating admixture (kg/m3)		14.7	14.7	14.7
Water (kg/m3)		210	210	210
Polypropylene fiber (kg/m3)		0	4	4
w/c		0.5	0.5	0.5

Prismatic beam specimens were subjected to a bending moment by the application of load through upper and lower rollers. The first peak, maximum and residual loads sustained are recorded and the corresponding flexural strengths calculated.

A fibre reinforced prism specimen, sawn from a test panel in accordance with EN 14488-1 was subjected to a bending moment by the application of load through upper and lower rollers under deflection control to obtain its load/deflection response (the latter exclusive of non-bending deformations). The first peak, ultimate and residual flexural strengths are determined from the load/deflection curve [6].

The application of load through upper and lower rollers made the prismatic beam specimens subjected to a bending moment. The first peak, maximum and residual loads sustained were recorded and the corresponding flexural strengths were calculated. All test specimens were cut from a sprayed panel into sawn prisms with dimensions of 75 mm x 125 mm x 500 mm, as shown in Figure 1, and prepared to meet the requirements of EN 12390-1. The bottom uncut mould face should be identified on the specimen (indicating the direction of spraying).
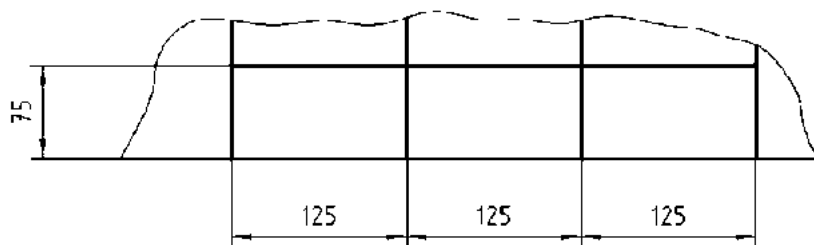
Figure 1: Cutting arrangement for beams [5].

The disposition of the beam test is shown in Figure 1. Beams were tested at 28 days of age. The distance, l, between the outer rollers (i.e. the span) was 450 mm, and the distance between the inner rollers was 150 mm. The inner rollers were equally spaced between the outer rollers as shown in Figure 2. All rollers were adjusted to the positions illustrated in Figure 2.
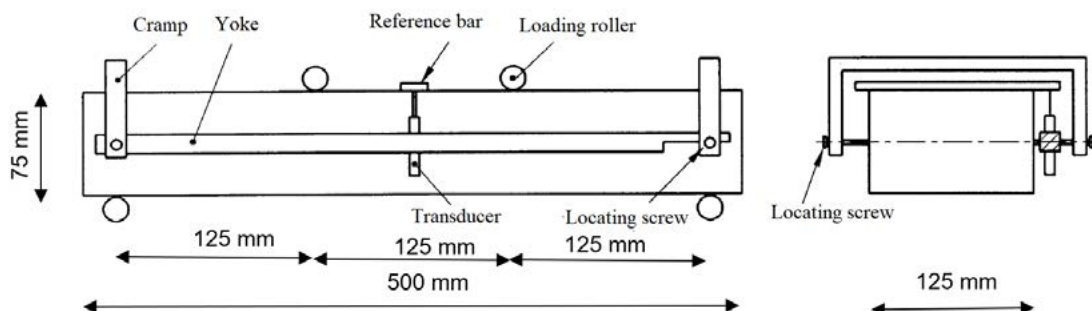
Figure 2: Disposition of the beam for bending deflection measurement

3 RESULTS AND DISCUSSION

For the flexural strength testing of concrete, beams with dimensions of 75 mm x 125 mm x 500mm and a digital hydraulic press with the range of 300kN were used. At the top of the beam, an inductive displacement meter LVDT is placed in the central part.

The load was constantly applied by a digital hydraulic press. Flexure strength testing for each type of shotcrete was performed on three samples. The obtained values for each type of shotcrete are shown in the diagram as the mean of three tests. Considering that the samples were obtained by cutting from the same plate, the variation of the results is minimal. The minimum value of force was obtained with concrete that was not reinforced with fibers (Control beam). The maximum fracture force of 6.0 kN was achieved at a beam deformation of 0.132mm. The beams were broken in half lengthwise.

The shotcrete samples reinforced with PM 39 fibers reached a maximum value of 7.1 kN at a deformation of 0.207 mm. In this condition, a crack formed on the underside of the beam. The bending force from the concrete is transmitted to the fibers. In the part of the diagram after the maximum force, the force decreases to the value of 7.012 kN at a deformation of 0.364 mm. The concrete cross-section of the beam loses its load-bearing capacity and the entire load is taken over by the fibers. The fibers maintain a force of 0.52kN with a beam deformation of 0.4mm and up to 4mm.

The obtained load - deflection diagram is very similar in shotcrete reinforced with T 40 fibers. Beams exposed to bending reached a maximum force value of 7.8 kN at a deformation of 0.278 mm, when the first crack and weakening of the cross section formed. Concrete withstood load up to 6kN and a deformation of 0.4 mm when the entire load was taken over by fibers with values of 0.61mm and up to 4mm.

 Load – deflection diagrams are shown in Figure 3.
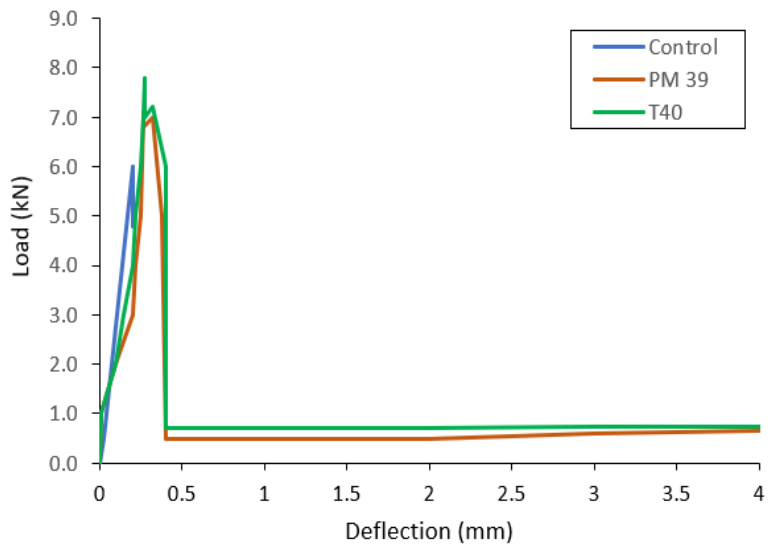

Figure 3: Diagrams of load-deflection curves for the determination of first peak load P_{f_p}

Based on the calculation formula according to SRPS EN 14488-3, the ultimate flexural strengths in N/mm^2 were obtained. Residual deformation strengths of 1, 2 and 3 mm beams were less than 1 MPa except for the control fiber-free concrete. The obtained test results are shown in Table 4.

Table 4 - Test results for shotcrete beams at the age of 28 days

	Maximal load	Ultimate flexural strength	Residual flexural strength			X
	P_{ult}	f_{ult}	f_{r_1}	f_{r_2}	f_{r_3}	
	kN	N/mm^2	N/mm^2			mm
Control - without fibers	6.0	3.9	-	-	-	22.5
Beam with Sika fibers PM 39	7.1	4.5	<1	<1	<1	22
Beam with Sika fibers T 40	7.8	5.0	<1	<1	<1	21

4 CONCLUSIONS

Based on the results obtained from testing the fibre reinforced concrete beams, the following can be concluded:

- Control beam (shotcrete without polypropylene fibres) had lower load compared to other concrete mixes and brittle fracture,

- Beams with polypropylene fibres Sika fibres PM 39 had achieved maximum load of 7.1 kN and ultimate flexural strength of 4.5 N/mm^2,

- The highest load was obtained for shotcrete with 4kg/m^3 polypropylene Sika fibres T-40. The fibres were well distributed and oriented in the cement matrix, the maximum load was 7.1kN and ultimate flexural strength 5.0 N/mm^2,

- Beams reinforced with polypropylene fibres had residual flexural strengths of less than 1 N/mm^2.

Both types of shotcrete with fibres (Sika fibres PM 39 and T 40) were D1S4 residual strength class according to SRPS EN 14487-1:2005.

The obtained test results suggest that a slight advantage can be given to Sika fibre T-40 fibres. Beams with these fibres achieved higher maximum load, ultimate flexural values and ultimate flexural strength.

ACKNOWLEDGMENTS

REFERENCES

[1] Franzen, T., 1992. Shotcrete for underground support: a State-of-the-art report with focus on steel-fibre reinforcement. Tunn. Undergr. Sp. Tech. 7 (4), 383-391
[2] S.A. Austin, P.J. Robins, C.I. Goodier, Construction and repair with wet-process sprayed concrete and mortar, a preview of the forthcoming UK Concrete Society technical report, Shotcrete Mag. 4 (1) (2002) 10–12
[3] P. Gupta, N. Banthia, C. Yan, Fiber reinforced wet-mix shotcrete under impact, J. Mater. Civ. Eng. 12 (1) (2000) 81–90.
[4] A.A. Shah, Y. Ribakov, Recent trends in steel fibered high-strength concrete, Mater. Des. 32 (8–9) (2011) 4122–4151.N. Banthia, R. Gupta, Influence of polypropylene fiber geometry on plastic shrinkage cracking in concrete, Cem. Concr. Res. 36 (7) (2006) 1263–1267
[5] SRPS EN 14487-1:2010, Sprayed concrete - Part 1: Definitions, specifications and conformity
[6] SRPS EN 14488-3:2010, Testing sprayed concrete - Part 3: Flexural strengths (first peak, ultimate and residual) of fibre reinforced beam specimens
[7] SRPS EN 14488-5:2010, Testing sprayed concrete - Part 3: Determination of energy absorption capacity of fibre reinforced slab specimens.

18

Jakob Šušteršič, David Polanec, Rok Ercegovič, Andrej Zajc

Evaluating the impact of age on the behaviour of SFRC during flexural loading

UP

EVALUATING THE IMPACT OF AGE ON THE BEHAVIOUR OF SFRC DURING FLEXURAL LOADING

Jakob Šušteršič[1], David Polanec[2], Rok Ercegovič[3] and Andrej Zajc[†4]

[1,2,3,4] IRMA Institute for Research in Materials and Applications
Špruha. 18, 1236 Trzin
e-mail: jakob.sustersic@irma.si, david.polanec@irma.si, rok.ercegovic@guest.arnes.si

SUMMARY: The paper gives and evaluates the results of flexural tests of 3-day-old to 4-year-old Steel Fibber Reinforced Concretes (SFRCs). Flexural behaviour of SFRC was measured on beams with dimensions 100 × 100 × 400 mm (span length of 300 mm). A static four-point flexural configuration was used for measurements in accordance with the Japanese standard JSCE-SF4. Deflection measured at midspan increased with a constant rate of 0,5 mm/min during the testing. The parameter that was used to evaluate the impact of age on the behaviour of SFRC during flexural loading is equivalent flexural strength $\overline{\sigma}_b$. It is proposed by JSCE-SF4 and calculated by considering area under load-deflection curve up to the deflection of L/150 = 2 mm (span L = 30 cm). In addition, the impact of age on the behaviour of SFRC during flexural loading was further evaluated by ductility factor 1/B. It is a parameter for evaluating the behaviour of SFRC, which considers the entire surface under the load – deflection curve. Both parameters ($\overline{\sigma}_b$ and 1/B) show a similar impact of age on SFRC behaviour. A slightly different estimate of the impact of age is obtained when the equivalent strength is considered, which is calculated from the surface under the load-deflexion curve to the characteristic deflexion of fracture zone Δ_δ, which also varies with the age of the SFRC.

KEY WORDS: Steel Fibre Reinforced Concrete, flexural load, equivalent flexural strength, ductility factor, characteristic deflection of fracture zone.

1   INTRODUCTION

The ability of fibre reinforced concrete (FRC) to withstand large deformations after cracking, before failure, is often measured by the toughness index. However, what is the best definition of toughness index is still the subject of numerous research papers. The main parameters influencing the toughness rating are fibre type and geometry, fibre quantity, matrix composition and quality, test body size, load configuration and speed, deformation measurement accuracy, load control method and stiffness of the test machine relative to the stiffness of the test body.

While uniaxial tension tests provide the most fundamental material properties, conducting closed-loop tension tests are difficult to accomplish; therefore, methods based on indirect measurement of tensile properties using flexural tests are typical used [1]. In the standardized slow flexure methods, JSCE SF-4 and ASTM C 1018, a measure of toughness is derived from analysis of the load-deflection curve [2–4].

In our investigations, which we discuss in this paper, static four-point flexural configuration was used for measurements in accordance with the Japanese standard JSCE-SF4. In this standard, the ratio between toughness and deflection (L / 150) gives the average load. The equivalent flexural strength $\overline{\sigma}_b$, determined from the average load, is denoted as the flexural toughness index. Equivalent flexural strength $\overline{\sigma}_b$ was used as the parameter to evaluate the impact of age on the behaviour of SFRC during flexural loading. The ductility factor 1/B was also used for the subject estimate. The ductility factor 1/B was already used to assess the ductile behaviour of 4-year-old SFRCs in a related study [5], where wedge splitting test (WST) method was used [6].

The hardened cement paste connects the aggregate particles and the fibres. Physical interactive influences are mostly decisive, and only rarely is there a chemical bond. Crystals from a highly saturated solution, calcium hydroxide lamellae, grow on the surfaces of aggregate particles and fibres. This layer has less hardness and strength than hardened cement paste. The test shows that the thickness of the transition zone is difficult to influence by changing the w/c ratio, like the mean distance between the aggregate particles in concrete [7]. For this reason, the mechanical properties of concrete

and FRC are highly dependent on the transition zone. The transition zone is about 3 times more porous than compact cement paste mortar, which coincides very well with the experimental results [8]. It can be observed that the porosity of the transition zone decreases during the maturation of the mortar, while the porosity of the compact cement paste remains relatively equal. These tendencies can be explained by various phenomena. The diffusion of ions, due to the porosity gradient, from the compact cement paste towards the transition zone [9-10], which allows non-hydrated cement particles to hydrate, contributes to the reduction of the porosity of the interface. As the cement paste contains less water than the transition zone, the hydration kinetics are lower and its porosity does not vary significantly during mortar aging.

The transition zone can be significantly thickened by adding additives such as silica fume, fly ash and slag and thus increase the strength of the concrete. Silica fume is the most efficient, because small particles increase the volume, which surrounds cement particles and, due to their large specific surface area, hydrate much faster than fly ash or slag. In addition, CH is converted to CSH, reducing the amount of CH crystals in the cement paste-aggregate and fibre particles interface.

2 EXPERIMENTAL DETAILS

2.1 Concrete without fibres and SFRC mix-proportions

The mix-proportions of concrete without fibres and SFRC are given in Table 1.

Table 1: Mix-proportions (per 1 m^3 of concrete mixture)

Designation	w/b ratio	Cement (C)	Silica fume	Steel Fibres	Super-plasticizer	air-entraining admixture	Aggregate D_{max}
	(-)	(kg)	(% of C)	(% by vol.)	(% of C)	(% of C)	(mm)
FC-0	0,35	320	9,4	0	2,0	0,20	16
FC-0,5	0,35	330	9,4	0,5	2,0	0,15	16
FC-1	0,35	348	9,4	1,0	2,0	0,30	16
FC-1,5	0,35	375	9,4	1,5	2,0	0,20	16
FC-2	0,35	393	9,4	2,0	2,0	0,20	16

2.2 Characteristic properties of the materials used for concretes

Steel Fibres: hooked steel fibres with length l_f = 33 mm and diameter d_f = 0,50 mm, aspect ratio l_f/d_f = 66. The fibres are produced from wire with an average maximum tensile strength R_m = 841 N/mm^2.

Cement: Portland cement CEM I 42,5 was used to prepare the concretes.

Silica fume: fine amorphous dust in the form of balls of average diameter 0,1 µm; SiO_2 content is 94,0%.

Superplasticizer: modified polycarboxylate; its density is 1,2 kg/dm^3.

Air-entraining admixture: it is made based on vinyl resin; its density is 1,1 kg/dm^3.

Gravel aggregate: fraction of fine aggregate is 0-4 mm, fractions of coarse aggregate are 4-8 and 8-16 mm.

2.3 Program of investigations

A load-deflection diagram was obtained for each test (Figure 1). Each concrete was tested on 3 prisms at ages 3, 7, 28, 90, and 1440 (4 years) days. The Japanese standard JSCE-SF4 prescribes a procedure for testing the flexural strength and toughness of FRC on prisms loaded with concentrated forces in thirds of the range. The toughness of FRC is determined by the area under the load-deflection diagram up to a certain limit. The standard selects the limit at a point for which the deflection is equal to 1/150 of the range. If the deflection limit is taken too small, the influence of fibre content and type on the toughness parameter is not sufficiently pronounced. On the other hand, if an excessive deflection limit is taken, in many cases deflection measurement problems will arise. Considering the results of tests on prisms 10 ×

10 × 40 cm, if the deflection limit of 2 mm is taken, the differences in the quantities and types of fibres are well recognized for most fibres in use.
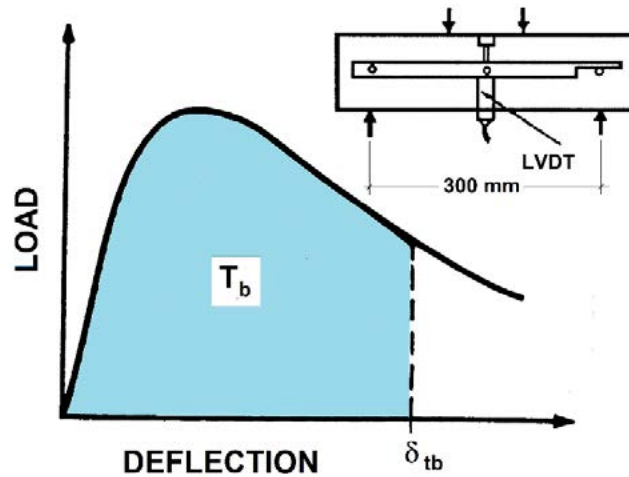

Figure1: Schematic diagram of the load-deflection and test configuration according to the JCSE-SF4

Equivalent flexural strength is calculated from the equation:

$$\bar{\sigma}_b = \frac{T_b}{\delta_{tb}} \times \frac{L}{w \times h^2} \tag{1}$$

where are: $\bar{\sigma}_b$ – equivalent flexural strength (MPa); T_b – toughness (N.mm); δ_{th} – deflection (δ_{th} = 1/150 × L) (mm); L – span length = 300 mm: w – specimen width (mm); h - specimen hight (mm).

An estimate of the ductile behaviour of the FRC can also be determined from the load-deflection diagram. For this purpose, the characteristic deflection of fracture zone is determined by the equation:

$$\Delta_\delta = \frac{W_{FZ}}{F_{LP}} \tag{2}$$

where are: Δ_δ - characteristic deflection of fracture zone (mm); W_{FZ} – absorbed energy of fracture zone (N.mm); F_{LP} - load at limit of proportionality (N).

When defining the absorbed energy can be considered that the formation of the FRC fracture zone begins after the limit of proportionality. In the fracture zone, all further fracture processes proceed until the final separation of the test body. W_{FZ} represents the required absorbed energy to completely separate the test body.

The characteristic deflection of the fracture zone Δ_δ is the property of the material (composite, in our example FRC) based on which we can assess the ductility of the material with respect to the deflection at the limit of proportionality (δ_{LP}); the material is ductile if $\Delta_\delta > \delta_{LP}$ and conversely the material is brittle if $\Delta_\delta < \delta_{LP}$. Ductility can be expressed by the dimensionless ductility factor 1/B, which is the next parameter for evaluating the behaviour of FRC over time and which is expressed by the equation:

$$1/B = \frac{\Delta_\delta}{\delta_{LP}} \tag{3}$$

where are: 1/B - ductility factor (-); Δ_δ - characteristic deflection of fracture zone (mm); δ_{LP} - deflection at the limit of proportionality (mm).

The ductility factor 1/B is higher and thus the ductility of the tested FRC, the higher the characteristic deflection of the fracture zone Δ_δ, which means that the FRC must achieve the highest absorbed energy of the fracture zone W_{FZ} at the corresponding load at the limit of proportionality F_{LP}.

The ductility factor 1/B expresses the ability of FRC to achieve a characteristic deflection Δ_δ = 1/B × δ_{LP} in the fracture

zone, i.e. after the limit of proportionality. 1/B actually represents a multiple of the deflection at the limit of proportionality δ_{LP}. Up to this multiple of δ_{LP}, that is, up to the characteristic deflection of fracture zone Δ_δ, the equivalent strength $\overline{\sigma}_{\Delta\delta}$ can be calculated (equation (4)), like the equivalent strength $\overline{\sigma}_b$ according to the Japanese standard JSCE-SF4 (equation (1)).

$$\overline{\sigma}_{\Delta_\delta} = \frac{T_{\Delta_\delta}}{\Delta_\delta} \times \frac{L}{w \times h^2} \tag{4}$$

where are: $\overline{\sigma}_{\Delta\delta}$ – equivalent flexural strength up to characteristic deflection of fracture zone (MPa); $T_{\Delta\delta}$ – toughness up to Δ_δ (N.mm); Δ_δ - characteristic deflection of fracture zone (mm); L – span length = 300 mm: w – specimen width (mm); h - specimen hight (mm).

3   RESULTS AND DISCUSSION

The increase in the value of the maximum flexural strength (f_{max}), concrete of different ages, depending on the volume percentage of added steel fibres can be seen from Figure 2. Exponential regression curves were determined.
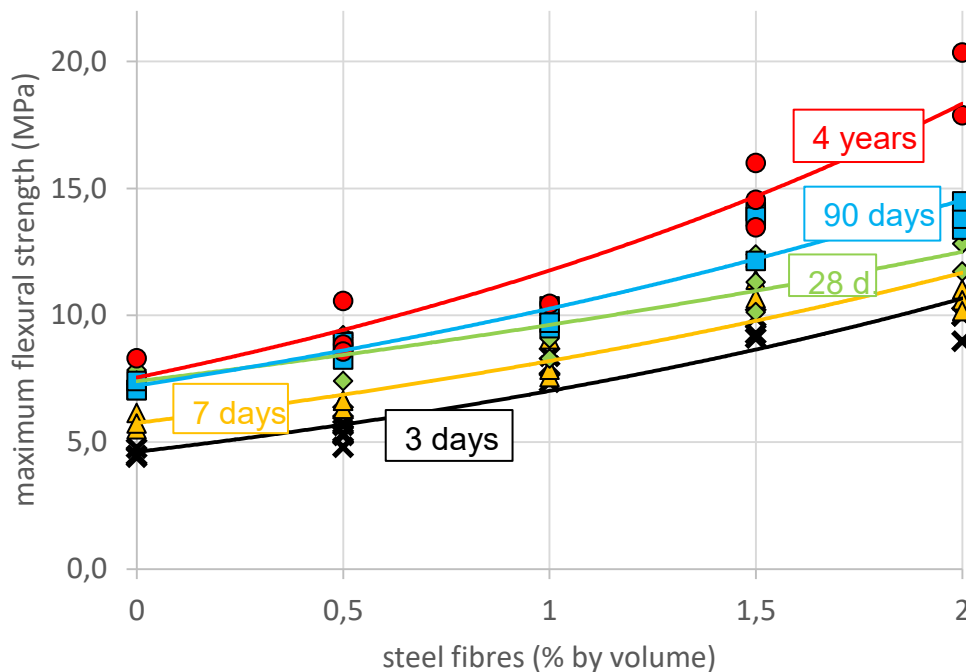

Figure 2: Increasing the value of f_{max}, concrete of different ages, depending on the volume percentage of steel fibres

The maximum flexural strength f_{max} increases with respect to the age of the concrete and the volume percentage of steel fibres. In the first 28 days, with more "intensive" hydration of cement, the matrix gains in strength and the strength at the limit of proportionality increases more than f_{max} due to the lower efficiency of a certain quantity of fibres (adhesion to cement stone). After that the adhesion increases which leads to a more intense increase in f_{max}.

Similar SFRC behaviour over time was obtained by evaluating the equivalent flexural strength $\overline{\sigma}_b$ according to the Japanese standard JCSE-SF4 (Figure 3). The equivalent flexural strength $\overline{\sigma}_b$, as the index of flexural toughness to deflection L/150, evaluates the behaviour of SFRC after the highest load where the fibres become more active. Therefore, the increase in $\overline{\sigma}_b$ after 28 days is higher in SFRC with a higher quantity of fibres (Figure 3).

The correlation between the age of SFRC and the volume percentage of steel fibres by the ductility factor 1/B is given in Figure 4. The ductility factor 1/B is calculated by equation (3) and is a parameter for evaluating the behaviour of SFRC, which considers the entire surface area of the load - deflection diagram. In this way, it is possible to evaluate the behaviour of SFRC with only one parameter. Ductility factor 1/B is an index, which expresses the relationship between absorbed energies (fracture zone and elastic zone).
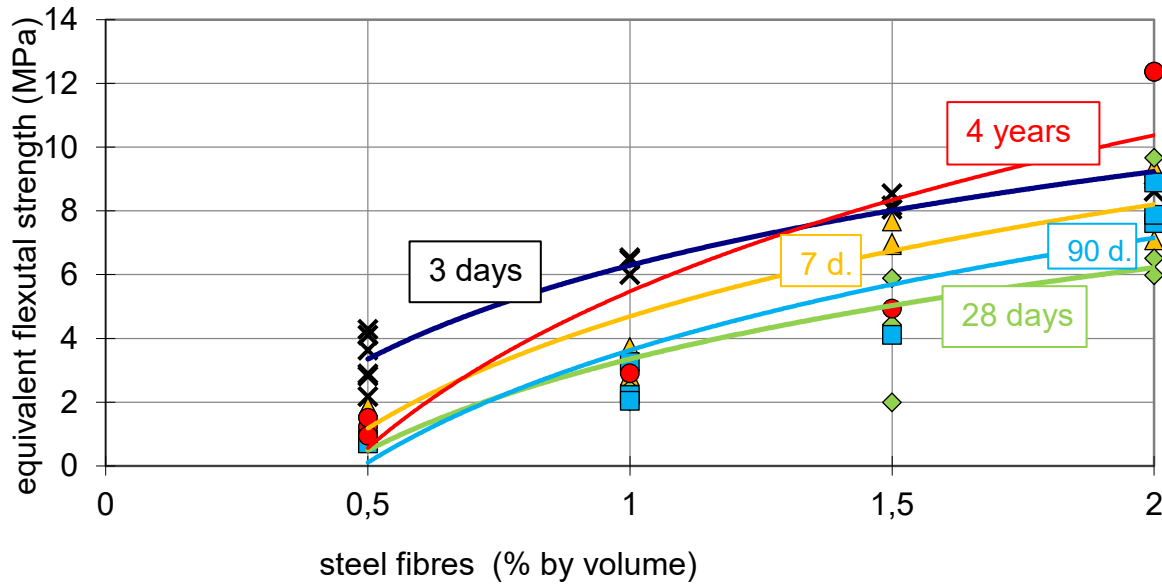
Figure 3: Ratio of equivalent flexural strength $\overline{\sigma}_b$ of SFRC of different ages and volume percentage of added steel fibres
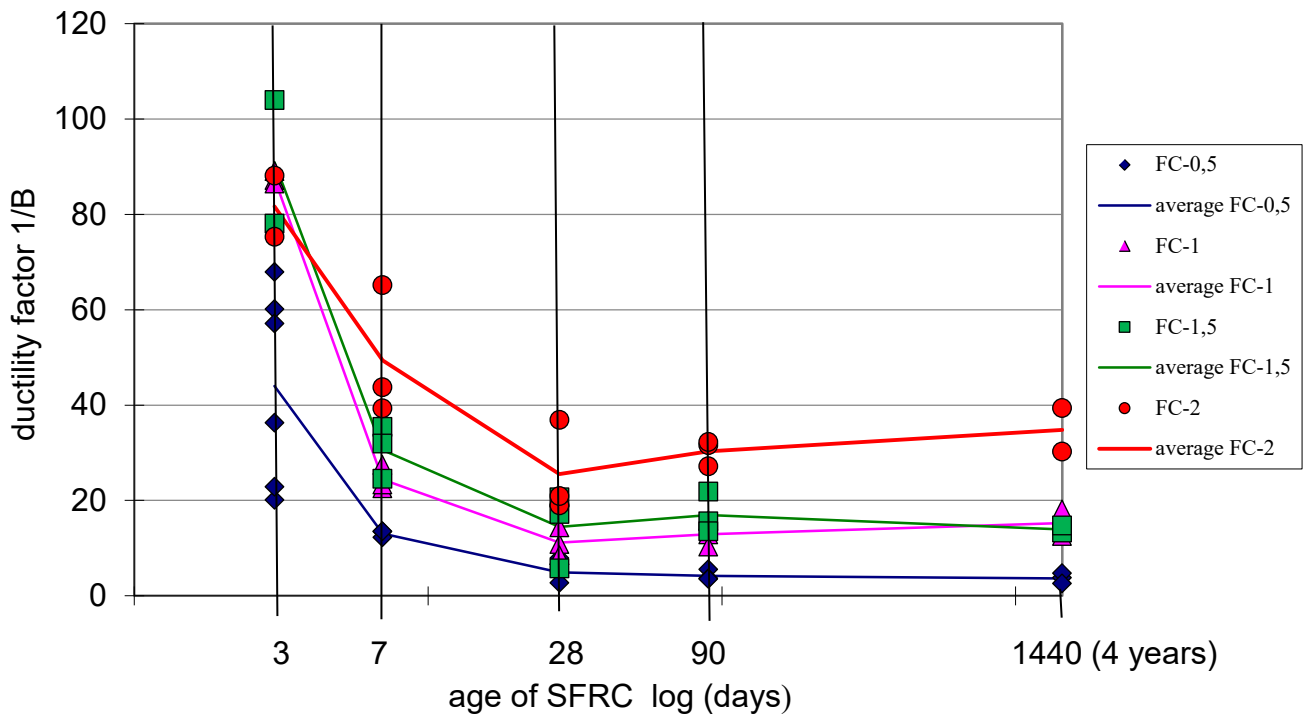

Figure 4: Correlation of ductility factor 1/B, SFRC age and steel fibre volume percentage

The equivalent flexural strength up to characteristic deflection of the fracture zone $\overline{\sigma}_{\Delta\delta}$ was calculated according to equation (4). Figure 5 shows the dependence of the quantity of steel fibres, the equivalent flexural strength up to characteristic deflection $\overline{\sigma}_{\Delta\delta}$ and the age of the SFRC.

If we compare the equivalent strengths $\overline{\sigma}_b$ (Figure 3) and $\overline{\sigma}_{\Delta\delta}$ (Figure 5) of individual SFRCs, we can see the difference in behaviour over time (Figure 6). Equivalent strengths $\overline{\sigma}_b$ are highest in all SFRCs at 3 days of age, after which the values decrease to 28 days and then increase. The lowest values of $\overline{\sigma}_{\Delta\delta}$ were obtained at the age of SFRC 3 days, and with age these values increase. The mutual comparison of the average values of $\overline{\sigma}_b$ and $\overline{\sigma}_{\Delta\delta}$ at individual ages is well visible from Figure 6.
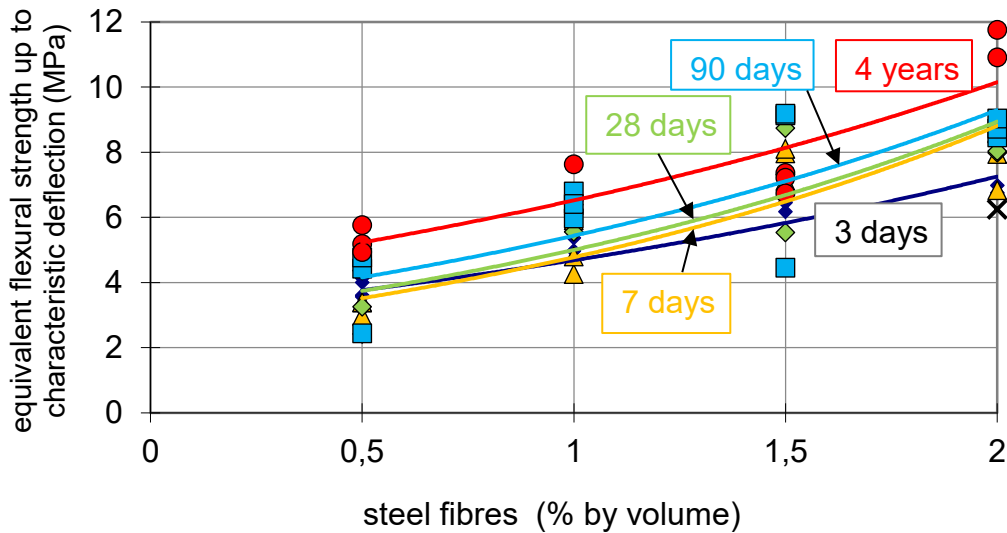
Figure 5: Correlation of the quantity of steel fibres and equivalent strength to the characteristic deflection $\overline{\sigma}_{\Delta\delta}$ at different ages of SFRC
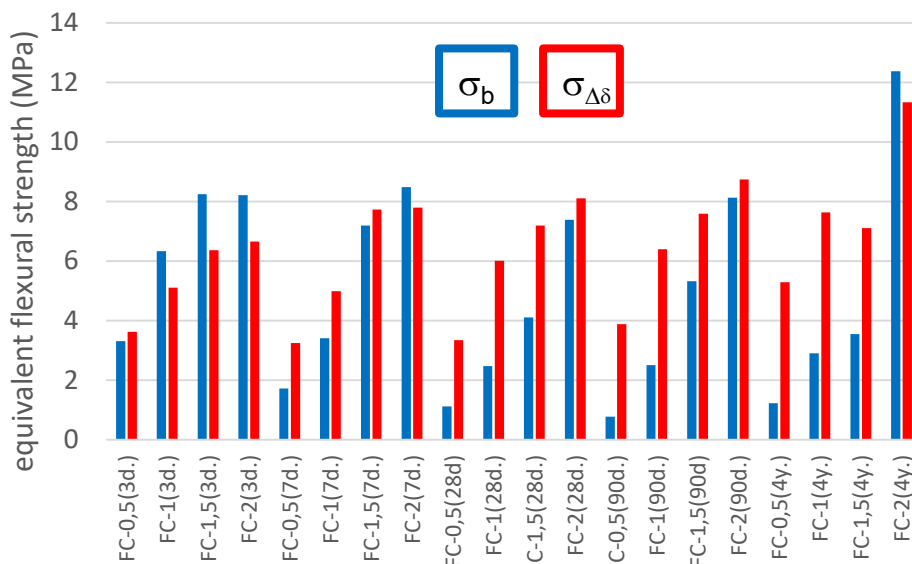

Figure 6: Comparison of average equivalent flexural strengths $\overline{\sigma}_b$ and $\overline{\sigma}_{\Delta\delta}$ at individual ages of SFRC

In all SFRCs, except FC-2, $\overline{\sigma}_b$ is greater than $\overline{\sigma}_{\Delta\delta}$ only at 3 days of age, and after that age $\overline{\sigma}_{\Delta\delta} > \overline{\sigma}_b$. For FC-2, the values of both equivalent strengths differ slightly. $\overline{\sigma}_b$ is calculated to a constant deflection, regardless of the change in concrete behaviour over time, while $\overline{\sigma}_{\Delta\delta}$ is calculated to the characteristic deflection of the fracture zone, which changes over time. For this reason, it can be said that with equivalent strength up to the characteristic deflection of the fracture zone $\overline{\sigma}_{\Delta\delta}$ the behaviour of SFRC is better evaluated due to considering its actual capacity. The changes in the values of $\overline{\sigma}_b$ and $\overline{\sigma}_{\Delta\delta}$ (Figure 6) can thus be explained by changes in the values of the characteristic deflection of the fracture zone Δ_δ. It can be said that $\overline{\sigma}_{\Delta\delta} > \overline{\sigma}_b$ when $\Delta_\delta < L/150 = 2$ cm. The equivalent flexural strength expresses the required strength, which the SFRC must have to achieve a certain prism deflection.

4   CONCLUSIONS

To conclude, we summarize the findings of the discussion of test results of 3-day to 4-year-old SFRCs obtained by a four-point flexural test according to the Japanese standard JSCE-FC4.

Similar SFRC behaviour over time was obtained by evaluating the maximum flexural strength f_{max}, the equivalent flexural strength $\overline{\sigma}_b$ according to the JCSE-SF4, as well as ductility factor 1/B. The equivalent flexural strength $\overline{\sigma}_b$, as the index of flexural toughness to deflection L/150, evaluates the behaviour of SFRC after the highest load where the fibres become more active. Therefore, the increase in $\overline{\sigma}_b$ after 28 days is higher in SFRC with a higher quantity of fibres.

The ductility factor 1/B is a parameter for evaluating the behaviour of SFRC, which considers the entire surface area of the load - deflection diagram. It is an index, which expresses the relationship between absorbed energies of fracture zone and elastic zone.

The difference in SFRC behaviour over time was obtained by evaluating the equivalent flexural strength $\overline{\sigma}_b$ and the equivalent flexural strength up to characteristic deflection of the fracture zone $\overline{\sigma}_{\Delta\delta}$. $\overline{\sigma}_b$ is calculated to a constant deflection, regardless of the change in concrete behaviour over time, while $\overline{\sigma}_{\Delta\delta}$ is calculated to the characteristic deflection of the fracture zone, which changes over time. For this reason, it can be said that with equivalent strength up to the characteristic deflection of the fracture zone $\overline{\sigma}_{\Delta\delta}$ the behaviour of SFRC is better evaluated due to considering its actual capacity. It can be said that $\overline{\sigma}_{\Delta\delta} > \overline{\sigma}_b$ when characteristic deflection of fracture zone $\Delta_\delta < $ L/150 = 2 cm.

ACKNOWLEDGMENTS

REFERENCES

[1] ACI Committee 544: Report in Indirect Method to Obtain Stress-Strain Response of Fiber-Reinforced Concrete (FRC), *ACI Collection of Concrete Codes, Specifications, and Practices, Part 8*, American Concrete Institute, ISBN 978-1-64195-087-9, (2020), pp. ACI 544.8R-16: 1 – 22.

[2] Johnston, C.D.: Toughness of Steel Fiber Reinforced Concrete, *Steel Fiber Concrete*, Elsevier Applied Science Publishers, Ltd, (1986), pp. 333 – 360.

[3] Nanni, A.: Ductility of Fiber Reinforced Concrete, *Journal of Materials in Civil Engineering*, ASCE, V.3, No. 1, (1991), pp. 78 – 90.

[4] Gopalaratnam, V.S., Shah, S.P., Batson, G., Criswell, M., Ramakrishnan and Wecharatana, M.: Fracture Toughness of Fiber Reinforced Concrete, *ACI Materials Journal*, V. 88, No. 4, (1991), pp. 339 – 353.

[5] Šušteršič, J., Ercegovič, R., Polanec, D. and Zajc, A.: Ductility of the Four-Year-Old Steel Fibre Reinforced Concrete, *Fibre Reinforced Concrete: Improvements and Innovations, RILEM-fib International Symposium on FRC (BEFIB) in 2020*, Serena, P., Llano-Torre, A., Marti-Vargas, J.R. and Nevarro-Gregori, J (Eds), pp. 290 – 300, ISBN 978-3-030-58481-8 (RILEM Bookseries), ISBN 978-3-030-58482-5 (e-Book), RILEM, Springer, (2020).

[6] Linsbauer H. and Tschegg, E.K.: Die Bestimmung der Bruchenegie an Würfelproben (Fracture Energy Determination of Concrete with Cube-Shaped Specimens), *Zement und Beton*, (1986) 31 (1), pp. 38 – 40.

[7] Diamond S., Mindess S., Lovell J.: On the Spacing between Aggregate Grains in Concrete and the Dimension of the Aureole of Transition, *RILEM Colloquium*, Toulouse, (1982), pp. C42 - C46.

[8] Scrivener K.L., Crumble A.K., Pratt P.L.: Bonding in Cementitious Materials, *MRS*, 114. Ed.: S. Mindess, S.P. Shah, (1988).

[9] Maso J.C.: 7ème Congrès International de la Chimie des Ciments. *Septima*. Paris, (1980), pp. VII-1/3.

[10] Scrivener K.L., Pratt P.L.: State of the Art Report. RILEM TC 108.

19

Arta Sylejmani, Ivana Banjad Pečur, Bojan Milovanovic

Consumption and potential energy savings in the office building

CONSUMPTION AND POTENTIAL ENERGY SAVINGS IN THE OFFICE BUILDING

Arta Sylejmani[1], Ivana Banjad Pečur[2] and Bojan Milovanovic[3]

[1] Municipality of Prishtina, St.UÇK 2, 10000 Prishtina, Kosovo,
e-mail: selimiarta@gmail.com

[2, 3] University of Zagreb, Faculty of Civil Engineering, Department of Materials
Kačićeva 26, 10000 Zagreb, Croatia
e-mail: ivana.banjad.pecur@grad.unizg.hr; bojan.milovanovic@grad.unizg.hr

SUMMARY: This research illustrates the concept of using dynamic simulation as an instrument for the assessment and analysis of the final energy performance for the new office building of the Municipality of Prishtina. The aim is to analyse the energy performance in this building by predicting energy consumption during the phase of further interventions. The same analysis were done also for other two cities such as Peja and Ferizaj.

In this study, the total energy consumption was examined for this building model according to the detailed design project through dynamic simulation calculated by ARCHICAD tool and add-in EcoDesigner Star. The results of this paper suggest that much better improvement can be achieved by intervening in building envelope than in high-cost equipment.

KEY WORDS: Building of Prishtina Municipality, energy performance, dynamic simulation, energy consumption, intervention.

1   INTRODUCTION

People spend 60-90% of their lives indoors [1] hence the quality of indoor air in buildings is essential for healthier living. Achieving natural thermal comfort requires the expenditure of natural resources. Today, buildings and construction sectors have accounted for almost 40% of final energy consumption globally [2], [3]. Although European countries have determined that all new buildings by the end of 2020 should achieve the nZEB [4] and this is one of the biggest challenges that these countries are facing. These problems are much worse in most underdeveloped countries that are going through rapid urbanization, such as Prishtina. Currently, in Prishtina, in addition to this urban growth and daily needs, the production of electricity is insufficient [5]. The construction sector, especially in Prishtina, shows high figures of the final energy consumption [6]. Only in the first quarter of 2020 compared to 2019, the amount of electricity for consumption has increased by 6.4% [7]. This trend of increasing electricity consumption definitely requires in-depth studies aimed at research on taking measures for its more rational use.

Improving the energy efficiency of the building has so far not received enough attention from the central and local government of Kosovo [8], although a variety of efforts, activities and strategies have been identified, such as laws, administrative instructions, regulations as well as a series of concrete projects where their use is proving to be challenging for many decision makers in Kosovo. Interventions to improve energy performance in buildings are mainly made in public buildings, although they represent only 4.5% of the total construction area [9]. This initiative, although good, is still considered to be insufficient to achieve energy savings of up to 32% by 2030 [10], [11].
Intervention in public buildings regarding energy efficiency is one of the most cost-effective ways to increase security of energy supply and reduce demand for it. Access to these buildings is much easier and the opportunities for saving public money are more favourable, so Prishtina as the capital has had the opportunity to absorb larger funds from the central budget as well as various donors. But the interventions are mostly becoming ad-hoc, short-term and not where it is really needed and, in most cases, what is expected is not being achieved.

Today there are many studies on the ways and definition of interventions in public buildings regarding simulations and measures to be taken to save energy in them. While some studies aim to create a model building to be used to assess energy saving opportunities in buildings with the same categories and features, others do simulations and measures separately in each building with the purpose of all possibilities for interventions in them are precisely defined.
Over the last few decades, there have been many researches on the office building energy performance and its evaluation [12–18]. Hernandez et al. [12] have evaluated the energy demand in an administrative building with a large

glazed area. Moreover, they have shown that only the HVAC system for cooling is effortless and the use of shading devices affects both the thermal aspect and the visual comfort. A similar study on the influence of window wall ratio of different orientation and size of windows on the energy performance of have done also [13] and [14]. While Boyano et al. [15] have analysed the energy demand and the possibilities for its conservation through several European office buildings. Moreover, they have demonstrated that in some places where thermal insulation had to be added to the building envelope, in other places for the building with the same performance energy had to be spent on cooling. Ferrari and Beccali [16] explored some reconstruction options for an existing administrative building in Milan with the aim of achieving very high energy performance. They managed to improve the thermal insulation of roof, facades and improvements in monitoring technology, is the reduction of the primary energy consumption costs was about 40%. Improvement of building envelope has also been studied by Yu et al. [17] and Corgnati et al. [18] where they have analysed the energy required for heating and cooling of a public administrative building in three different climatic zones.

Therefore, taking into account all the practices and methods of these studies, the purpose of this paper is to calculate the energy performance in the new building of the municipality of Prishtina with the main purpose to analyse its current state and identify through computer simulations measures to be taken for its energy consumption and reduction up to 50%. Energy simulations of this building, in addition to the current location in the neighborhood Arbëria 3, in Prishtina, have been calculated in the city of Peja and Ferizaj. These locations were selected because the Administrative Instruction of the national calculation methodology consider these cities as a reference for the entire territory of Kosovo [19].

The whole work is structured as follows: after the introduction, chapter II contains the working methodology and to continue with chapter III with calculation of energy consumption and energy saving potentials which summarizes the results and conclusions of the elaborated discussions.

2   METHODOLOGY

The proposed methodology is based on research and simulation process which consists of three main phases. First, to evaluate the energy consumption calculation process, a model of this office building was created for simulation in the add-in application EcoDesigner Star which operates within the ARCHICAD software [20]. The second phase involves the same building located in two other cities, to analyses and compare the results of this energy performance. Third, measures are foreseen for the intervention in the building, so that the reduction of the total energy is up to 50%.

The work process is related to building energy performance and has followed these steps:

- Building modelling as a building reference;
- Calculation of energy consumption based on the detailed project of the building;
- Calculation of energy consumption in two other cities;
- Possible interventions for energy improvements.

2.1 Building characteristics and locations

The Municipality of Prishtina, has two main buildings which are in function for services to citizens. The first building was built during the 1950s to the 1970s, when under the motto "destroy the old and build the new" parts of the city's neighborhoods were demolished, including the old city bazaar, on which this building was built [21]. Since then, the administrative-political city, in addition to urban growth and population growth, increased the demand for access to municipal services, so in 2009 the other building of the Municipality of Prishtina in the neighborhood Arbëria 3 was built and released for use. The building which was studied for energy performance is exactly the one that was functionalized in 2009 and since it does not have documentation of the as-build project, this work relies only on the detailed design project of this building.

Figure 1.Office building of Prishtina Municipality [22]

Arbëria 3 is a relatively new neighborhood, and is considered a strategic place where currently most of the embassies are located there and where is a connection of the highways of Prishtina with other northern cities. The Municipal Building has an almost rectangular base, 5 floors above ground and a capacity of about 250 workplaces. The organization of this building is open with common workspaces including offices, meeting rooms, and secondary rooms. The building is surrounded by a structural facade around which these workspaces are organized. External envelope area is 5745.02 m^2. Also, in the envelope of this building on each floor are integrated shading devices to prevent the penetration of sunlight. Further data on the design and organization of this office building are provided in table 1 and figure 3.

Table 1. Constructive characteristics of the new building of the Municipality of Prishtina

Location:	Prishtina	**Latitude:** 42˚ 39ʹ 24ʺ N	**Longitude:** 21˚ 8ʹ 41ʺ E
	Peja	**Latitude:** 42˚ 39ʹ 33ʺ N	**Longitude:** 20˚ 17ʹ 20ʺ E
	Ferizaj	**Latitude:** 42° 22ʹ 5ʺ N	**Longitude:** 21˚ 9ʹ 13ʺ E
Geometry:	Rectangular shape	**Altitude: Prishtina:** 602.70 m	**Peja:** 516.00 m, **Ferizaj:** 581.00 m
Gross Floor Area:	7774.57 m^2	**Orientation:**	East-West, North-South
Floors:	B+P+4	**External Envelope Area:**	5778.23 m^2
Ventilated Volume:	24471.91 m^3	**Prishtina HDD:** 3381.25	**CDD:** 1692.74
		Peja HDD: 4039.28	**CDD:** 1268.26
		Ferizaj HDD: 3381.25	**CDD:** 1692.74
Walls:	Autoclaved aerated concrete (25 cm)		
Roof:	Truss steel construction, 10 cm insulation, covered by corrugated metal sheet		
Glazing:	double glazing basic –air fill clear		
Floor:	recessed ceiling, insulation and artificial granite tiles		
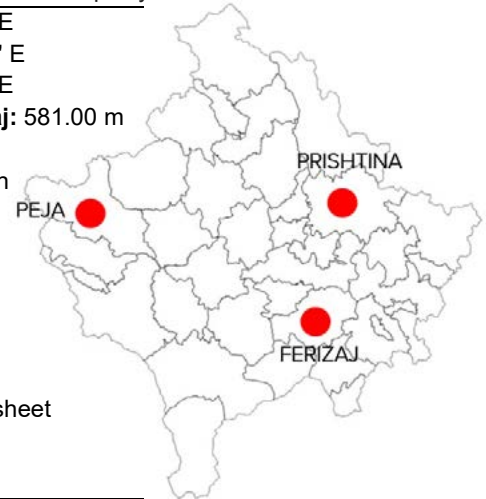
In the north-west of this building, the elevators and the central hall are oriented, while the working spaces are spread on all other sides. Offices and primary work areas are heated or cooled from 20 ◦C to 26 ◦C. Except the city of Prishtina, the same building is copied also in the city of Peja and Ferizaj, in order to analyses the energy performance in these cities and to make a comparison between them.

Figure 3, presents the project description through the thermal zones, wherefrom this we can conclude that 45% of the gross floor area is dedicated for offices, 25 % is the area for communication, 9 % multi-purpose area.


Figure 2. Project description - thermal zones

2.2 Project measurements and simulation details

Energy consumption for space heating and cooling, electricity, lighting is calculated separately but considers the influence of the internal heat loads. The office building is occupied from Monday to Friday from 7:00 to 17:00 hours. Energy consumption is simulated every hour, also office equipment were considered during the energy simulation. The city of Prishtina has continental climate, and other cities also have almost similar characteristics of the temperature but they have different sunny days. The simulation was carried out using representative Strusoft climate server [23] which contains meteorological data for each selected city for this research. Total energy demand and consumption were simulated based on project documentation, which also serves as a reference building.

After analyzing this project, 8 possibilities of intervention in the building envelope have been selected, which can be indicators or possible interventions to improve energy performance in this office building.

Figure 4, shows these parameters where the interventions were made mainly in thermal insulation, improvement of thermal bridges, building shading devices and structural facades.
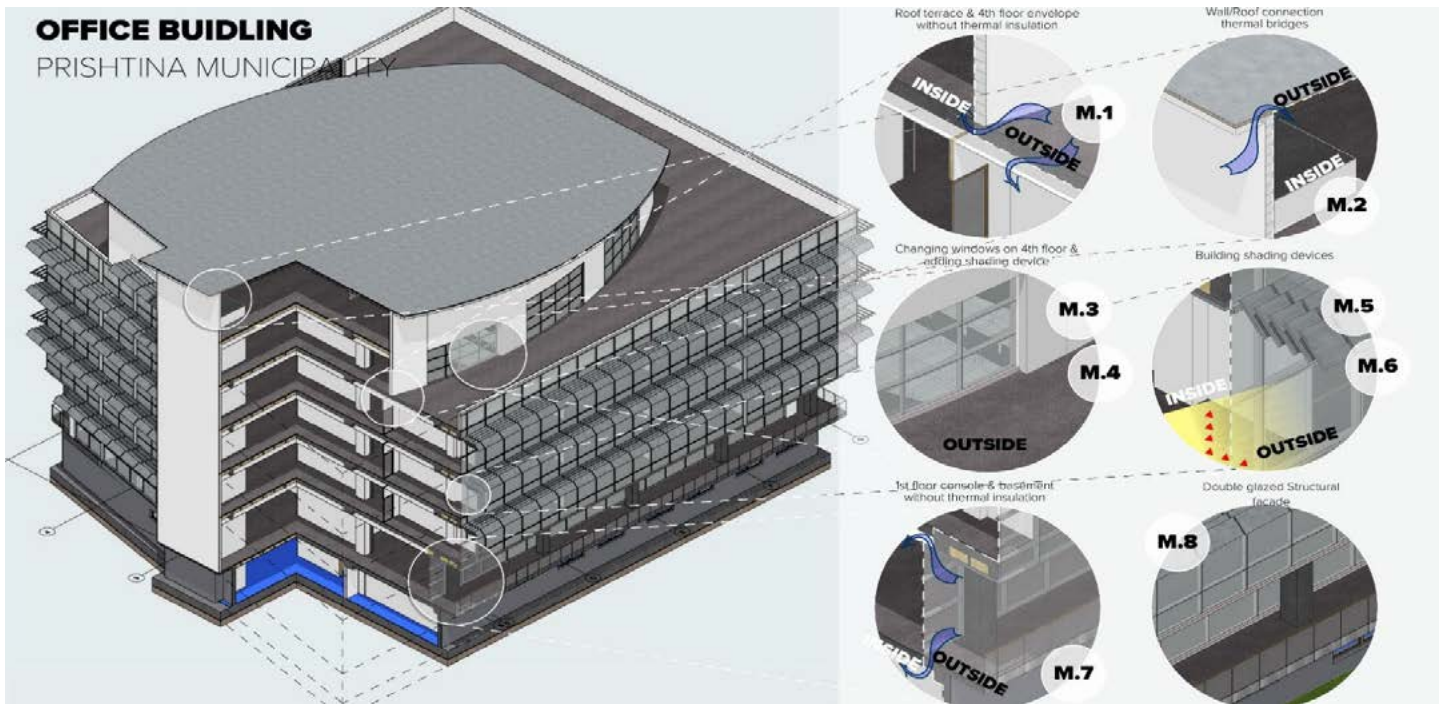
Figure 3. Possible intervention to reduce the energy demand

On the other hand, the solar radiation shown in the figure 5, are calculated for the 23ʳᵈ of July and the 19ᵗʰ of December as the most extreme periods of the year. The red colour represents the highest solar radiation.

- Solar analysis on the north-east façade shows that the existing shading devices don't have any effect;
- On the 4ᵗʰ floor on the south-west facade, solar radiation has a negative impact because it increases the demand for cooling and it is proposed to install shading devices;
- In the South-East facade, also is a need for intervention in shading devices;
- Intervention in the structural façade.
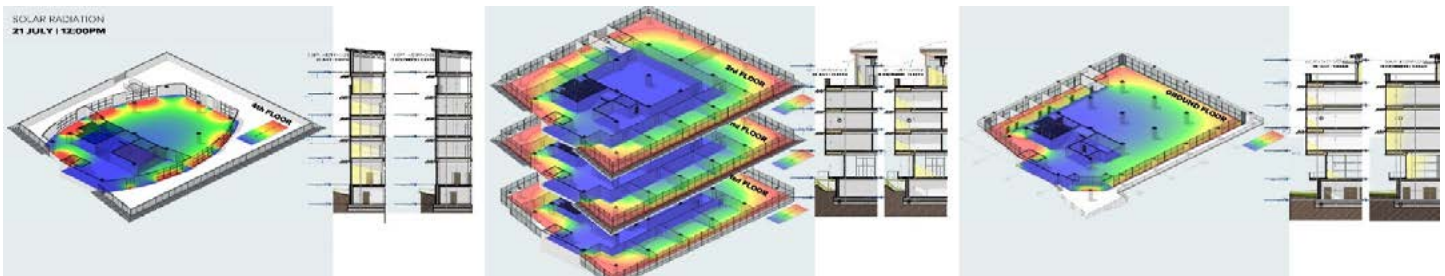
Figure 4. Analysis of solar radiation

3 RESULTS AND DISCUSSION

Based on objective data, computer simulations through EcoDesigner Star tool, we have been enabled to initially calculate the energy for cooling and heating in the new building of the municipality of Prishtina based on the project. The performance of the office building of the municipality of Prishtina during the study is clear that it is not with big differences comparing with three cities of Kosovo such as Prishtina, Peja and Ferizaj. Figure 6-a, shows the results for heating and cooling energy demand for the baseline building in Prishtina.
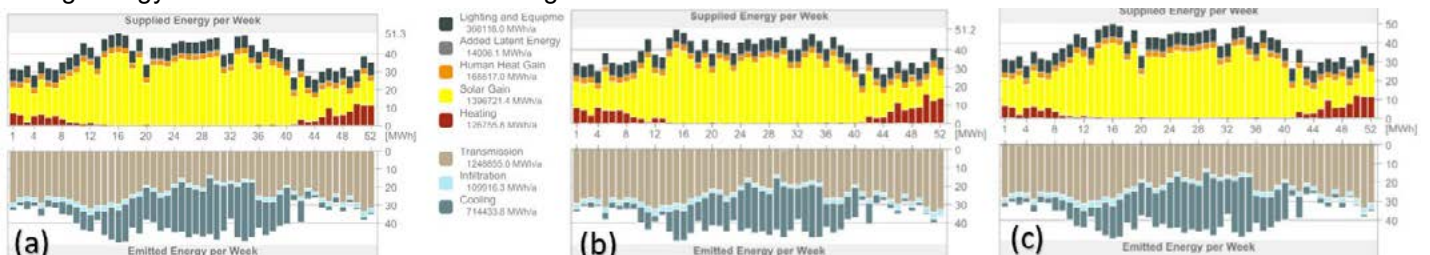
Figure 5. (a) Project of energy balance for current situation for the office building of Prishtina Municipality, (b) Peja, (c) Ferizaj

At the first phase, after the energy simulation of the detailed project, we can see that the demand for cooling is much higher (94.48 kWh/m²a) than that for heating (17.79 kWh/m²a), hence it can be seen that the high coefficient of thermal transmission in the building envelope allows large heat losses and gains between the interior and the external environment during different seasons. In the table 2 and figure 7, are presented the details of heating and cooling demand for each thermal zone and orientations, specifically the high demand for cooling is presented in thermal zones 001-3, 001-4.1, 006, 007-1, 007-3, 007-4 and 008-2. This poor performance generates high demand for cooling during the summer to achieve thermal comfort inside.

Table 2.Heating and cooling energy demands and main characteristics of the some thermal blocks

| Thermal Block	Heating Demand [kWh/a]	Cooling Demand [kWh/a]	Number of Zones	Gross Floor Area [m²]	Volume [m³]
001 Circulation and traffic areas	4710	18647	5	723.54	2063.08
001-3 Circulation and traffic areas (Mu…	**8857**	**47639**	1	681.47	2647.81
001-4 Circulation and traffic areas (Lo…	14420	27321	5	670.92	2119.46
001-4.1 Circulation and traffic areas (Lo…	**4383**	**13444**	1	239.21	656.60
003 Toilets and sanitary facilities (non …	1892	0	11	215.18	610.23
006 Meeting, conference or seminar room	**23461**	**60921**	1	431.03	1689.61
007-1 Landscaped office (South-West)	**22134**	**147945**	12	749.12	2159.19
007-2 Landscaped office (South-West…	513	1258	1	72.09	204.88
007-3 Landscaped office (South-East)	**26841**	**164486**	6	1118.37	3261.68
007-4 Landscaped office (North-East)	**2679**	**44650**	3	167.17	482.45
008 Personal office	386	1639	2	41.62	149.11
008-1 Personal office (South-West)	2776	3519	4	162.12	444.1
008-2 Personal office (North-East)	**13430**	**115682**	12	397.3	1207.1
009 Canteen	0	25950	4	147.76	414.67
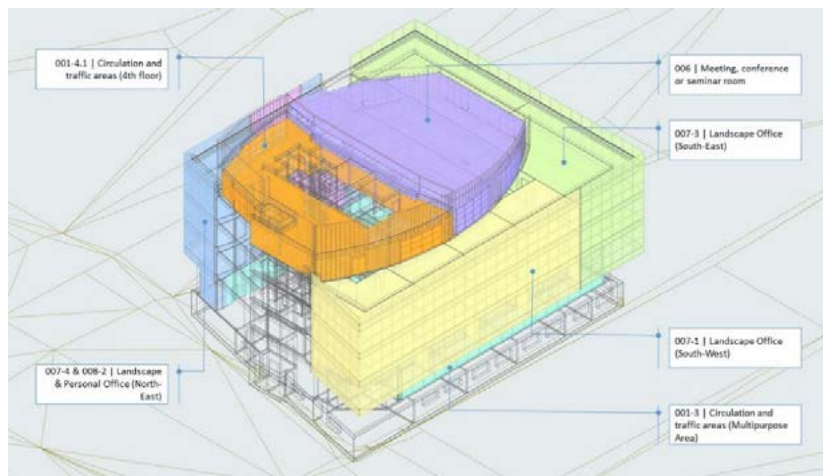
Figure 6. Thermal zones with high demand for cooling

Similar results are presented in the simulations in two other cities, and if we compare them with Prishtina the demand for heating varies from 17.79 – 22.94 kWh/m²a while the demand for cooling varies from 83.13 - 94.41 kWh/m²a. It seems to be clear that the difference in energy demand between these cities is 22% for heating and 12% for cooling as shown in figure 6 (b) and (c).

3.1 Energy consumption and energy saving potentials

Since the third part of this paper includes proposals for some interventions that will help the energy efficiency of this building, then after the intervention in the 8 positions mentioned before it was achieved the reduction of energy consumption by 51 %. Using a dynamic tool, it is possible to obtain a lot of information about the thermal behaviour of the building. In this case, through EcoDesigner Star tool, the study allows to provide information about possible energy consumption after each intervention in its envelope. As shown in figure 4, some measures have been taken to improve these parameters that have helped to reduce energy consumption, and for each measure are given many options for improvement, however, in the table 3, are presented only those that are most favourable together with some thermal zones where they are most affected.

Table 3. intervetntions and some the most affected thermal zones

HEATING & COOLING DEMAND			Baseline Building	Measures M.1		Measures M.2		Measures M.3		Measures M.4		Measures M.5		Measures M.6		Measures M.7		SUMMARY		Measures M.9	
			kWh/a	kWh/a	Savings	kWh/a	Savings	kWh/a	Savings	kWh/a	Savings	kWh/a	Savings	kWh/a	Savings	kWh/a	Savings	kWh/a	Savings	kWh/a	Savings
006	Meeting, conference or seminar room	Heating	23712	22852	4%	22832	4%	19613	17%	24197	-2%	23511	1%	23509	1%	23510	1%	18965	20%	18985	20%
		Cooling	60290	60548	0%	60466	0%	54305	10%	56100	7%	60404	0%	60407	0%	60455	0%	50848	16%	50814	16%
007-1	Landscape Office (South-West)	Heating	23550	23311	1%	23541	0%	23541	0%	23550	0%	2202	91%	2147	91%	10865	54%	2018	91%	5171	78%
		Cooling	144495	144077	0%	144503	0%	144500	0%	144491	0%	125044	13%	130124	10%	147405	-2%	125147	13%	81656	43%
007-3	Landscape Office (South-East)	Heating	28368	28044	1%	28363	0%	28363	0%	28369	0%	3017	89%	2962	90%	13044	54%	2855	90%	5832	79%
		Cooling	161069	160490	0%	161074	0%	161073	0%	161064	0%	152985	5%	155195	4%	172106	-7%	152874	5%	127138	21%
001-4.1	Circulation and traffic areas (4th floor)	Heating	4383	3347	24%	3371	23%	2413	45%	4447	-1%	4095	7%	4094	7%	4084	7%	826	81%	820	81%
		Cooling	13444	14058	-5%	13841	-3%	10617	21%	12201	9%	13730	-2%	13739	-2%	13893	-3%	10656	21%	10578	21%
008-2	Personal Office (North-East)	Heating	14307	14304	0%	14299	0%	14300	0%	14307	0%	1426	90%	1425	90%	7363	49%	1628	89%	1632	89%
		Cooling	109596	109500	0%	109604	0%	109600	0%	109593	0%	88702	19%	88711	19%	103428	6%	79511	27%	79410	28%
007-4	Landscape Office (North-East)	Heating	2930	2907	1%	2929	0%	2929	0%	2931	0%	228	92%	228	92%	1228	58%	215	93%	217	93%
		Cooling	41096	41091	0%	41098	0%	41097	0%	41094	0%	34709	16%	34713	16%	42637	-4%	34553	16%	34511	16%
001-3	Circulation and traffic (Multipurpose area)	Heating	8863	8843	0%	8832	0%	8851	0%	8864	0%	1492	83%	1490	83%	8845	0%	3456	61%	1878	79%
		Cooling	47525	47564	0%	47558	0%	47533	0%	47510	0%	39588	17%	39616	17%	33325	30%	25976	45%	31955	33%

In M.1 and M.2, interventions were done in the roof (22 cm), terrace (18 cm) and building envelope (18 cm) of the 4th floor, respectively the thermal insulation with U_{roof} = 0.14 W/m^{2}K, U_{wall} = 0.16 W/m^{2}K, U_{slab} 0.05-0.07 W/m^{2}K was added. Therefore, we can say that in the thermal zone 001- 4.1 the demand for heating is reduced by 23% and 24% respectively. Figure 9, presents the details of thermal bridges for baseline building and those after interventions.
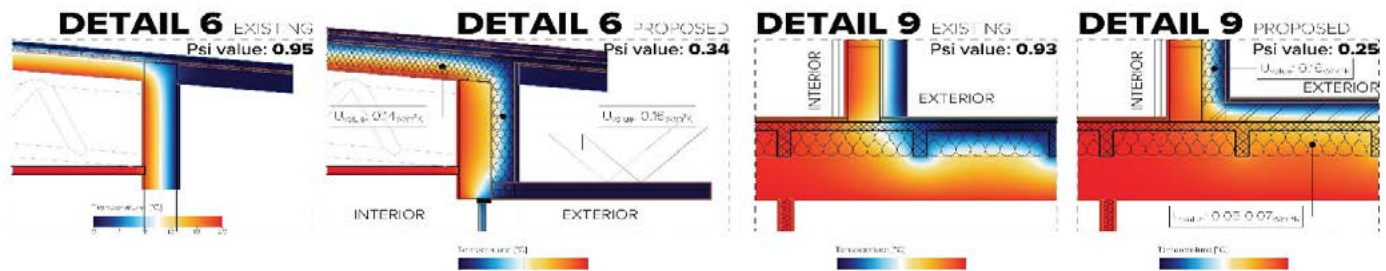

Figure 7. Thermal bridges (detali 6 is for intervention M2 and detali 09 is for M1)

In the intervention M.3, the doors and windows on the 4th floor were replaced by double glazing basic –air fill clear $U_{glazing}$ = 2.8 W/m^{2}K and basic aluminium frame U_{opaque} = 2.11 W/m^{2}K in triple glazing argon fill clear low E with $U_{glazing}$ = 0.6 W/m^{2}K and premium aluminium frame U_{opaque} = 1.86 W/m^{2}K where the reduction for heating in the thermal zone 001-4.1 is reached at 45% while for cooling at 21%. On the other hand, in the thermal zone 006 the demand for heating is reduced to 17% while for cooling 10%. After placing the shading devices on the 4th floor (M.4), in the thermal zone 001-4.1 the demand for cooling has been reduced to 9% while in the thermal zone 006 it has been reduced to 7%.

In terms of energy consumption in the office building, windows play an important role. Good design and orientation of glazed surfaces can reduce energy requirements for heating or cooling. Windows are also important for providing daylight and visibility, both of which have psychological effects. But on the other hand, glow and passive solar gain can be problematic. In addition, based on the initial analysis, we can say that here we are dealing with great solar benefits, but in this case, it is clear that the factor of reducing sunlight is more important than their gain, so we are dealing with reducing solar gains through the building envelop. But nowadays there are a lot of researches and practices that tell us about using many alternatives to improve them. In the M.5, among the available options, in this paper, in addition to the redesign of shading devices, the glasses have also been replaced from double glazing basic –air fill clear $U_{glazing}$ = 2.8 W/m^{2}K with triple glazing argon fill clear low E with $U_{glazing}$ = 0.6 W/m^{2}K, which have helped reduce the demand for heating from 83 - 92% in thermal zones where offices are organized on the south-west, south-east and north-east facades. While in the north-east facade the reduction for cooling has reached 16 - 19%, while in the south-east and south-west facades it has had a small effect at only 4-10%. Therefore, in the case when the ratio of the window surface to the floor is quite high then the difference in energy consumed between the double-glazing system and the triple glazing system indicates the contribution of the triple glazing system over the double glazing which is more stressed when windows are more exposed to sunlight in the south-west orientations, and in this case the demand to cool the indoor environment decreases as a result of lower solar benefits. The use of the triple glazing system reduces the thermal conductivity of the glass, while the thickness of the window layers increases, the thermal conductivity decreases consequently proving to us that the ability of windows to transmit heat has an inverse relationship with their thickness. So, we can say that the building envelope which is characterized by lower transmission is considered as a better thermally insulated building. From this we can say that the greater effect was in reducing the demand for heating than for cooling, and then have been made interventions in M.6

where shading devices have been extended by 0.35 cm from those existing in the South-east facade and the South-western, where the demand for heating is reduced by 89 - 91% while that for cooling only 1 - 3%. Additionally, in terms of the effect of using different types of windows and increasing or decreasing shading devices, some benefits are worth mentioning. While in M.7 interventions were made in the walls, floor and ceiling, in this case for thermal zones 007-1, 007-3, 008-2, 007-4 where the reduction of energy for heating is achieved from 49-58% while in the thermal zone 001-3 the reduction of energy for cooling is reached to 30%. Figure 10 presents thermal bridges on these interventions.
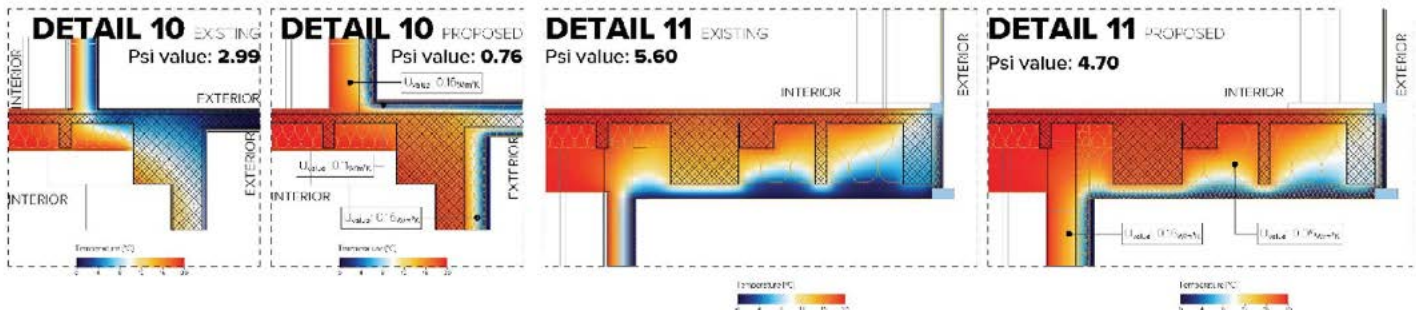

Figure 8. Thermal bridges between walls, floor and ceiling of M.7 intervention

After all these interventions, has been achieved the reduction for heating to 75%. For baseline building net heating energy was 17.79 kWh/m^{2}a and the reduction was reached to 4.48 kWh/m^{2}a. While for cooling for baseline building net heating energy was 94.48 kWh/m^{2}a was reduced to 82.54 kWh/m^{2}a or only 12%. In total the reduction of energy consumption, after many simulations and compared to baseline building has been reduced to 22%.
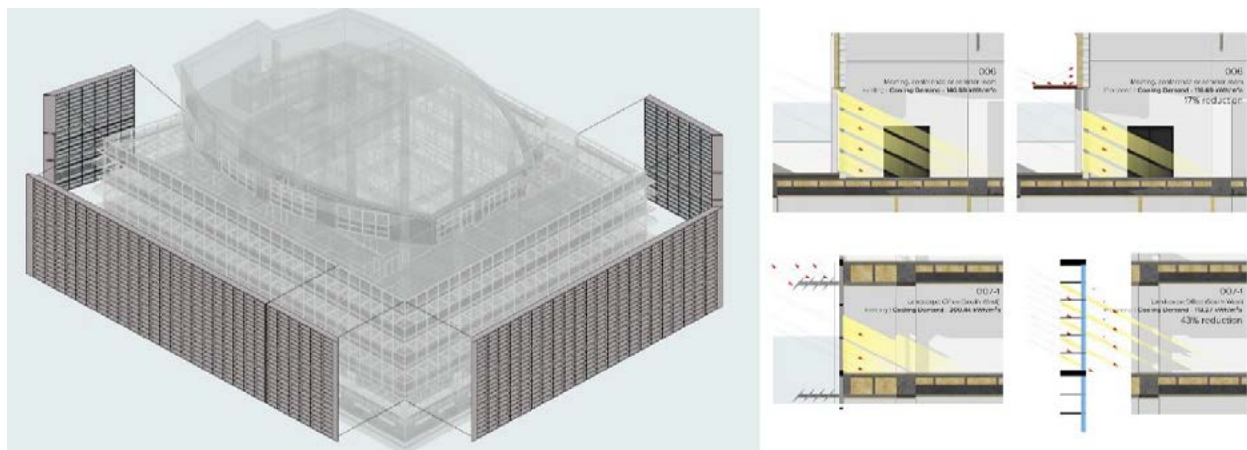

Figure 9. New structure of the facade and Integration of shading devices in 4th floor after the intervention (M.4 and M.8)

Since this result has shown that the demand for cooling is still high, and if we propose to change the structure of the facade presented in figure 12 or M.9 intervention, we can achieve the reduction of energy consumption to 51% or (heating: 17.79 in 4.96 kWh/m^{2}a while cooling: 94.48 - 49.68 kWh/m^{2}a).

4 CONCLUSIONS

To conclude, the main contribution of this paper is the calculation of energy performance in the new building of the municipality of Prishtina as well as the possibilities for interventions in buildings with the same characteristics regarding the components of the building envelope in relation to heating/cooling demands.

In order to meet the requirements for energy reductions of up to 50%, many energy simulations were performed with the aim of possible improvements, through changes and additions to the eight potential points/places in the envelope of this building.

It is clear that the results obtained after the improvements at these points in the building envelope have influenced the demand for heating and cooling to be achieved as per this target.

Annual, monthly and daily simulations were performed for the same model in the city of Peja and Ferizaj, in order to compare the results between these three different locations and to analyze whether it is acceptable for the entire territory of Kosovo to have one climatic zone. Moreover, all the simulations showed that these differences in heating and cooling demand for these cities ranged from 12 – 22%, indicating that the continental climate is acceptable for the whole country.

REFERENCES

[1] P. V. Dorizas, M. D. Groote and J. Volt, "The inner of a building - linking indoor environmental quality and energy performance in building regulation," Buildings Performance Institute Europe (BPIE), 2018.

[2] IEA and UN, "2019 Global Status - towards a zero-emissions, efficient and resilient buildings and constructi on sector," United Nations Environment Programme, 2019.

[3] D. Cottafava, S. Magariello, R. Ariano, O. Arrobbio, M. Baricco, V. Barthelmes, G. Baruzzo, M. Bonansone, L. Console, L. Contin, S. P. Corgnati and S. Dotta, "Crowdsensing for a sustainable comfort and for energy saving," *Energy and Buildings,* vol. 186, pp. 208-220, 2019.

[4] A. Toleikyte, L. Kranzl, R. Bointner, F. Bean, J. Cipriano, M. D. Groote, A. Hermelink, M. Klinski, D. Kretschmer, B. Lapilonne, R. Pascual, A. Rajkiewicz, J. Santos, S. Schimschar and C. Sebi, " Nearly Zero - Energy Building Strategy 2020," ZEBRA 2020, Wien, 2016.

[5] P. Ahmeti, I. Dalipi, A. Basha and I. Kistelegdi, "Current Heating Energy Demand by the Residential Sector in City Prishtina Based on the Main Resources," *Pollack Periodica,* vol. 12, no. 1, p. 147–158, 2017.

[6] IBRD, "Energjia në Kosovë," The Wold Bank, 30 July 2013. [Online]. Available: https://www.worldbank.org/en/country/kosovo/brief/al-energy-in-kosovo. [Accessed 01 November 2020].

[7] KAS, "Bilanci i Energjisë TM1 2020," Kosovo Agency of Statistics, Prishtina, 2020.

[8] M. Rashani and A. Mahdavi, "Energy Performance Assessment of Existing Multi-Family Apartment Buildings in Kosovo," *Energy Procedia,* vol. 78, pp. 782-787, 2015.

[9] MED, "Strategjia e Ngrohjes e Republikës së Kosovës 2011-2018," Official Gazette of the Republic of Kosovo, Prishtina, 2011.

[10] MED, "Strategjia e Energjisë e Republikës së Kosovës 2016-2025," Official Gazette of the Republic of Kosovo, Prishtina, 2016.

[11] M. Hallaqi and P. Ahmeti, "Udhëzuese Teknik i Aplikimit të masave të Efiçiencës së energjisë në Ndërtesat PUblike," Asociacioni i Arkitektëve të Kosovës, Prishtina, 2020.

[12] F. F. Hernández, J. M. Cejudo-López, J. M. Peña-Suárez, M. C. G. Muriano and S. C. Rueda, "Effects of louvers shading devices on visual comfort and energy demand of an office building. A case of study," *Energy Procedia,* vol. 140, pp. 207-216, 2017.

[13] G. Feng, D. Chi, X. Xu, B. Dou, Y. Sun and Y. Fu, "Study on the Influence of Window-wall Ratio on the Energy Consumption of Nearly Zero Energy Buildings," *Procedia Engineering,* vol. 205, pp. 730-737, 2017.

[14] G. Murano, E. Primo and V. Corrado, "The effect of glazing on nZEB performance," *Energy Procedia,* vol. 148, pp. 320-327, 2018.

[15] A. Boyano, P. Hernandez and O. Wolf, "Energy demands and potential savings in European office buildings: Case studies based on EnergyPlus simulations," *Energy and Buildings,* vol. 65, pp. 19-28, 2013.

[16] S. Ferrari and M. Beccali, "Energy-environmental and cost assessment of a set of strategies for retrofitting a public building toward nearly zero-energy building target," *Sustainable Cities and Society,* vol. 32, pp. 226-234, 2017.

[17] C. Yu, L. Tian, X. Xu and J. Wang, "Evaluation on energy and thermal performance for office buildingenvelope in different climate zones of China," *Energy and Buildings,* vol. 86, pp. 626-639, 2015.

[18] S. P. Corgnati, E. Fabrizio, M. Filippi and V. Monetti, "Reference buildings for cost optimal analysis: Method of definition and application," *Applied Energy,* vol. 102, p. 983–993, 2013.

[19] MESP, "Regulation MESP No. 02/18 on National Calculation Methodology for Integrated Energy Performance of Buildings," Ministry of Environment and Spatial Planning, Prishtina, 2018.

[20] GRAPHISOFT, "ARCHICAD - EcoDesigner STAR Computer software," [Online]. Available: https://www.graphisoft.com/archicad/ecodesigner_star/.

[21] Prishtina Municipality, "Narrativa e Prishtinës - Historik konciz i Prishtinës," Municipality of Prishtina, Prishtina, 2018.

[22] "Wikimapia," [Online]. Available: http://wikimapia.org/18665264/sq/Komuna-e-Prishtin%C3%ABs. [Accessed 2020 10 20].

[23] StruSoft, "VIP-Energy Climate data creator," NOAA-CIRES Climate Diagnostics Center, Colorado, USA, 2010.

UP

20

Vesna Zalar Serjun, Lidija Korat

Temperature pre-treatment of gypsum for powder based 3D printing technology

CoMS_
2020/21

TEMPERATURE PRE-TREATMENT OF GYPSUM FOR POWDER BASED 3D PRINTING TECHNOLOGY

Vesna Zalar Serjun[1] and Lidija Korat[2]

[1,2] Slovenian National Building and Civil Engineering Institute, Department of Materials
Dimiceva ul. 12, 1000 Ljubljana
e-mail: lidija.korat@zag.si

SUMMARY: In recent years many researchers have been involved in studies in the field of pre-treatment of various raw materials. Temperature treatment of materials results in several advantages, which have been already recognised and successfully applied in various fields of applications. Where at the same time, the practices has been adopted also in the field of 3D printing. Enhanced strength and stiffness, assuring desirable performance criteria of the 3D printed models, reflect the most important characteristics. 3D printing binder jetting technology is based on the application of liquid binders onto powdered material, where gypsum powders have been commercially used as a base raw material. As natural raw materials can be replaced by other materials, such as recycled industrial by products, the aim of this research work was to evaluate the potential usage of three synthetic gypsum powders from different industrial processes for 3D printing. The investigation covered (a) mineralogical and microstructural characteristics of gypsums from different origin and (b) the effect of pre-treatment of gypsum powders at different temperatures (up to 500 °C). On the basis of the results, the most promising temperature regime for each different waste gypsum powder treatment, reflecting in the most optimal setting time, was defined. Synthetic gypsums were characterized by X-ray diffraction (QXRD), scanning electron microscopy (SEM) and differential thermal analysis (TG/DTA). The results showed that all three synthetic gypsums (calcium sulfate dihydrate, $CaSO_4 \cdot 2H_2O$) thermally degrade into calcium sulfate anhydrite ($CaSO_4$) via an intermediate calcium sulfate hemihydrate ($CaSO_4 \cdot \frac{1}{2}H_2O$, bassanite) phase. Microstructural and mineralogical differences were observed when temperature treated gypsums from different origins were compared. The detailed knowledge of gypsum powder properties at different temperature regime is important parameter for the assurance of 3D printing key parameters such as flowability, roughness and wettability, especially for determination of saturation levels and setting time. After all, these parameters define final mechanical properties of 3D printed structures. By using such approach, the understanding of material compatibility for 3D printing technology can be defined and improved if necessary.

KEY WORDS: synthetic gypsum, 3D printing, binder jetting, pre-treatment, temperature.

1 INTRODUCTION

3D printing or additive manufacturing is well-known technology, usable in different fields of application, distinguished in terms of their approach to joining the layers [1]. Products are made by means of specialized digital geometric models, using layer-by-layer technology, where different binders form solid objects with defined properties. One of the seven generic groups is binder jetting technology, which is based on the application of liquid binders onto particles of "gypsum like" powder base material [1]. To improve environmental awareness and achieve an economically viable solution, **synthetic gypsum** as industrial by-product, can be used **to replace commercially available powders in 3D printing**.

Synthetic gypsum is generated in vast quantities, but its disposal is an ongoing issue. In order to achieve the efficient recycling of synthetic gypsum a long-term strategy is vitally needed [2]. Its **recycling** leads to socioeconomic and environmental benefits and is already used in several applications, such as in cement production [2,3], as material for soil stabilization [4], as building material and binder [5], as asphaltic bitumen modifier and as material for road pavement [6,7]. Recently, only few researchers have investigated recycling materials for their usage in 3D printing [8,9]. To the best of the author's knowledge, no cases of application of the waste gypsum as a raw material for 3D printing are described in the literature. It should be noted that such powders should have comparable characteristics to conventional ones. To achieve such properties, some pre-treatment processes are usually applied.

Research in the field of **pre-treatment** of various raw materials have been broadly engaged in last year's [10,11] using different processes (kiln residence time, high and low temperatures) [2,12], focused on converting gypsum to hemihydrate or anhydrite. Calcium sulphate dihydrate (gypsum) starts to convert at temperatures less than 200°C into two different modifications of calcium sulphate hemihydrate (basanite): α-hemihydrate and β-hemihydrate. The α-hemihydrate is obtained at temperatures between 120 – 160 °C with a hydrothermal reaction at high pressures (up to 8 bar) which demands a more complex production process [2]. The α-hemihydrate is applied in applications where higher strengths of the products are expected (e.g. sculptures) [2]. β-hemihydrate is obtained at temperatures between 120 – 180 °C through the dry calcination of gypsum which is more economical process. The β-hemihydrate is commonly applied in applications as a binding material in civil construction (e.g., plasterboard production) [2,13,14,15].

In order to systematically define the **calcination mechanism**, Liu et. al. [16] evaluated phosphogypsum calcination treatment at the temperature of 150 °C, 350 °C, 600 °C and 800 °C with calcination time of 0.5 h, 1 h, 1.5 h and 2 h. The modification effect varied with calcination temperature and calcination time. The results have shown that 90% of the setting time was shortened after calcination temperature of 350 °C for 2 h. Bumanis et al. [17] researched calcination of phosphogypsum at temperatures of 100 °C, 120°C, 140 °C, 160 °C and 180 °C for 4 h to obtain a binder material. The results have shown that higher heat temperature treatment of phosphogypsum reduces time of decomposition of phosphogypsum to hemihydrate and slightly increase the initial setting time of obtained binder. Another conclusion was that the increase of heat temperature from 120 °C to 180 °C did not improve the final compressive strength of the pastes. Koper [11] investigated four different temperatures ranging from 170 to 190 °C (samples with a constant water to gypsum ratio of w/g = 0.75). It was noted that the calcination temperature influenced the setting time of the gypsum. As concluded by Rossetto et. al. [18], the gypsum setting can be described as a physical phenomenon where gypsum crystal nuclei are formed, so dihydrate crystals start precipitating, increasing the consistency of the paste (initial setting time). With the increase in the rate of hydration reaction the paste attains sufficient hardness to support stress (final setting time). The gain of strength is defined as hardening. Recently, knowledge has progressed in the field of 3D printing, reflecting the enhancement in the strength and stiffness of the 3D printed models which meet their performance criteria.

Present research is focused on evaluation of the influence of calcination conditions (temperature) of different gypsums powders on setting time. This parameter is crucial in 3D printing technology. Different analytical techniques were used to characterize calcined gypsum powders (e.g., thermogravimetry (TG), differential thermal analysis (DTA), X-ray diffraction (XRD), and scanning electron microscopy (SEM)).

2 MATERIALS AND METHODS

Synthetic gypsum powders used within this work were originated from different industrial processes. The first one originated from flue gas desulfurization process (designated as G1), the second one from acid-neutralizing industrial processes (designated as G2) and the third one from the wastewater treatment process during crystal glass production (designated as 3). Thermal pre-treatment of samples was performed in a laboratory furnace at different temperatures between 40-500 °C for ~5h (150 °C/h and 2h holding). QXRD, TG/DTA and SEM were used for mineral and microstructure characterisation. As a reference, commercial powder Zp151 from the 3DSystems manufacturer was used in Vicat testing.

The thermal **gravimetry and differential thermal analysis (TG/DTA)** measurements were performed using a STA 409 PC Luxx thermal analyser. Powders of 25 mg were used and analysed in the Al_2O_3 crucibles in the temperature range of 25 to 600 °C with heating rate of 10 K/min in the atmosphere of synthetic air 5.0 was used.

The phase composition was defined by quantitative **X-ray diffraction analysis (QXRD)**, using an Empyrean (PANalytical, Netherlands) diffractometer with Cu-Kα radiation and Rietveld refinement procedure. Powder diffraction data were collected at a tube tension of 40 kV and a tube current of 45 mA using a 2θ step size of 0.01° and measurement time of 100 s per step. The results were analyzed by Highscore (PANalytical, Netherlands) diffraction software, using the Powder Diffraction File PDF-4+ (ICDD, USA) database as the reference source of data. The data was collected at ambient temperature in a range from 5 to 70° (2θ). For the quantification of gypsum, basanite and anhydrite, the ICSD collection codes 2057, 69060 and 16382 respectively, was used.

Morphology and microstructure were investigated, by means of a scanning electron microscope (SEM, JEOL JSM IT500, Japan), equipped with energy dispersive spectroscopy (EDS, Oxford instruments, UK). The SEM/EDS analyses

were performed in low-vacuum mode with a chamber pressure of 90 - 100 Pa, and an accelerating voltage of 15- 20 kV. These analyses were performed on raw samples.

Setting time of gypsum powders were tested by Vicat consistency needle penetration method, following the standard SIST EN 196-3:2017 [19]. Water binder ratio was 0.62, where the needle was indented into paste with the interval off 1 min. All powders used in this testing have the same granulation, 48 % were <45 μm, 31 % in the range between 45-63 μm and 21 % in the range between 63-90 μm.

3 RESULTS

3.1 Thermal behaviour of synthetic gypsums

The results of the TG-DTG analysis are presented in Fig. 1. The TG curves shows a total mass loss of all the samples in the temperature range up to 180°C, which corresponds to the loss of structural water. DTA data involves two overlapped processes in the range from 120 to 180°C, assigned to endothermic effect. First major peak at ~150°C is attributed to the partial dehydration of the gypsum to calcium sulphate hemihydrate, while the second one at ~165°C corresponding to the complete dehydration of the gypsum. Small exothermic effect appears around 350°C and is assigned to the phase transition of hexagonal anhydrite III to orthorhombic anhydrite II [10]. Total mass loses are similar for samples G1 and G2, while for G3 larger total mass loss was defined.
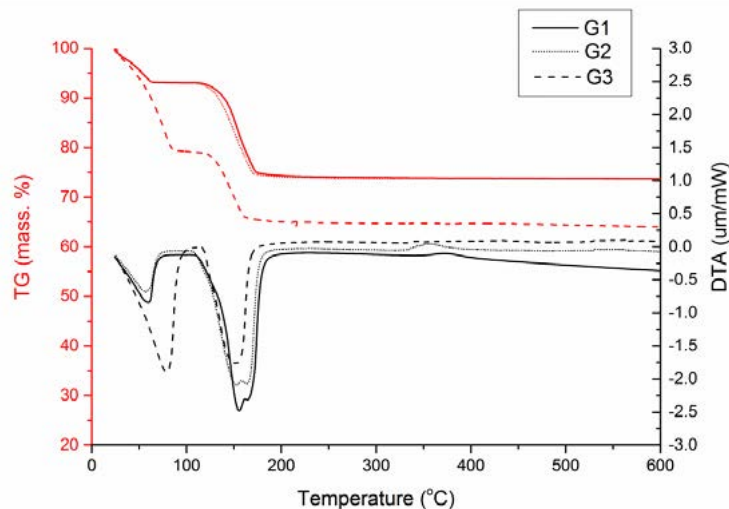

Figure 1: Thermal curves of the synthetic gypsum powders

3.2 XRD analysis

Qualitative analysis of the gypsums treated at different temperatures is shown in Fig 2. The results show, that in the temperature range of 80-90 °C, the gypsum starts to convert to basanite. The newly formed basanite is present in the samples up to 400 °C while with further increase in temperature it is fully converted to anhydrite.

Quantitative XRD was further performed on the samples treated at 40 °C, 200 °C and 300 °C in order to define the ratios of the different phases present in each sample. The results are shown in Table 1. The samples G1 and G2 exposed to temperature 40 °C are composed of gypsum (> 99 wt.) while only a very small fraction (< 1 wt. %) appears to be present as constituent phases in traces (quartz, calcite). The sample G3 composes fully of gypsum. After calcination at 200 °C, gypsum dehydrates completely to calcium sulphate hemihydrate (basanite) in all the investigated samples. The 1 wt. % of anhydrite defined in G3 at 200 °C was assigned to the effect of sample preparation. After the calcination at the temperature of 300 °C the basanite starts to convert to anhydrite. At this temperature of pre-treatment, the differences in the phase composition of the investigated gypsums are the most prominent. The highest quantity of basanite converted to anhydrite was characterized for the G2, while the smallest for the G3.
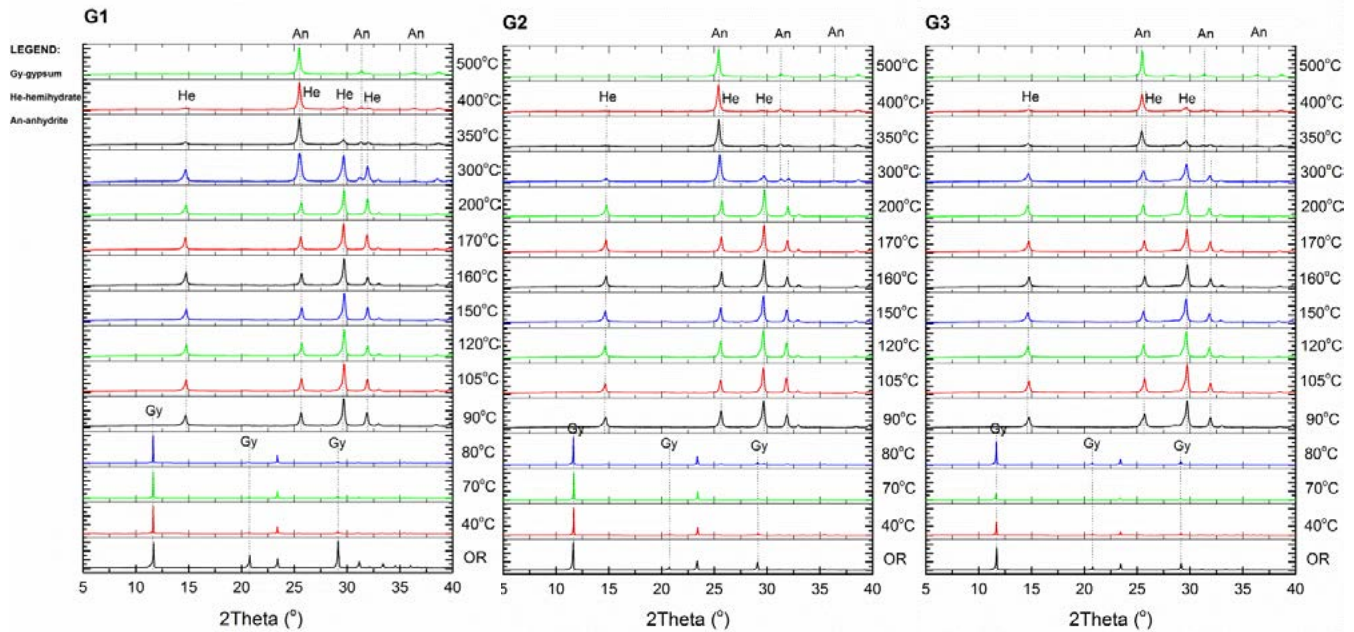
Figure 2: XRD patterns of the synthetic gypsum powders, pre-treated at different temperatures (OR: non-treated powder)

Table 1: QXRD analysis (wt. %) of phases within synthetic gypsum powders

Sample designation with temperature range (°C)	40°C			200°C			300°C		
	G1	G2	G3	G1	G2	G3	G1	G2	G3
Gypsum (wt. %)	99.3	99	100	0	0	0	0	0	0
Bassanite (wt. %)	0	0	0	100	100	99	71.8	36.3	93.8
Anhydrite (wt. %)	0	0	0	0	0	1	28.2	63.7	6.2

3.3 Scanning electron microscopy

Fig. 3 shows the effects of temperature treatment on gypsum powders microstructure. SEM images of powders exposed to the lower temperature present their different morphological appearance. Typical prismatic and short thick prismatic gypsum crystals were identified in powder G1. In G2, elongated gypsum crystals are prevailing over thick short prismatic crystals. The grains of G3 appear mostly in lenticular prismatic form. Twinned gypsum crystals are well defined in all the three of the samples. Calcination of the gypsum samples resembles in the surface morphology of the grains. As temperature increases, the etch pits are increasing on the grain surfaces and the stratification along the cleavage by the crystalline domains is expressed more distinctly.
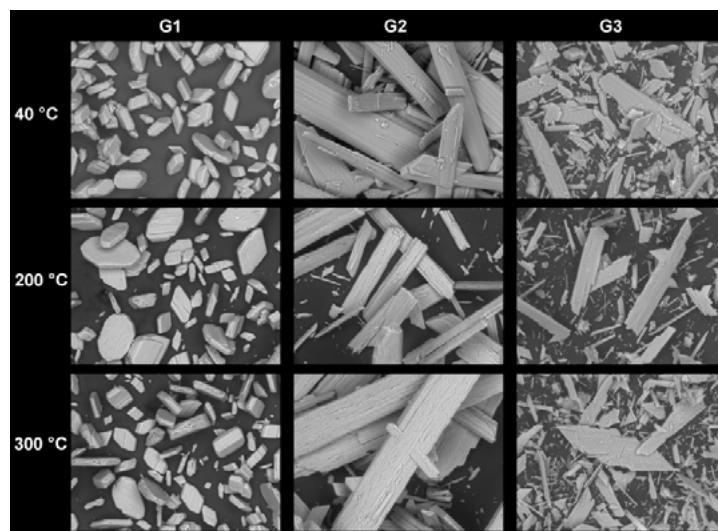

Figure 3: SEM microimages of the synthetic gypsum powders, pre-treated at different temperatures (400x magnification)

3.4 Setting time

The results of setting times are given in Table 2 and as is seen, setting times of all powders are very short, especially those which were exposed at higher temperatures. Setting times differs slightly between powders regarding the powder origin and different amount of present mineral phases. The results of gypsum powders, treated at 40 °C, have shown very prolonged setting time, even up to one day. The initial setting time decreases with the increasing temperature and decreased amount of bassanite, even less than 1 min. The final setting time ranges from 5 minutes to 13 minutes, regarding the chosen powder. The results were compared with the behaviour of reference powder, showing longer setting time. Our results are in comparison with the literature [20], where commercially obtained calcined gypsum initial setting time was 8 min and final 11 min (w/b=0.67 and 75 wt. % of bassanite). Rossetto et al. [18] have shown similar setting time of recycled gypsum plaster where initial setting time was 5.3 min and final 8.3 min (w/b=0.7 and 150°C for 4h).

The results have shown that with decreasing amount of basanite the setting time in powders is faster. Also small volume changes have occurred during setting. This needs to be highlighted, because volume instability may greatly affect the the properties of material in solid state [20]. After mixing gypsum powders with water, calcium sulphate hemihydrate starts to shrink immediately after it gets in contact with water. Further, it expands only slightly. The shrinkage is caused by the chemical reaction between the water and hemihydrate [20] while the expansion of gypsum during its setting is caused by the crystallization [20].

Table 2: Setting time (min) of synthetic gypsum powders

Sample designation with temperature range (°C)	Reference Zp151	200°C			250°C			300°C			400°C		
		G1	G2	G3	G1	G2	G3	G1	G2	G3	G1	G2	G3
Initial setting time (min, s)	17	7	6	<1	3,20	9	8	1,30	4	9,30	<1	<1	4
Final setting time (min, s)	27	9,20	8,30	-	5	11	13	2,30	6,30	13	-	-	8

4 CONCLUSIONS

Within this research, thermal analysis, mineralogical compositions and microstructure of thermally treated gypsums from different origin were analysed. Additionally the influence of calcination temperature on setting time was determined. On the basis of the research, it was found that the increase in temperature changed physical-chemical properties of powders and showed higher hemihydrate content. XRD results proved that calcination affected the hemihydrate formation, showing that the calcination condition was important for setting time. A temperature of 200 °C were found as adequate parameter to obtain considerable hemihydrate content and still performed setting time of 6-7 min. Therefore, such synthetic gypsum powders are very promising substitutes for commercial gypsum in additive technology, and consequently, it may lead to the mitigation of the environmental impact related to the waste gypsum production. Future studies must include additional research in the field of defining the influence of calcination temperature below 200°C and possible additives on setting time, as well as mechanical properties.

ACKNOWLEDGMENTS

REFERENCES

[1] ASTM International F2792-10, Standard Terminology for Additive Manufacturing Technologies, ASTM International, West Conshohocken, PA (2010)
[2] Geraldo, R.H., et al: Calcination parameters on phosphogypsum waste recycling, *Construction and Building Materials*, Vol. 256 (2020), pp. 119406

[3] Shen, P. et al., Hydration of quaternary phase-gypsum system, *Construction and Building Materials*, Vol. 152 (2017), pp. 145–153

[4] Xue, S. et al., Phosphogypsum stabilization of bauxite residue: conversion of its alkaline characteristics, *Journal of Environmental Sciences*, Vol. 77 (2019), pp. 1-10

[5] Tian, T., et al., Utilization of original phosphogypsum for the preparation of foam concrete, *Construction and Building Materials*, Vol. 115 (2016), pp. 143-152

[6] Cuadri, A.A., et. Al., Valorization of phosphogypsum waste as asphaltic bitumen modifier, *Journal of Hazardous Materials*, Vol. 279 (2014) pp. 11–16

[7] Amrani, M., et.al., Phosphogypsum recycling: new horizons for a more sustainable road material application*, Journal of Building Engineering*, Vol. 30 (2020), 101267

[8] Domingues, J. et al., An additive manufacturing solution to produce big green parts from tires and recycled plastics, *Procedia Manufacturing*, Vol. 12 (2017), pp. 242-248

[9] Asgari, H. et. al., On microstructured and mechanical properties of additively manufactured AlSi10Mg_200C using recycled powder, *Materials Science and Engineering: A*, Vol. 707 (2017), pp. 148-158

[10] El Hazzat, M., et. al., Novel approach to thermal degradation kinetics of gypsum: application of peak deconvolution and Model-Free isoconversional method, *Journal of Thermal Analysis and Calorimetry* Vol. 140 (2020), pp. 657–671

[11] Koper, A., et al., Influence of the Calcination Temperature of Synthetic Gypsum on the Particle Size Distribution and Setting Time of Modified Building Materials, *Energies*, Vol. 13 (2020) pp. 5759

[12] Ma, B., et. al., Utilization of hemihydrate phosphogypsum for the preparation of porous sound absorbing material, *Construction and Building Materials*, Vol. 234 (2020), pp. 117346

[13] Gurgul, S.J., et al., A kinetic and mechanistic study into the transformation of calcium sulfate hemihydrate to dihydrate, *J. Synchrotron Radiat.,* Vol. 26 (2019) pp. 774–784

[14] Singh, N.B. and Middendorf, B., Calcium sulphate hemihydrate hydration leading to gypsum crystallization, *Prog. Cryst. Growth Charact. Mater.*, Vol. 53 (2007), pp. 57–77

[15] Geraldo, R.H., et. al., Gypsum plaster waste recycling: a potential environmental and industrial solution, *J. Clean. Prod.*, Vol. 164 (2017), pp. 288–300

[16] Liu, S., et. al., Mechanism of calcination modification of phosphogypsum and its effect on the hydration properties of phosphogypsum-based supersulfated cement, *Construction and Building Materials*, Vol. 243 (2020), pp. 118226

[17] Bumanis, G., Technological properties of phosphogypsum binder obtained from fertilizer production waste, *Energy Proc.* Vol. 147 (2018), pp. 301–308

[18] Rossetto, J.R.M., et. al., Gypsum plaster waste recycling: analysis of calcination time, Key Eng. Mater., Vol. 668 (2016), pp. 312–321

[19] SIST EN 196-3:2017, Methods of testing cement - Part 3: Determination of setting times and soundness. Brussels, European Committee for Standardisation